NOTE TO USERS

This reproduction is the best copy available.

uOttawa

L'Université canadienne
Canada's university

FACULTÉ DES ÉTUDES SUPÉRIEURES ET POSTDOCTORALES

uOttawa

L'Université canadienne
Canada's university

FACULTY OF GRADUATE AND POSTDOCTORAL STUDIES

Benjamin Moulton
AUTEUR DE LA THÈSE / AUTHOR OF THESIS

M.Sc. (Earth Sciences)
GRADE / DEGREE

Department of Earth Sciences
FACULTÉ, ÉCOLE, DÉPARTEMENT / FACULTY, SCHOOL, DEPARTMENT

Volcanology and Geochemistry of the Prosser Township Rhyolites, Timmins, Ontario: A Study of Submarine Coulées, Alteration and the Mobility of Elements

TITRE DE LA THÈSE / TITLE OF THESIS

Dr. A. Fowler
DIRECTEUR (DIRECTRICE) DE LA THÈSE / THESIS SUPERVISOR

Dr. J. Ayer
CO-DIRECTEUR (CO-DIRECTRICE) DE LA THÈSE / THESIS CO-SUPERVISOR

EXAMINATEURS (EXAMINATRICES) DE LA THÈSE / THESIS EXAMINERS

Dr. B. Cousens

Dr. M. Hannington

Gary W. Slater
Le Doyen de la Faculté des études supérieures et postdoctorales / Dean of the Faculty of Graduate and Postdoctoral Studies

Volcanology and Geochemistry of the Prosser Township Rhyolites, Timmins, Ontario: A study of submarine coulées, alteration and the mobility of elements.

By

Benjamin John Albert Moulton

Thesis submitted to the
Faculty of Graduate & Postdoctoral Studies
University of Ottawa
In partial fulfillment of the requirements for the
M.Sc. degree in the Earth Sciences

Ottawa-Carleton Geoscience Center
And
University of Ottawa
Ottawa,Canada

Your file Votre référence
ISBN: 978-0-494-58185-8
Our file Notre référence
ISBN: 978-0-494-58185-8

Abstract

Large scale mapping in Prosser Township has revealed an entirely felsic subaqueous volcanic sequence containing both pyroclastic and effusive high silica rhyolites which are exceptionally well preserved. The eruption sequence alternates between thin coulées and tuffaceous units, all of which are covered by two distinct units, a pumice- and spatter-rich tuff breccia and a quartz porphyritic rhyolite.

Aphyric coulées are well preserved, having flow banding, perlite, and hyaloclastite, which are indicative of a glassy protolith. In the coulée interior there is no evidence of sea-floor clay alteration; the former glass has been isochemically recrystallized to an inter-grown mixture of quartz and plagioclase during metamorphism.

These formerly glassy rhyolites formed thin flows by normal effusive eruption without the intervention of high temperatures or volatile depolymerising agents. The crystal-poor rocks were not erupted near their liquidus temperatures (ca. 980°C) as suggested by earlier work using zircon saturation thermometry, but instead the Ti-in-zircon thermometer demonstrates they were erupted around 830°C.

Detailed petrography has allowed the robust determination of a protolith composition which is used to assess mobility of the rare earth and high field strength elements. The rare earth elements are shown to be considerably mobile, approximately by a factor of three within a single, 6 m thick coulée. In contrast the HFSE, with the exception of Pb and Y, have only been mobilized up to 10%, largely as a result of sericitization and chloritization. The Nb/Zr vs. Al_2O_3/TiO_2 diagram reliably discriminates between aphyric and quartz porphyritic rhyolite units which respectively correlate with the Lower and Upper members of the nearby Kidd Creek deposit. Furthermore the Hf-Th-Ta diagram shows a clear magmatic evolutionary trend towards the Hf apex. This is consistent with observed zircon abundances within the aphyric rhyolite coulées.

The volcanological, textural and lithogeochemical work allows for the correlation of the Prosser Township rocks to the adjacent Kidd Creek mine stratigraphic sequence. However, the Middle member at the mine, a volcanoclastic unit which separates aphyric and quartz porphyritic lavas, is found as a pyroclastic pumice- and spatter-rich tuff breccia at Prosser Township that has not been previously described in the area. As such it may provide a suitable host rock for hydrothermal massive sulphide mineralization.

Résumé

Cartographie à grande échelle de Prosser Township révèlent un système volcanique sous-marin entièrement felsique ayant des produits rhyolitiques explosives, pyroclastiques et effusives bien préservées. Les séquences d'éruption comprend une alternation de minces coulées et unitées tufacées qui sont recouverts de deux unités distincts; une brèche de tuf riche en ponce et en 'spatter' *(pumice- and spatter-rich tuff breccia)* et une rhyolite porphyrique à phénocristal de quartz.

Les coulées aphanitique sont bien préservées et contiennent des bandes d'écoulement, de l'hyaloclastite et de la perlite, qui sont tous des indicateurs dune roche mère vitreux. Il n'y à pas d'évidence d'altération argileuse (hydrothermal?) a l'intérieur de ces coulées. Tant qu'il n'y a pas de vitre observée, le mélange enchevêtrées de quartz et de plagioclase est inférer d'être l'équivalent isochimique métamorphosé et recrystallizé. Les rhyolites vitreux ont formées de minces coulées par éruption effusif normal et non par éruption près de la liquidus thermique, ni à cause de concentration de volatiles. Bien que ces roches aphanitiques n'aient pas enté en éruption près de leur liquidus thermique, suggéré par la thermométrie à zircons saturées, les températures Ti-in-zircon indiquent que ces laves ont étés mis en éruption à approximativement 830°C.

La composition de la roche-mère à été déterminée avec confiance en employant des observations pétrographique détaillées des roches. À tour de rôle, la composition à été utilisé pour évaluer la mobilité des éléments terre rare et les HFSE. Les éléments terre rares sont très mobiles, ayant des variations de jusqu'à, ou plus que, trois fois sur un interval de 5 m dans une seul coulée. Par contraste les HFSE, avec l'exception de Pb et Y, ont été mobilisé à 10% avec la sericitization et chloritization.

Par conséquent, la discrimination des rhyolites aphanitique et porphyrique, ainsi que leur positionnement relative dans les membres Lower et Upper du gisement Kidd Creek, est possible en visant la relation Nb/Zr vs. Al_2O_3/TiO_2. L'évolution magmatique vers un apex HF est clairement démontrée dans le diagramme Hf-Th-Ta. Cela est d'accord avec les abondances de zircon observées dans les coulées de rhyolite aphanitique et suggère que le thermomètre Ti-in-zircon enregistre une estimation plus exacte des conditions d'éruption.

Cette corrélation positive volcanologique, textural et lithogéochimique confirme que la stratigraphie associé au gisement Kidd Creek est partagée avec Prosser Township. Par conte, le membre Central, qui séparent les laves aphanitique et porphyrique, et qui comprend une brèche pyroclastique riche en ponce et 'spatter', fut une nouvelle unité d'après les expériences de l'auteur. Néanmoins ces roches poreuses et perméables pourraient fournir un endroit convenable pour des sulfures massifs hydrothermaux.

For my family, who have been there for me
throughout the trials and tribulations involved in this process.

Though a challenge, we've faced this past year
we are not weakened but stronger for it.

You've prepared me for whatever comes next,
Love your son and brother.

Acknowledgements

First and foremost I would like to thank Tony Fowler for his supervision, guidance and support throughout all of the trials involved in finishing this thesis. You have provided opportunity after opportunity for me and have truly enhanced my education.

This study would also not be possible without the help of Patrick Mercier-Langevin from the Geological Survey of Canada, who through TGI-3, provided honest and critical reviews at each phase of this study. I would like to thank you for your mentorship and for the time you've invested in me to make this thesis that much better.

Thank-you Ben Berger and John Ayer of the Ontario Geologic Survey who repeatedly helped in the field and gave me the opportunity to present my research. Both of you also made dinners up in Timmins much more interesting!

Furthermore I would like to thank George Mrazek who makes the most beautiful thin sections which have allowed for the photomicrographs show here.

Peter Jones, thank-you, for help navigating through the physics that is electron microprobe work. You've spent a lot of time working on the zircon thermometry standards and the rare earth minerals and I really appreciate that.

I would also like to thank Richard Taylor, who first introduced me to rare earth minerals and all the wonder and complication associated with them! I would like to also thank Dr. Anthony Mariano who identified these weird and wonderful beasts.

Finally to my many friends (of who there are too many names to record) at the Ottawa-Carleton Earth Science Departments who have kept life fun and provided endless nights of philosophy. I would like to especially thank John Jamieson with whom I have had countless insightful discussions and even more beers which have had a great impact on this thesis. Also I would like to thank Steve Zhang and Lilian Navarro both of whom have opened up their worlds to me and have greatly alleviated my ignorance.

Last but not least I would like to thank Nick Proulx, for putting up with me in the field and who also threw Tony's pillow in the mud and got the truck stuck at the end of the Black Pearl road!

Table of Contents

List of Tables

List of Figures

Chapter 1 – Introduction

1.1 Kidd-Munro Assemblage

The Kidd-Munro Assemblage (KMA) is a collection of Archean lithological and time equivalent volcanic rocks and minor argillaceous sedimentary rocks that discontinuously extend as a narrow (<20 km) belt over ~200 km within the Abitibi greenstone belt of northern Ontario (Fig. 1.1) and possibly continues into Québec as the Lanaudière Formation (Pilote et al., 2007). It was originally defined as a "THOLKOM-type" assemblage by Jackson and Fyon (1991) as it predominantly consists of komatiitic and tholeiitic affinity volcanic rocks. Ayer et al. (2002; and references therein), on the basis of U-Pb zircon geochronology (TIMS and SHRIMP) have dated the KMA rocks as ranging from 2719 to 2710 Ma. The KMA conformably overlies the Stoughton-Roquemaure Assemblage (2723 – 2720 Ma) and in turn is overlain by the Tisdale Assemblage (2710 – 2703 Ma; Ayer et al. (2002). The lower part of the KMA consists of calc-alkaline intermediate to felsic volcanic rocks (~10%) whereas the upper part consists mainly of tholeiitic basalt (~75%) and lesser amounts of komatiite (~10%), and intermediate to felsic tholeiitic rocks (~5%; Ayer et al., 2005 and references therein).

The KMA hosts the giant Kidd Creek volcanic massive sulphide deposit that contains 181 Mt of ore grading 9.47 wt % metals (Cu + Zn + Pb; Galley et al., 2007). This deposit is by far the most important deposit in the KMA as the next largest deposit, west of Kidd Creek, is the Kam-Kotia mine which has produced only ~6 million metric tons of low grade ore (2.26 wt. % Cu + Zn; Hannington et al., 1999a). Roughly 100 kilometers to the east, the nearest past producer to Kidd Creek is found in Munro Township; the Potter mine (Ayer et al., 1999). This is a low grade (1.13 wt. % combined Cu + Zn), low tonnage (485 210 metric tons) volcanic massive sulfide deposit (Hannington et al., 1999a). Between the Kidd Creek and the Potter deposits the stratigraphy is almost continuous, however no deposits have been defined. Therefore exploration and research of the nearby KMA rocks is warranted as there is a lack of deposits in between Kidd Creek and the Potter Mine.

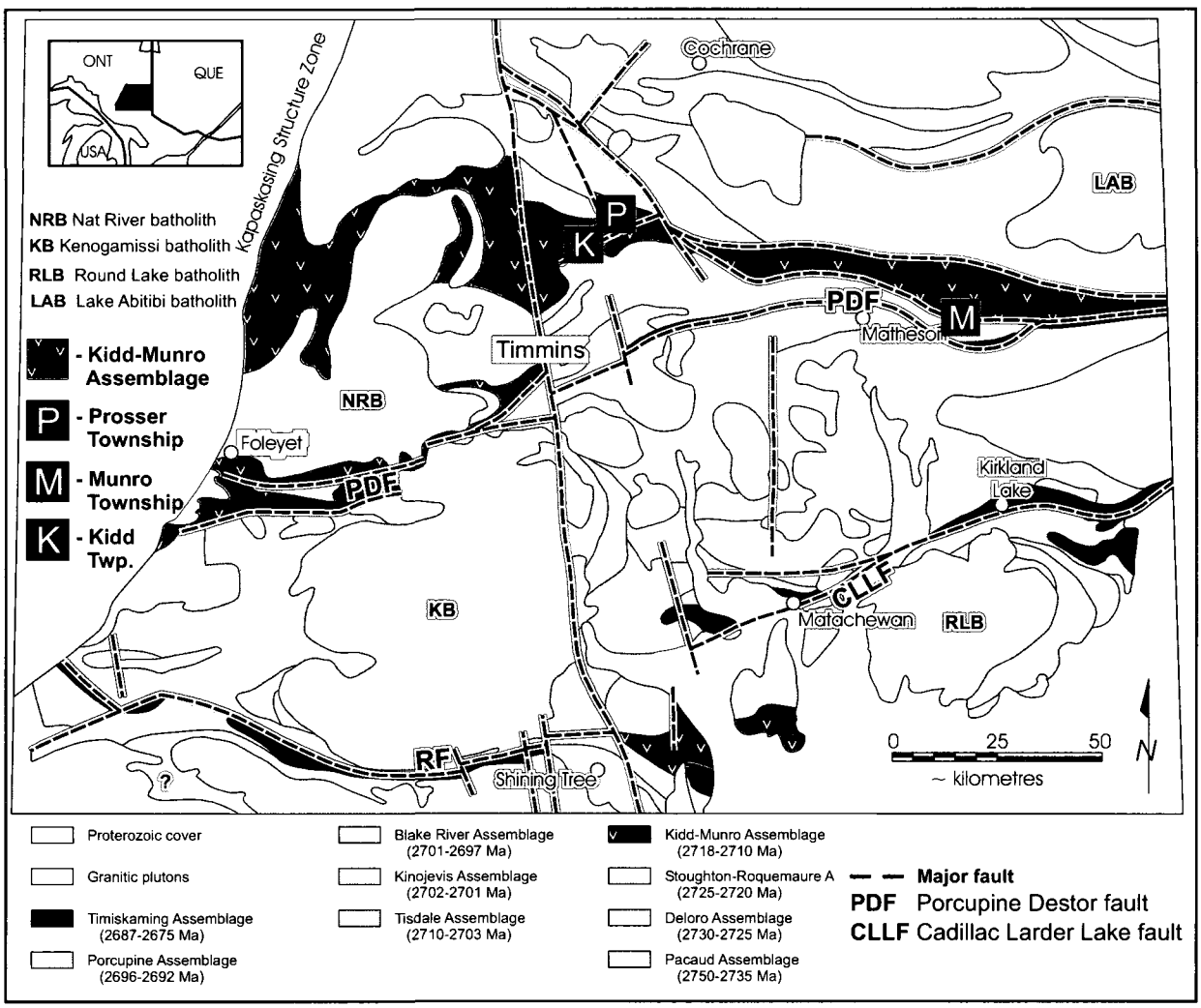

Figure 1.1. Regional geology showing the position of Prosser Township as well as the distribution of the Kidd-Munro Assemblage (modified from Ayer et al., 2002). The Kidd Creek mine is located near the center of Kidd Township.

1.2 Purpose of Study

1. First and foremost this study aims to describe the stratigraphy of the KMA in Prosser Township (~15 kilometers northeast of Kidd Creek) in order to compare the Prosser Township rocks with the stratigraphy established at the Kidd Creek deposit. This study focuses on three key outcrops identified by Ben Berger of Ontario Geological Survey who recently mapped Prosser Township (OGS, 2007).
2. The regional scale map patterns indicate that rhyolitic units of the KMA are unusually thin and therefore another objective of this study to determine the mode of emplacement of these atypical felsic units. Very large scale mapping is used to document the stratigraphy and depositional facies (Chapter 2) and to characterize the rocks in terms of modern volcanology.
3. Upon determining the macroscopic facies, petrographic descriptions were used to further understanding the mineralogy and to provide context for the interpretation of lithogeochemical data. (Chapter 3).
4. The lithogeochemistry in tandem with petrography is used to determine a least altered protolith composition in order to compare with least altered compositions of Schandl et al., (1999), Prior et al., (1999b) and Koopman et al., (1999) allowing for a robust comparison between the lithogeochemistry of Prosser Township and the Kidd Creek deposit (Chapter 4).
5. Lastly, Chapter 5 compares the titanium-in-zircon thermometer of Watson et al., (2006) with the older zircon saturation thermometer of Watson and Harrison (1983) to assess their respective results and provide an updated view of zircon geothermometers. Further more these results are used to test the inference that these lavas were erupted at or near their liquidus temperature as put forth by Barrie, (1995).

Field work was carried out from a base camp along Black Pearl Road, Prosser Township, during six weeks in the summer of 2006 with many subsequent short duration excursions to the outcrops. Outcrops were gridded at the 2 and 5 meter scales. The grid centers, 0 mN, 0 mE, were measured using a Garmin GPSMap 76CX. Grid centers are an

average reading accurate to within 3 meters. A portable rock saw was used to cut precise samples for lithogeochemistry and petrography from the units of interest.

Chapter 2 – Volcanology of Prosser Township

2.1 Detailed volcanology of select outcrops in Prosser Township

Prosser Township (Fig. 2.1) is located directly northeast of Kidd Township and approximately 13 km northeast of the Kidd Creek mine (Fig. 1.1). Outcrops are sparse, comprising only 1% of the area within the township. Cleavage bedding relationships in nearby pillow basalts and township mapping by Berger et al., (2007) and the Ontario Geological Survey (2007) indicate that the mapped outcrops are located close to a fold hinge responsible for steep to vertical lithological contacts. All outcrops are described from oldest to youngest as inferred by facing directions and correlation with the Kidd Creek mine stratigraphy. Individual outcrops are described in stratigraphic order. Facing directions were determined by reliable indicators such as peperitic injections, sedimentary reworking, draping of ash and rhyolite flow morphologies. Structural complications are inferred to be minor due to excellent preservation of primary structures, weak development of structural fabric and close proximity of outcrops, generally less than 500 m. A generalized stratigraphy of these outcrops is shown in Figure 2.2. All rock units throughout are described using the nomenclature of White and Houghton (2006; based upon the grain size classification of Fisher (1961).

2.1.1 Prosser Outcrop 1

Rocks of Prosser Outcrop 1 in are interpreted to be the oldest (Fig. 2.3) in the exposed stratigraphic sequence and were mapped at the 1:500 scale. Bedding is sub-vertical, the rocks show little deformation and consist of interfingered intermediate tuff, rhyolitic volcaniclastic rocks and coherent rhyolite. Stratigraphy youngs to the south based on peperitic injections of rhyolite into the underlying tuff and general rhyolite flow morphology where flow-banding is parallel adjacent to the lower contact and more contorted towards the upper margin (Cas and Wright, 1987; McPhie et al., 1993)

The oldest unit mapped is a massive, very fine-grained grey-brown rock composed of ash and minor lapilli-sized fragments (Fig. 2.4A). This tuff contains sparse vesicles, quartz amygdules, related to the formation of peperite (Brooks et al., 1982;

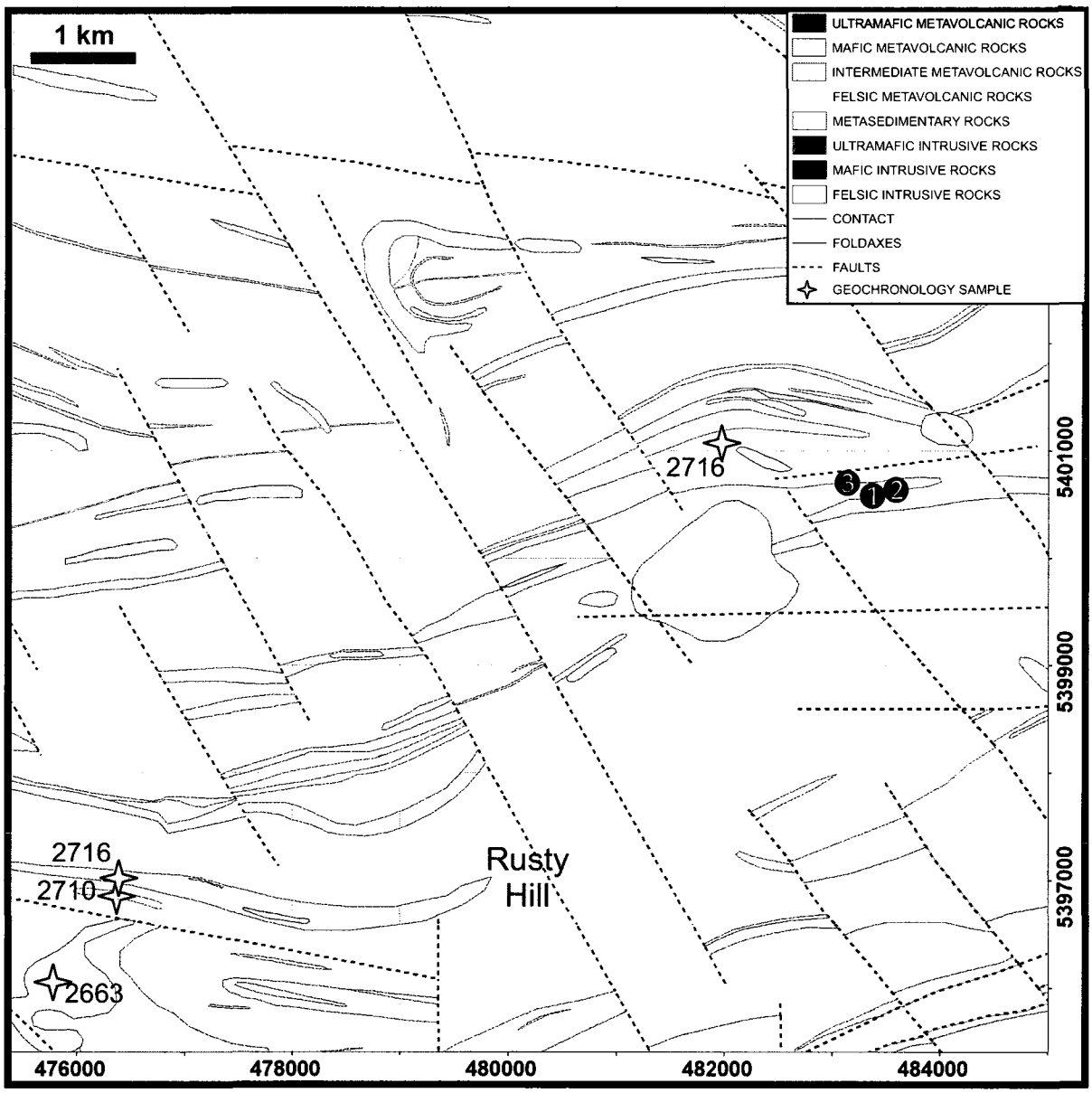

Figure 2.1 Location of Outcrops 1, 2 and 3 within Prosser Township. (modified from OGS, 2007 and Berger and McIlraith, 2007). Coordinates are UTM, NAD 1983.

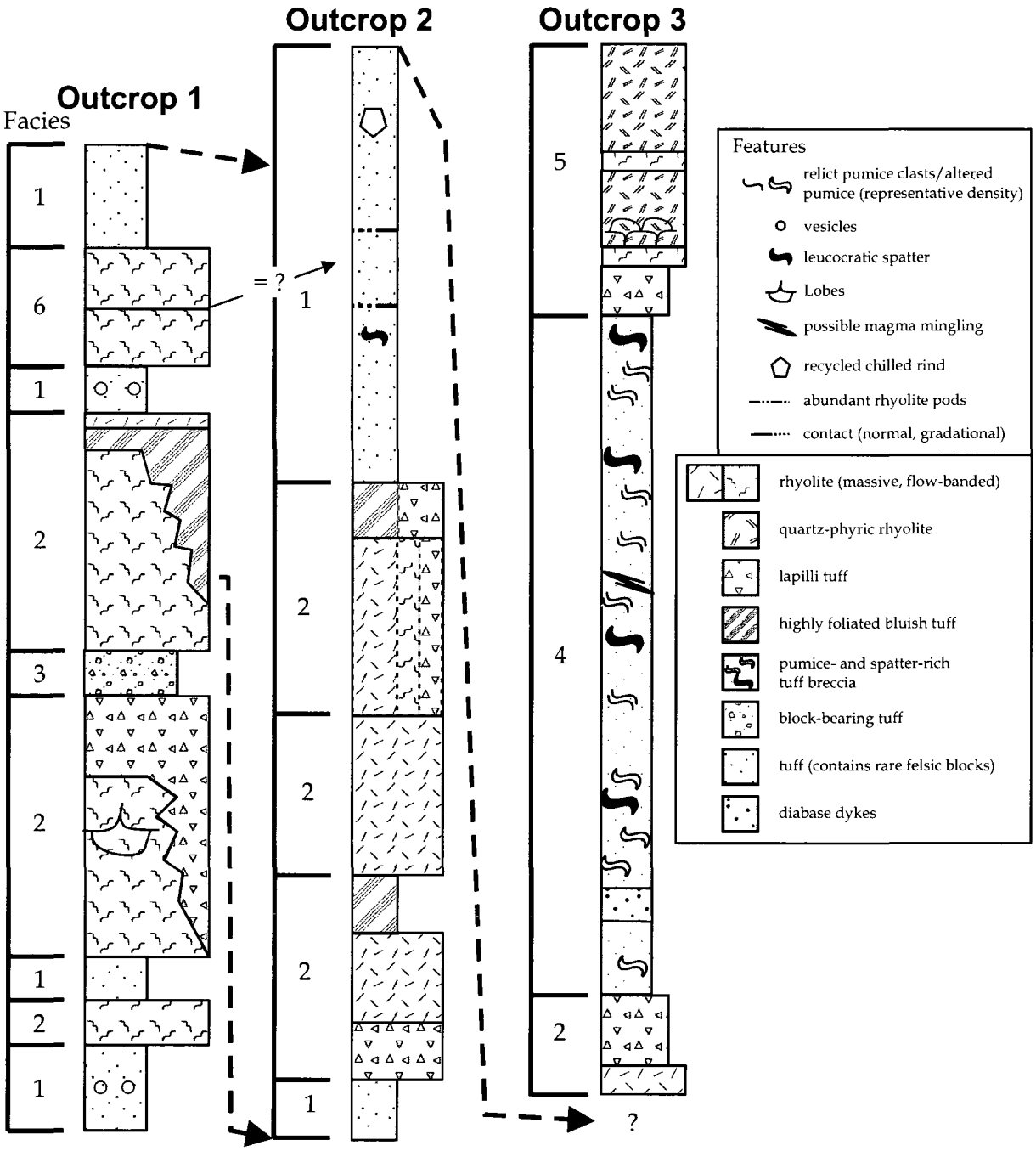

Figure 2.2: Generalized stratigraphy of outcrops in Prosser Township. Not to scale. Facies: 1 = Brown tuff, 2 = Rhyolite flows and associated autobreccias, 3 = Block-bearing tuff, 4 = Pumice- and spatter-rich tuff breccia, 5 = Quartz-porphyritic rhyolite flow.

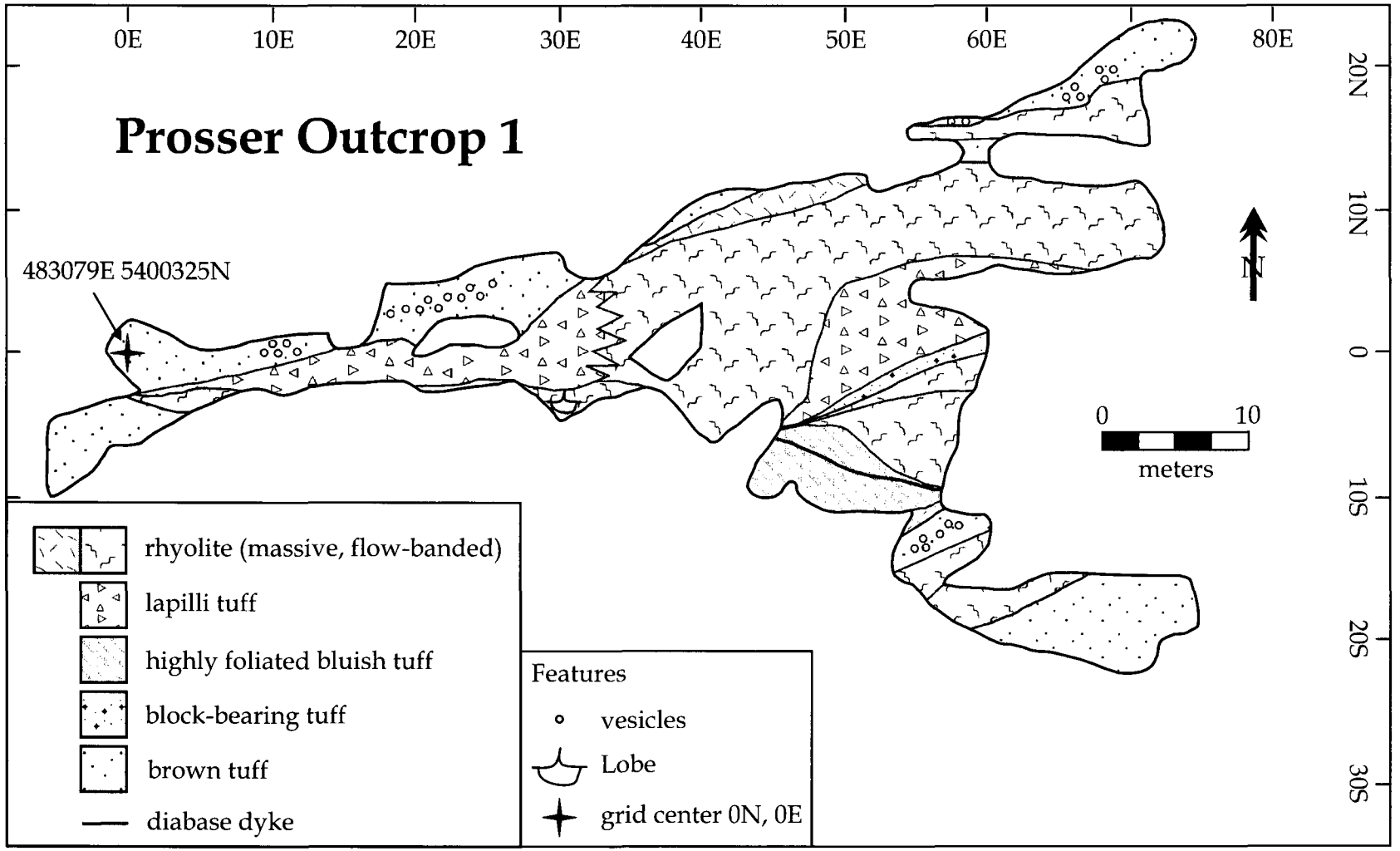

Figure 2.3. Geologic map of Prosser Township Outcrop 1. UTM grid. Local grid center (NAD 27, Zone 17). Stratigraphic tops to the south.

White et al., 2000; Skilling et al., 2002) upon emplacement of overlying rhyolite. This overlying rhyolite is a flow-banded, poorly quartz-phyric white rhyolite that grades laterally into a pink rhyolitic breccia containing lenticular-shaped lapilli and blocks. The mixture of tuff and rhyolite form several texturally distinct types of peperite; the first being small isolated fragments generally in the ash-size-range; the second type is very thin wisps of rhyolite a few mm across, and lastly is the fluidal (Skilling et al., 2002) anastamosing rhyolite that connects to the main rhyolite body. Vesicles and amygdules are more abundant closer to the coherent injections, however they are still present at least 1 m from the contact. This peperitic rhyolite is only exposed for 15 meters at the east end of the outcrop (Fig. 2.3) and is capped by a further ~2 m of tuffaceous material. In the west of the outcrop the tuff thickens to 5 m and shows similar vesiculation, small leucocratic fragments and amygdules.

The peperite is overlain by a rhyolitic breccia, containing lapilli-sized clasts, that pinches out to the west (Fig. 2.3). Towards the east, this breccia grades into a flow-banded rhyolite similar to the rhyolite at 70 mE and 15 mN. This unit, at its maximum, is roughly 14 m thick and has an exposed length of 75 m (maximum aspect ratio = 0.2). There is a massive, poorly quartz-phyric rhyolite at the base of this unit in the north-center of the outcrop that is likely the same unit as the flow-banded rhyolite. The presumed contact is a thin iron-stained band, and the change in intensity of flow-banding across it is very subtle. The bulk of the flow-banded material is variably cut by at least three generations of quartz veins and as a result, there are very few extensively continuous flow-bands preserved. Due to this, flow-banding is difficult to trace, or is perhaps absent locally; nonetheless, it is mapped throughout the unit. Near the gradational contact between the lapilli tuff and the coherent flow-banded material is a distinctly bulbous lobe (Fig. 2.4B, Fig. 2.3) with a more coherent core and sheared rim that suggests endogenous growth. There is no basal breccia identified in the field. However, the flow-banded rhyolite grades vertically into an almost 7 m thick breccia containing lapilli to block sized particles. The clasts of this rhyolite breccia show flow-banding identical to the coherent part of the lava and therefore most probably make up a flow-top breccia.

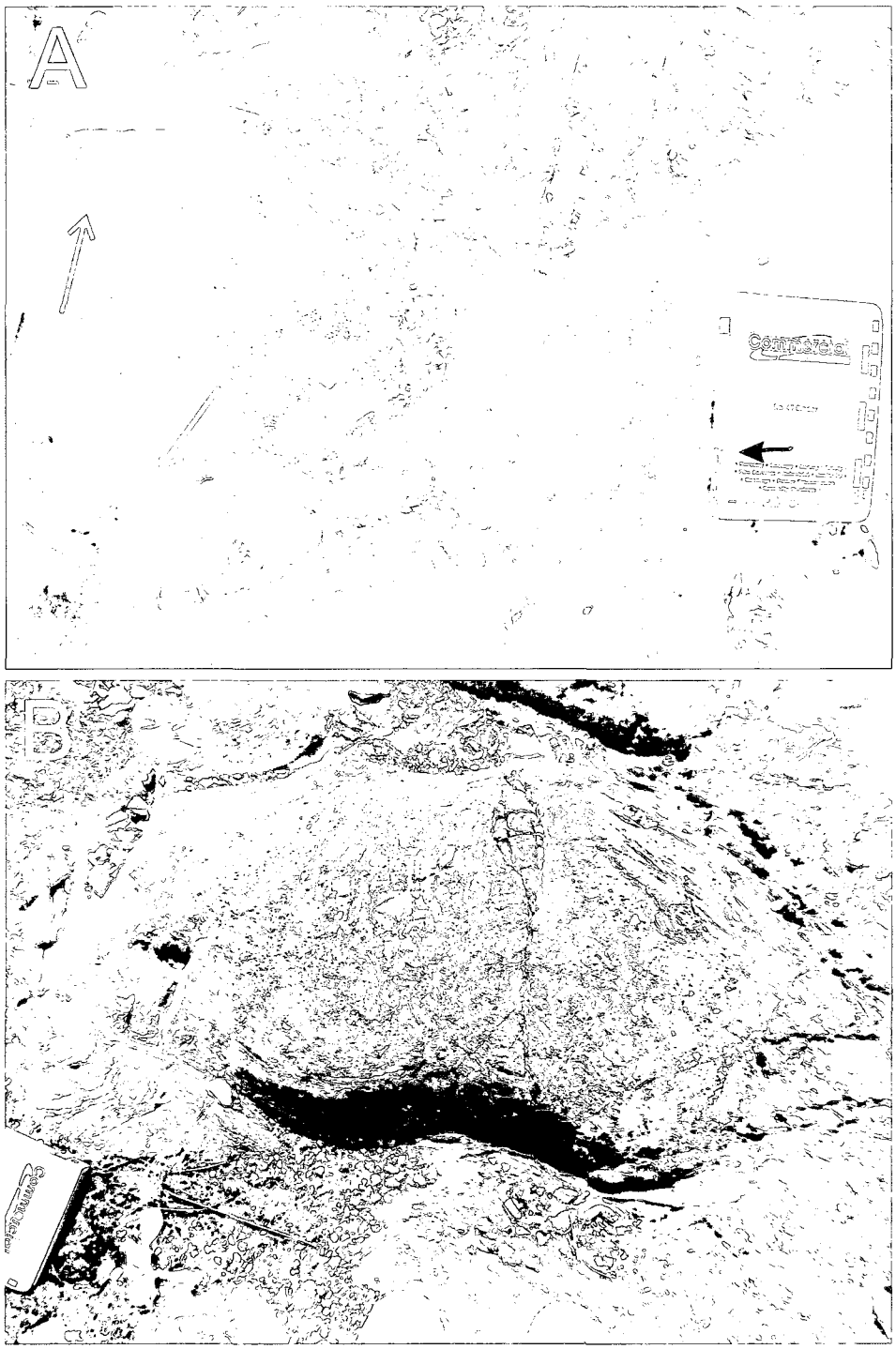

Figure 2.4: Prosser Outcrop 1. A) Tuff in peperitic contact showing irregular fluidal (purple arrow) and anastomosing (red arrow) peperite. Also note vesicles (blue arrow). B) Bulbous rhyolite lobe showing sheared margin and more massive core.

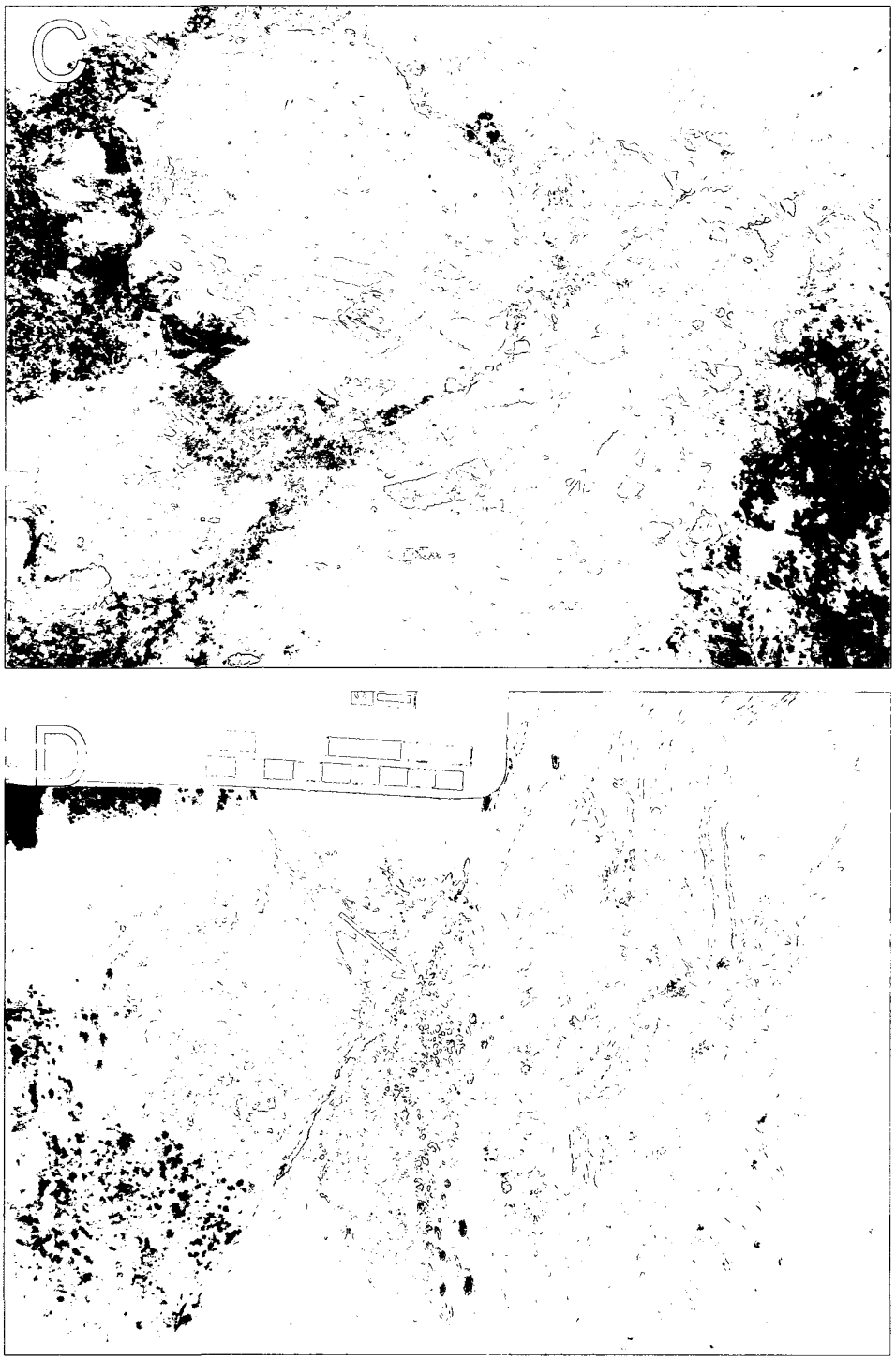

Figure 2.4: Continued. C) Poorly sorted matrix-supported block-bearing tuff, note angularity of clasts. Accidental clast (red arrow). D) Highly contorted chaotic flow-banding within rhyolite overlying C. Flow-bands are accentuated by weathering and separated by vesicular layers (purple arrow).

There is a sharp contact between the flow-top breccia and the overlying block-bearing tuff, (1 m south, 55 m east; Fig. 2.4C) which pinches out to the west and reaches a maximum thickness of 1.7 m. The block-bearing tuff is very poorly sorted, matrix-supported and contains angular to sub-angular white rhyolite clasts that are a few cm to a few dm across. This tuff is monomictic, except for one grey accidental clast that contains angular quartz fragments less than 2 mm across. The clasts within the block-bearing tuff are poorly quartz-phyric to aphyric, devoid of flow-banding and contain abundant centimeter-scale round to lenticular quartz amygdules that are weakly aligned.

Overlying the block-bearing tuff is a rhyolite unit which shows well developed and well preserved flow-banding (Fig. 2.4D). This rhyolite is fine-grained, sericitized and weakly quartz-phyric. It pinches out abruptly to the west. The flow-banding in this rhyolite is chaotic, convoluted and mixed with highly vesicular domains. No brecciated margins are seen on this flow-banded rhyolite but, is in contact, to the west, with a highly foliated, very fine-grained bluish-grey tuff. Identical material in Outcrop 2 (see below) is interpreted as highly deformed, fine-grained marginal breccia. The bluish tuff is cut by a mafic dyke and has a well developed cleavage trending 271°/89°.

The thin, poorly exposed area in the southern part of Outcrop 1 (between 10 m south and 19 m south) consists of a sequence of black and brown flow-banded rhyolite, vesiculated tuff, quartz-phyric rhyolite, and highly chloritized green tuff. The quartz-phyric rhyolite in this sequence is cut by a felsic dyke.

The southernmost part of Outcrop 1 is better exposed and contains a rhyolite (beyond 16 m south) that is grey and flow-banded. This grey rhyolite is vesicular, has deformed quartz amygdules and contains quartz and sparse plagioclase phenocrysts. Texturally, it is similar to a grey flow-banded rhyolite in the northeast corner of Outcrop 2 (see below) and, provided there are no significant structural features in the roughly 5 m separating the two outcrops, are correlative. The grey rhyolite is overlain by a massive brown unit interpreted to be a tuff.

2.1.2 Prosser Outcrop 2

Barring any major structural disruption, rocks on Outcrop 2, which are more or less on strike with Outcrop 1, cover the upper 25 m of stratigraphy exposed on Outcrop 1

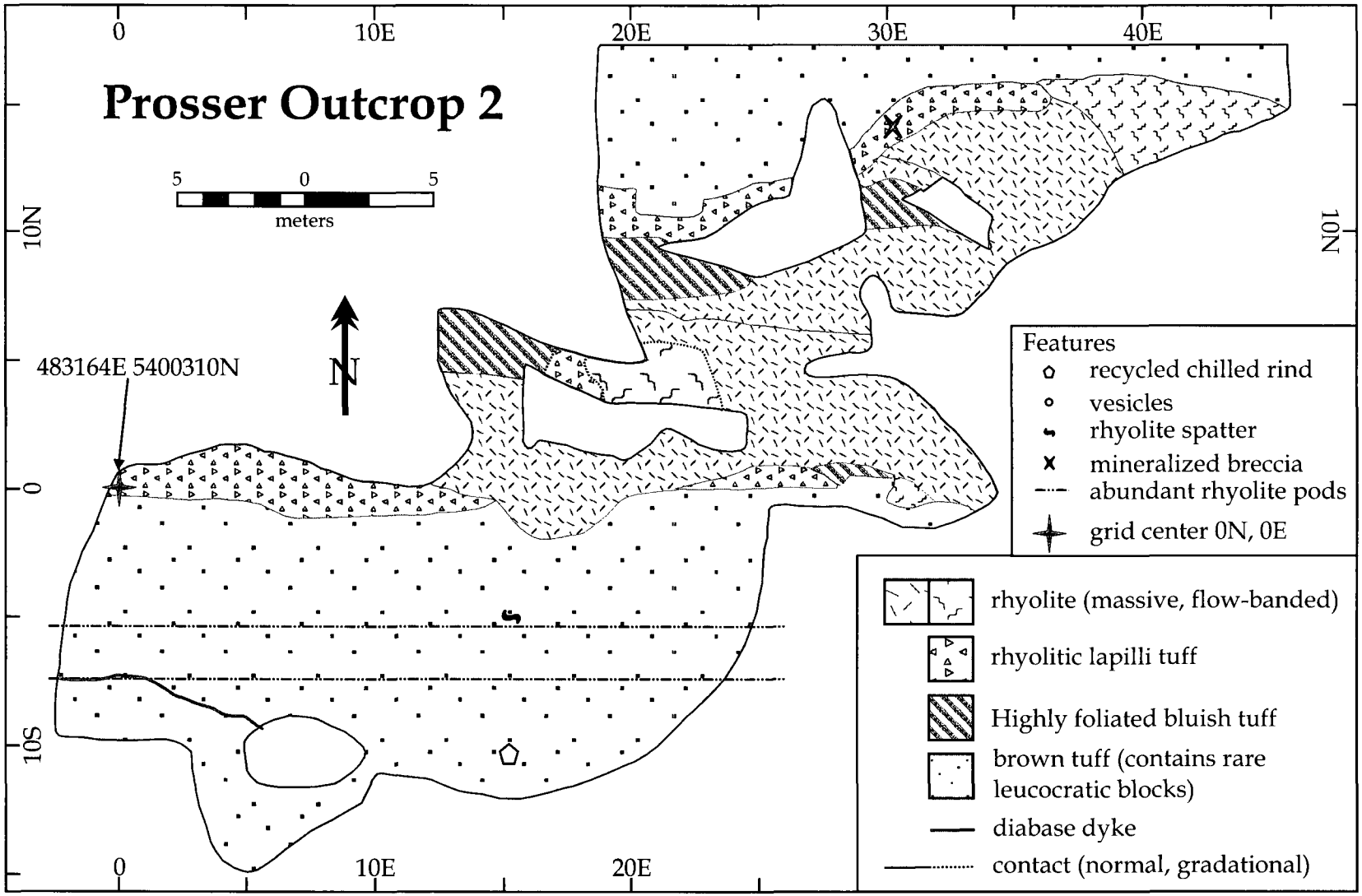

Figure 2.5: Geologic map of Prosser Township Outcrop 2. UTM grid. Local grid center (NAD 27, Zone 17). Stratigraphic tops to the south.

and expose another 5 m of stratigraphy (Fig. 2.1). With the exception of the grey flow-banded rhyolite, there does not appear to be a stratigraphic correlation between the exposed overlapping portions, suggesting lateral facies changes.

The oldest unit is a brown block-bearing tuff which is continuous for at least 27 m in the northern part of the mapped outcrop (Fig. 2.5). Locally the blocks, which have conchoidal margins, are densely concentrated along the same stratigraphic level, and all together have an irregular pod-like morphology. These concentrations may represent injected felsic lobes which have fragmented *in situ*. One such possible fragmented lobe (Fig. 2.6A) located only 1 m from the upper contact, has a pervasively mineralized matrix evident by iron staining.

In the north-central area of the outcrop overlying the brown block-bearing tuff is a rhyolitic lapilli tuff that displays a distinct contact between hematized lapilli tuff and lapilli tuff that contains iron stained sulfide alteration along with pervasive green and yellow epidotized zones (Fig. 2.6B). This mineralization is only present within 1-2 m of the contact with the underlying tuff. The lapilli tuff contains 1-5 cm clasts of sub-angular to sub-rounded grayish white, apparently aphyric rhyolite. To the east, the mineralized lapilli tuff is in contact with a grey, flow-banded, apparently aphyric rhyolite, similar in texture to the flow-banded rhyolite in the southeast of Outcrop 1. To the west, beyond a covered gap, there is a tuff breccia which is significantly coarser-grained and has unmineralized clasts up to 15 cm long that have a strong enveloping foliation (Fig. 2.6C).

Overlying the mineralized lapilli tuff is a massive, poorly quartz-phyric coherent rhyolite that contains patches of iron-stained material concentrated along fractures. The massive rhyolite is continuous to the south, with various lateral equivalents. In the center of the outcrop, above the mineralized lapilli tuff, there is a small sinuous rhyolite dyke that cuts the massive rhyolite. This dyke hosts 1-2 cm thick extensional quartz veins oriented normal to the highly sheared margins of the sinuous dyke.

Overlying the rhyolite dyke and the foliated tuff breccia is a massive, very fine-grained bluish-grey, highly foliated bluish tuff (described below) that is interpreted to be a deformed equivalent of the tuff breccia. The bluish tuff is overlain by a massive rhyolite. Above the massive rhyolite, a contact has been interpreted based on a recessive domain across the width of the outcrop. This contact defines the boundary between two

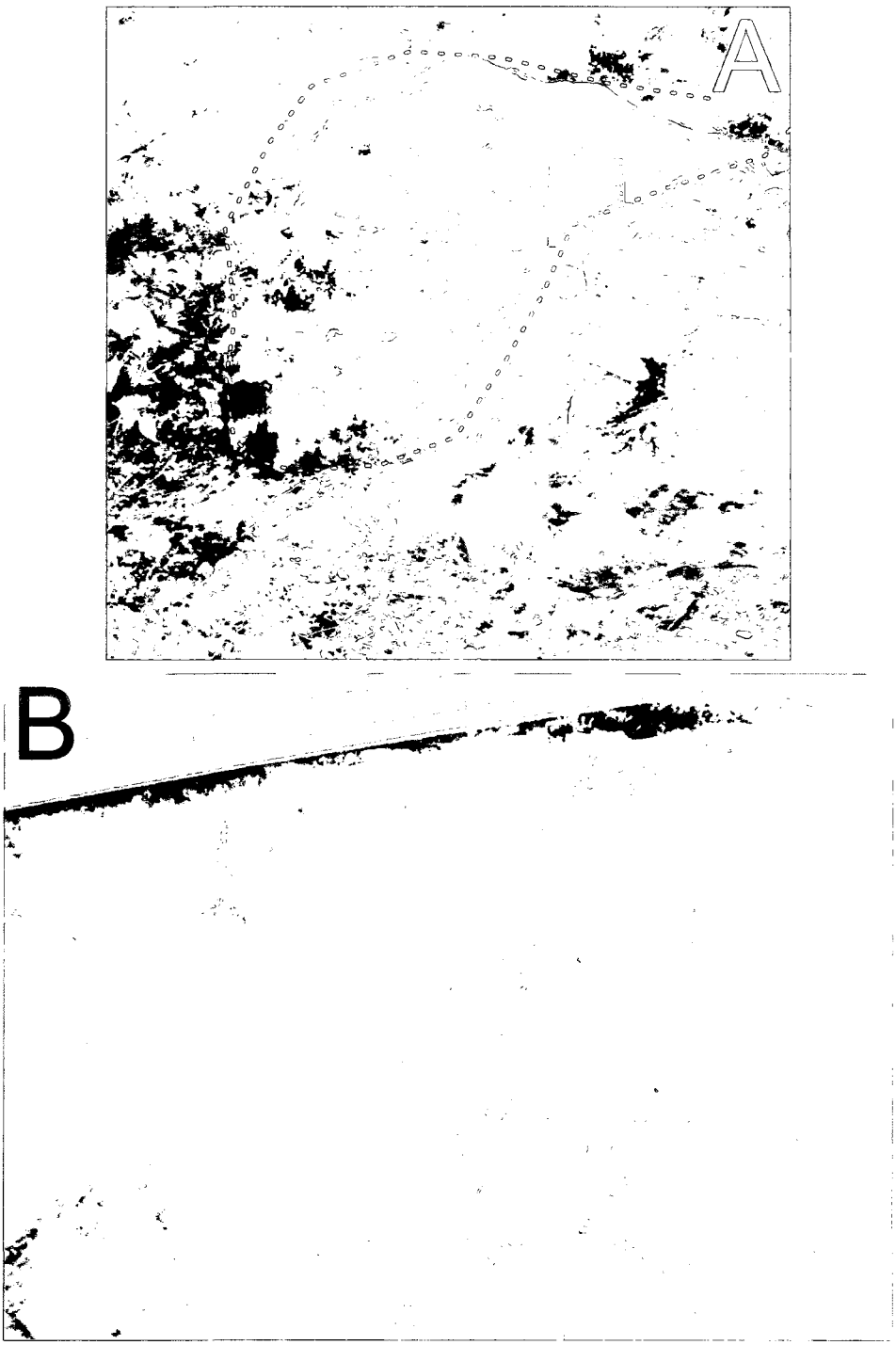

Figure 2.6: Prosser Outcrop 2. A) Mineralized fragmented leucocratic lobe (outlined). B) Epidotized (left) and hematized (right) lapillistone.

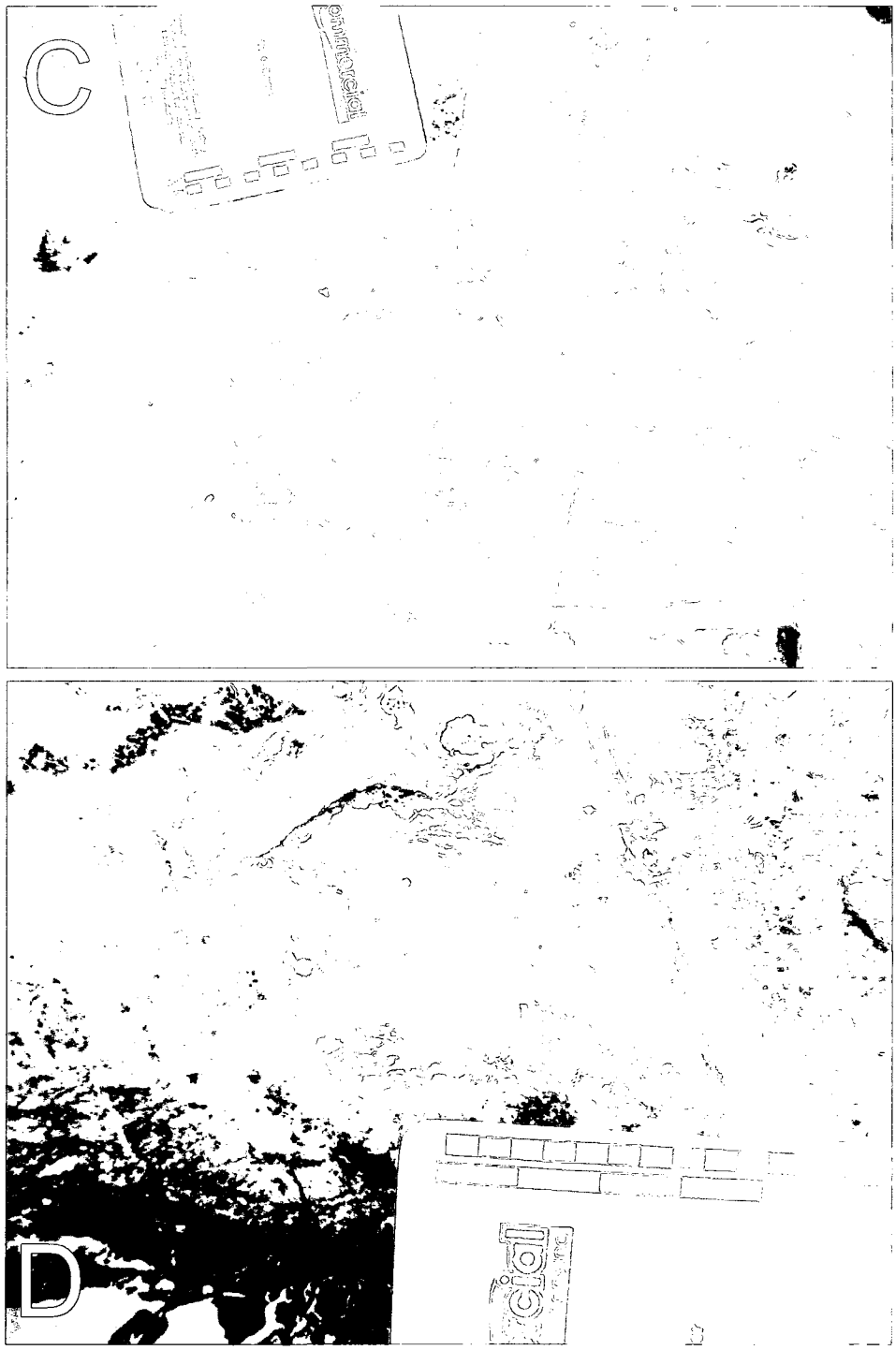

Figure 2.6: Prosser Outcrop 2 continued. C) Deformed lapilli tuff. D) Flow fold within rhyolite.

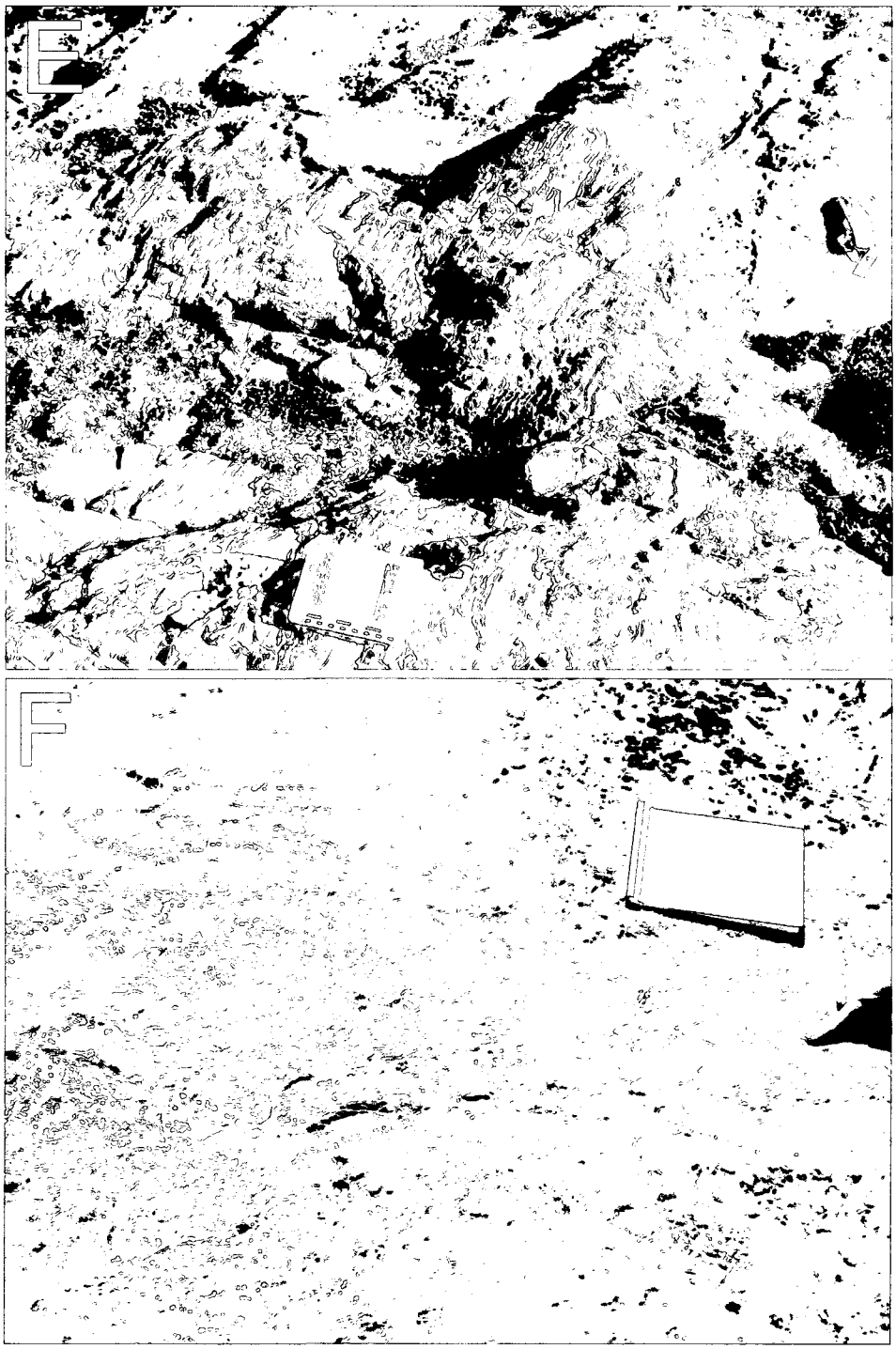

Figure 2.6: Prosser Outcrop 2 continued. E) Tuff draped over flow-banded rhyolite. F) Leucocratic lobe of coherent lava.

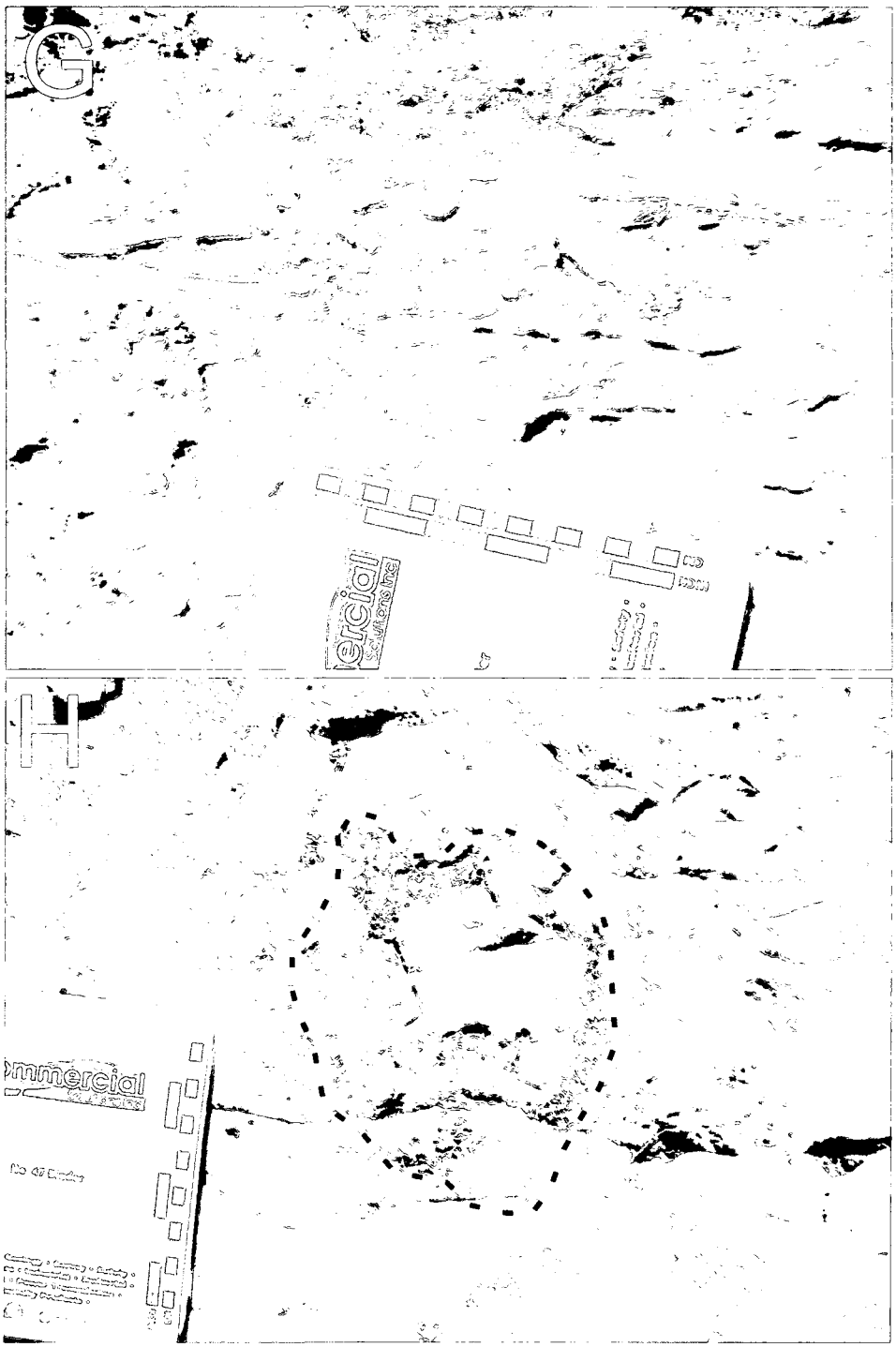

Figure 2.6: Prosser Outcrop 2 continued. G) Plastically deformed spatter. H) Recycled chilled rind clast within bomb.

massive, poorly quartz-phyric rhyolites. Texturally these are identical except that the overlying rhyolite has preserved a lateral gradation from massive to flow-banded to breccia to highly foliated bluish tuff. Within the overlying rhyolite unit, near a locality where the underlying rhyolite is covered by vegetation (at roughly 20 m east, 5 m north), the massive rhyolite grades into a flow-banded rhyolite that shows well developed flow folds (Fig. 2.6D) with distinct grey and white domains. Individual flow-bands are evident on the mm-scale. Further to the west, the flow-banding grades into a breccia containing lapilli-sized clasts that shows increasing foliation toward the west. This breccia grades directly into the highly foliated bluish-grey tuff, suggesting that it is an intensely deformed equivalent of a fine-grained rhyolite breccia.

Stratigraphically above the bluish tuff there is more rhyolite that has been heavily silicified and cut by numerous quartz veins, destroying primary textures. The silicified rhyolite becomes flow-banded towards the east. Flow-banding changes in orientation from contact-parallel, proximal to the interior of the flow, to perpendicular at the contact with the overlying very fine-grained brown tuff.

The overlying brown tuff in this area appears draped around the very prominent irregular surface of the flow-banded rhyolite (Fig. 2.6E), consistent with stratigraphic tops being to the south. There is a breccia lag infilling a paleotopographic low, around 27 m east (Fig. 2.5), separated from the flow-banded rhyolite by a small area of foliated bluish-grey tuff. In the overlying brown tuff there are some isolated and rounded blocks of flow-banded rhyolite as well as a concentrated layer of aligned leucocratic vesicular blocks within a meter of the contact. These vesicular blocks are resistant and form positive relief features within the brown tuff and can be up to 40 cm across. This layer is only seen to the west of a prominent knob of rhyolite around 16 m east, 0 m north (Fig. 2.5).

Around 10 m east and 1 m south, this brown material is extensively chloritized and highly vesiculated. This occurs overlying a rhyolite breccia that shows similar conchoidal clast morphology and overall geometry to the rhyolite blocks underlying the mineralized breccia. The brown tuff is quite homogeneous with the exception of a few features: (1) between 5 and 7 meters south there is a layer of abundant leucocratic lenticular irregular pods (Fig. 2.6F) up to 30 cm-thick that pinch out laterally. These pods

are coherent and usually not more than 2 meters in lateral extent; (2) just below this layer of pods is an abundance of leucocratic plastically deformed material in a wide variety of distinctive morphologies (Fig. 2.6G) that range from discrete millimetric beads to thin wisps a few millimeters long, to thicker (~2 cm) sigmoidal strips up to 10 cm in length. This is interpreted to be spatter (Sumner et al., 2005) and makes up 5-15 % of the area within 0.5 meters beneath the pod-rich layer; (3) further up the stratigraphy is a bomb that contains an apparent recycled chilled rind showing (Sumner et al., 2005) preserved vesicular domains (Fig. 2.6H) within a coherent clast.

2.1.3 Prosser Outcrop 3

Outcrop 3 in Prosser Township (Fig. 2.7), the northernmost of the three mapped outcrops, consists of intermediate volcaniclastic rocks that lie between coherent rhyolites and their autoclastic breccias. Both the upper and lower contacts of the volcaniclastic unit are sub-vertical. The lower contact of the volcaniclastic unit is undulatory over its 10 m exposed length and trends east-southeast whereas the upper contact is planar, again consistent with stratigraphic tops to the south.

The basal, most northerly unit is a sericitized massive rhyolite that is poorly exposed. The massive rhyolite has a breccia carapace composed of angular to sub-angular (2-10 cm) polylithic clasts and is classified as a rhyolitic lapilli tuff. It grades from monolithic clast supported, near to the coherent rhyolite, to matrix-supported and polylithic (probably reworked) in contact with the overlying unit (Fig. 2.8A). The breccia is well sorted near the coherent rhyolite and poorly sorted in the matrix-supported portion. Rhyolite breccia clasts are generally massive and uncommonly have quartz phenocrysts. There are rare iron-stained clasts within the upper 25 cm of the matrix-supported breccia. The progression from clast- to matrix-supported, and from well to poorly sorted, along with the rare foreign clasts, suggests that this was a flow top breccia which was partially reworked when the overlying unit was emplaced.

The overlying pumice- and spatter-rich tuff breccia has a minimum exposed thickness of 20 m. Clasts are often deformed near the base of this unit and preserve less of their original texture (Fig. 2.8B) while clasts halfway up show a distinctly pumiceous texture (Fig 2.8C). Just above the basal contact, the pumice clasts show a distinct margin

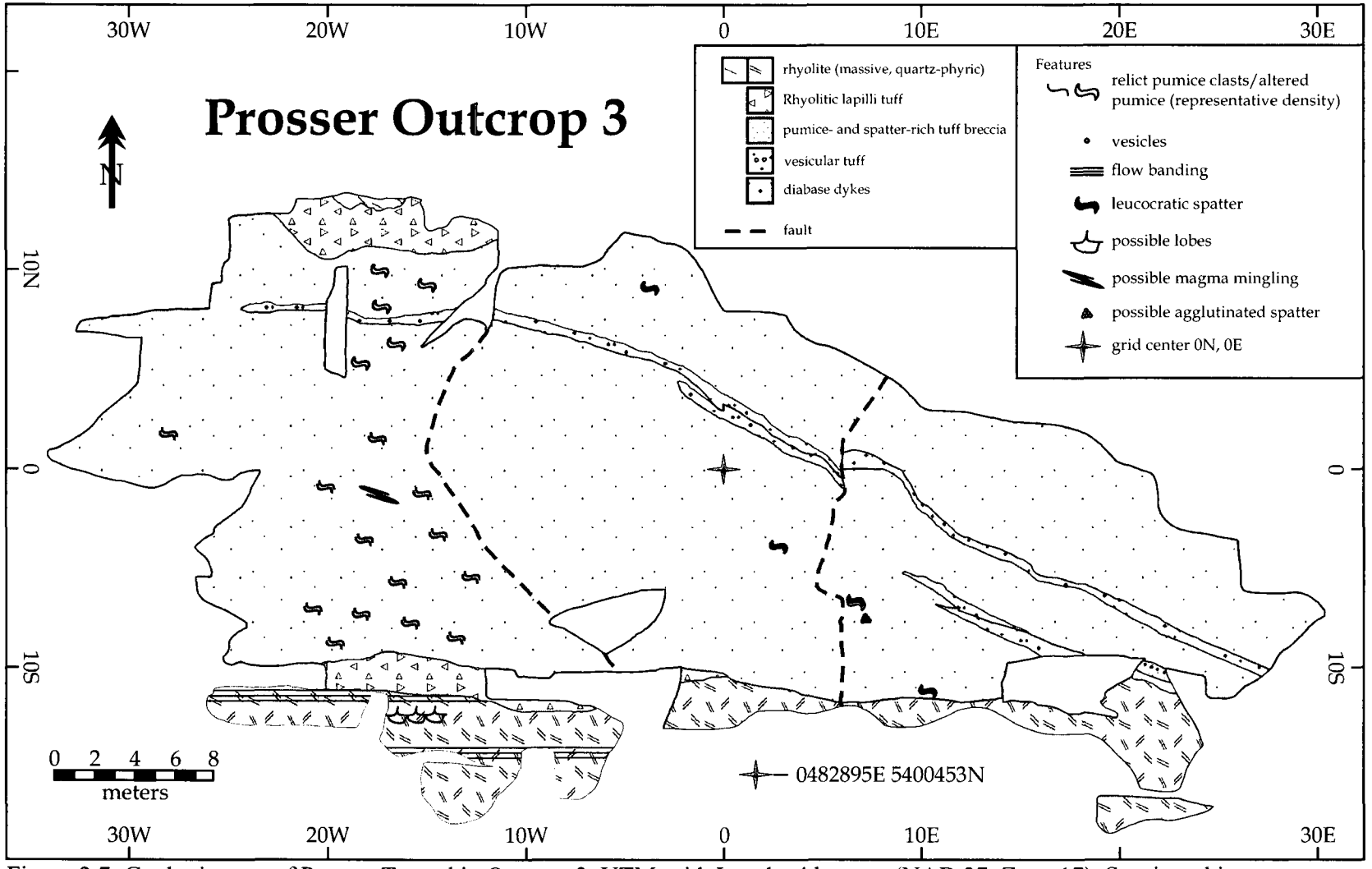

Figure 2.7: Geologic map of Prosser Township Outcrop 3. UTM grid. Local grid center (NAD 27, Zone 17). Stratigraphic tops to the south. For clarity the vertical column between 10 and 20 mW of relict pumice and pumice clasts is representative of clast density and does not indicate that the rest of this unit lacks pumice clasts.

to core zoning from red to purple to black (Fig. 2.8B). Near the upper contact, the pumice blocks are leucocratic, have contact normal fractures and show no zoning on fresh surfaces. This suggests that the zoning is synvolcanic, as one would expect that if the zoning was due to a post-emplacement process it would alter both clasts to a similar degree. There appears to be a concentration of pumice blocks at the base and near the top of the unit. This could indicate that the unit is symmetrically graded (normal then reversely graded) suggesting two separate depositional processes and/or possibly two separate units whose contact is now indiscernible.

Along with the pumice blocks there are very contorted fragments (spatter) present throughout this unit. Towards the top of the unit this spatter is leucocratic (Fig. 2.8D) whereas it is characterized by a red to green alteration near the base. This alteration is similar to that developed in the pumice blocks described above. These leucocratic bombs have an apparent even distribution of quartz filled amygdules and display contact-normal fractures which are interpreted as quenched margins. The spatter clasts are commonly oriented parallel to the overlying contact however, some are oriented within their long axis normal to the overlying planar contact. Foliation within the matrix is deflected around the blocks and spatter, indicating that they retained their primary morphology through deformation. Moreover the fold pattern within adjacent spatter clasts is not consistent. Some spatter has a distinctive morphology resembling an accumulation of small lava globules and may be agglutinated spatter (Fig. 2.8E). The matrix of this unit consists of chloritized, fine-grained, grey-brown material that is interpreted to be altered ash.

There are also numerous highly magnetic mafic dykes cutting the outcrop. As shown on the map (Fig. 2.7), these dykes vary in thickness from ~10 cm to 1 m. They have blunt terminations, are sinuous, intrude at low angle to the stratigraphy and may be the cause of the alteration within the pumice and spatter. The dyke morphology and their relationship (lacking consistent orientation perpendicular to least principle stress) to the host rock suggest that they are synvolcanic.

The upper contact of the pumice- and spatter-rich tuff breccia shows some peperitic injection of the tuff breccia into a rhyolite lapillistone basal flow breccia. This breccia is equigranular with a dominant clast size between 2 and 4 centimeters across.

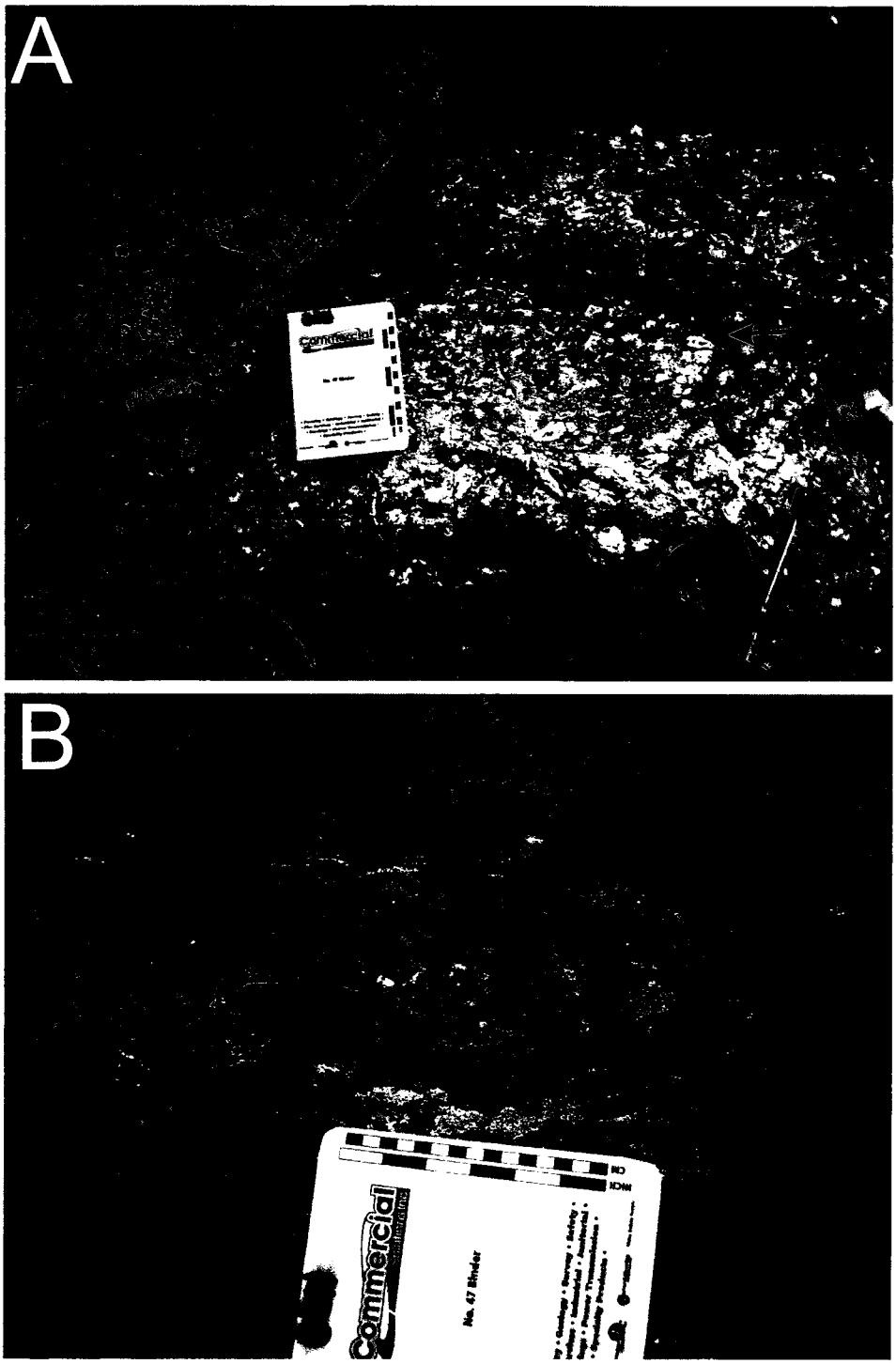

Figure 2.8: Prosser Outcrop 3. A) Rhyolite lapillistone showing progression from clast- to matrix-supported towards the top of the photo. Note mafic 'rusty' clast in matrix-supported lapillistone (arrow). B) Zoned clast containing abundant quartz amygdules interpreted to be altered pumice. On fresh cut surface this zoning progresses from red to purple to black in the core.

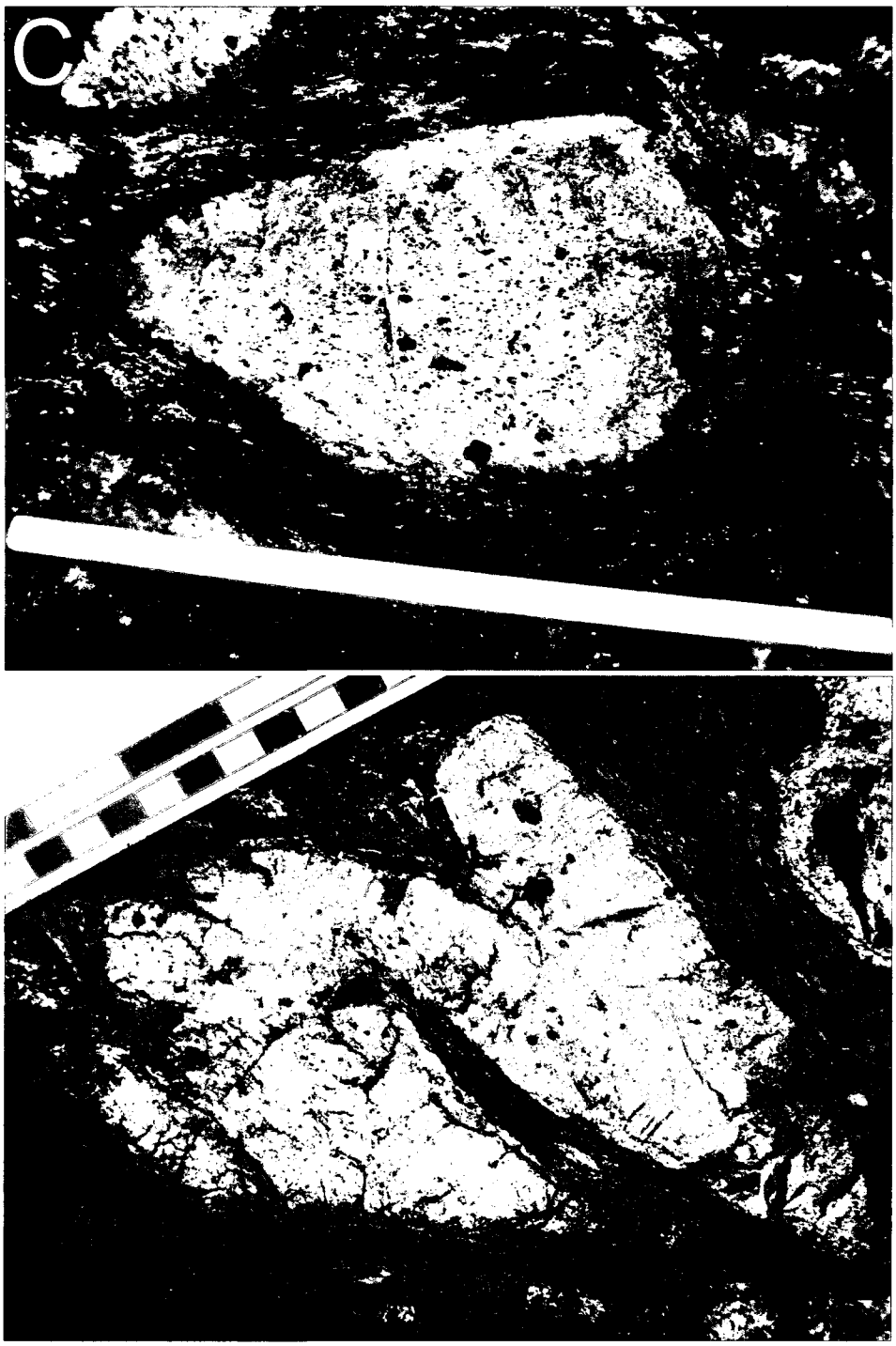

Figure 2.8: Prosser Outcrop 3 continued. C) Pumice block. Unzoned version of B, note vesicular texture. D) Leucocratic plastically deformed spatter containing undeformed quartz amygdules. Note contact normal fractures.

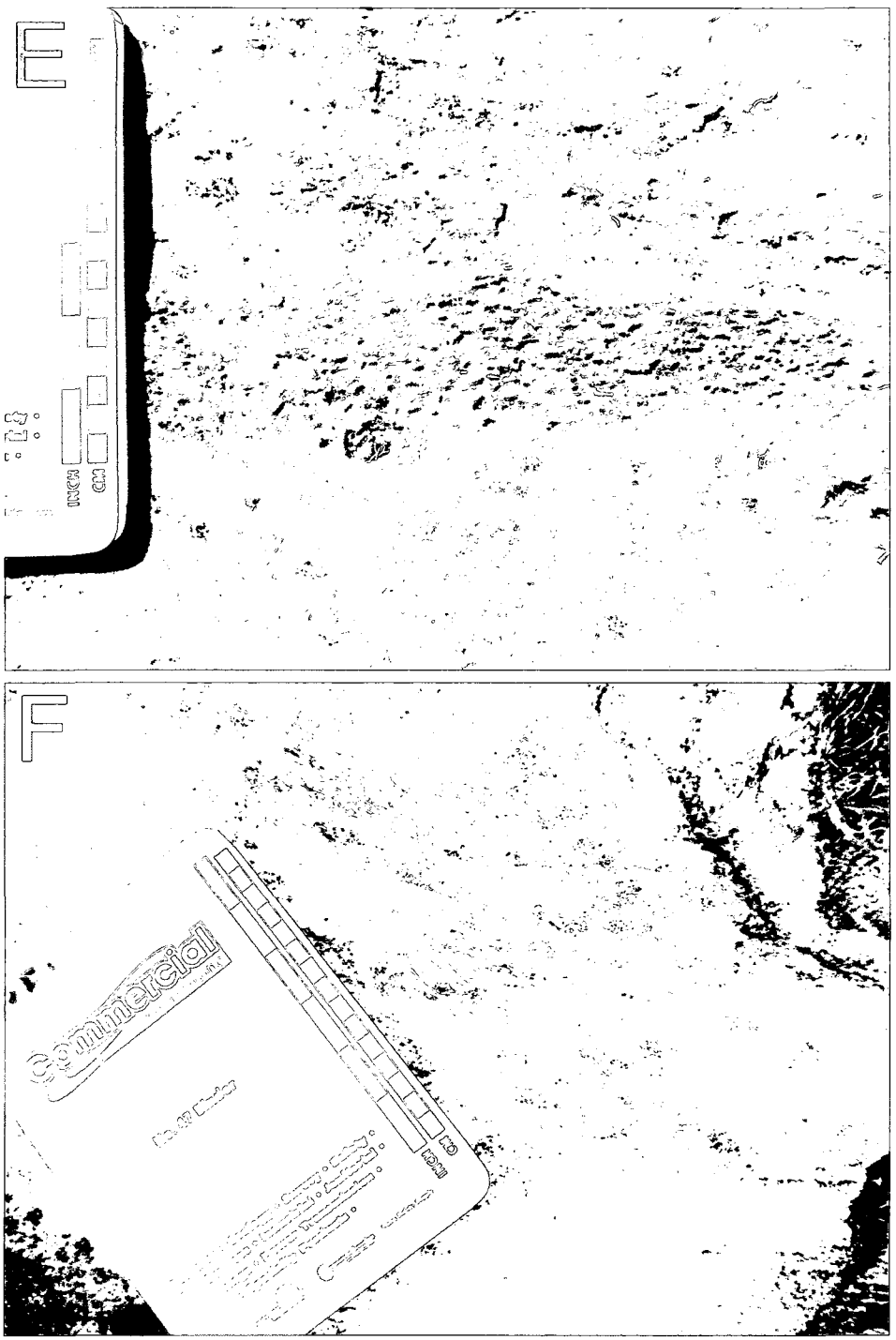

Figure 2.8: Prosser Outcrop 3 continued. E) Possible agglutinated spatter. F) Accidental cognate clast of flow-banded rhyolite within flow-banded quartz porphyritic rhyolite.

The breccia is silicified and contains abundant quartz veins up to 4 cm in thickness and grades into a flow-banded rhyolite with rare quartz phenocrysts (Fig. 2.8F). The flow-banding is more prominent in the west end of the outcrop whereas further south the rock becomes a massive, predominantly quartz-rich rhyolite containing 5-15% phenocrysts. Within the quartz-rich rhyolite there are rounded polygonal to arcuate-features which may be lobes. Alternatively they could be a product of shear or an artifact of preservation along conjugate fracture sets. Several low angle faults that show a maximum sinistral displacement of approximately 1 meter cut across the units exposed in Outcrop 3.

2.2 Facies Interpretation of Prosser Township

Prosser Township can be divided into five main facies (Fig. 2.2) several of which are repeated. The lower stratigraphy is dominated by interfingered tuffs and rhyolite flows while the uppermost pumice- and spatter-rich tuff and quartz-phyric rhyolite units represent a major change in eruption products and styles.

2.2.1 Facies 1 – Brown tuff

This unit is characterized by abundant peperite which has formed at all of the contacts with rhyolite, with the exception of the uppermost contact in Outcrop 2. During peperite formation a variety of different juvenile clasts were formed from ash- to lapilli-sized particles as well as thin tapered wisps and coherent rhyolite apophyses forcefully intruded into the host tuff. The smaller fragments and amygdules are classified as 'dispersed' (Skilling et al., 2002) and found up to 1 m from the lava flow contact. Abundant vesicles in the peperite are indicative that the rhyolite was hot and vaporized pore fluid within the tuff (Skilling et al., 2002). The peperite becomes more irregular, with fluidal clasts, and then grades into a network toward the contact with the rhyolite flows. The abundance of peperite at all contacts, the morphology of the juvenile clasts and the evidence of forceful intrusion of rhyolite into the host tuff suggests that the tuff was unconsolidated and contained a pore fluid.

This rock is interpreted as a tuff based on a few distinctive features, the degree of deformation and the presence of pumice and spatter in Outcrop 2. However, it could

represent a myriad of facies such as; 1) an ash fall unit, 2) a lapilli or ash pumice unit, or 3) a hyaloclastite unit derived either from the rhyolite units, or from the abundant local mafic rock units. Further investigation of the petrology and geochemistry of the volcanic and volcaniclastic units exposed on Outcrops 1 to 3 of Prosser Township will provide more evidence to establish the nature of the protolith(s). However, one important interpretation drawn from the field work is that the abundant peperite and clasts demonstrate that this tuff unit was unconsolidated before burial and is not an altered lava flow(s).

2.2.2 Facies 2 – Aphyric rhyolite flows and associated autobreccias

The majority of the rhyolites are white, poorly quartz-phyric to apparently aphyric lavas. They are variably sericitized and often cut by quartz veins. Rare lobe features are observed within these flows, suggesting endogenous growth as is commonly seen in basalt flows. Associated with each coherent rhyolite is a marginal breccia facies, either a flow tongue-, flank-, basal- or flow-top-breccia. Generally these breccias contain ash- to block-sized clasts and show variable degrees of alteration and deformation. The bluish tuffs are laterally continuous with the flow breccias but show no distinct features. In Outcrop 2 the bluish tuff grades into a rhyolite lapillistone and therefore both are interpreted as highly strained, fine-grained rhyolite breccias. The bluish tuff may have been a fine-grained rhyolitic hyaloclastite breccia. Rhyolite glass may readily be hydrated to form clay minerals such as smectite that undergo stress shear along cleavage planes producing a highly foliated rock (Fisher and Schmincke, 1984). Due to incomplete preservation of these flows, no definitive internal structure is apparent compared to those of Cas and Wright, (1987) and McPhie et al., (1993). However, almost all units exhibit chaotic flow-banding. Basal breccias are not evident in the majority of these flows, suggesting that either they were not formed, or that they are not recognized due to poor preservation. The largest flow, in Outcrop 1, contains a massive unit (Figure 2.3) at its base which may be a basal breccia silicified to the point of ambiguity.

These flows are a maximum of 14 meters thick and have maximum estimated aspect ratios of 0.2, indicating that they are coulées (Cas and Wright, 1987). The coulées of Prosser Township are significantly thinner than many modern rhyolite coulées such as

those of the Long Valley Caldera. The north and south coulées at Long Valley are 6 km long and 50 m thick (aspect ratio = 0.008, Bailey et al., 1976). In Iceland, rhyolite lava coulées are approximately 60 m thick (Gibson and Walker, 1963). However, many others are significantly thicker (e.g. the Roche Rosse obsidian coulée of Italy; Hall, 1978; or the Badlands lava, Idaho; Manley, 1996).

The viscosity of the Kidd-Munro rhyolites may have been significantly lower than that of modern rhyolite coulées to explain the apparent thinness. As discussed below, it is unlikely that the flows were superheated, therefore viscosity may have been reduced by melt depolymerizing agents such as H_2O, F or Cl. In addition, a low melt viscosity could explain the absence of domes, the sinuous outcrop pattern, the relatively low aspect ratio of the flows, and the lack of flow-base breccias. In contrast, the flow-top breccias locally make up half the thickness of some flows. This may result from the continual exposure to cool water as a product of progressive inward cooling and fracturing during and after emplacement in a subaqueous environment.

Temporally equivalent rhyolites near the Kidd Creek mine have been interpreted to have formed in a high heat flow environment (Barrie, 1995), thus explaining the large size of the associated Kidd Creek deposit (Campbell et al., 1981; Barrie et al., 1999; Hannington et al., 1999b). None of the described rhyolites in Prosser Township appear to have been super-heated. Super-heating requires that the melt was above its liquidus temperature and is therefore aphyric. Most of the Prosser Township rhyolites do contain sparse phenocrysts and microphenocrysts, demonstrating that these flows were not erupted above their liquidus temperature.

2.2.3 Facies 3 – Block-bearing tuff

The block-bearing tuff facies is only seen in Outcrop 1. It is limited in exposure and appears to infills topography. This tuff is poorly-sorted, matrix supported and contains amygdule-rich rhyolite clasts within a grey matrix. This tuff likely represents a block and ash flow but definitive observations are limited due to its extent. Because of the angularity of the clasts and the fact that it has formed in a paleotopographic depression, it is interpreted to be a proximal to medial facies. If this was a block and ash

flow, it may very well have been derived from the collapse of an edifice and therefore would indicate the former presence of domes.

2.2.4 Facies 4 - Pumice- and spatter-rich tuff breccia

The pumice- and spatter-rich tuff breccia facies, which underlies the youngest rhyolite, is a poorly sorted tuff breccia containing abundant leucocratic spatter and pumice blocks. Pumice blocks can be quite large, up to 0.5 m across. Their distribution gives this unit an apparent weak symmetrical grading. This suggests that there were multiple sorting processes ongoing during deposition, or that this unit represents two units deposited at separate times by separate processes.

The pumice and spatter clasts show distinct alteration zoning that is more prominent within the pumice presumably because its original permeability would have been much greater than that of the spatter, allowing for a more progressive alteration. This zonation is only found in the bottom half of the outcrop and alters much of the original texture of the pumice clasts near the base. The observed distinct pumice clast found near the middle of the unit also exhibits a zonation, which bolsters the interpretation that clasts near the base, even though deformed, are in fact relict pumice clasts. Based on the distribution of the zoning near the base and because it has affected both the pumice and the spatter to a proportional degree, it is argued that this alteration is synvolcanic, and not a product of later hydrothermal alteration or metamorphism.

Pumice blocks are rounded to sub-rounded and require water to sink (Allen et al., 2008). The spatter displays quenched margin (e.g. contact-normal fractures) but does not display any compaction and is not oriented parallel to the contacts and therefore is interpreted to have been deposited as a solid and not to have been re-worked. The lack of sorting, evidence for primary deposition, the intimate association of spatter and water-logged pumice and synvolcanic alteration results in the conclusion that this is a subaqueous pyroclastic flow.

2.2.5 Facies 5 - Quartz-porphyritic rhyolite

The youngest and most crystalline lava is the quartz-porphyritic rhyolite facies. It shows the most complete flow structure, exhibiting a basal breccia that grades into a

flow-banded zone followed by alternating zones of massive and flow-banded lava. This rhyolite also contains what are interpreted to be lobes, indicating endogenous growth. As the only contact observed is the underlying one, it was impossible to determine the overall thickness, however it is at least 8 m thick. The flow texturally resembles the QP rhyolite at Kidd Creek which represents the last, and capping, rhyolite in the mine sequence (Prior et al., 1996; Prior et al., 1999; DeWolfe, 2004). Further comparisons are made below.

2.2.6 Facies 6 - Synvolcanic dykes

There are three different sets of dykes cutting these outcrops from thin rounded leucocratic and mafic dykes to much thicker and extensive mafic dykes and leucocratic pods confined to certain levels of stratigraphy. The leucocratic dykes are found in the north of Outcrop 1 while the mafic dykes are seen in the pumice- and spatter-rich tuff breccia.

Both the thin (less than 20 cm) mafic and leucocratic dykes are very sinuous, and have rounded terminations. Typically, one expects dykes to have straight planar contacts in part because they are intruded at depth within a stress field. These dykes are sinuous and rounded suggesting that they were intruded at a high level (i.e. under low pressure). This observation and the fact that most lack chilled margins, indicates that they were intruded while the hosts were still hot.

The thicker mafic dykes (< 1 m) cross cut the outcrops. These fine-grained mafic dykes, commonly having layered chilled margins and planar to curved contacts, indicating that their emplacement was much later than that of the more sinuous dykes.

The third type of intrusion, herein termed leucocratic lobes (see Chapter 4), consists of coherent injected lobes that are concentrated along distinct horizons within the southern tuff in Outcrop 2. These lobes neither exhibit chilled margins nor fracturing although they are associated with underlying fine fragmental rhyolite. It is uncertain, although highly probable that these two features (the lobes and fine fragmental material) are related. However, none of the observed lobes appear fragmented. Alternatively the fine fragmental material could have been produced during peperite formation.

2.3 Brief summary of the Kidd Creek mine stratigraphy

The following is a synopsis of the mine sequence found within the upper part of the KMA as discussed by Prior (1996), Prior et al. (1999, and references therein) and DeWolfe (2004). The Kidd Creek deposit consists of mineralization within a basal ultramafic unit overlain by several felsic volcanic sequences that were intruded by gabbro sills and capped by a 1300 m thick sequence of hanging wall basalt and andesite flows. The felsic sequence is informally divided into the Lower, Middle and Upper members. The lower member is made up of massive and autobrecciated facies that have been interpreted to be domes and cryptodomes (e.g. Prior et al., 1999b). These rocks are conformably overlain by a bedded volcaniclastic facies containing monolithic and heterolithic deposits of the Middle Member. The heterolithic fragments contain sulfide clasts which are found above and below the main ore zones which are hosted in the Middle Member. The upper member is a distinct quartz-phyric (8-12 vol. % phenocrysts) rhyolite named the 'QP rhyolite'. Gabbro sills separate the Upper Member from the Middle Member and the overlying mafic flows.

The Lower Member, ~300 m thickness, consists of aphyric rhyolite that is divided into three facies, a coherent rhyolite, an in-situ rhyolite breccia and a rhyolite breccia. Though termed aphyric the coherent rhyolites contain (<5 vol. %) quartz and rare euhedral plagioclase phenocrysts in a fine-grained groundmass. The aphyric rhyolite facies is locally flow-banded and seldom contains spherulites. The change to in-situ rhyolite breccia from coherent facies is gradational, consistent with the interpretation it represents the progression from a coherent flow or dome interior to a marginal breccia.

The Middle Member consists of monolithologic and heterolithologic rhyolitic volcaniclastic rock facies. The monolithologic facies is divided into four distinct units, rhyolite lapillistone, rhyolite lapilli tuff, rhyolite tuff and rhyolite tuff breccia. The heterolithologic facies is divided into a heterolithologic rhyolite lapillistone and a tuff breccia with mafic blocks. The monolithologic facies is mineralized, well-bedded (<50 cm thick beds) and normally graded, although reverse grading is present. Clasts of block

size are exceedingly rare except for the mafic clasts within the tuff breccia. The mafic clasts are interpreted to have been produced through the intermittent collapse of domes within a synvolcanic subsidence structure, or episodic faulting along the walls of a subsidence structure that allowed the denudation of basalt flows outside of, or in the walls of, the subsidence structure. These volcaniclastic units comprise the Middle Member of the mine stratigraphy.

The ~130 m thick QP rhyolite, that has an aspect ratio of less than 10, is divided into two main facies; a massive facies and a breccia facies. The massive facies consists of massive and flow-banded aphanitic and quartz-feldspar porphyritic rhyolite that form two parallel ridges. The QP rhyolite is made up of massive lobes that are several meters to >10 m thick and have flow-banded margins. This flow-banding is contact-parallel near the lower contact of the unit and more chaotic, wrapping around the lobes higher in the stratigraphy. The lobe margins contain up to 5% elongate quartz amygdules.

The breccia facies consists of block- to lapilli-sized fragments containing minor amounts of an ash-sized quartz and feldspar matrix. In general, the flow-top and flank breccias consist of clasts which are white quartz porphyritic rhyolite blocks up to 30 cm across forming an unsorted and non-graded framework- to matrix-supported breccia. The flow-foot breccias are 0.5 to 2 m thick, consisting of blocky, angular to sub-angular, white, variably altered, massive and flow-banded clasts. The breccia facies is interpreted as flow-top breccia (autoclastic or hydroclastic). The flow-foot breccias are thought to have been produced by the lava overriding its own flank breccia.

On a larger scale, based on the geometry and distribution of these facies, the QP rhyolite is interpreted to have formed from two separate parallel fissures roughly 400-800 m apart. The material represents the formation of multiple domes and their associated breccias. The distribution of massive and breccia facies indicates that the direction of rhyolite flows was to the east and northeast of the main Kidd Creek deposit. The areal extent of the QP rhyolite is limited due to a higher estimated viscosity (DeWolfe 2004) and a lower effusion rate relative to the aphyric rhyolite (coherent plus autoclastic volcanic rock volume for the studied deposit of Kidd Creek, QP rhyolite = 0.06 km^3 compared to 0.13 km^3 for aphyric rhyolite; DeWolfe 2004).

The QP rhyolite is the uppermost felsic rock found in the mine sequence and it has been hydrothermally altered (Prior 1996; Prior et al., 1999; Koopman et al., 1999; DeWolfe, 2004). However, no mineralization has been found above the QP rhyolite and therefore it represents an important horizon in terms of exploration for new ore bodies. Finding equivalents to the Kidd Creek mine stratigraphy elsewhere in the KMA might have significant implication for exploration.

2.4 Comparison with Prosser Township outcrops

The sequence described within Prosser Township shows substantial similarities to the facies described at Kidd Creek. The Lower Member aphyric rhyolites at Kidd Creek are texturally similar to the aphyric rhyolite flows and associated autobreccia facies described above. Both have a similar colour, phenocryst content, local flow-banding and grade into a rhyolitic lapilli tuff that are interpreted to have formed as autobreccias. Similarly, there is a progression from in-situ to framework autobreccias, however, the jigsaw-fit breccia is less apparent in the Prosser Township rhyolites. These autobreccias range in grain-size distribution from tuff to lapilli tuff to tuff breccia characteristic of the monolithologic rhyolitic volcaniclastic facies described by DeWolfe (2004). What is not observed are the heterolithologic volcaniclastic facies or rocks containing mafic blocks, except for the rhyolite lapillistone at the base of Outcrop 3 that contains rare iron-stained clasts, but not to the extent of the heterolithologic facies (up to 10 volume % mafic clasts).

The quartz-porphyritic rhyolite described in Outcrop 3 shows significant similarities to the QP rhyolite. Both contain abundant quartz phenocrysts, have a basal breccia of similar character (e.g. lapilli-size, ~2 m thickness, white, quartz-phyric) and show distinct internal flow structure. Both have basal flow-banded sections that are not chaotically folded but rather planar, mimicking the underlying contacts. Both are also characterized by alternating massive and flow-banded sections.

2.5 Summary

Prosser Township appears to show a variety of environments progressing from subaqueous coulées at the base to a possible subaqueous pyroclastic flow, capped by a distinctly quartz porphyritic lava. This quartz porphyritic rhyolite is volumetrically small as it was likely more viscous than the relatively phenocryst free aphyric rhyolite and therefore had lower effusion rates (DeWolfe, 2004). In addition, in Prosser Township the explosive pumice- and spatter-rich tuff breccia would be equivalent to the mineralized Middle member as it underlies the quartz porphyritic (QP) rhyolite although nothing similar to the pumice- and spatter-rich tuff breccia has been described at the Kidd Creek deposit. The rhyolite coulées described here appear to be very different to their modern counterparts and may have had different rheological properties in terms of the individual coulée scale and inferred rheologic properties from modern rhyolites and will be further discussed and compared in Chapter 6.

The Prosser Township felsic volcanic rocks appear (with the exception of the pumice- and spatter-rich tuff breccia) to directly correlate texturally with those described at the Kidd Creek mine. Prosser Township has both Lower and Upper member, aphyric and QP rhyolites as well as their autoclastic breccias. The stratigraphy described in Prosser Township covers the entire felsic portion of the mine sequence, although there is no significant mineralization present at the surface in the studied section of Prosser Township.

Chapter 3 – Petrography of Prosser Township outcrops

3.1 Petrography of Prosser Outcrops

The main enigma unanswered by the field descriptions is the nature of the protolith of the brown tuffaceous units which are present throughout the stratigraphy. These units are nondescript macroscopically and contain many different leucocratic materials from pumice blocks to very thin wispy clasts. For clarity, the petrography has been organized to mirror the field descriptions by moving up stratigraphy. It is then summarized by depositional facies as determined from field mapping.

3.1.1 Prosser Outcrop 1

The oldest unit in this outcrop (Fig. 3.1) is a grey-brown tuff that is represented by three samples 07-P2-52, 07-P2-54 (peperite contact) and 07-P2-55 (see map Fig. 3.1 for sample locations). Sample 07-P2-52 consists of a fine-grained matrix of chlorite>calcite>quartz (up to 0.7 mm in size) >titanite(?) (subhedral crystals approximately 0.1 mm and masses up to 0.4 mm) with minor amounts of pyrite and very fine-grained white mica. The pyrite appears to replace specific minerals however no precursor morphology is preserved. Sample 07-P2-52 also contains amygdules <4 mm of calcite-chlorite-quartz. Adjacent to the peperitic contact the intermediate tuff material is a fine-grained mixture of turbid feldspar needles, cryptocrystalline material with minor amounts of dusty brown round patches (possibly relict titanite) and minor amounts of calcite and chlorite. This material has a slight remnant felty texture possibly due to crystallization of the groundmass. Sample 07-P2-55 is a coarser tuff that has a recrystallized groundmass of amphibole>chlorite>dusty opaque material>quartz with minor amounts of calcite, Fe oxide minerals and epidote. The contact between the rhyolite and the tuff is evident in sample 07-P2-54 which consists of spherulitic (recrystallized; see below) quartz-feldspathic rhyolite with minor zircon, epidote, chlorite and calcite. The adjacent grey-brown tuff has abundant fine translucent needles too small to be resolved, chlorite-filled amygdules and a dusty groundmass of carbonate and

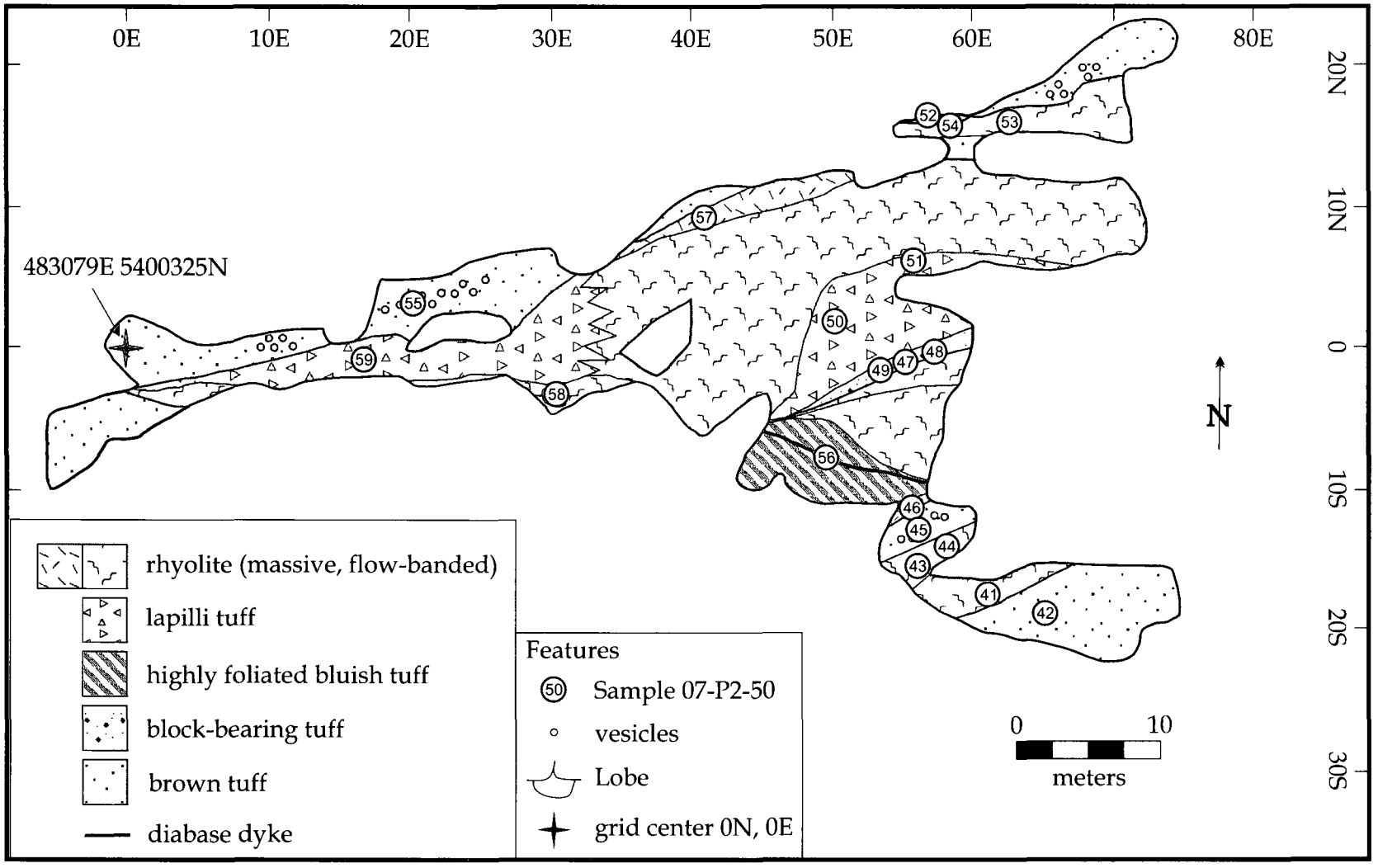

Figure 3.1: Map showing sample locations on Prosser Outcrop 1 map. Note only the sample number suffixes are reported.

chlorite. The contact between the tuff and the rhyolite is marked by a sharp concentrated zone of Fe Ti oxide minerals (Fig. 3.2A).

The grey-brown tuff is in peperitic contact (07-P2-54) with a pink rhyolite that is the lateral equivalent to the massive rhyolite (07-P2-53). Sample 07-P2-53 contains ~10 % quartz phenocrysts that are no larger than 0.1 mm. These are set in a flow foliated (Fig. 3.2B) groundmass of recrystallized glass, now polycrystalline quartz and feldspar, with minor amounts of chlorite, calcite and dusty cryptocrystalline material. Also, it uncommonly contains zircon microphenocrysts and albite veins.

The rhyolite (07-P2-57) overlying the grey-brown tuff is very similar to the underlying pink rhyolite (07-P2-53). Sample 07-P2-57 contains roughly 10 % quartz phenocrysts (<1.0 mm, average ~200 μm) with a similar flow foliated texture to the pink rhyolite however the foliations in this rock are accentuated by sericite that has formed along the flow bands. The groundmass of this rock is composed of similar quartz, sericite and dusty orange cryptocrystalline material, with minor chlorite and carbonate in both the groundmass and amygdules.

The sample 07-P2-57 rhyolite laterally grades into a lapilli tuff breccia (07-P2-59) that contains quartz spherulites <0.3 mm and quartz-phyric lithic fragments <0.3 mm set in a dusty quartz groundmass that contains interstitial brown titanite(?), calcite laths (likely replacing plagioclase), chlorite, minor sericite and Ti oxide minerals. There appears to be two domains, a more brecciated zone that is defined by chlorite and interstitial titanite and, a more coherent domain that contains rare euhedral quartz phenocrysts and a dusty quartz groundmass. There are also recrystallized spherulites in the groundmass which exhibit sweeping but non-symmetric extinction (Fig. 3.2C) upon rotation of the microscope stage.

This unit is intruded by a rhyolite lobe (07-P2-58A-core, 58B-rim) that had relict rhombohedral (likely carbonate) minerals that were altered to a dusty orange-brown opaque mineral (possibly rutile) all of which are set in a groundmass of polycrystalline quartz (~20 μm) and zircon microphenocrysts (<40 μm), with minor amounts of chlorite, sericite, and carbonate. This rock also contains discrete domains (Fig. 3.2D) of chlorite and an unknown brown mineral that appear to outline quartz-filled vesicles that resemble vesicular zones within modern flow-banded material (Chapter 4; Fig. 4.3B). This lobe

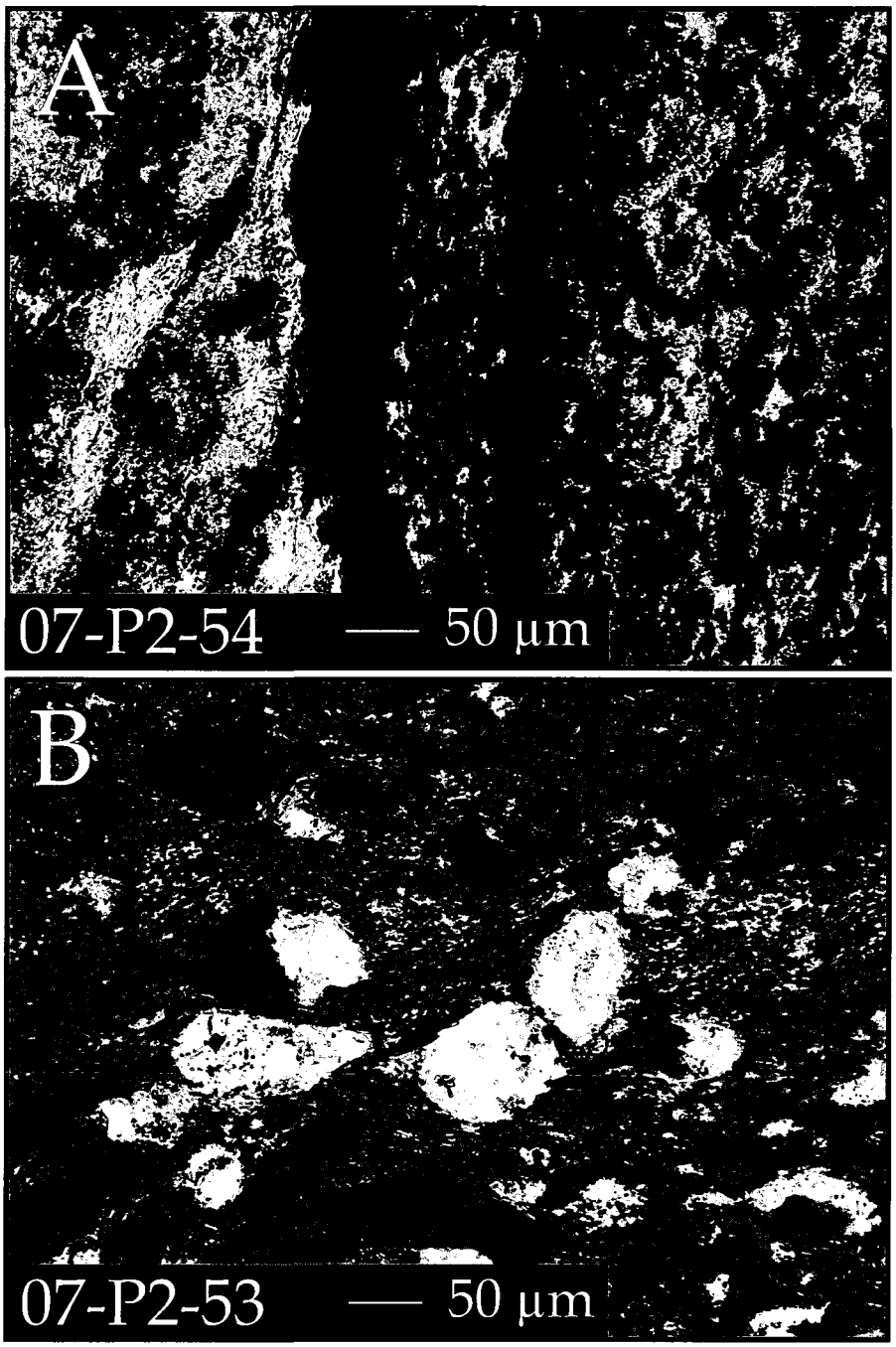

Figure 3.2: Prosser Outcrop 1 microphotographs. A) Peperitic contact with rhyolite (left) projection into brown tuff (right). Note the thick black opaque Fe oxide mineral margin. Plane polarized light (PPL) B) Flow banding within aphryic rhyolite showing quartz phenocrysts that have strain shadows where flow was deflected around the phenocrysts. Crossed nicols (XPL)

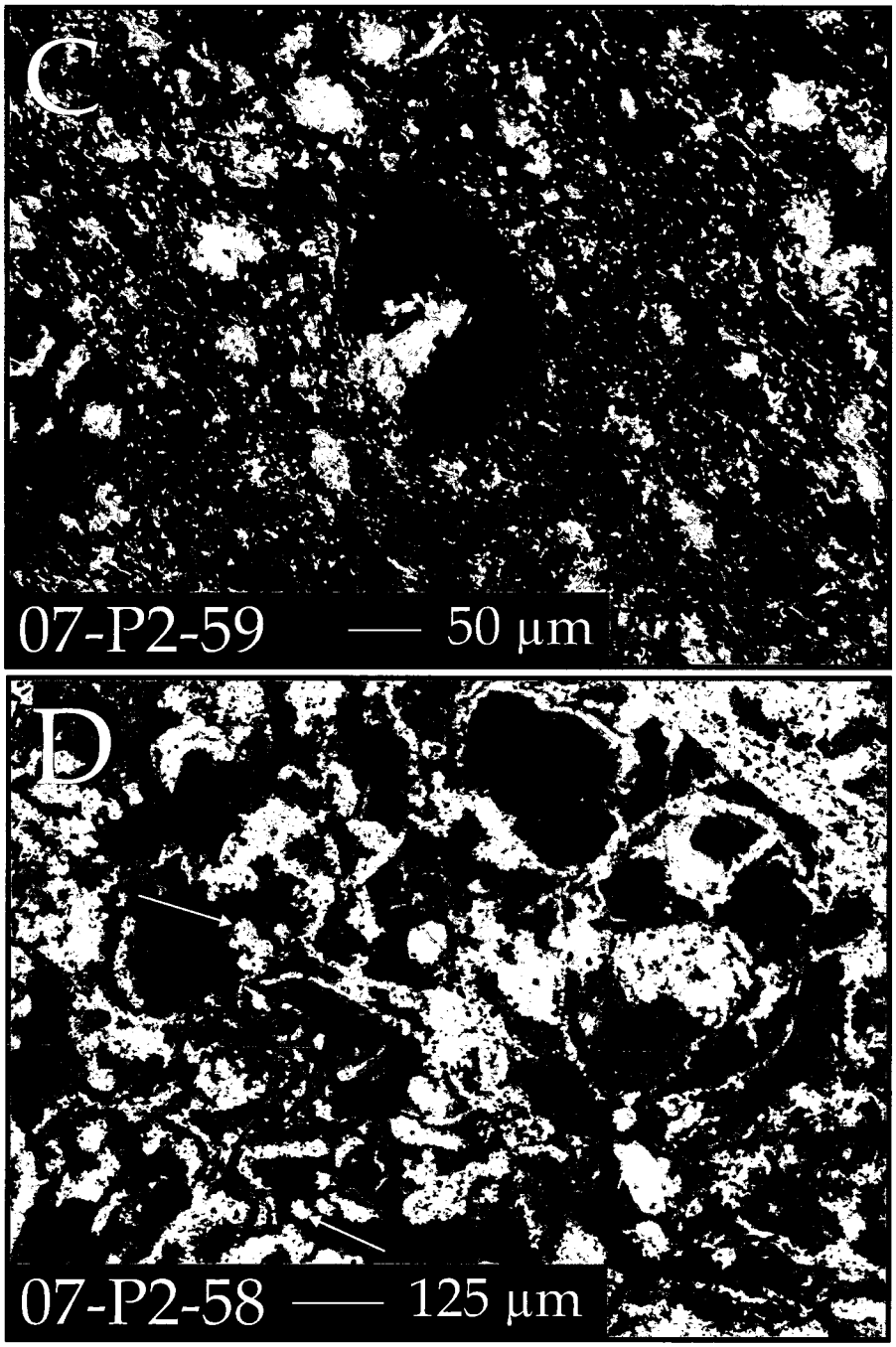

Figure 3.2: Continued. C) Spherulites showing typical fine radial texture but coarser zones of extinction interpreted to be due to recrystallization. (XPL) D) Chlorite and unknown brown mineral replacing and filling in vesicular domain within rhyolite. Arrows point to quartz amygdules. (PPL)

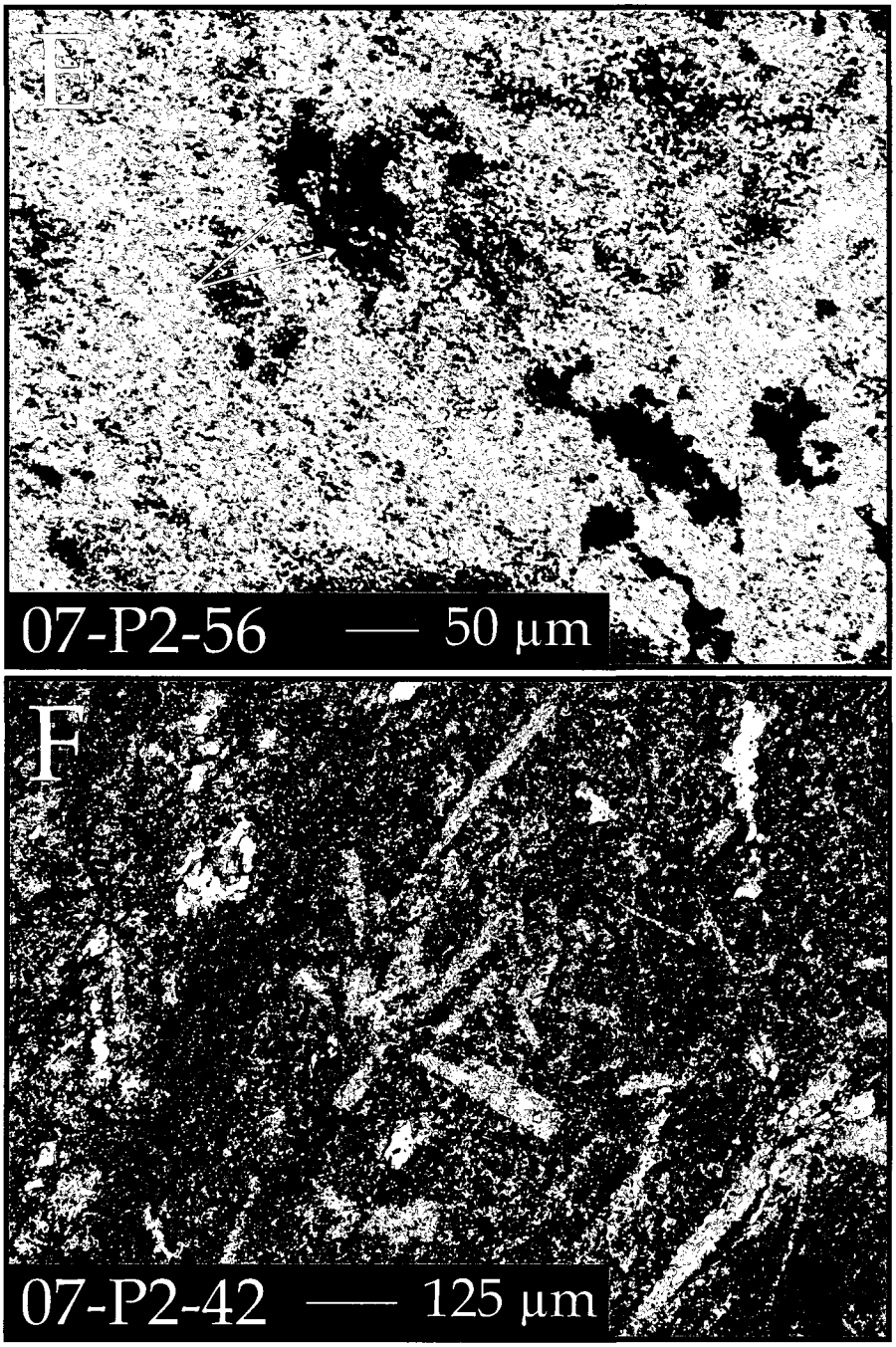

Figure 3.2. Continued. E) In situ brecciation of a zircon microphenocryst where the two halves (arrows) which are in crystallographic continuity are separated by a narrow vein of groundmass material. (PPL) F) Relict hyalopilitic texture showing randomly oriented altered plagioclase phenocrysts set in a groundmass of dusty grey cryptocrystalline material. (PPL)

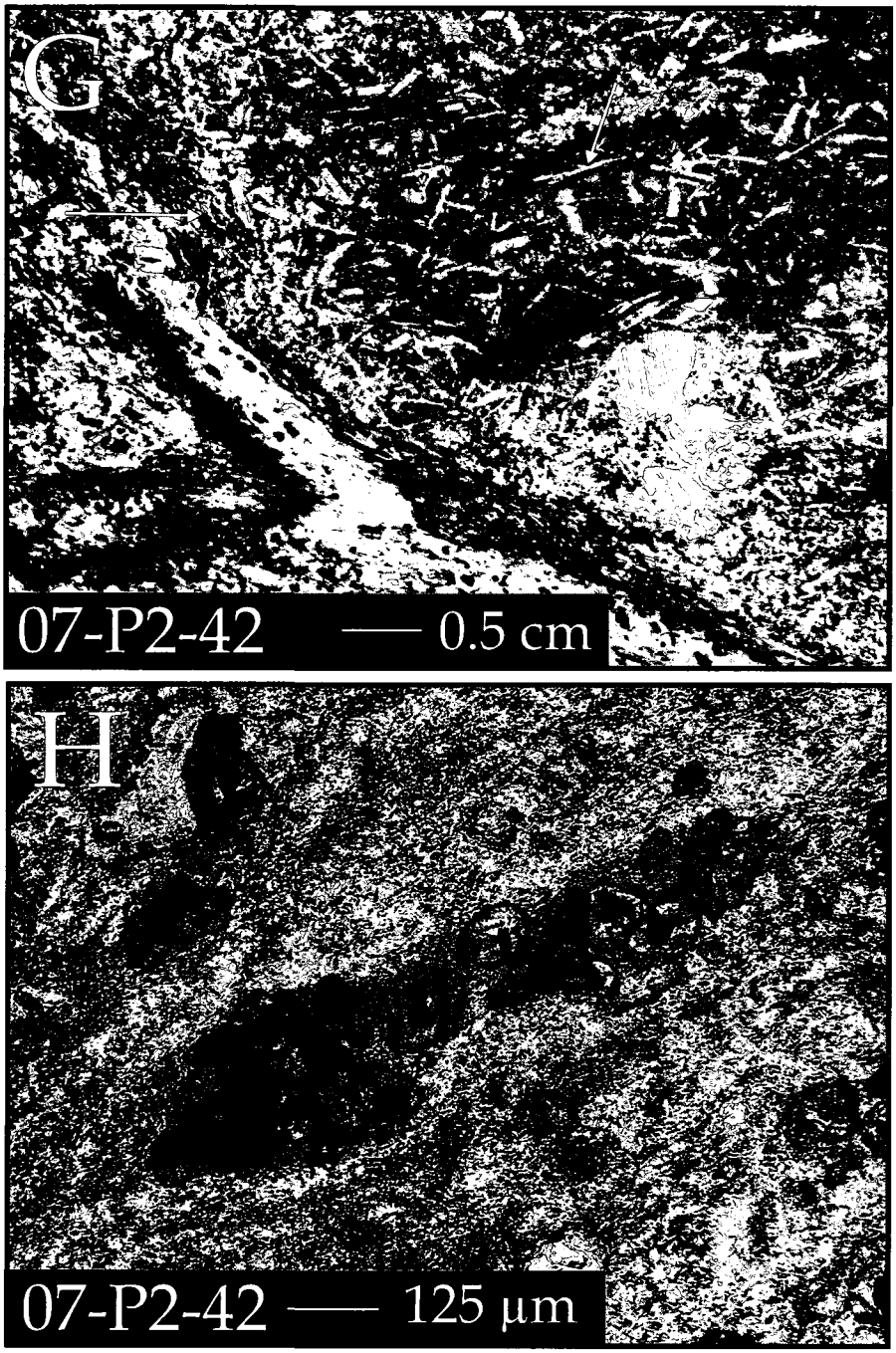

Figure 3.2. Continued. G) Possible intrusive lobe showing a fine grained margin (left arrow) with larger relict plagioclase near centre of clast (right arrow). (PPL) H) Amoeboid titanite in the matrix around a hyalopilitic groundmass show in F. Note the darker cores on some crystals. (PPL)

has albite veins of coarse (0.3 mm) twinned albite. The lobe rim (07-P2-58B), for which there is no thin section, has been completely altered to a very fine-grained mainly sericite mixture.

The flow banded rhyolite is overlain by flow top breccia that includes flow banded blocks and lapilli (07-P2-50). Flow bands are defined by fine and coarse zones of recrystallized quartz groundmass and outlined by chlorite and sericite. In thin section this breccia has no phenocrysts and is dominated by quartz, albite-carbonate-brown/orange rhombohedral minerals and quartz-carbonate veins. There is significant sericitization and chloritization that dominate the more permeable zones of the breccia. The brown-orange rhombohedra are again associated with carbonate, but euhedral unaltered carbonate rhombohedra are also present within the groundmass.

In sharp contact with the flow top breccia is a block-bearing tuff (07-P2-47) that is composed of embayed, rounded and broken quartz phenocrysts up to 1.4 mm in size. These are set in a groundmass of dusty pale brown polycrystalline quartz, spherulites, sericite, chlorite and uncommon dusty brown opaque minerals. This tuff is cut by quartz-albite and quartz-chlorite veins. There are two types of clasts described in the outcrop; 1 a white clast with deformed quartz amygdules and quartz phenocrysts, and 2 a grey clast with undeformed quartz amygdules. The type 1 clasts (07-P2-48) consist of quartz phenocrysts (<<1 vol %; <0.4 mm in size) set in a matrix of recrystallized quartz spherulites and variable coarse (~0.3 mm; quartz amygdules) and fine zones (<50 μm; recrystallized glass). Type 1 clasts also have uncommon carbonate laths as well as very fine dusty and black Fe oxide minerals. Type 2 clasts (07-P2-49) consist of roughly equal proportions of quartz and relict feldspar phenocrysts (~5%) set in a dusty groundmass of quartz, sericite and quartz spherulites (<0.5 mm). The quartz phenocrysts are up to 1.8 mm, subhedral to round, are commonly embayed, and have spherulitic overgrowths on them. The carbonate laths are interpreted as relict feldspars based on the morphology along with the acid replacement components (calcite and sericite). This rock also contains rare Fe Ti oxide minerals.

Overlying the block bearing tuff (07-P2-47) is a flow banded rhyolite that laterally becomes a bluish highly foliated rock (07-P2-56). Sample 56 consists of a very fine-grained mixture of quartz, sericite and dusty black opaque Fe Ti oxide minerals. In

addition to this are common zoned quartz phenocrysts and euhedral zircons. One of the zircons exhibits in-situ brecciation, where the constituent pieces are separated by less than 20 μm but maintain their original orientation (Fig. 3.2E). This indicates that during alteration and elemental exchange zircon was; a) resistant to the fluids that have altered the rock, and b) that this rock has not been significantly deformed at the small scale by tectonic processes. This sample is almost identical to 07-P3-09 in outcrop 2.

The overlying rocks are a poorly exposed sequence of black and brown flow banded rhyolite, vesicular tuff, quartz-phyric rhyolite and highly chloritized tuff. The black and brown flow banded rhyolite (07-P2-46) has a recrystallized groundmass of quartz and sericite with dusty to disseminated brown opaque minerals and also abundant amoeboid titanite that commonly have quartz inclusions. Spherulites and possible polycrystalline quartz amygdules or veins are present in the groundmass. This rock also contains biotite, accessory zircon, minor calcite and chlorite alteration. The foliated white rhyolite (07-P2-45) contains a sericitized groundmass of recrystallized spherulites (<1%) and recrystallized quartz. This rock also contains veins of carbonate, plus veins of quartz and albite-carbonate. There is also a large, 14 mm, polycrystalline quartz aggregate that has calcite laths and is interpreted to be either a clast or amygdule.

Sample 07-P2-44 was interpreted as vesicular tuff in the field however petrographic study demonstrates that it has a relict hyalopilitic textures with abundant relict intergrown feldspar laths, ~5 mm by ~1 mm, that have been converted into a mixture of dusty opaque minerals, carbonate, quartz and epidote. This sample also contains chlorite-carbonate-epidote and carbonate-quartz-pyrite veins. The coarse grained texture of this rock suggests that this rock is a highly altered intrusive intermediate magma. The hyalopilitic texture suggests that this is an analoguous phase to the intrusive lobes that have been described within the tuffaceous units in Outcrop 2 (Sample 07-P3-03).

This intrusive unit is bound on the south side by a quartz-phyric rhyolite (07-P2-43B) that is cut by a leucocratic dyke (07-P2-43A). Sample 07-P2-43B contains 10-15 % quartz phenocrysts up to 2.5 mm in size that are commonly rounded and embayed. They are set in a groundmass of dusty brown cryptocrystalline material, very fine-grained quartz and Fe Ti oxide minerals with minor amounts of chlorite and carbonate. There are

also minor recrystallized spherulites, zircon microphenocrysts and chlorite-carbonate-quartz veins.

The leucocratic dyke (07-P2-43A) contains rare round quartz phenocrysts (<1%; <1 mm in length) which are optically zoned from core to rim and have an inclusion charged interior zone. This rock is mostly composed of disseminated dusty opaque minerals (40-60%) and groundmass quartz (15-25%) with approximately 5 % or less of each, quartz phenocrysts, carbonate, muscovite and Fe oxide minerals. There are also minor amounts of chlorite, pyrite and relict plagioclase(?) phenocrysts. This rock is not nearly as coarse but is reminiscent of the texture of 07-P2-44 however it is definitely a dyke which is consistent with the interpretation that these dykes were emplaced into the volcanic pile which allowed the time for crystal growth.

This rhyolite and its leucocratic dyke are overlain by an intermediate tuff (07-P2-42) that is coarsely crystalline. Relict hyalopilitic texture (Fig. 3.2F) with randomly oriented relict feldspars that have been completely altered to very fine dusty grey cryptocrystalline material, interstitial quartz and dusty Fe Ti oxide minerals which make up this rock. The relict plagioclase laths show a coarsening towards the interior of the clasts (Fig. 3.2G). Calcite filled amygdules are also present within the hyalopilitic domains. This rock is brecciated with clasts of relict hyalopilitic material around which the matrix has been replaced with chlorite, abundant brown amoeboid titanite (Fig. 3.2H), calcite, quartz and minor epidote. Overlying this is a grey flow banded rhyolite (07-P2-41) containing between 10 and 15 vol. % embayed subhedral to round quartz phenocrysts and ~1 vol. % relict subrounded feldspar phenocrysts (<2.2 mm) that have been altered to sericite but are identified based on their preserved twinning. This rock has been variably altered to chlorite, sericite, albite (veins) and epidote. Microphenocrysts of zircon plus minor amounts of amoeboid titanite are present.

3.1.2 Prosser Outcrop 2

At the base of the stratigraphy of Outcrop 2 (Fig. 3.3) is a brown tuff that hosts ample leucocratic blocks that have conchoidal margins. This brown tuff (07-P3-13) has been destructively altered to a fine-grained mixture of quartz, chlorite, dusty opaque

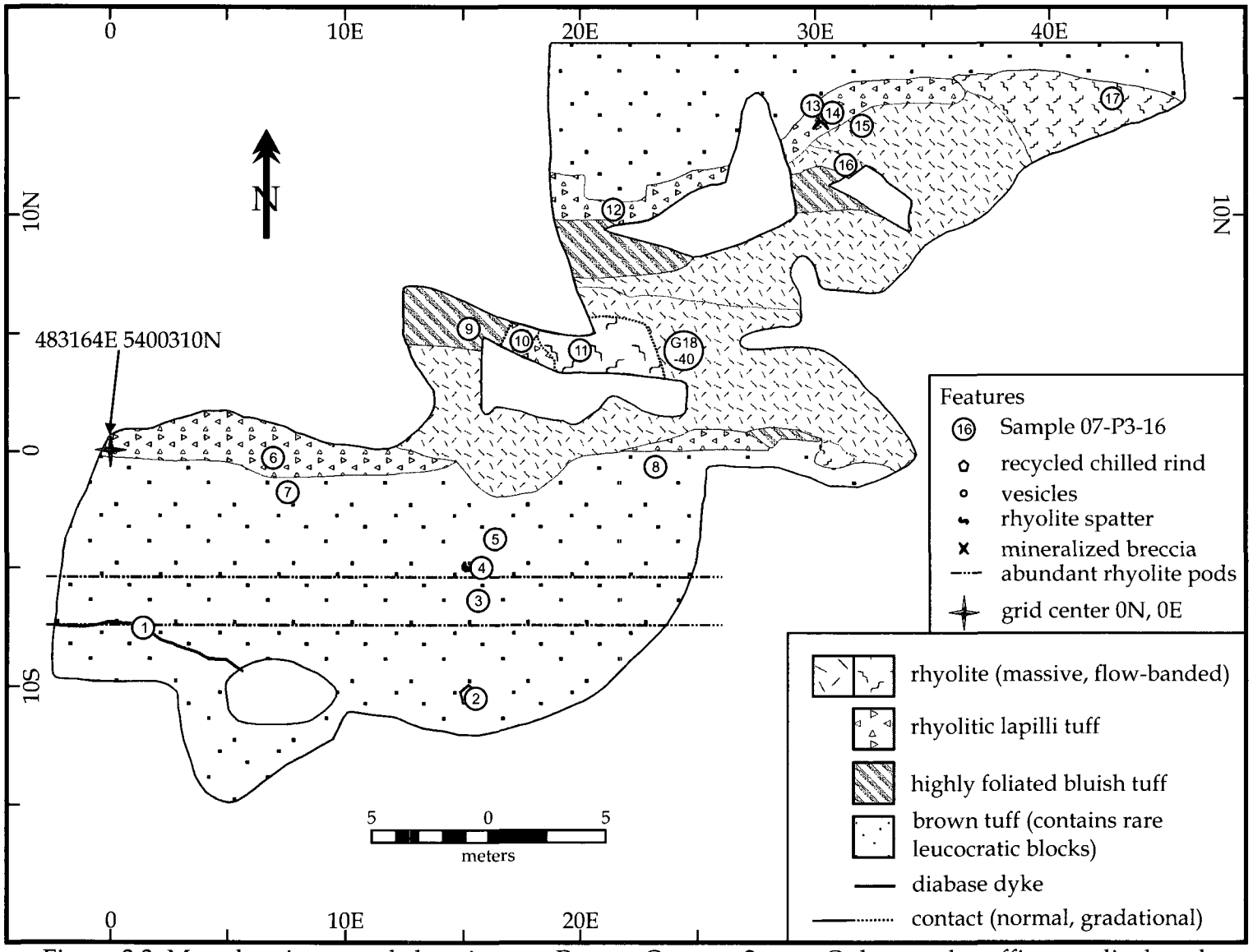

Figure 3.3: Map showing sample locations on Prosser Outcrop 2 map. Only sample suffixs are displayed.

minerals and Fe-Ti oxide minerals. The leucocratic blocks (07-P3-14) have a coarse relict hyalopilitic groundmass of relict feldspars (<0.25 mm) that have been altered to quartz and fine-grained dusty opaque mineral. It also contains large relict plagioclase phenocrysts up to 2.5 mm in length that have been altered to clay and sericite but preserve their original Carlsbad twinning. This rock also hosts quartz-carbonate-muscovite veins.

The brown tuff is overlain in the east by a grey flow banded rhyolite (07-P3-17). Flow banding is defined by a fine-grained (~30 μm) polycrystalline quartz matrix with pervasive sericitization and lesser chloritization, Fe Ti oxide minerals (hematite?) and dusty opaque minerals. Zircon microphenocrysts are preserved unaltered.

In the north central part of the outcrop the brown tuff is overlain by two rhyolitic lapilli tuff units, a coarse unmineralized breccia and a hematized and epidotized breccia. The unmineralized breccia (07-P3-12) contains euhedral quartz phenocrysts up to 0.3 mm set in a groundmass containing round quartz. These are interpreted to be amygdules (Fig. 3.4A) and the rock a pumice. There are also oval Fe Ti oxide minerals which have radial overgrowths of quartz. Macroscopically the mineralized breccia consists of two distinct zones, a hematized zone (07-P3-15B) and a epidotized zone (07-P3-15A). Both breccias have similar microscopic texture containing many well developed quartz spherulites (Fig. 3.4B) which contain randomly oriented alkali feldspar microphenocrysts (<30 μm) as well as anhedral interstitial alkali feldspar crystals. There are also minor amounts of interstitial albite, rare allanite-like minerals (Fig. 3.4C) and euhedral zircons that show a patchy zonation. These samples have calcite, muscovite and pyrite matrices, as well as albite veins.

Overlying these breccias is a coherent rhyolite (see Table 4.2 for individual descriptions of grid samples 07-P3-18 → 40) that is composed of <1% quartz phenocrysts (<0.3 mm in size) and a relict-glassy groundmass that exhibits a perlitic texture where conchoidal fractures form nested groups (Fig. 3.4D). The conchoidal fractures have now been filled with polycrystalline quartz and the material between these is dusty albite. Generally this rock is composed of rare quartz phenocrysts (<0.5 mm) within a fine grained quartz groundmass with varying degrees of albite, chlorite and sericite alteration, zircon microphenocrysts and combinations of quartz, calcite, chlorite,

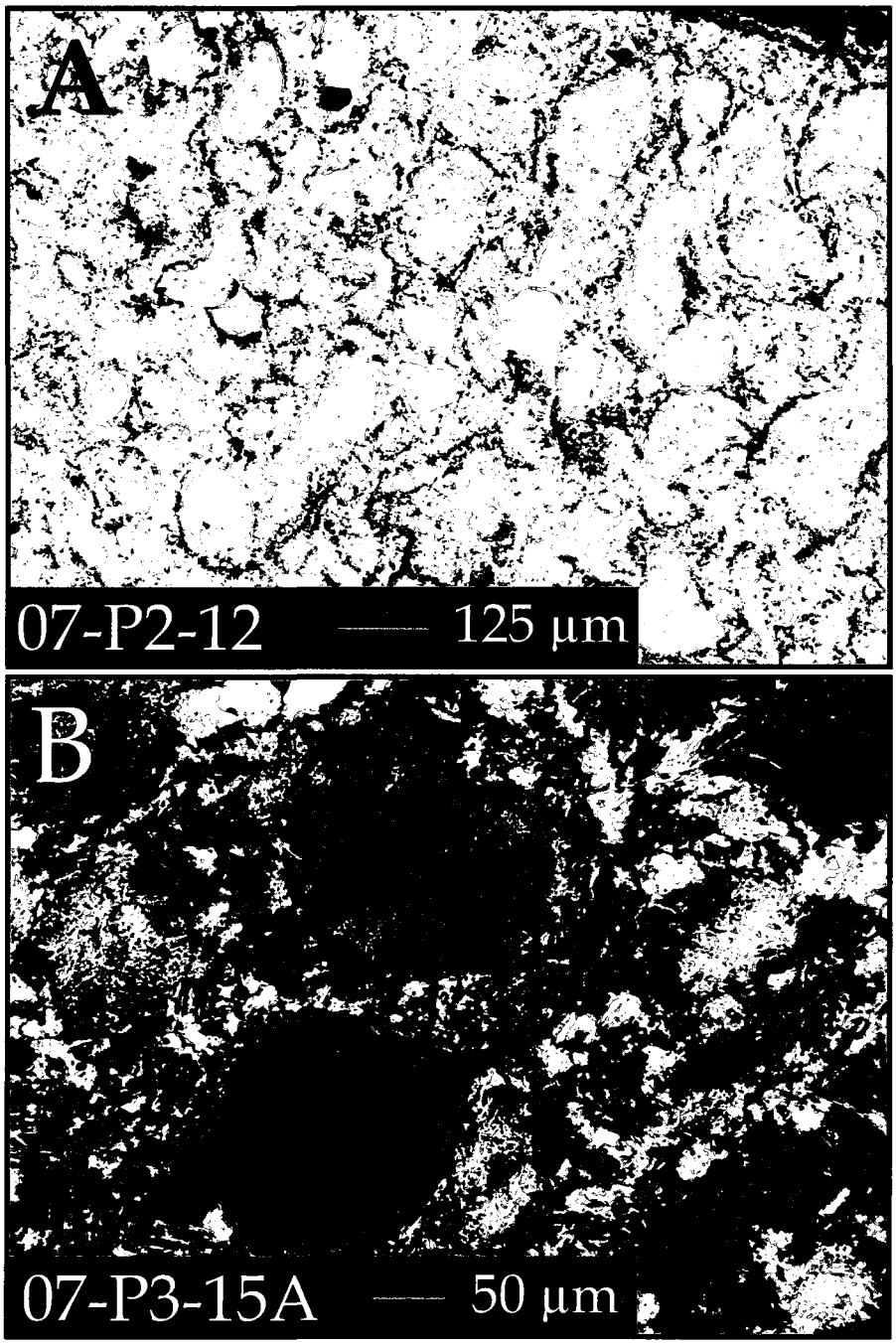

Figure 3.4: Prosser Outcrop 2 microphotographs. A) Quartz-filled amygdules within a pumice. PPL. B) Spherulite showing symmetric extinction. XPL.

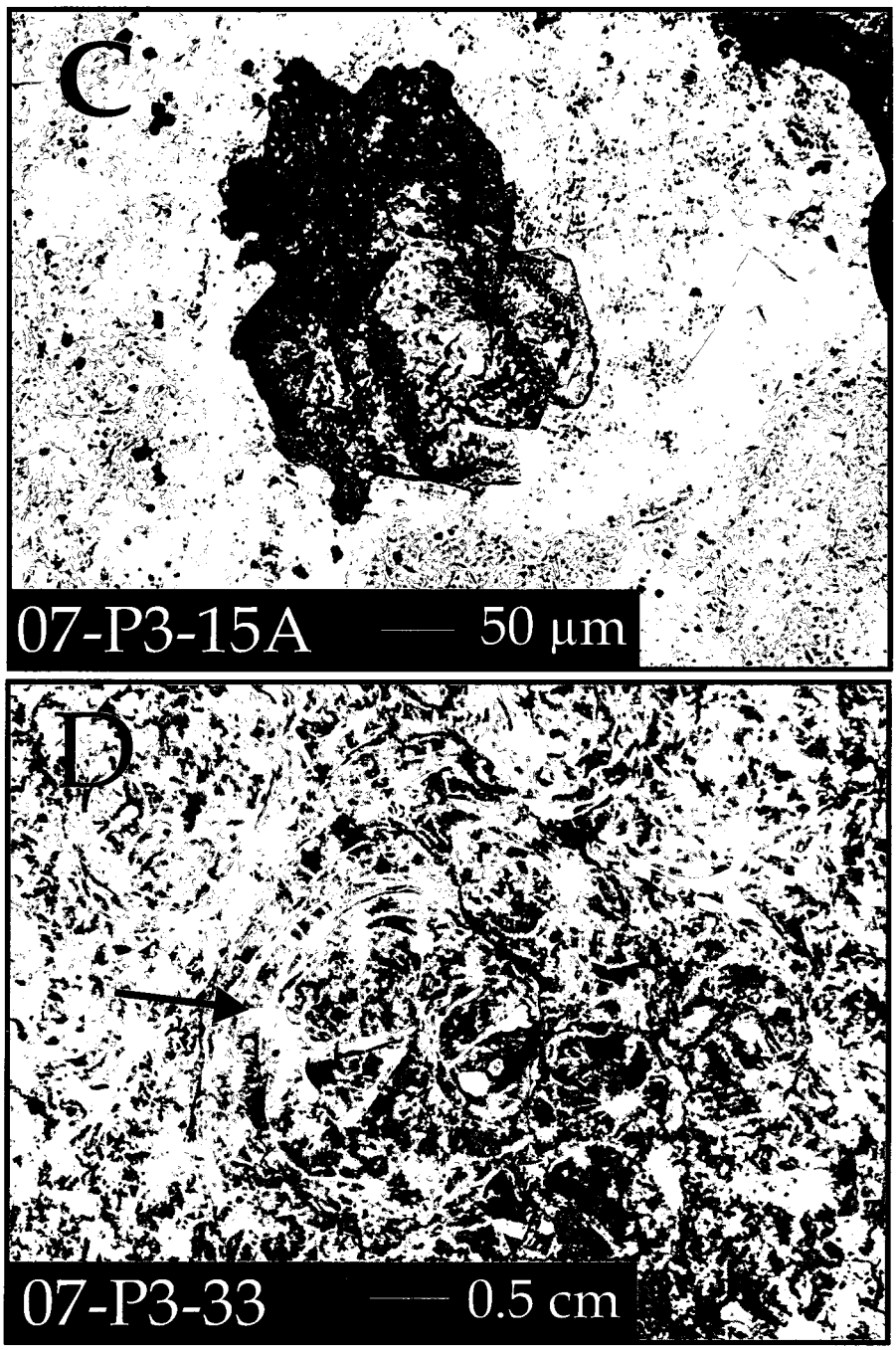

Figure 3.4: Continued. C) REE-concentrated allanite-like mineral. (PPL) D) Concentric conchoidal fractures within a phenocryst poor groundmass interpreted as perlitic fracturing. (PPL)

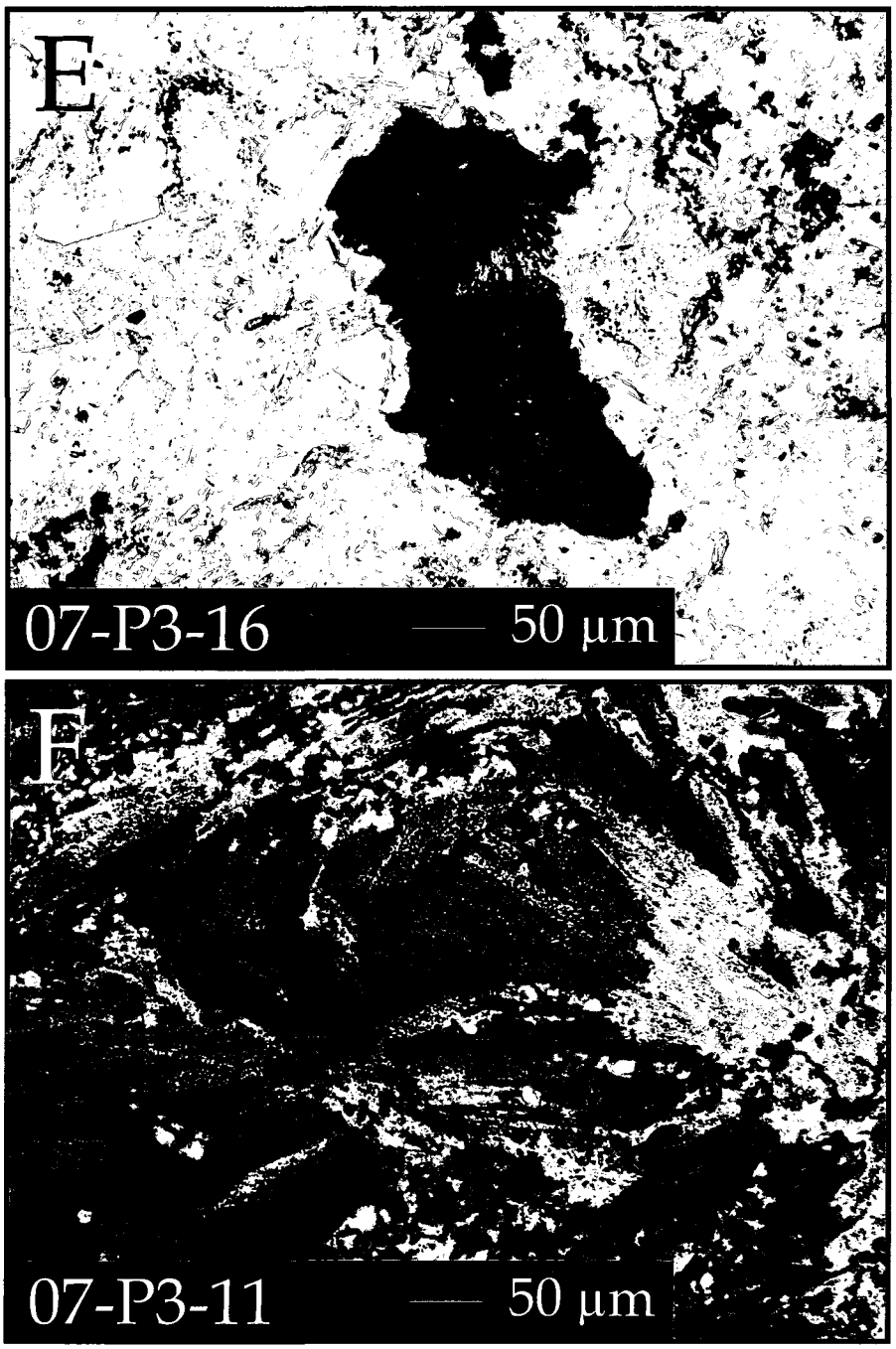

Figure 3.4: Continued. E) Undetermined brown mineral (synchysite?). (PPL) F) Albite intergrowth with fine dusty sericite alteration. Commonly seen in veins and domains within a typically fine-grained polycrystalline quartz groundmass. (XPL)

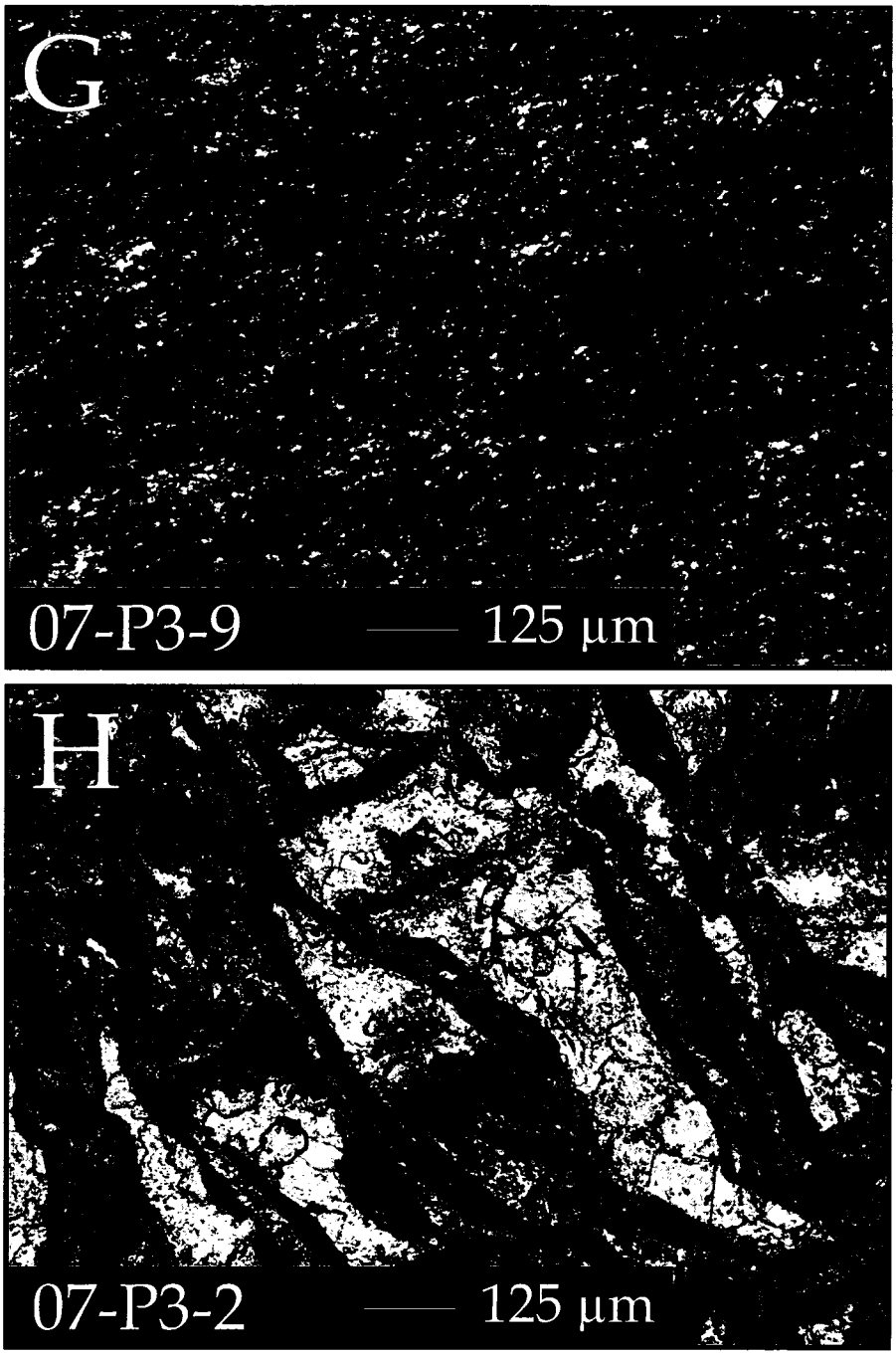

Figure 3.4: Continued. G) Bluish grey fine-grained tuffaceous rock. Completely altered to quartz, chlorite, sericite and dusty opaque minerals. Note zircon in top right corner is unaltered throughout alteration. (PPL) H) Relict glass shards of a hyaloclastite margin have been altered to chlorite, calcite and epidote. Note thick opaque rims. (PPL)

albite and pyrite within veins. The presence of perlite and lack of phenocrysts is consistent with the interpretation that these were originally very glassy lavas that have been subsequently recrystallized into a polycrystalline quartz and albite rock. For further description see section 4.2.3.

This aphyric rhyolite is cut by a sinuous rhyolite dyke (07-P3-16) containing large (< 1.0 mm) anhedral quartz phenocrysts, rare radiating sheaths of an undetermined dusty pale yellow mineral (Fig. 3.4E) and euhedral microphenocrysts of zircon (<0.2 mm) which have melt inclusions, very fine needle inclusion (apatite?) and exhibit a concentric zonation. Euhedral calcite rhombohedra are found in the groundmass as well as anhedral calcite in veins. There is also secondary albite and chlorite.

The massive aphyric rhyolite has a flow banded margin (07-P3-11) in the central west part of the outcrop that grades into an *in situ* lapilli tuff (07-P3-10) and further into a very fine-grained highly foliated bluish tuff (07-P3-09) which are described below. The flow bands in Sample 07-P3-11 are defined by polycrystalline quartz domains and intergrown alkali feldspar crystals (Fig. 3.4F). These crystals are up to 0.8 mm and commonly show a very fine dusty sericite alteration. This rock also contains euhedral zircon microphenocrysts, quartz-chlorite veins and small blebs of an unknown brown mineral that contains inclusions of quartz and opaque rims inferred to be titanite. Laterally the rhyolite becomes a lapilli breccia, sample 07-P3-10, that has anastomosing veins of sericite and polycrystalline quartz, some of which are elongated and round resembling amygdules. The lapilli breccia also contains equant microphenocrysts of zircon <50 μm in size that have inclusions and are concentrically zoned. The western most equivalent of the breccia is a very fine grained bluish rock (07-P3-09) that now, in decreasing proportion, consists of quartz, chlorite, sericite, dusty opaques, epidote and Fe Ti oxide minerals (Fig. 3.4G). The micro-fabric is well developed and deflects around relict quartz phenocrysts (<0.3 mm) that are now polycrystalline and have quartz filled strain shadows. The foliation has not altered the numerous euhedral zircon microphenocrysts <0.2 mm that contain melt inclusions and are concentrically zoned.

Overlying the aphyric rhyolite is a brown tuff (07-P3-05 and 07-P3-07). The matrix of the tuff (07-P3-07) is from near the contact with the rhyolite which in outcrop has abundant vesicles. Microscopically there is a contact between a zone that contains 30-

40% groundmass quartz, 30-40% chlorite, 5-15% small round blebs of a brown titanite and very fine-grained dusty opaque minerals and a second more siliceous zone. Within this first zone there are polycrystalline quartz domains as well as chlorite-brown mineral domains which could represent a coarse breccia. The brown opaque minerals occur as small fans or as ovoidal rims around chlorite. The second zone contains 50-70% quartz with interstitial chlorite (15-25%), and lesser amounts of a brown mica (5-10%), Fe oxide minerals (5%), zircon(?) and epidote. There are also relict phenocrysts of quartz and feldspar which together make up less than 1% of the rock. These zones while ill defined likely represent relict lithic fragments much more altered than those described in the following outcrop (section 3.1.3 Outcrop 3). The second, quartz-rich zone is likely a fine-grained felsic breccia or peperite as it is adjacent to a rhyolitic lapilli tuff in outcrop. The other sample of matrix 07-P3-05 has a similar mineralogy to the first zone described above however there is more turbid cryptocrystalline material in the matrix and the lithic clasts are better defined. These pumiceous clasts have abundant chlorite, calcite and quartz amygdules which become progressively flattened and more chlorite filled and less quartz filled towards the margins of the clasts. Together the matrix of this rock is composed of a fine-grained assemblage of chlorite, dusty opaque minerals, titanite, epidote and minor quartz. The intense chloritization has destroyed any texture that might have been preserved within the matrix.

Several macroscopic features have been described from this tuff including the layer of abundant leucocratic pods, the adjacent spatter-like material, pumice blocks, and a bomb with a recycled chilled rind. A leucocratic lobe (07-P3-03) has a somewhat felty texture groundmass with rare sericitized feldspar phenocrysts (<0.3 mm) set within a dusty matrix of cryptocrystalline material, white mica, chlorite and minor epidote and quartz. There is also a minor amount of calcite disseminated throughout. The adjacent spatter has been pervasively chloritized but exhibits an amygdaloidal texture similar to the spatter described below in Outcrop 3. The amygdules range from undeformed to flattened and are filled with chlorite, quartz and uncommonly epidote. The groundmass of the spatter has been converted to roughly equal proportions of chlorite, dusty cryptocrystalline material and Fe Ti oxide minerals. The matrix of this rock has much more chlorite and again it is commonly seen that Fe oxide minerals are concentrated

within the matrix along the contact. Epidote is more common in some of the other pieces of spatter within this thin section. The pumice block (07-P3-08) is similar to those described below, having quartz and chlorite filled, variably deformed amygdules set in a mottled grey groundmass that has a size gradation and minor calcite replacement. Near the top of the stratigraphy is a bomb (07-P3-02) that has been interpreted as a containing a recycled chill rind where highly vesicular domains surround a more coherent core. Microscopically the coherent part of this bomb is similar in texture and mineralogy to that of the above described leucocratic lobes as it contains sericitized plagioclase phenocrysts within a felty mottled groundmass. However the adjacent vesicular zones exhibit a distinct hyaloclastite texture (Fig. 3.4H). The shards of glass are defined by a dusty brown opaque mineral rim and have been replaced by chlorite, epidote, calcite and quartz.

Finally the top-most brown tuff is cut by a late mafic dyke that has not retained any primary mineralogy or texture. The mafic dyke has been altered to a mixture, in decreasing proportion, of mottled opaque minerals, chlorite, Fe Ti oxide minerals, quartz, epidote and carbonate laths. The carbonate laths appear to have replaced feldspars in a relict hyalopilitic groundmass texture preserved in parts. This rock also has 1-2 vol. % calcite and chlorite amygdules.

3.1.3 Prosser Outcrop 3

The base of Outcrop 3 (Fig. 3.5) is an aphyric rhyolite and its flow-top breccia. Sample 07-P1-60 (Fig. 3.6A), the coherent part of the flow, contains a few percent phenocrysts of quartz and minor plagioclase (<<1%). The groundmass is composed of fine-grained quartz, dusty opaque minerals, calcite rhombohedra, chlorite and minor amounts of discrete Fe Ti oxide minerals. The overlying breccia (07-P1-61) has a similar mineralogy with more euhedral quartz phenocrysts, a coarser groundmass of similar mineralogy and pervasive small (<0.1 mm) opaque minerals. The clasts within this breccia (07-P1-62) are defined by a margin of vesicles, chlorite, opaque minerals, fine-grained yellowish-orange mica, dusty opaque minerals and quartz. Albite veins also cut this flow-top breccia.

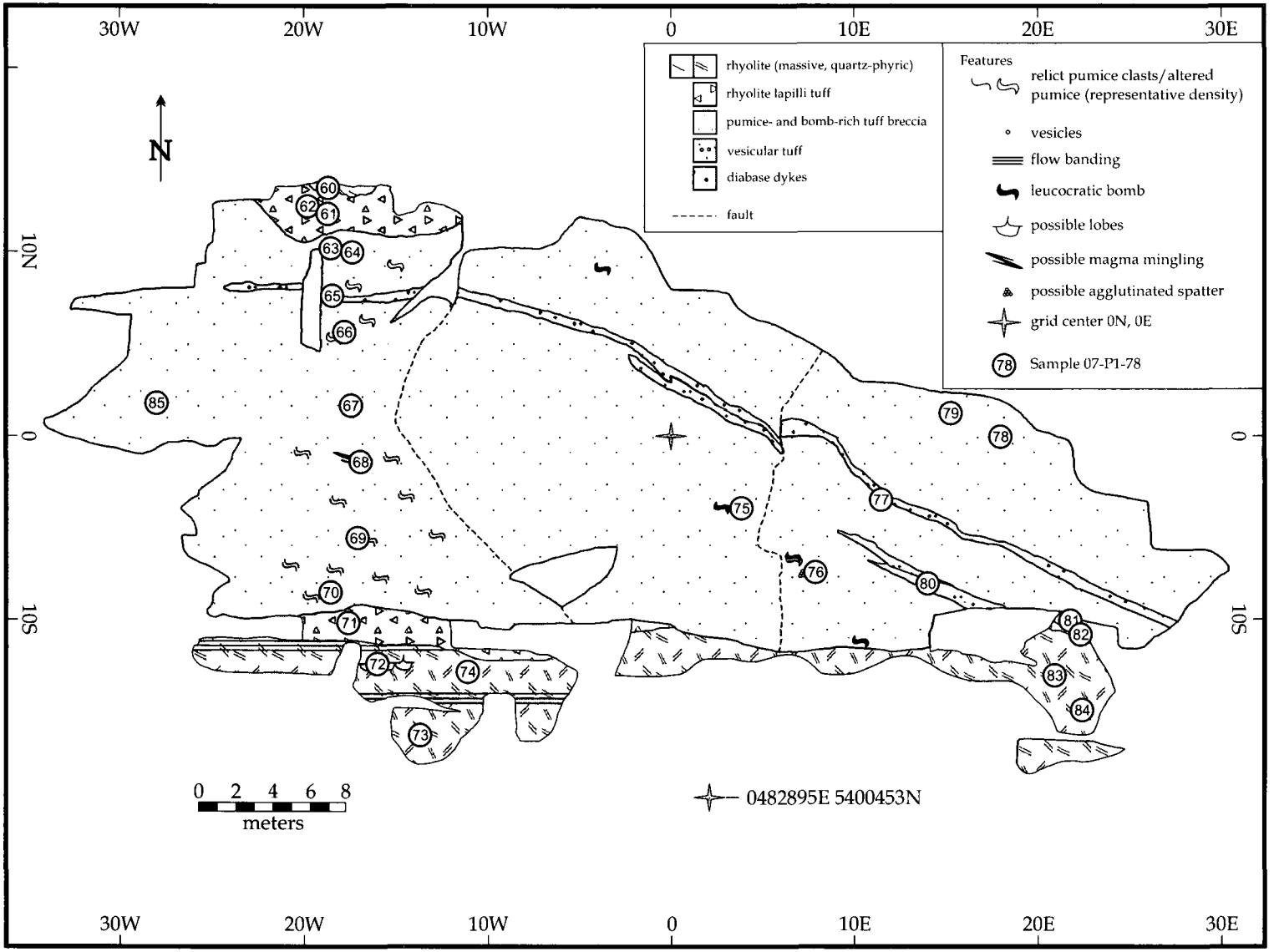

Figure 3.5: Prosser Outcrop 3 map showing sample locations. Sample suffixes are displayed.

The overlying pumice- and spatter-rich tuff breccia is composed of variable proportions (in decreasing order of abundance) of chlorite, mottled brown and grey cryptocrystalline materials, amygdules, opaque minerals (mainly pyrite), fine polycrystalline quartz, epidote, carbonate (mainly calcite), titanite, stilpnomelane, rutile and altered lath-shaped feldspars. Amygdules are mostly filled with chlorite and also quartz and microcline (Fig. 3.6B). The carbonate occurs as either anhedral dusty masses or as laths interpreted to be replacing plagioclase. The matrix of this rock also contains phenocrysts of quartz and sericite-altered-relict plagioclase identified by the preservation of albite and/or Carlsbad twinning and their habit. Locally there are several different veins present composed of various combinations of quartz, calcite, chlorite, albite and stilpnomelane. The stilpnomelane is almost uniquely associated with the calcite (Fig. 3.6C). Albite veins are much less abundant in this tuff relative to their abundance within the rhyolite units.

Set within the groundmass are fluidal spatter and pumice blocks that macroscopically appear to have different alteration-defined-zonations and whose morphologies are quite unique. Microscopically, the difference between the types of zonation is evident in the proportions of dusty brown-orange-grey-black cryptocrystalline materials to chlorite to groundmass quartz, and by the sizes, compositions and morphologies of vesicles. Sample descriptions have been organized starting with the pumice blocks at the base of this tuff breccia and continuing up through the unit. The spatter clasts are than described in a similar ascending order.

The zonation within clasts is quite complex at the base of this unit, for instance the zonation of the pumice clast, 07-P1-64, has over 7 zones observed in thin section. The core (zone 1; Fig. 3.6D) of this block (07-P1-64B) is almost entirely composed of dusty black opaque minerals, sub-rounded quartz filled amygdules and is highly veined by quartz, calcite and stilpnomelane. Surrounding this core, zone 2, are quartz, quartz-chlorite and quartz-chlorite-stilpnomelane amygdules that are stretched into ovals, some of which are pinched out at their ends. Zone 3, which surrounds zone 2, is mostly dusty grey cryptocrystalline material with moderately deformed amygdules of mainly quartz and lesser amounts of chlorite ± stilpnomelane. Further outward, zone 4, alternates back to mainly dusty opaque cryptocrystalline material with undeformed vesicles that are

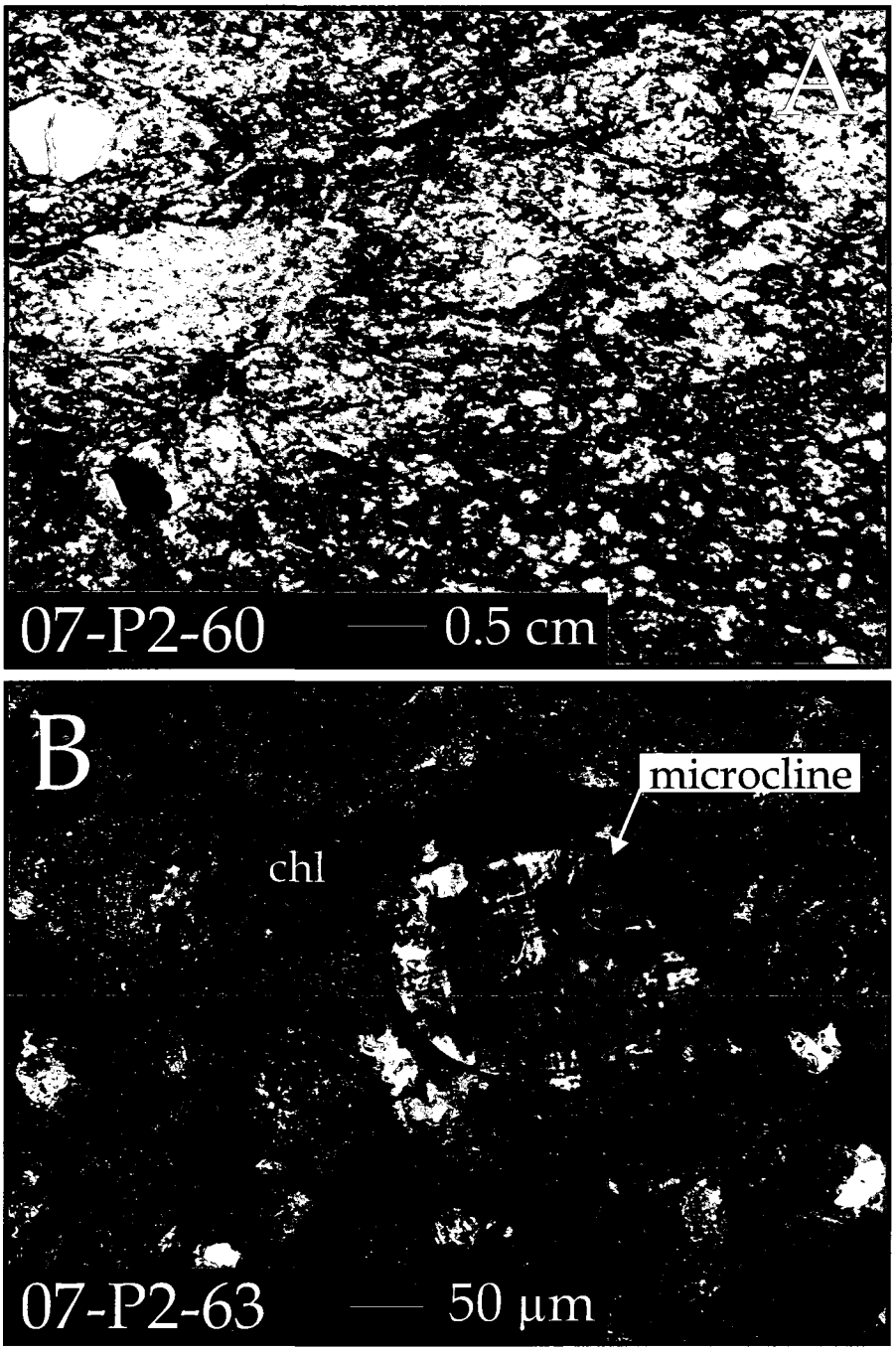

Figure 3.6: A - Aphyric rhyolite 07-P2-60. B - Microcline amygdule rimmed in cryptocrystalline material and chlorite.

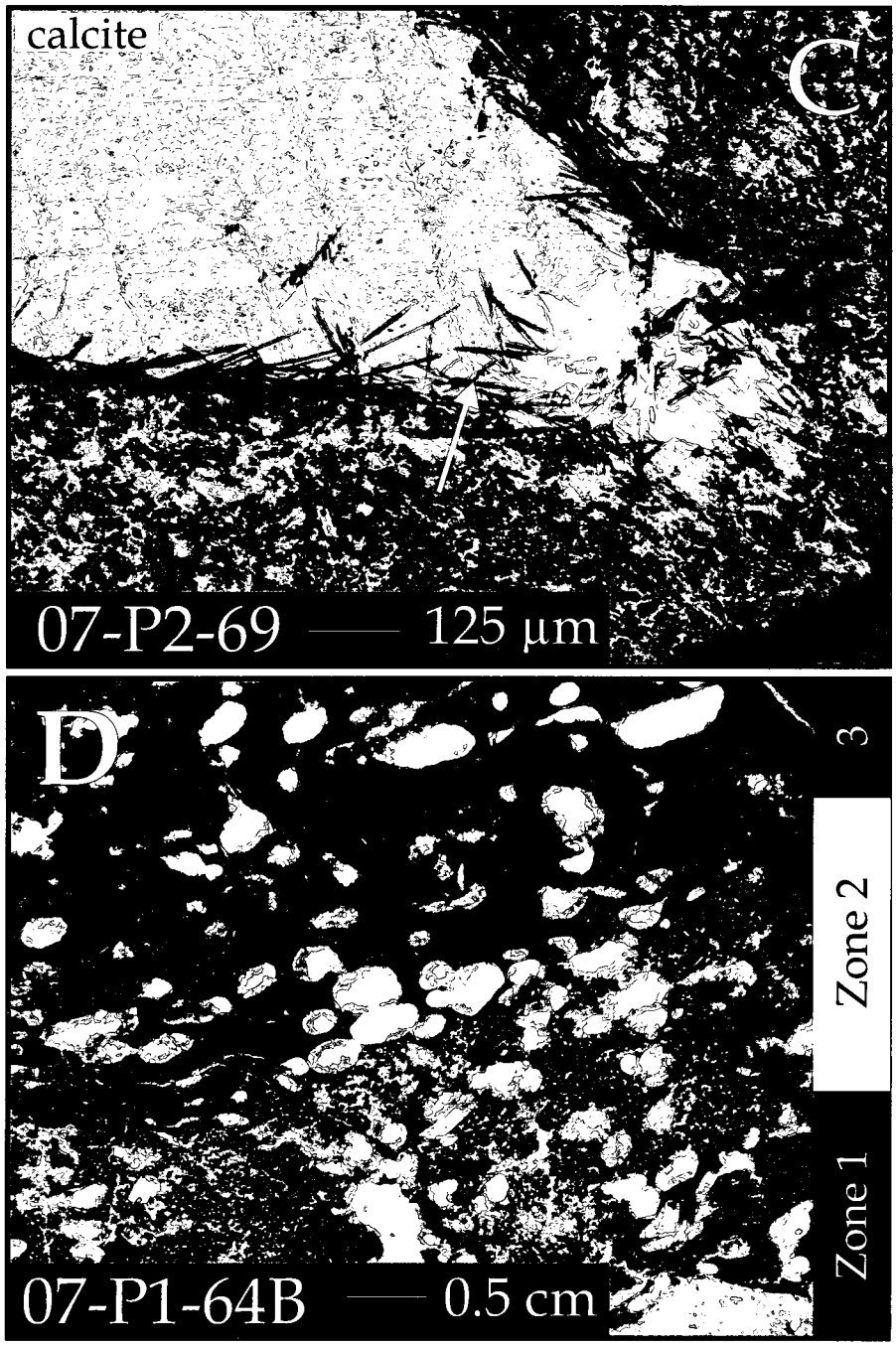

Figure 3.6: Continued. C - Stilpnomelane needles (arrow) rimming calcite vein. D - Core zonation within a pumice block 07-P1-64B. Zones are labeled along right margin.

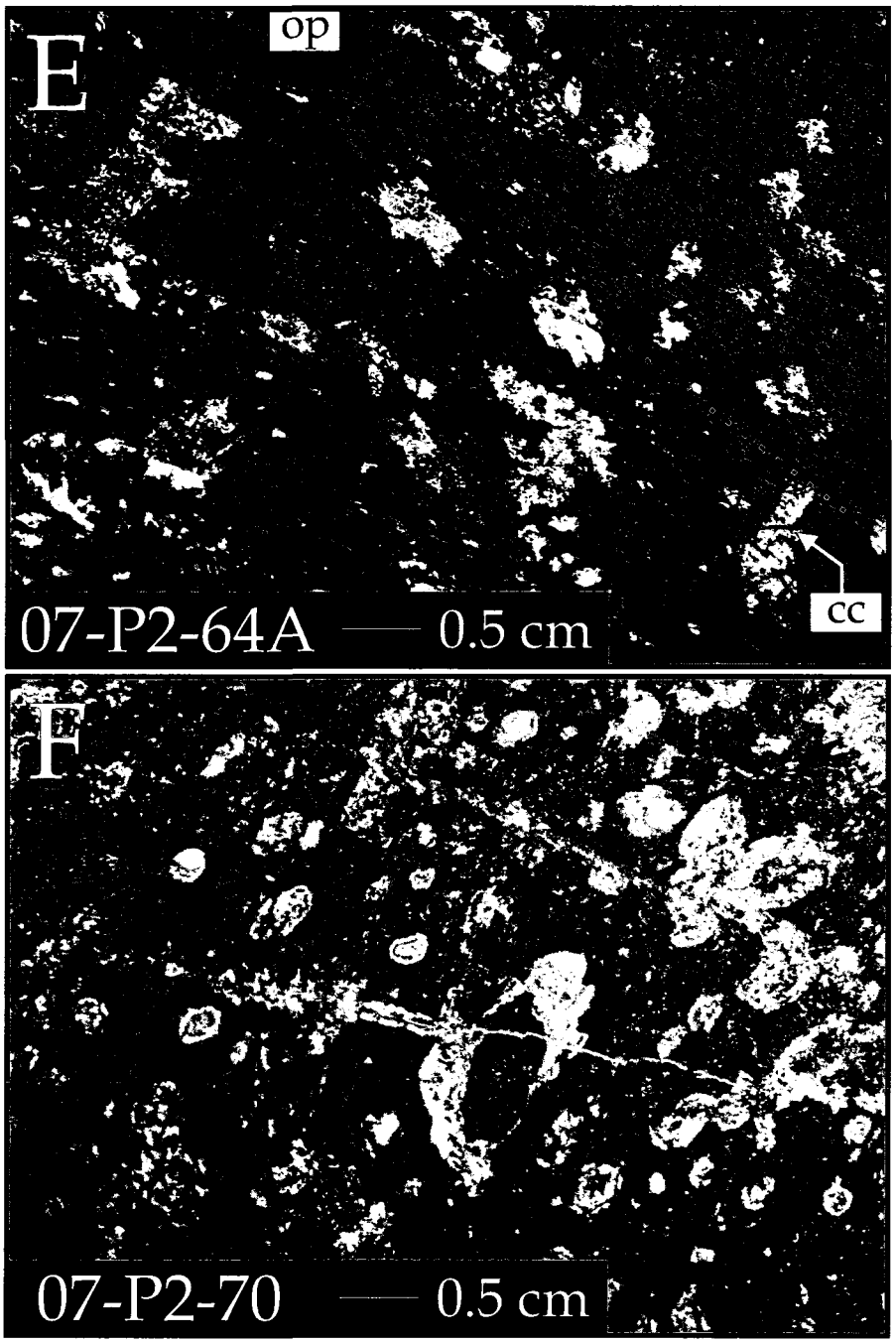

Figure 3.6: Continued. E - Outer rim of pumice clast in D. Note Fe Ti oxide mineral-rich margin (op; red line) and calcite laths (cc). The groundmass of the clasts (bottom left) contains higher concentration of dusty orange cryptocrystalline material. F - Less altered pumice block near the upper contact of the pumice- and bomb-rich tuff breccia.

commonly zoned with quartz in the interior and around the rim whereas chlorite fills the intervening domain. This alternation in zonation progresses outward for many more zones and in hand sample gradually becomes more orange-red near the margins of the clast (07-P1-64A). Macroscopically the clast margin is distinctly red in outcrop with calcite laths growing across the contact. Microscopically, the margin can be divided into two zones. Zone 5 (Fig. 3.6E) is red due to a dusty orange-red cryptocrystalline groundmass, presumably fine-grained stilpnomelane. At the contact there is a thin zone (6) roughly two millimeters thick where the groundmass becomes dusty grey with chlorite amygdules, <0.2 mm quartz microphenocrysts, groundmass epidote and calcite laths. Zone 6 is devoid of the stilpnomelane and Fe-Ti oxide minerals. The matrix around the clast adjacent to this stilpnomelane depleted layer is concentrated in chlorite and Fe oxide minerals. The groundmass here also contains patchy anhedral calcite crystals and a much higher abundance of epidote relative to the rim of the clast. This complex alternation in zoning is similar to that seen in a pumice block (07-P1-85) higher in the stratigraphy toward the middle of this tuff breccia, although there the zones are less diffuse and phenocrysts of microcline are present.

In the top half of the pumice- and spatter-rich tuff breccia the two pumice clast samples (07-P1-69 and 07-P1-70) show a consistent low degree of alteration relative to that described above (samples 64 and 85). Sample 07-P1-70 is from a pumice block near the upper contact. This clast contains dominantly quartz-filled amygdules (Fig. 3.6F) with rare chlorite and calcite filled vesicles. These vesicles, some of which are coalesced, make up 30-40 % of the rock, are generally oval and up to 1.5 mm in diameter. They are set in a groundmass containing mostly fine-grained quartz and dusty grey cryptocrystalline material with ~10 % anhedral to euhedral calcite crystals. In addition to the quartz and cryptocrystalline material there is less than 1% of both Fe Ti oxide minerals and stilpnomelane. This rock also contains veins of calcite, stilpnomelane and quartz. Sample 07-P1-69 is slightly lower in the stratigraphy and is composed of the same essential components as sample 07-P1-70 however there are higher percentages of the secondary minerals calcite, stilpnomelane, chlorite and dusty grey cryptocrystalline material as well as trace epidote crystals.

The observations that the degree of zonation/alteration within pumice blocks decreases with height in the stratigraphy is consistent with the field observation that the alteration is much more prominent at the base of the unit. This reaffirms the synvolcanic nature of the alteration as suggested from the field observations.

In contrast, the spatter clast, sample 07-P1-75, in thin section shows two clasts with contrasting contact relationships. The first spatter clast shows a gradation with the matrix of the rock (Fig. 3.7A). Near the core of the clast chlorite-filled amygdules are round, whereas toward the rim they are progressively flattened. This indicates that the vesicles were deformed after formation. The groundmass of the spatter clast is composed of chlorite-mottled cryptocrystalline material ± quartz ± Fe Ti oxide minerals. A similar groundmass is present in the second type of clast however the proportions of groundmass chlorite to dusty brown-grey cryptocrystalline material, progressively increases towards the margin of the clast (Fig. 3.7A). The second clast (Fig 3.7B) has a sharp contact between clast and groundmass containing undeformed, zoned amygdules exhibiting a chlorite core and a quartz rim. At the contact several of these amygdules are truncated by the matrix (Fig. 3.7C). This indicates that the vesicle wall on the exterior of the clast was broken upon impact and therefore the material was brittle at the time of deposition. The adjacent matrix of the rock is mainly chlorite containing quartz, opaque minerals and dusty brown cryptocrystalline material.

Sample 07-P1-63 shows a similar gradation to that described in the spatter clast where, near the contact between clast and matrix, the groundmass of the clast has a decreasing concentration of the brown-orange cryptocrystalline component and the proportion of fine-grained quartz and light grey dusty cryptocrystalline material increases. Adjacent to this lighter quartz-rich zone the matrix of the rock is concentrated in dusty Fe oxide minerals and grey cryptocrystalline material. This contact is also highly irregular and can be traced as an arcing projection into the matrix, giving it a fluidal (Skilling et al., 2002) morphology (Fig. 3.8A, B), consistent with the interpretation that it is a spatter clast. The core of this clast is quartz-rich within the groundmass and, in common with many samples (Samples 07-P3-2, 07-P2-42, 07-P2-54, 07-P1-75), just external to its contact with the matrix has an opaque rim. The macroscopic and microscopic observations that there are intricate digitate morphological projections of

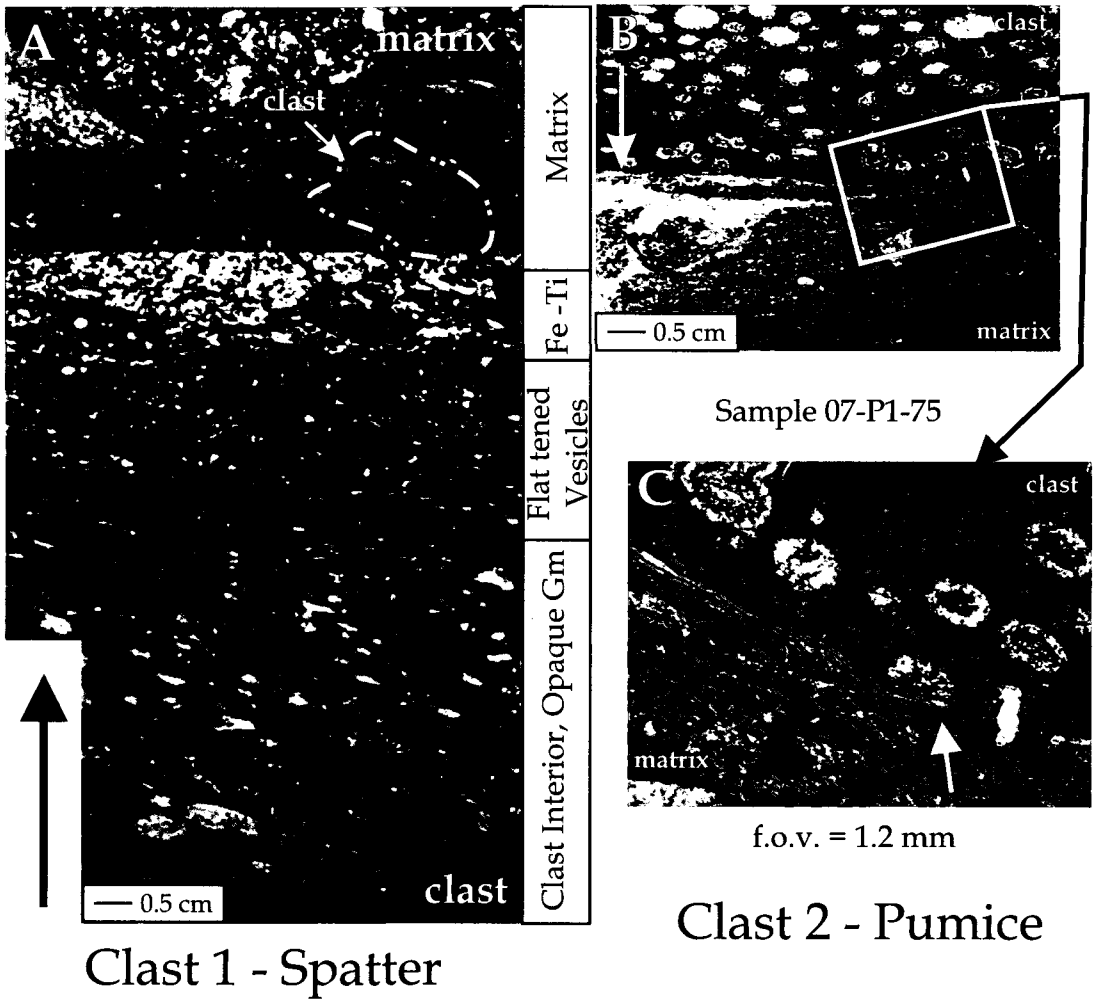

Figure 3.7: Sample 07-P1-75. Photomicrographs of the two types of clasts within the tuff breccia. A) Shows a clast with progressive gradation into the matrix material. Note how vesicles become flattened in the direction of the black arrow (bottom left). To the right of the composite photo the zones have been defined. Fe-Ti = Fe-Ti oxide-mineral-rich zone; Gm = groundmass. B) Photomicrograph of a pumice lapillus shown in C, the second clast type. Note the vesicle size decreases in direction of arrow. C) Detailed photo of B. Note the sharp contact that cuts the amygdule wall (arrow).

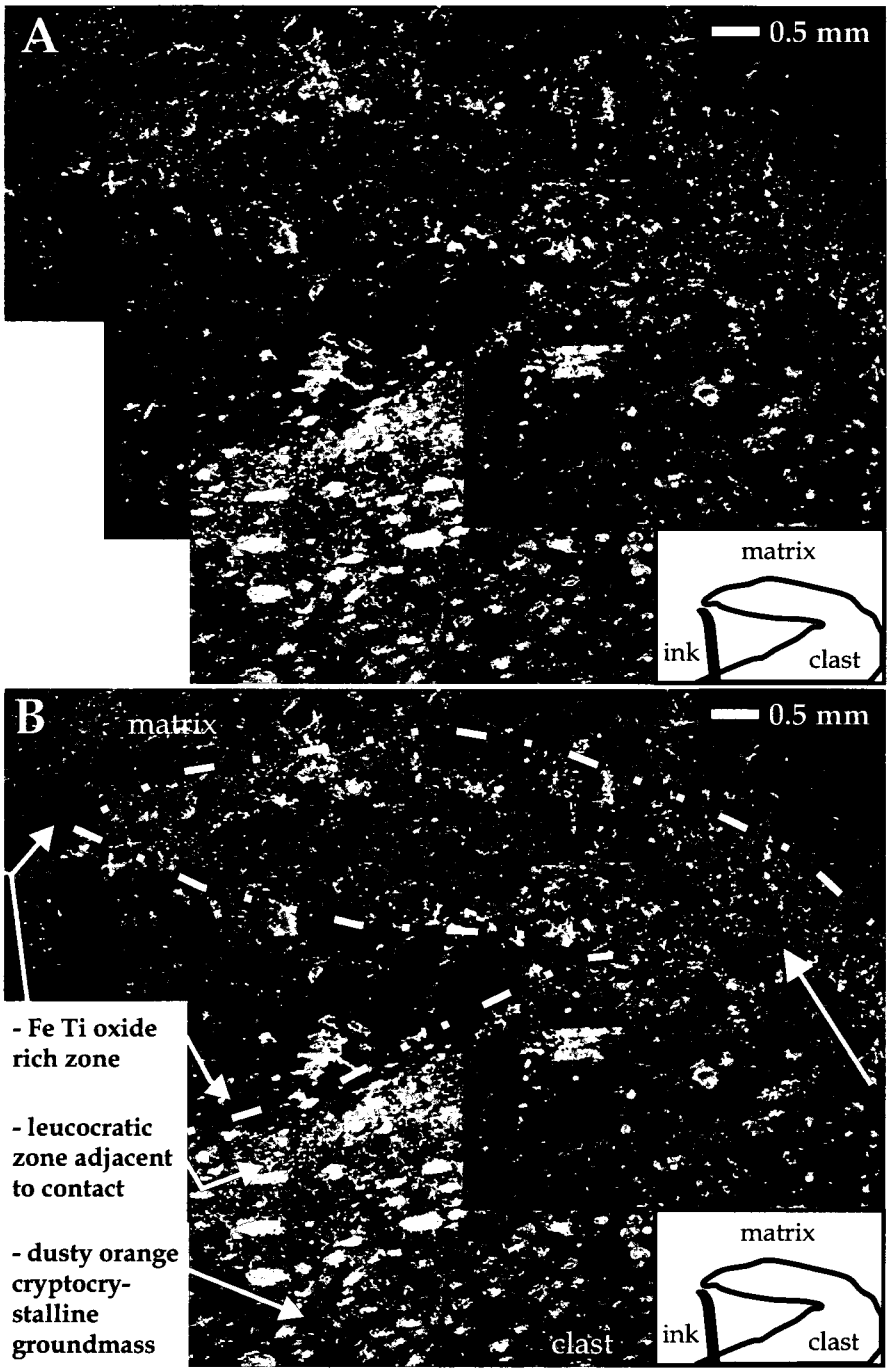

Figure 3.8: Sample 07-P1-63. Spatter clast projecting into the matrix of the pumice- and spatter-rich tuff breccia. A) Un-retouched collage of photomicrographs of clast. B) Same as A with clast outline defined. Note the thin projection into the matrix is defined by a dusty orange groundmass that becomes dusty grey near the contact (grey arrow). Also near the contact the host matrix is concentrated in Fe Ti oxide minerals. Note the vesicles are flattened towards the margin as indicated by the grey arrow.

lava into the matrix of the rock strengthens the interpretation that bombs/spatter are a major component of this tuff breccia. Furthermore the observation of the juxtaposed brittle and plastically deformed clasts confirms that there are two interpreted clast populations. These observations suggest a unique eruptive regime that exhibits both energetic explosive and more passive fire-fountaining within the same eruptive sequence.

However, the synvolcanic alteration masks the stratigraphic relationships within the pumice- and spatter-rich tuff breccia and as a result there is no consistent difference in alteration between the pumice and spatter clasts. The observation that there are clasts with undeformed vesicles cut by the matrix of the breccia adjacent to clasts with the more commonly observed progressive flattening of the vesicles towards the matrix clearly indicates contrasting rheological behaviors. Therefore the distinguishing features of the pumice blocks are their overall morphology being round or blocky whereas the bombs have a fluidal and contorted shape and the contact relationships described above (typified in Fig. 3.8). Furthermore the contrasting vesicle deformation textures observed demonstrates that this resulted form primary volcanological processes.

A third type of clast was described macroscopically as a possible agglutinated spatter (07-P1-76) however in thin section this rock contains a coarse felty groundmass composed of ~30 % relict plagioclase laths (Fig. 3.9A). These laths are up to 0.5 mm by 0.1 mm in dimension as well, rare (<1%) larger more euhedral relict feldspar phenocrysts are found. These crystals are hosted in a groundmass of Fe Ti oxide minerals, dusty semi-opaque cryptocrystalline material, chlorite, disseminated pyrite and very rare blebs of an unknown brown mineral (possibly titanite or REE fluoro-carbonate; see Chapter 4). Vesicles filled with chlorite+quartz or calcite+stilpnomelane also compose about 5% of this rock. Its coarse nature suggests that it cooled much slower than the surrounding tuff breccia and explains the contrasting texture observed in this clast relative to the blocks and spatter that are dominant in this outcrop. The observation and interpretation that felsic lobes have been injected into the other tuffaceous units is consistent with the coarse felty groundmass described. This also indicates that this unit was unconsolidated at the top. These lobes have different mineralogy to the matrix and lack the quartz observed in the overlying tuff and therefore must come from a different magma source.

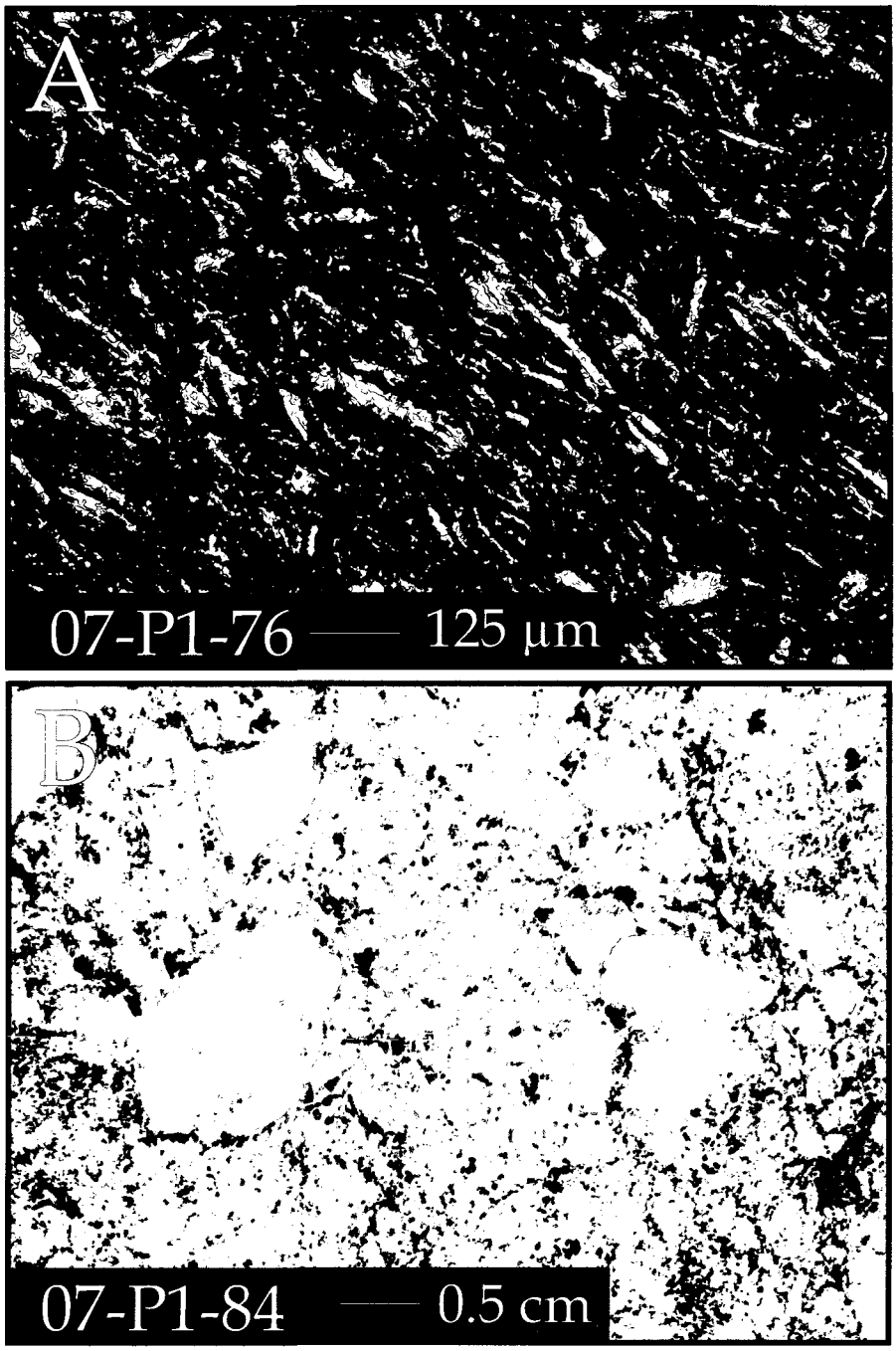

Figure 3.9: A - Relict hyalopilitic texture of coarse feldspar laths grown in random orientation in a mottled crypto-crystalline groundmass. B - Quartz porphyritic rhyolite containing embayed subhedral quartz phenocrysts.

The pumice- and spatter-rich tuff is overlain by a quartz-porphyritic rhyolite. Four samples were collect (07-P1-73, 74, 83 and 84). The freshest sample, in terms of the degree of sericitization and chloritization is 07-P1-84 (Fig. 3.9B), contains 10-15 % quartz and ~5 % plagioclase phenocrysts. These are set in a groundmass of recrystallized quartz and minor amounts of Fe Ti oxide minerals, chlorite and dusty opaques. These rocks also contain accessory zircon and one sample, P1-83, contains spherulitic titanite. Plagioclase phenocrysts (~5%) are only present in sample 07-P1-84 which contains only minor amounts of sericite alteration. All QP rhyolite samples contain roughly 10-15 % quartz phenocrysts which are round and commonly have embayments and fractures. All zircons are less than <0.25 mm in size, are sub- to euhedral and contain melt inclusions.

3.2 Petrographic Summary

3.2.1 Facies 1 – Brown Tuff

The brown tuffaceous units in this stratigraphic sequence have been destructively altered to a fine-grained mixture of chlorite, Fe Ti oxide minerals, mottled opaque minerals, rare relict plagioclase and quartz phenocrysts, epidote, minor titanite, sericite and carbonate. The lack of remnant primary texture precludes a positive identification however, the paucity of a coarse matrix and lithic clasts suggest that these brown tuffs are indeed tuffs and neither mafic lavas nor a more coarse-grained volcaniclastic rocks. The association with leucocratic material, rare phenocrysts of quartz and feldspar suggest that they had a felsic precursor and confirms the tuffaceous nature of these units.

3.2.2 Facies 2 – Aphyric rhyolite flows and their associated autobreccias

Sparsely phyric so-called aphyric lavas and their autoclastic carapaces dominate this stratigraphy. These rhyolites typically contain 1-2 vol. % quartz phenocrysts and zircon microphenocrysts. Calcite laths are interpreted to have pseudo-morphically replaced feldspar laths but are not a dominant phase. These lavas are variably altered to sericite plus chlorite, and commonly have a distinct quartz-albite intergrowth texture within their groundmass. The mineralogy of veins cutting these lavas is variable but commonly includes sericite, quartz, albite, calcite and chlorite. The aphyric rhyolites

have a spherulitic groundmass, flow banding, hyaloclastite, and perlitic textures strongly suggesting a glassy protolith.

3.2.3 Facies 3 – Block bearing tuff

The block-bearing tuff (07-P2-47) composed of embayed, rounded and broken quartz phenocrysts up to 1.4 mm in size, has a groundmass of dusty pale brown polycrystalline quartz, spherulites, sericite, chlorite and dusty opaque minerals. There are two types of blocks in this facies. The first type of clast (07-P2-48) consist of quartz phenocrysts (<<1 vol %; <0.4 mm in size) set in a matrix of recrystallized quartz spherulites, minor carbonate laths and variable coarse (~300 μm; quartz amygdules) and fine zones (<50 μm; recrystallized glass). The second type of clast (07-P2-49) consist of roughly equal proportions of quartz and relict feldspar phenocrysts (~5 vol. %) set in a dusty groundmass of quartz, sericite and quartz spherulites (<500 μm). The quartz phenocrysts are up to 1.8 mm, subhedral to round, are commonly embayed, and have spherulitic overgrowths. The carbonate laths are interpreted as relict feldspars based on the morphology along with the felspathic replacement components (calcite and sericite). The accidental clast described within this otherwise monolithic tuff is consistent with the interpretation that this is a block and ash flow resulting from a proximal dome collapse facies.

3.2.4 Facies 4 – Pumice- and spatter-rich tuff breccia

Spatter and pumice are the dominant clast lithologies in this tuff breccia which is a unique unit within the described stratigraphy. Both clast types have a varied degree of alteration from relatively intense alteration near the base and relatively 'fresh' near the contact with the quartz porphyritic rhyolite. The clast alteration has a similar composition to that of the groundmass of the tuff containing mottled opaque minerals, chlorite, quartz, Fe Ti oxide minerals, stilpnomelane and calcite but contains almost no titanite and epidote. The pumice clasts are larger and exhibit a complex zonation defined by the varying proportions and textures of amygdules (texture: flattened to round; composition: quartz, chlorite, calcite and microcline) and groundmass material (proportions: dusty opaque minerals, chlorite, quartz). More importantly pumice clasts show brittle contact

with the groundmass as exhibited by incised vesicles. This indicates that the vesicle wall on the exterior of the clast was broken and therefore brittle at the time of deposition.

In contrast, the spatter clasts show opposing contact relationships, for example the apophyses that project into the groundmass material. The vesicles within the spatter clasts show a progressive flattening towards the rim of the clast. Compositionally the spatter clasts have a similar mineralogy to the pumice clasts. In both the spatter and the pumice clasts the contact with the matrix is commonly defined by a domain of Fe Ti oxide minerals.

The macroscopic and microscopic observations that there are intricate digitate morphological projections of lava into the matrix as well as brittle clasts, strengthens the interpretation that there are both pumice and spatter clasts in the tuff breccia. Furthermore the observation of the juxtaposed brittle and plastically deformed clasts suggests a dynamic eruption where both pumice, produced by explosive fragmentation, and less viscous, more tranquilly produced, spatter have been produced simultaneously.

3.2.5 Facies 5 – Quartz-porphyritic rhyolite

The 'freshest' quartz-porphyritic rhyolite contains 10-15 vol. % quartz and <5 vol. % plagioclase phenocrysts set in a groundmass of recrystallized quartz and minor amounts of Fe Ti oxide minerals, chlorite and dusty opaque minerals. Zircon and spherulitic titanite are also prominent accessory phases. All quartz porphyritic rhyolite samples contain well preserved quartz phenocrysts however feldspars are either mildly sericitized or completely sericitized. The quartz porphyritic lavas, which are only seen at the top of the sequence, are relatively phenocryst-rich compared to the underlying 'aphyric' lavas but are otherwise texturally and mineralogically analogous and are similarly interpreted to be glassy rhyolite lavas.

3.2.6 Facies 6 – Synvolcanic dykes

There are three general types of late intrusive phases: thick late mafic dykes, thin synvolcanic felsic and mafic dykes and intrusive leucocratic lobes. The thin synvolcanic felsic dykes and felsic lobes are micro-texturally very similar and are treated together.

The late mafic dykes have not retained any primary mineralogy having been altered to a mixture of mottled opaque minerals, chlorite, Fe Ti oxide minerals, quartz, epidote, stilpnomelane and carbonate. Carbonate laths appear to have replaced feldspars in a relict hyalopilitic groundmass texture. These dykes also contain 1-2 vol. % calcite and chlorite amygdules.

The thin mafic synvolcanic dykes have been altered to a similar extent as the thicker mafic dykes. The also have relict hyalopilitic groundmass however, vesicles are not present in these dykes.

The thin felsic dykes and leucocratic lobes are treated together because both contain rare phenocrysts of sericitized plagioclase and quartz within an altered groundmass that has a relict felty texture. These intrusive rocks are composed of sericite (or calcite after relict feldspar laths), interstitial dusty opaque minerals, and groundmass chlorite, quartz, sericite, epidote, Fe Ti oxide minerals and rare pyrite. These are texturally distinct containing a coarse relict felty or hyalopilitic texture which is not evident in the deformed spatter clasts.

The observation that all intrusive units have a coarse groundmass confirms their slow cooling history and the interpretation that they are intrusive magmas emplaced into a volcanic pile. The observation of a relict hyalopilitic groundmass provides independent confirmation that these dykes are a different facies than the deformed spatter clasts.

Chapter 4 - Geochemistry of high-silica rhyolites and volcaniclastic rocks of the Kidd-Munro Assemblage

4.1 Introduction to lithogeochemistry

Recent studies of the geochemistry of the Kidd-Munro Assemblage rhyolites have largely focused on the Kidd Creek deposit area on which extensive studies of alteration (e.g., Koopman, et al., 1999; Muirhead and Hutchinson, 1999; Prior et al., 1999a; DeWolfe, 2004); protolith composition (e.g., Prior, 1996; Prior et al., 1999b); and, various aspects of trace element geochemistry (e.g., Koopman, et al., 1999; Muirhead and Hutchinson, 1999; Prior et al., 1999a; Prior et al., 1999b; Schandl et al., 1999) have been published. Data of these studies have been compiled with many other data sets to infer the volcanic setting (Schandl et al., 1999; Schandl and Gorton, 2002; Ayer et al., 2002) and economic potential (Thurston, 1981; Campbell et al., 1982; Lesher et al., 1986; Barrie et al., 1993; Schandl and Gorton, 2002; Hart et al., 2004) of Archean rhyolites. The two most critical goals of these studies have been to determine protolith compositions, in order to infer volcano-tectonic environments and to develop volcanic massive sulfide deposit exploration vectoring tools.

For all of the above studies it is essential to have a reliable protolith composition as it is the protolith composition that is the product of the magmatic processes that have formed the rock and provides a baseline for alteration studies. Therefore the question of element mobility is paramount in the interpretation of lithogeochemical data. As shown in the above studies, the high field strength elements (HFSE) are commonly the least mobilized during typical low temperature alteration and metamorphism whereas the rare earth elements (REE), particularly the light REE (La, Ce, Pr and Nd) may be relatively mobile. However, almost all of the studies cited above used data sets from a variety of rock types from all parts of the mine stratigraphy and as such they lack a critical examination of the scale of element mobility.

This leads to number of questions: 1) Are the indications of element mobility shown expected across a single coulée, across a volcanic center or over the regional

scale? 2) Can the criteria for least altered sample be updated as each of the three cited studies use different criteria? 3) What are the processes that are responsible for this mobility? 4) What minerals host the REE and HFSE elements as only tantalite, Ta-cassiterite, allanite, xenotime and monazite have been observed thus far? 5) Clearly it has been shown that there is a significant variability in the concentration of some elements across the volcanic center. Accordingly one goal of this study is to determine if the same degree of mobility is found on the local (i.e. coulée to hand specimen) scale. And if so, what are the implications for ore deposit trace element based vectoring tools (e.g. Lesher et al., 1986; Hart et al., 2004)?

To answer some of these questions an experiment was designed to test the mobility of various elements within a single flow, in Prosser Outcrop 2, at the local (hand specimen and coulée) scale for variations in the REE and HFSE contents. The aphyric rhyolites of Prosser Township are prime candidates for this experiment because they do not show evidence of VMS-related mineralization and have preserved primary textures (i.e. flow banding). Therefore these rhyolites do not appear to have been subjected to significant high-temperature mass and fluid flow that is present as additional alteration around the giant Kidd Creek deposit. Thus the coulée experiment should provide useful information on 'baseline' rock geochemistry.

One assumption of this study is that the lithogeochemical variation is due to alteration. This is justified as a companion study (Proulx, 2008) has shown that unaltered Neogene high-silica, phenocryst-poor, flow banded rhyolites of the Mono-Inyo Volcanic sequence in Long Valley, California, exhibit virtually no variation beyond statistical fluctuations on comparable scales to this study. The other assumption is that this coulée has not been modified by VMS-associated alteration. Therefore the alterations are limited to subaqueous synvolcanic and diagenetic alteration and to possible subsequent modifications during metamorphism and tectonism.

First, it is necessary to understand the current state of the lithogeochemistry of the Kidd-Munro assemblage which has been most deeply studied on the Kidd Creek deposit. A summary of the most pertinent studies follows.

4.1.1 Previous Studies

Koopman et al. (1999) have done a rigorous study defining the alteration assemblages (silicification, sericitization, sphalerite staining, chloritization, Fe-Mg carbonatization, tourmaline alteration, ablitization and late quartz veining) and have assembled drill core data of samples from within the mine to three kilometers distant. They determined a 'least altered' sample in order to interpret the geochemistry. There are several alteration styles (textural/structural variations) associated with each of these alteration assemblages. Koopman et al. (1999) constructed a paragenetic sequence which they relate to the temperature of the alteration according to work of Hannington et al. (1999b). This led to the interpretation that silicification was ongoing throughout hydrothermal activity, whereas sphalerite mineralization, sericitization and most of the chloritization occurred in the early, low temperature and waning stages of hydrothermal alteration but were minimal during peak alteration. At peak hydrothermal (>300°C) alteration it is shown that many of the transition metals and high field strength elements (Ti, Fe, Al, Y, LREE) were mobile. Chloritization did occur during high temperature alteration but it occurs as a texturally distinctive mottled "alligator" (see Koopman et al., 1999) or black chlorite. The dolomitization was restricted to the early synvolcanic alteration while Fe-carbonitization occurred only during low temperature hydrothermal activity. An important observation is that both the footwall chlorite and sericite have a consistently higher Fe/(Fe+Mg) ratio than the hanging wall rocks.

The Koopman et al. (1999) study defines the chemical enrichments and depletions relative to the average of five least altered high silica rhyolite samples, chosen based on three criteria: 1 - Comparison with other least altered samples (e.g. Prior et al., 1999); 2 – comparison of rare earth element profiles of appropriate rocks elsewhere within the Abitibi subprovince (e.g. Lesher et al., 1986; Barrie et al., 1993); and, 3 – comparison of whole rock $\delta^{18}O$ with rocks having typical magmatic values (e.g. Huston and Taylor, 1999). The mass gains and losses during enrichment/depletion were quantified using Gresen's (1967) method and the necessary corrections where made for mass and volumes changes. Zirconium was chosen as the best precursor (i.e. conserved element with respect to alteration) because of its abundance and low overall variance.

Prior (1996; Prior et al., 1999b) has studied the footwall rhyolites and has compared the Kidd Creek rhyolites with a post-Triassic analogue based on the REE and

HFSE. To do this, Prior et al. (1999b) have had to determine a protolith composition with which to compare to these analogues. They used Na_2O, loss on ignition (L.O.I.), CO_2, H_2O^+, Cu, Zn contents as well as the Alumina saturation ([Al/(2Ca+Na+K)], Shand, 1951), Isikawa (Isikawa et al., 1976) and Goodfellow indices (Goodfellow, 1975; Riverin and Hodgson, 1980) as discriminants. Prior et al. (1999b) normalize six least altered samples to the single most, least altered sample and show that relative to the least altered sample the mass change effects are minimal because the variation of the six samples is low. However they do not compare multi-element ratios as they are normalizing the same elements against themselves in different samples. They argue that Al, Ti, Zr, Nb, Th, and U ratios of the six least altered samples normalized against a least altered sample are constant and therefore immobile even between two chloritized, one sericitized and five cherty breccia samples.

Moreover, in 7 of 10 of their samples the HREE, Dy and Yb, are also immobile but the LREE (La, Nd and Eu) show considerable loss in a sample from the strongly altered stringer zone. When compared to post-Triassic lavas (in REE and HSFE terms) the footwall rhyolites at Kidd Creek are most comparable to subalkaline rhyolites from the mid-ocean ridges. More specifically the rhyolites from the Askja volcano in the eastern axial rift zone of Iceland are an almost exact match to the Kidd Creek rhyolites. Prior et al. (1999b) then bolster their argument noting that, like Askja, Kidd Creek is associated with fissure swarms and is a bimodal volcanic system.

Schandl et al., (1999) focused on the REE and the HFSE and have shown that the REE are mobile even up to distances of two kilometers from the deposit. The LREE were particularly mobile within the rhyolites directly underneath the massive sulfide lenses, in the altered stringer zones, the bornite zone and in some of the fragmental units. Schandl et al. (1999) along with the previous studies of Campbell et al. (1984) and Schandl and Gorton (1991) have documented mobilization of the REE during metamorphism and also during hydrothermal alteration. According to these authors the high field strength elements remained relatively immobile during alteration. They examined plots of various elements against each other for many different rhyolite alterations. Linear correlation coefficients of 0.99 and 0.97 for Th and Ta vs. Hf, were calculated respectively, whereas the correlation versus Hf for the following elements is significantly lower (Al_2O_3 r =

0.86; Yb r = 0.53 and La r = 0.29). Schandl et al. (1999) state that the high-value positive coefficients are attributed to the immobility of high field strength elements in felsic rocks, and by the same logic, the lower-value coefficients are therefore indicative of element mobility. With regards to the REE Schandl et al., (1999) have documented LREE depletion of 14 % (depletion % = $100*[(REE/Ta)_{sample}-(REE/Ta)_{least\ altered}] / [(REE/Ta)_{least\ altered}]$) within a sericitized massive rhyolite sample and HREE enrichment up to 78 % in tuffs both of which are approximately 2 kilometers away from the Kidd Creek deposit.

4.2 Grid experiment: Element mobility in an coherent Archean phenocryst-poor rhyolite

In order to understand the degree of element mobility a grid sampling scheme was carried out on Prosser Outcrop 2 (Fig. 4.1). A rectilinear grid was setup with tabular samples, taken at the meter scale (Fig. 4-1A). Samples were cut oriented north-south (N-S) in the east-west (E-W) coordinate and east-west in the north-south direction. A further 17 samples where taken at a fine, 10 cm, hand specimen scale (Fig. 4-1B) around the grid center. During sample preparation large late quartz veins were removed because quartz will have solely a dilution affect and will not significantly alter the rare earth and high field strength element contents. Nonetheless veins are observed in thin section and therefore constitute a minor fraction of the lithogeochemical concentrations.

4.2.2 Analytical Methods

The samples (typically 4 x 5 x 20 cm in size) were cut with a diamond blade saw and than were individually cleaned and examined prior to removal of as much weathering and as many large veins as possible. Polished and regular thin sections were made by Jiri Mrazek at the University of Ottawa and whole rock samples were analysed at Geoscience Laboratories in Sudbury, Ontario. They were prepared using an agate ring mill according to the procedure outlined in their schedule of fees and services available at http://www.mndm.gov.on.ca/mines/ogs/labs/default_e.asp. A complete list of their accuracy and precision has been published by Burnham and Schweyer (2004) which includes their results of both in house and international standards. Using the standards of

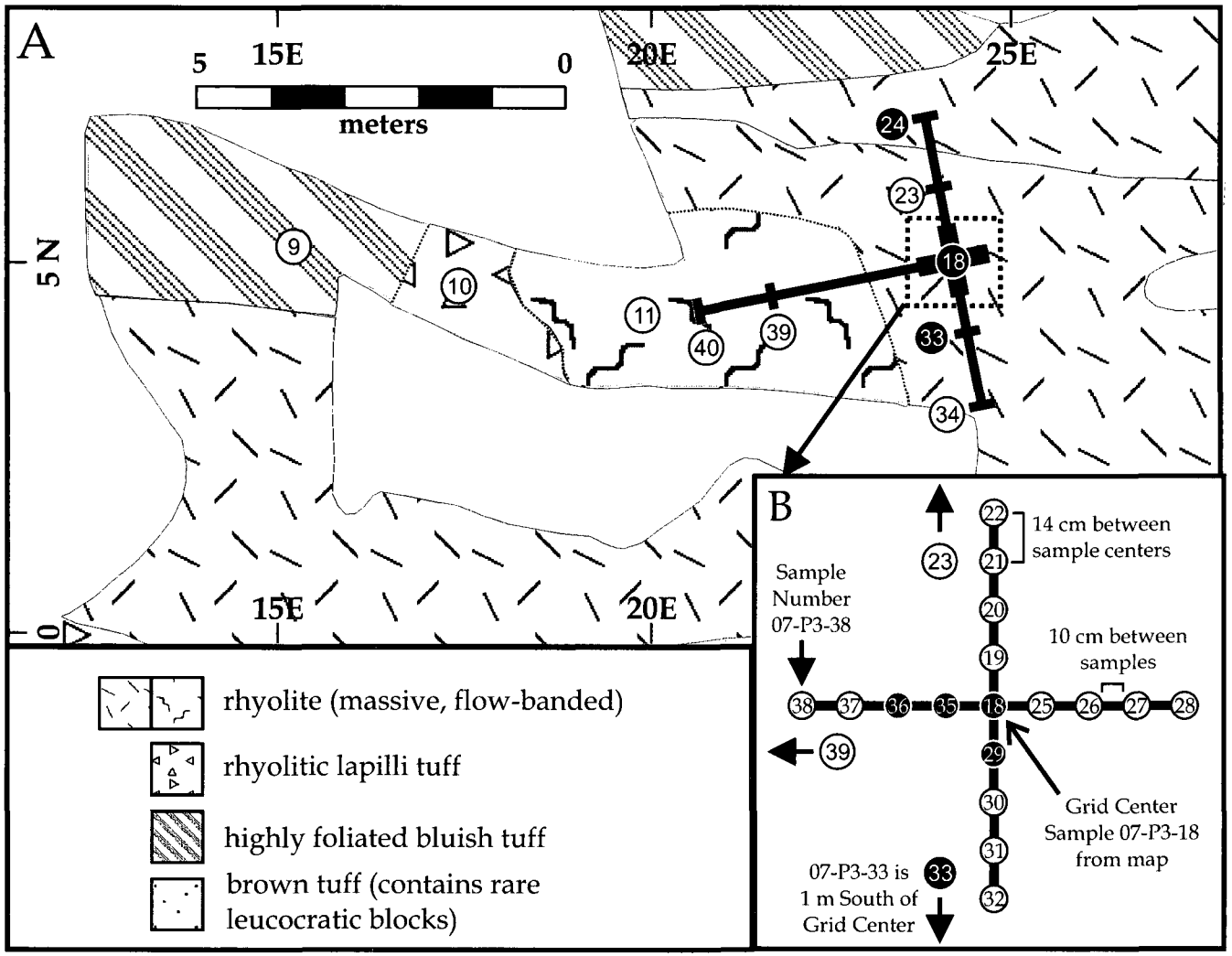

Figure 4.1:A. Large scale map of Prosser outcrop 2 modified from Figure 2.5. Grid sampling experiment showing the exact sample locations. Samples number 07-P3-XX, where XX is the number in the circle. B. Inset map of the very large scale, hand specimen scale sampling .

Burnham and Schweyer (2004), the REE and HFSE elements analyses done by ICP-MS are generally better than ± 5 % (2σ) error for most elements except Ta (see section 4.2.6) which is for compiled solutions were too low for the instrumental precisions.

Major elements and select trace elements were determined using wavelength dispersive x-ray florescence (XRF). The rest of the trace elements were determined using inductively coupled plasma mass spectrometry (ICP-MS). CO_2 and S were measured using infrared absorption during combustion (IRC) of the samples. Bound water and free moisture were measured by infrared absorption (IRW) of the moisture driven off at 1000°C and 105°C, respectively. Cl analyses were done by instrumental neutron activation analyses (INAA) and F was done by ion selective electrode analysis (ISE). The complete lithogeochemical analyses for all grid samples can be found in Table 4-1 while duplicate analyses can be found in Appendix A.1. Detection limits for all elements can be found in the fourth column of Table 4-1 and duplicate analyses for sample 07-P3-33 can be found at the end of Table 4-1.

4.2.3 Petrography

A complete petrographic description of individual samples can be found in Table 4-2. All samples are relatively crystal-free rhyolites which contain less than 1 % quartz phenocrysts except sample 07-P3-34, which contains 1-3 % and is 2 m south of the grid center. The quartz phenocrysts are euhedral to subround, commonly embayed and are up to 1.5 mm in size but most commonly they range between 0.2 and 0.6 mm. Zircon microphenocrysts are found up to 0.3 mm in size, and contain very small reddish-brown needles of rutile(?) plus melt inclusions. Recrystallized spherulites (Fig. 4-2A) have been observed in several thin sections based upon the observation of circular aggregates of fibro-radial quartz having radiating extinction. Perlitic fracturing (Fig. 4-2B) was unambiguously identified in two of the grid samples (07-P3-32 and 07-P3-33) which represent particularly well preserved samples. Sample 07-P3-36 has some very well defined hyaloclastite consisting of relict blocky to cuspate glass shards (Fig. 4-2C). Both of these textures are defined by pure polycrystalline quartz domains.

In summary these textures, i.e., macroscopic flow-banding, microscopic evidence of hyaloclastite, perlite, quartz phenocrysts, and lack of phenocrysts, are characteristic of

Table 4-1: Lithogeochemistry of aphyric rhyolites from the grid experiment on Prosser outcrop 2.

Sample	Analytical	Units	Detection	**07-P3-18**[2]	07-P3-19	07-P3-20	07-P3-21	07-P3-22	07-P3-23	**07-P3-24**	07-P3-25	07-P3-26	07-P3-27	07-P3-28
Comment	Method[1]		Limits							REE depleted				
Alteration				least altered	sericitized	sericitized	sericitized	sericitized	sericitized	**least altered**	albitized	albitized	albitized	albitized
Major Elements														
SiO_2	XRF	wt %	0.01	**76.62**	76.65	76.39	77.83	77.94	75.52	**76.69**	73.71	80.04	79.34	80.96
TiO_2	XRF	wt %	0.01	**0.13**	0.14	0.14	0.12	0.13	0.14	**0.12**	0.15	0.13	0.11	0.12
Al_2O_3	XRF	wt %	0.01	**11.63**	11.68	11.76	11.45	11.6	12.48	**11.64**	14	10.66	10.67	10.54
FeO	TIT	wt %	0.06	**1.71**	1.56	1.85	1.59	1.91	1.99	**1.56**	2.1	1.78	1.66	1.7
Fe_2O_3	Calc	wt %		**0.35**	1.33	0.74	1.00	0.66	1.02	**0.65**	0.58	0.45	0.43	0.45
MnO	XRF	wt %	0.01	**0.03**	0.03	0.03	0.04	0.04	0.04	**0.03**	0.04	0.04	0.04	0.03
MgO	XRF	wt %	0.01	**0.71**	1.45	1.37	1.25	1.35	1.76	**0.76**	0.83	0.54	0.48	0.5
CaO	XRF	wt %	0.01	**0.36**	0.09	0.13	0.12	0.15	0.09	**0.18**	0.18	0.32	0.24	0.1
Na_2O	XRF	wt %	0.01	**6.01**	2.1	2.41	3.65	3.25	1.49	**5.99**	6.64	5.66	5.82	5.7
K_2O	XRF	wt %	0.01	**0.53**	3.00	2.86	1.82	2.21	3.72	**0.43**	0.85	0.29	0.2	0.16
P_2O_5	XRF	wt %	0.01	**b.d.**[3]	0.01	0.01	0.01	0.01	0.01	**0.01**	0.01	0.01	0.01	b.d.
L.O.I.	XRF	wt %	0.05	**0.89**	1.8	1.65	1.44	1.54	2.1	**0.72**	0.94	0.8	0.65	0.64
Total	XRF	wt %		**99.16**	100.01	99.55	100.5	101	100.58	**98.95**	100.26	100.92	99.83	101.09
Crystalline Moisture	IRW	wt %	0.03	**0.84**	1.72	1.59	1.24	1.54	2.03	**0.83**	1.1	0.8	0.77	0.77
Free Moisture	IRW	wt %	0.01	**0.08**	0.18	0.12	0.1	0.11	0.13	**0.11**	0.09	0.06	0.1	0.1
Trace Elements														
F	ISE	ppm	30	**184**	873	1839	548	612	1063	**104**	273	86	129	216
Cl	INAA	wt %	0.01	**0.03**	b.d.	0.01	0.02	b.d.	b.d.	**b.d.**	b.d.	b.d.	b.d.	b.d.
CO_2	IRC	wt %	0.03	**0.19**	b.d.	b.d.	0.03	0.06	b.d.	**0.03**	0.05	0.16	0.1	0.04
S	IRC	wt %	0.01	**0.01**	b.d.	b.d.	b.d.	b.d.	b.d.	**0.06**	0.03	0.03	0.01	0.01
Ag	XRF	ppm	5	**b.d.**	b.d.	b.d.	b.d.	b.d.	b.d.	**b.d.**	b.d.	b.d.	b.d.	b.d.
As	XRF	ppm	1	**1**	b.d.	2	2	b.d.	b.d.	**1**	2	3	2	1
Ga	XRF	ppm	3	**23**	40	36	26	28	36	**20**	33	25	26	26
Mo	XRF	ppm	1	**1**	4	3	2	3	3	**1**	1	1	2	2
Sn	XRF	ppm	5	**5**	9	8	5	5	8	**b.d.**	11	9	6	7
Ti	XRF	ppm	8	**722**	723	749	618	617	711	**683**	903	714	670	672
Y	XRF	ppm	1	**168**	139	140	125	125	127	**92**	223	182	156	149
Ba	ICPMS	ppm	0.9	**94**	136.5	225.1	181	219.1	136.3	**88.3**	113.4	62.8	57.1	36.4
Be	ICPMS	ppm	0.06	**4.82**	3.26	3.36	3.04	3.09	2.62	**1.7**	7.05	5	3.33	2.49
Bi	ICPMS	ppm	0.009	**0.168**	0.16	0.287	0.211	0.209	0.239	**0.221**	0.172	0.173	0.24	0.165
Cd	ICPMS	ppm	0.01	**0.17**	0.15	0.21	0.13	0.18	0.2	**0.12**	0.22	0.16	0.13	0.11
Ce	ICPMS	ppm	0.2	**169.4**	87.6	124.8	106.4	120.1	83.2	**67.7**	241.5	184.8	154.5	141.7
Co	ICPMS	ppm	0.1	**0.1**	0.1	0.1	0.1	0.1	0.1	**0.2**	0.1	0.1	1.2	0.1
Cr	ICPMS	ppm	24	**b.d.**	b.d.	b.d.	b.d.	b.d.	b.d.	**b.d.**	b.d.	b.d.	25	b.d.
Cs	ICPMS	ppm	0.006	**0.348**	2.057	2.279	1.368	1.685	2.487	**0.135**	0.601	0.168	0.187	0.119
Cu	ICPMS	ppm	2	**8**	4	6	4	5	5	**4**	8	7	7	4
Dy	ICPMS	ppm	0.02	**30.4**	22.2	26	22	23.9	20	**17.6**	38.9	31.3	28.6	27
Er	ICPMS	ppm	0.02	**18.29**	13.86	16.35	13.69	14.69	12.56	**11.2**	23.65	18.86	17.05	16.21
Eu	ICPMS	ppm	0.005	**4.569**	2.091	2.504	2.939	3.257	2.217	**3.037**	5.683	4.327	4.017	3.594
Ga	ICPMS	ppm	0.05	**22.01**	38.1	35.4	25.77	26.77	34.25	**19.77**	33.03	24.4	25.84	23.96
Gd	ICPMS	ppm	0.02	**27**	16.04	18.47	17.66	18.97	15.16	**14.01**	35.43	28.03	24.87	23.58
Hf	ICPMS	ppm	0.09	**12.75**	13.58	13.73	12.6	12.94	14.1	**12**	16.09	12.88	12.48	12.2
Ho	ICPMS	ppm	0.003	**6.561**	4.93	5.732	4.747	5.075	4.374	**3.832**	8.441	6.784	6.158	5.743
La	ICPMS	ppm	0.09	**73.32**	32.46	39.98	45.39	50.46	34.71	**27.93**	98.35	80.53	63.77	55.61
Li	ICPMS	ppm	0.2	**7.8**	12.9	21.8	15.3	17.6	11.4	**6.9**	10.5	6.4	6.7	6
Lu	ICPMS	ppm	0.002	**2.841**	2.267	2.662	2.38	2.508	2.131	**2.076**	3.605	2.92	2.674	2.592
Mo	ICPMS	ppm	0.03	**1.81**	3.83	3.23	2.15	2.78	3.36	**2.51**	1.51	1.6	2.39	2.12
Nb	ICPMS	ppm	0.04	**40.89**	45.21	46.98	40.79	41.72	45.38	**38.86**	51.77	39.83	38.9	38.75
Nd	ICPMS	ppm	0.08	**104.96**	47.51	55.01	58.54	68.8	46.86	**41.63**	142.27	109.33	93.75	86.6
Ni	ICPMS	ppm	3	**b.d.**	b.d.	b.d.	b.d.	b.d.	b.d.	**b.d.**	b.d.	b.d.	b.d.	b.d.
Pb	ICPMS	ppm	0.4	**11.9**	4.3	6.5	8.7	9.4	6.1	**7.1**	11.4	9.6	9.5	8
Pr	ICPMS	ppm	0.02	**23.13**	10.77	12.35	13.24	15.67	10.71	**9.07**	31.3	24.39	20.52	18.69
Rb	ICPMS	ppm	0.2	**16**	84.6	121.2	73.3	86.9	67.6	**5.3**	29.5	6.2	5.8	2.7
Sb	ICPMS	ppm	0.04	**0.04**	0.04	0.04	0.04	0.04	0.05	**0.04**	0.05	0.04	0.05	0.04
Sc	ICPMS	ppm	0	**1.7**	1.4	1.9	1.6	1.7	1.4	**1.6**	2	1.5	2	1.5
Sm	ICPMS	ppm	0.02	**25.75**	12.77	15.12	15.28	17.23	12.51	**12.21**	35	26.73	23.62	22.41
Sn	ICPMS	ppm	0.08	**6.6**	9.47	8.58	6.42	7.28	8.88	**5.16**	11.28	7.71	7.21	6.44
Sr	ICPMS	ppm	2	**71**	28	38	56	53	31	**89**	57	50	47	33
Ta	ICPMS	ppm	0.2	**2.8**	3.1	3.1	2.7	2.9	3	**2.7**	3.5	2.8	2.7	2.7
Tb	ICPMS	ppm	0.003	**4.701**	3.204	3.688	3.341	3.52	2.926	**2.658**	6.144	4.784	4.401	4.171
Th	ICPMS	ppm	0.09	**8.46**	8.35	8.8	8.04	8.44	7.83	**7.86**	10.37	8.68	8.23	7.92
Ti	ICPMS	ppm	26	**624**	704	734	626	639	700	**596**	801	622	827	582
Tl	ICPMS	ppm	0.005	**0.056**	0.351	0.348	0.21	0.26	0.425	**0.029**	0.092	0.026	0.048	0.013
Tm	ICPMS	ppm	0.002	**2.96**	2.27	2.69	2.273	2.463	2.103	**1.935**	3.775	3.007	2.748	2.633
U	ICPMS	ppm	0.02	**1.94**	1.95	1.95	1.79	1.89	2	**1.73**	2.35	1.94	1.86	1.81
V	ICPMS	ppm	10	**b.d.**	b.d.	b.d.	b.d.	b.d.	b.d.	**b.d.**	b.d.	b.d.	b.d.	b.d.
W	ICPMS	ppm	0.5	**b.d.**	0.5	0.5	b.d.	0.5	0.6	**b.d.**	0.6	0.5	0.5	0.5
Y	ICPMS	ppm	0.08	**180.79**	136.48	159.81	141.81	139.02	114.09	**102.61**	243.12	196.94	169.01	158.47
Yb	ICPMS	ppm	0.009	**18.888**	14.771	17.697	15.417	16.412	13.922	**13.108**	23.932	19.412	17.915	16.892
Zn	ICPMS	ppm	8	**93**	111	129	58	94	131	**67**	91	91	64	65
Zr	ICPMS	ppm	3	**333**	347	366	337	337	378	**317**	418	323	327	316

[1] For analytical methods see section 4.2.2;[2] Bolded samples are least altered samples (Average Least Altered Composition in Table 4.4);[3] b.d. = below detection limit.

Table 4-1: Lithogeochemistry continued.

Sample	07-P3-29	07-P3-30	07-P3-31	07-P3-32	07-P3-33	07-P3-34	07-P3-35	07-P3-36	07-P3-37	07-P3-38	07-P3-39	07-P3-40	07-P3-33D
Comment				perlite	perlite								Duplicate
Alteration	least alterec	albitized	albitized	albitized	least alterec	chloritized	least altered	least alterec	sericitized	sericitized	albitized	albitized	least altered
Major Elements													
SiO_2	**77.31**	80.23	77.02	77.39	**75.26**	78.8	**74.57**	**75.47**	75.65	75.91	78.97	79.01	75.10
TiO_2	**0.14**	0.12	0.13	0.13	**0.14**	0.12	**0.14**	**0.15**	0.14	0.14	0.12	0.12	0.14
Al_2O_3	**12.74**	10.58	11.65	11.7	**12.5**	10.88	**13.32**	**13.16**	12.52	12.59	10.9	10.91	12.52
FeO	**1.57**	1.74	1.55	1.56	**2.60**	2.13	**1.54**	**1.59**	1.92	1.99	1.53	1.91	2.07
Fe_2O_3	**0.41**	0.36	1.18	0.76	**0.62**	0.68	**0.58**	**0.84**	1.00	0.76	0.70	0.66	1.20
MnO	**0.03**	0.03	0.04	0.03	**0.04**	0.04	**0.03**	**0.03**	0.04	0.03	0.03	0.03	0.04
MgO	**0.6**	0.61	0.73	0.59	**0.87**	1.26	**0.88**	**1.15**	1.53	1.45	1.06	1.22	0.88
CaO	**0.31**	0.42	0.18	0.38	**0.18**	0.33	**0.22**	**0.3**	0.14	0.12	0.2	0.23	0.18
Na_2O	**6.55**	5.48	6.06	6.25	**6.39**	4.12	**6.14**	**4.66**	2.71	3.19	4.89	5.01	6.41
K_2O	**0.55**	0.37	0.35	0.33	**0.23**	1.12	**1.05**	**1.95**	2.88	2.6	0.74	0.57	0.23
P_2O_5	**0.01**	0.01	b.d.	0.01	**0.01**	0.01	**0.01**	**0.01**	0.01	b.d.	0.01	0.01	0.01
L.O.I.	**0.77**	0.9	0.79	0.99	**0.96**	1.5	**1.11**	**1.58**	1.95	1.77	1.23	1.12	0.95
Total	**101.16**	101.04	99.85	100.29	**100.09**	101.23	**99.76**	**101.07**	100.7	100.77	100.55	101.01	99.96
Crystalline Moisture	**0.79**	0.85	0.94	0.83	**1.1**	1.34	**1.04**	**1.42**	1.87	1.71	1.07	1.18	1.06
Free Moisture	**0.08**	0.07	0.07	0.08	**0.08**	0.09	**0.07**	**0.12**	0.11	0.1	0.08	0.07	0.08
Trace Elements													
F	**385**	272	341	269	**295**	610	**590**	**708**	857	981	683	416	n.d.
Cl	**0.02**	b.d.	b.d.	0.03	**b.d.**	0.02	**0.02**	**b.d.**	b.d.	b.d.	b.d.	b.d.	n.d.
CO_2	**0.14**	0.26	0.08	0.25	**0.06**	0.23	**0.05**	**0.15**	0.07	0.03	0.04	0.03	0.06
S	**0.02**	0.01	0.01	0.01	**0.04**	b.d.	**b.d.**	**b.d.**	b.d.	b.d.	b.d.	b.d.	0.03
Ag	**b.d.**	b.d.	b.d.	b.d.	**b.d.**	b.d.	**b.d.**	**b.d.**	b.d.	b.d.	b.d.	b.d.	b.d.
As	**b.d.**	1	b.d.	b.d.	**b.d.**	1	**b.d.**	**2**	1	2	2	1	1
Ga	**25**	23	27	26	**34**	27	**25**	**31**	37	32	22	22	35
Mo	**2**	2	2	2	**1**	3	**5**	**4**	2	3	1	2	1
Sn	**8**	5	7	5	**7**	6	**7**	**7**	9	8	6	6	7
Ti	**779**	674	695	758	**826**	666	**780**	**800**	757	722	664	638	839
Y	**193**	168	149	185	**164**	157	**200**	**164**	158	146	146	149	162
Ba	**99.8**	74.6	78.1	77.3	**56.6**	100.9	**135.3**	**191.4**	225	240.6	105.7	90.4	57.4
Be	**5.95**	4.62	4.17	2.48	**2.39**	4.07	**7.62**	**4.4**	3.99	4.48	2.56	2.26	2.39
Bi	**0.252**	0.248	0.247	0.167	**0.231**	0.161	**0.213**	**0.125**	0.133	0.275	0.207	0.257	0.22
Cd	**0.2**	0.15	0.15	0.15	**0.12**	0.23	**0.21**	**0.16**	0.12	0.19	0.17	0.22	0.12
Ce	**207.3**	177.9	128.5	178	**144**	159.1	**204**	**140.8**	186.9	103.1	220	168.3	143.3
Co	**0.1**	0.2	0.2	0.2	**0.1**	0.1	**0.1**	**0.1**	0.2	0.1	0.1	0.1	0.1
Cr	**b.d.**	b.d.	b.d.	b.d.	**b.d.**	b.d.	**b.d.**	**b.d.**	b.d.	b.d.	b.d.	b.d.	b.d.
Cs	**0.339**	0.223	0.163	0.149	**0.112**	0.724	**0.777**	**1.486**	2.265	1.991	0.476	0.364	0.118
Cu	**8**	15	5	8	**7**	10	**9**	**5**	5	5	6	5	6
Dy	**34.3**	30.6	27.5	32.1	**30.2**	27.6	**36.5**	**30.6**	29.1	27.7	28.2	28.4	30.9
Er	**20.81**	17.8	17.25	19.6	**18.13**	16.95	**20.46**	**17.85**	17.54	16.4	16.16	16.58	18.32
Eu	**5.037**	4.532	3.827	4.688	**4.611**	3.75	**5.584**	**4.19**	3.888	3.482	4.907	4.745	4.79
Ga	**24.17**	22.72	26.34	25.7	**33.13**	25	**24.57**	**29.55**	34.93	30.74	21.54	20.32	32.87
Gd	**31.46**	28.42	23.42	28.4	**25.61**	25.78	**34.92**	**26.8**	26.29	23.7	28.59	26.43	25.92
Hf	**13.82**	12.21	12.73	14.01	**14.56**	12.76	**14.23**	**15.4**	14.45	14.35	12.42	12.89	14.86
Ho	**7.479**	6.501	5.951	7.048	**6.498**	6.055	**7.564**	**6.502**	6.192	5.914	5.85	6.009	6.611
La	**89.86**	81.02	48.13	75.6	**60.24**	70.02	**89.79**	**57.15**	68.52	41.01	98.09	75.54	59.78
Li	**6.5**	6.9	8.6	6.2	**9.6**	14.1	**10.5**	**15.9**	21.5	19.2	10.5	10.7	9.3
Lu	**3.155**	2.723	2.904	3.02	**2.876**	2.738	**3.152**	**2.897**	2.901	2.639	2.585	2.678	2.922
Mo	**2.35**	2.75	2.17	2.66	**1.67**	4.45	**5.35**	**3.78**	2.35	3.53	1.49	2.06	1.61
Nb	**44.06**	38.94	42.04	43.78	**47.2**	37.85	**44.92**	**48.81**	46.03	45.21	40.99	40.33	47.31
Nd	**125.97**	110.89	82.4	106.47	**87.55**	99.41	**124.62**	**83.67**	93.97	68.81	125.17	96.44	85.71
Ni	**b.d.**	b.d.	b.d.	b.d.	**b.d.**	b.d.	**b.d.**	**b.d.**	b.d.	b.d.	b.d.	b.d.	b.d.
Pb	**11.6**	11.7	12.1	11	**10.9**	8.5	**18.1**	**9.1**	5.3	7	8.8	15.6	11.4
Pr	**27.73**	24.37	17.56	23.67	**19.33**	21.34	**27.25**	**18.29**	20.76	14.17	28.35	21.13	18.93
Rb	**15.4**	9.8	6.3	5.4	**3.4**	41.9	**39.4**	**81.1**	120.7	106.9	25	17.7	3.6
Sb	**0.05**	0.04	0.04	0.04	**b.d.**	b.d.	**0.05**	**0.05**	0.04	0.04	0.04	0.04	0.04
Sc	**1.7**	1.7	1.7	1.8	**1.8**	1.5	**1.8**	**1.9**	1.9	1.8	1.8	1.7	1.8
Sm	**30.12**	26.93	22.53	26.8	**23.09**	24.61	**31.78**	**23.13**	24.47	20.52	29.02	24.44	23.67
Sn	**8.44**	6.72	6.57	7.14	**6.6**	6.75	**7**	**8.24**	9.07	8.02	7.15	5.89	6.68
Sr	**69**	54	54	50	**45**	25	**85**	**67**	41	57	82	90	46
Ta	**3.1**	2.7	2.8	3	**3.2**	2.8	**3.1**	**3.2**	3.3	3.1	2.8	2.8	3.2
Tb	**5.389**	4.791	4.237	4.966	**4.645**	4.333	**6.034**	**4.736**	4.57	4.344	4.653	4.47	4.698
Th	**9.33**	8.05	8	8.95	**9.35**	8.37	**9.3**	**9.82**	9.93	9.26	8.05	8.46	9.35
Ti	**653**	587	627	646	**711**	590	**676**	**717**	715	658	620	598	720
Tl	**0.055**	0.035	0.03	0.028	**0.018**	0.124	**0.122**	**0.236**	0.344	0.302	0.079	0.059	0.018
Tm	**3.318**	2.784	2.878	3.137	**2.905**	2.74	**3.228**	**2.889**	2.89	2.624	2.596	2.702	2.951
U	**2.13**	1.73	1.86	2.03	**2.11**	1.89	**2.1**	**2.2**	2.2	2.2	1.79	1.93	2.08
V	**b.d.**	b.d.	b.d.	b.d.	**b.d.**	b.d.	**b.d.**	**b.d.**	b.d.	b.d.	b.d.	b.d.	b.d.
W	**0.6**	0.5	0.5	0.5	**b.d.**	b.d.	**0.6**	**0.5**	0.7	0.6	b.d.	0.5	b.d.
Y	**208.49**	185.7	165.46	199.46	**186.21**	163.58	**212.97**	**182.1**	171.34	162.08	159.19	163.36	181.06
Yb	**21.463**	17.856	19.055	20.278	**18.953**	17.825	**20.87**	**18.886**	19.05	17.275	17.044	17.75	18.768
Zn	**84**	104	104	112	**92**	182	**101**	**90**	128	121	84	87	90
Zr	**352**	315	344	356	**389**	317	**357**	**409**	373	362	334	326	378

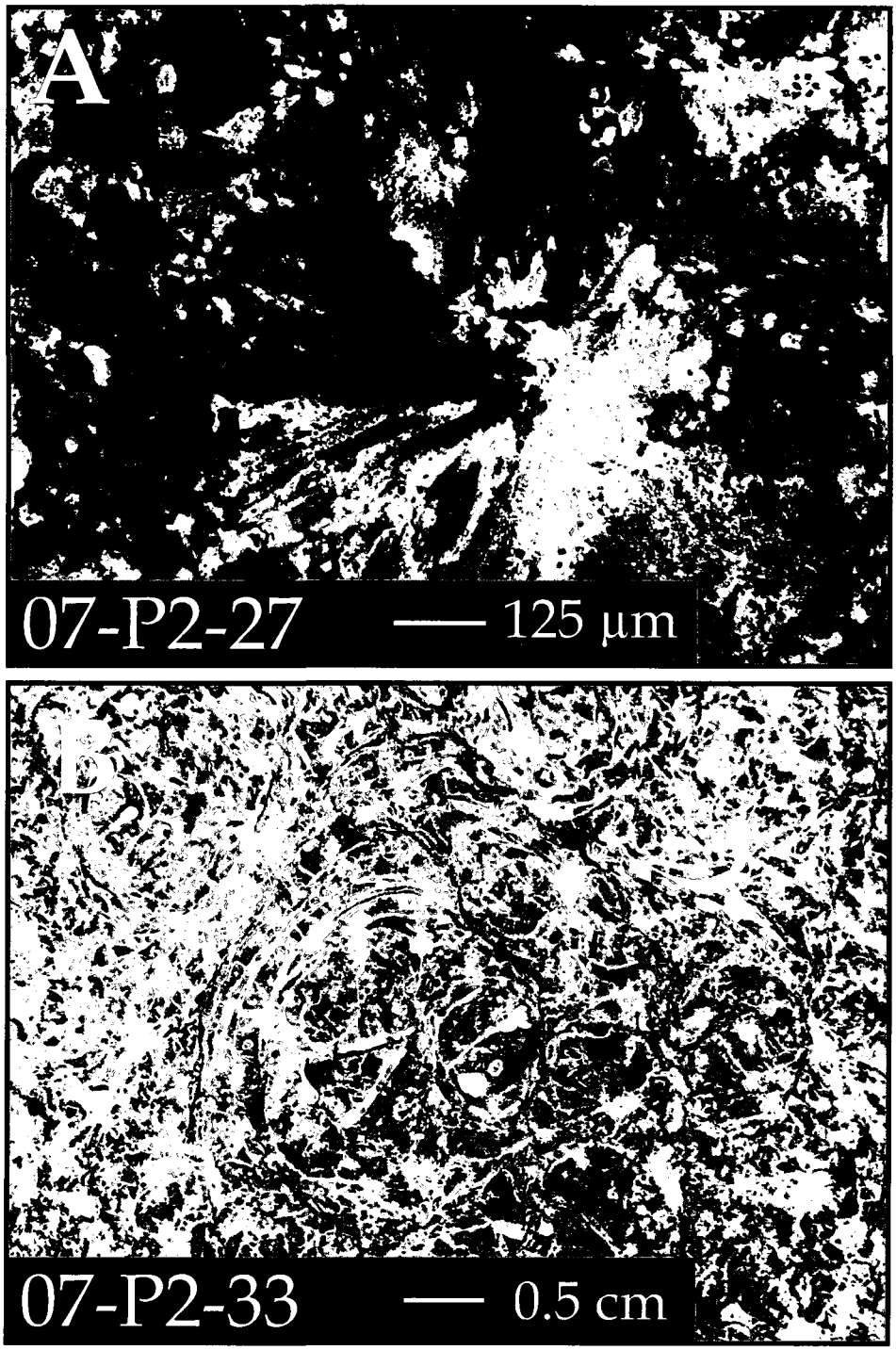

Figure 4.2: Textures of aphyric grid rhyolite. A. Recrystallized spherulite of albite exhibiting a radiating extinction and a light dusty sericitization. (XPL) B. Nested conchoidal perlitic fracturing defined by quartz domains separating mottled chlorite and sericite alteration. (PPL)

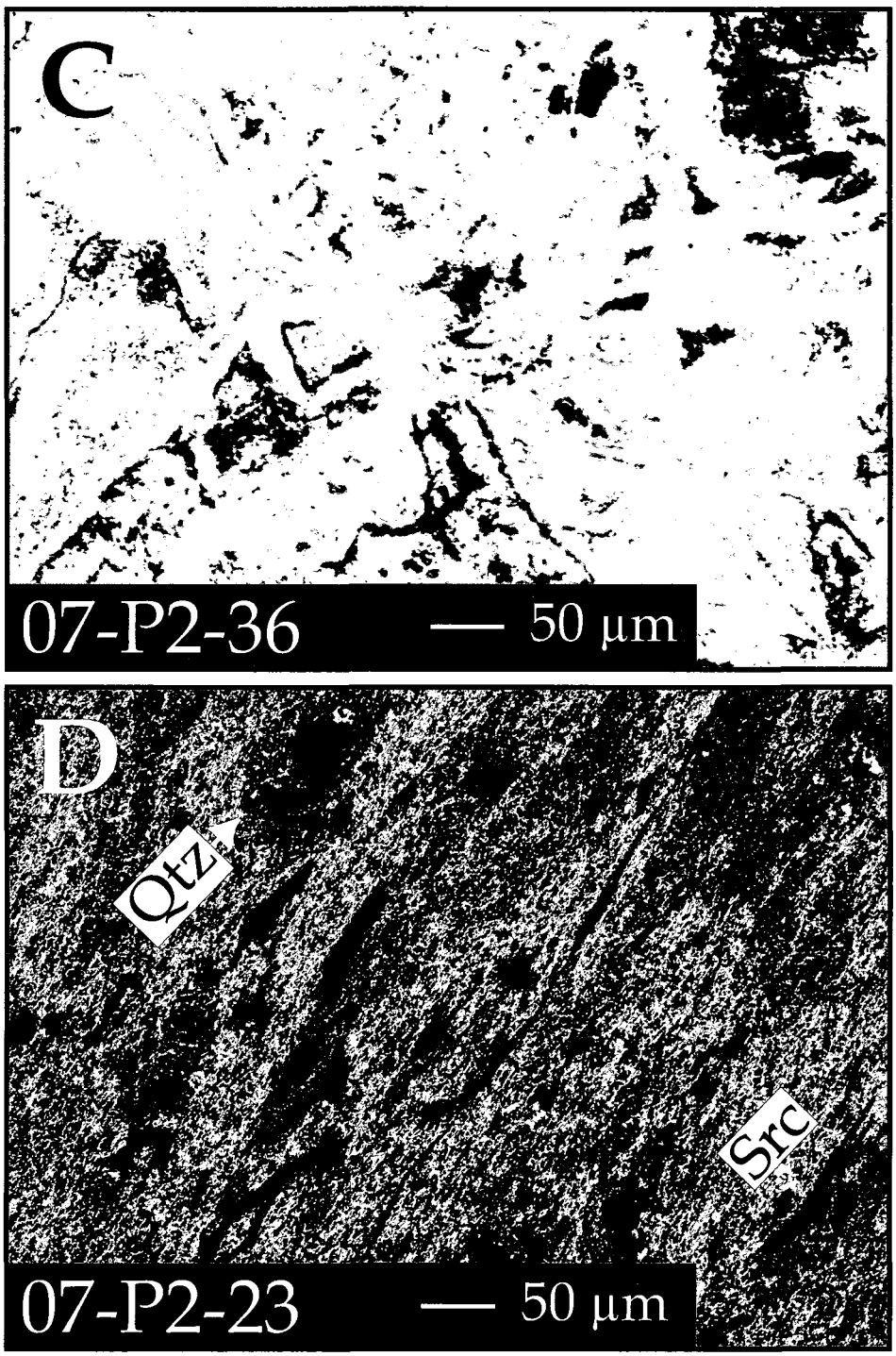

Figure 4.2: Continued. C. Blocky and cuspate relict vitrophyric clasts (i.e. hyaloclastite). (PPL) D. Highly sericitized rhyolite. Yellow domains of white mica and quartz at extinction. (XPL)

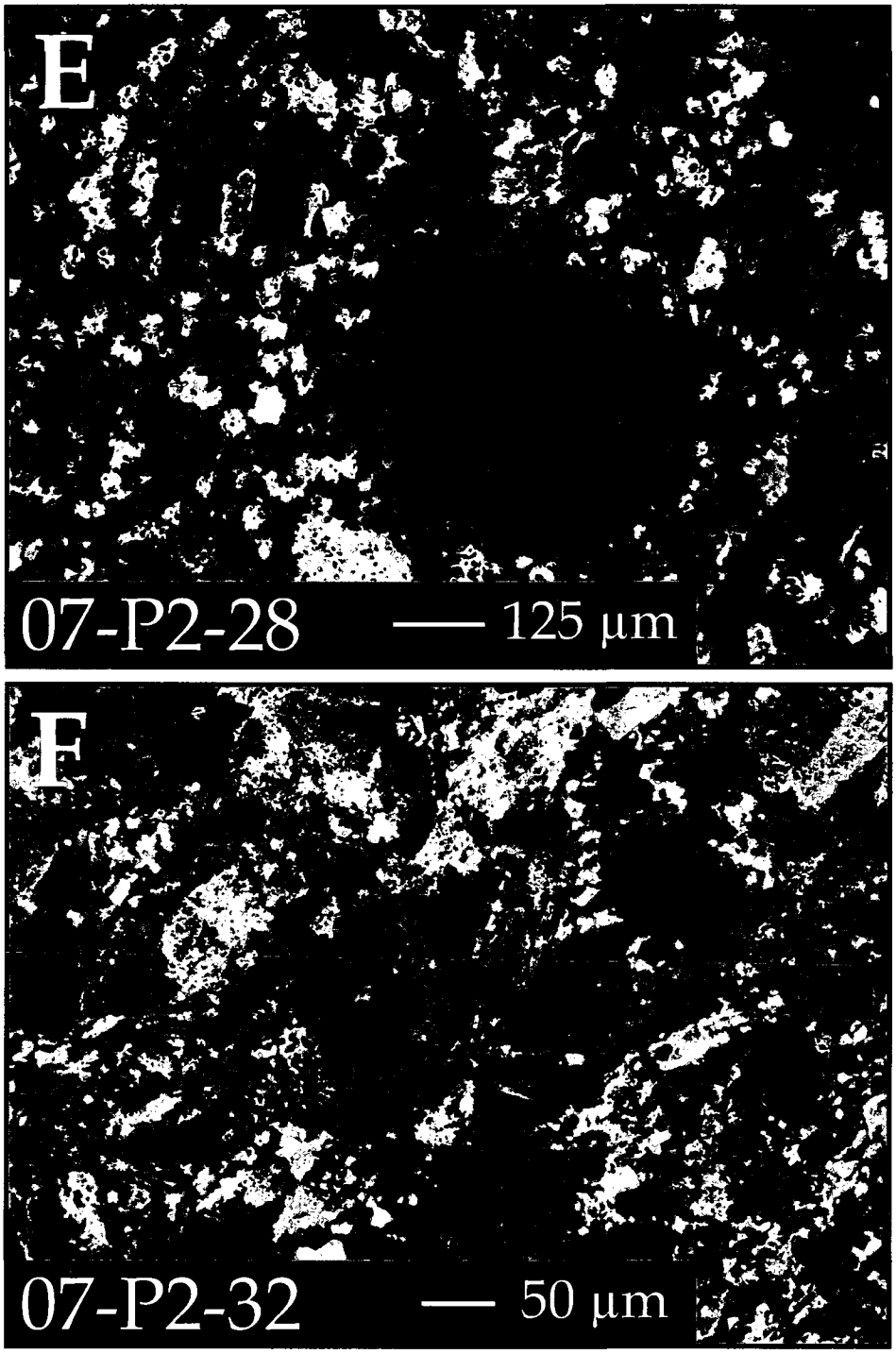

Figure 4.2: Continued. E. Polycrystalline groundmass around a euhedral quartz phenocryst. (XPL) F. Pervasive albitization has resulted in an intergrowth texture of albite crystals which often are poorly defined and have an uneven sweeping extinction. The associated quartz has a polycrystalline habit. (XPL)

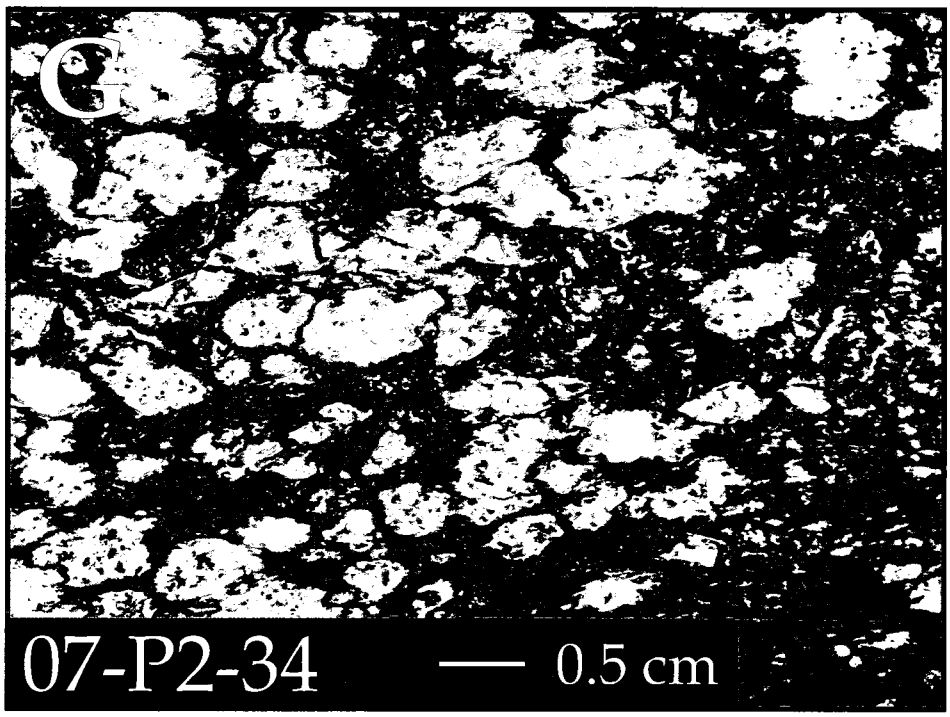

Figure 4.2: Continued. G. Pseudo-breccia texture where a originally coherent rhyolite is being replaced by chlorite. (PPL)

a quartz-bearing high silica rhyolites (Manley, 1996; Scutter et al., 1998). Although similar rhyolites have been repeatedly called "aphyric", they all contain minor amounts of quartz phenocrysts and therefore are not aphyric. Phenocryst-poor high-silica rhyolites that have formed coulées like these are not that common in the modern day but nonetheless are found locally in such places as the Torfajökull area of Iceland (Fig. 4-3AB) and the North Coulée of the Mono Craters in California (Fig. 4-3CD). The Torfajökull and Mono Craters rhyolites are vitrophyres that contain very few crystals (<3%) and exhibit perlite and pumaceous phases. Perlite and vesicles can define flow-banding or merely be discrete phases within a coulée and are present in the Prosser Township rhyolites (e.g. Fig. 3-2D).

By far the most common alterations are sericitization, albitization and chloritization although quartz veining and carbonization have also been observed. Some of the thin sections are pervasively altered such that no original textures are preserved (e.g. Sample 19 or 23; Fig. 4-2D). Others have little sericitization and their major constituents are polycrystalline quartz (Fig. 4-2E), and an inter-grown pseudo-spherulitic albite texture (Fig. 4-2F) both of which are interpreted to represent a recrystallized glass matrix. This albite texture is quite common and in some cases can be clearly interpreted as veins because they crosscut the rock, whereas more commonly it can not be separated from the matrix. All of the albite in these rocks has a light dusty sericitization to some degree, but there is also a major sericitization which replaces significant portions of these rocks. Intensely sericitized rocks are also commonly chloritized and have a pseudo-breccia texture (Fig. 4-2G). The dominant alteration present in each thin section is noted in Table 4-2. The main types of alteration are mirrored in the vein compositions (Table 4-2) which have various combinations of quartz, sericite, calcite, chlorite and hematite.

4.2.4 Petrographically "Least Altered" Protolith

In order to determine the least altered sample based on petrography the following criteria were considered: 1 – preservation of primary textures, and 2 – the abundance and type of alteration minerals. Samples 07-P3-**18, 24, 29, 33, 35** and **36** (**bold samples** in Tables 4-1, 4-2) are petrographically the least altered based strictly on the thin section observations of primary features and the intensity of the two prominent alterations

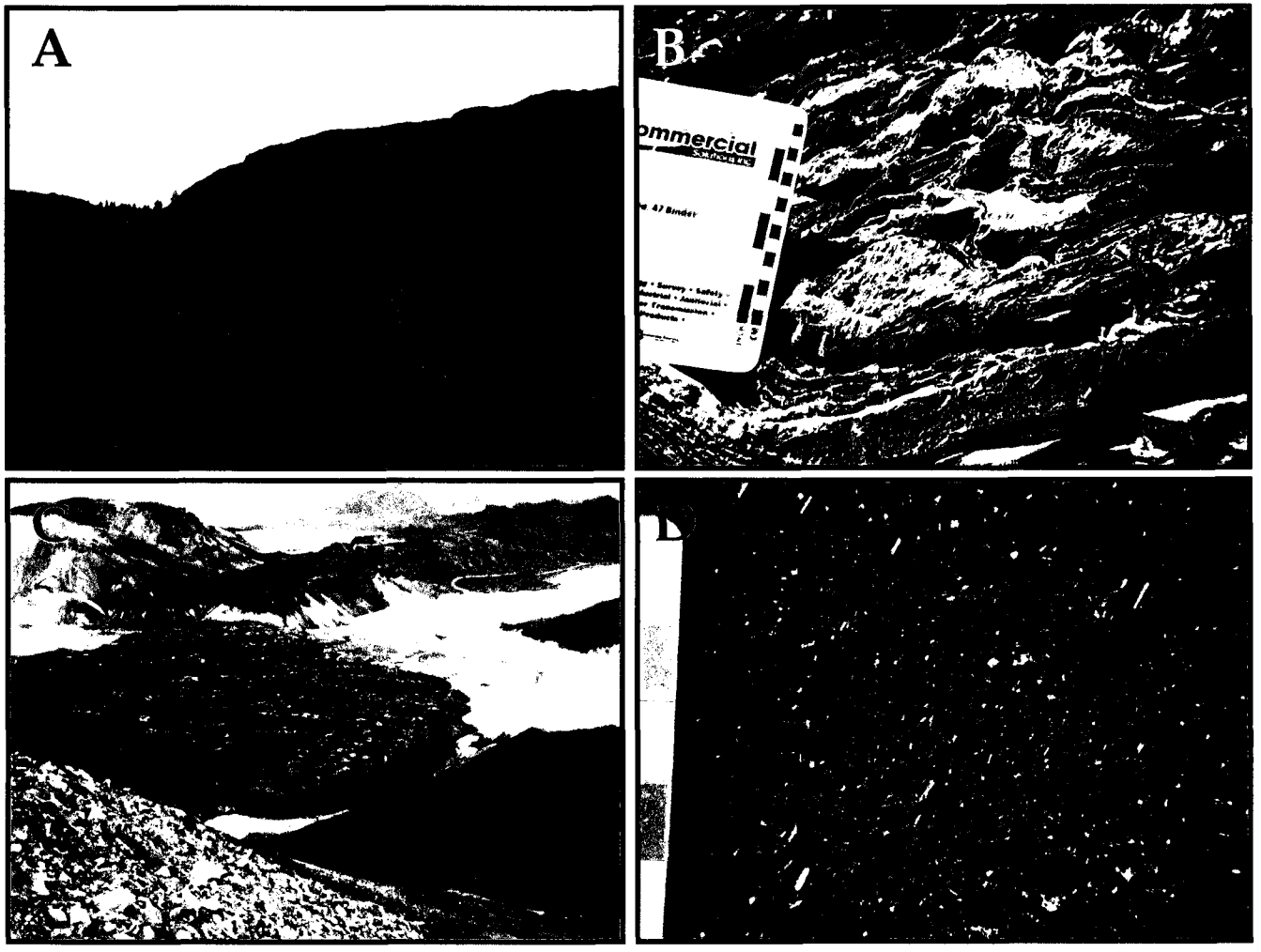

Figure 4.3: A. North Coulée, Mono Craters, Long Valley California. Note the coulée is roughly 30 m high and has an angle of repose around 30°. B. Close up showing flow-bands with vesicular, pumaceous zones. C. Coulées of the Torfajokull area, Iceland. Coulée in the foreground is 30 m in thickness while the coulée in the background fanning out into the valley is as thin as 4 m. D. Close up of the thin background coulée containing ~3% anorthoclase phenocrsysts.

Table 4-2: Petrography of aphyric rhyolites from the grid experiment on Prosser outcrop 2.

+	Sample	Grid Location	Phenocryst[2]	Microphenocrysts[3]	Alteration[4]	Veins[5]	Comments[6]
Grid Center	**07-P3-18**[1]	**Grid Center**	**Qtz <<1%**	**zrn**	**minor carb** and chl		**gm = 50-60% qtz, 30-40% plag** calcite replaces plagioclase laths recrystallized spherulites zircon contains unknown needles and melt inlcusions UTM Zone 17 5400319 N, 483189 E
North	07-P3-19	22 cm N		zrn	src, minor chl	qtz, src	gm = 40-50% src, 20-30 qtz, 5% chl, minor Fe oxides, orangy brown blebs sericitization is prevasive some qtz veins are quite convoluted possibly relict flow banding
	07-P3-20	36 cm N		zrn	src, chl		gm = 40-50% qtz, 20-30% src, <10% chl, <10% cryptocrystalline material, minor Fe oxide minerals completely fine-grained, pervasive src qtz, subhedral, <0.2 mm
	07-P3-21	50 cm N	Qtz <<1%	zrn	src, chl		gm = 10-20% src, 50-60% qtz, <5% dusty crypto-crystalline material, and minor chl, dusty brown minerals qtz commonly embayed, <0.8 mm
	07-P3-22	64 cm N	Qtz <1%	zrn	src, chl	qtz, ab, qtz-ab-chl	gm = 25-35% src, 40-50% qtz, 5-10% dusty opaques, minor chl, brown mineral, ~1% opaque clots qtz <0.4 mm, subhedral to round small clots of opaque/dusty opaque minerals, <0.2 mm
	07-P3-23	1 m N		zrn	src, chl		gm = 30-70% src, 10-50% qtz, 5% chl zircon <0.2 mm 1-3% opaque clots, some larger ones are brown
	07-P3-24	**2 m N**	**Qtz <1%**	**zrn**	**chl**	**qtz**	gm = 35-45% qtz, 45-55% fsp, 5% dusty opaque minerals odd dark red square minerals zrn, numerous, <0.25 mm cubic red/orange minerals, (hematite?)
East	07-P3-25	14 cm E	Qtz <<<1%	zrn	src, chl		gm coherent = 20-30% qtz, 55-75% albite, ~5% opaques, <5% chl gm breccia = 25-35% src, 10-20% qtz, 10-20% albite 5-10% dusty opaques, <5% chl, <5% dusty brown opaques qtz phenocrysts, <0.8 mm, subrounded spherulites zrn <0.1 mm brecciation texture with qtz and src domains

Table 4-2: Petrography of aphyric rhyolites from the grid experiment on Prosser outcrop 2.

+	Sample	Grid Location	Phenocryst[2]	Microphenocrysts[3]	Alteration[4]	Veins[5]	Comments[6]
East	07-P3-25						dusty brown alteration in veins
	07-P3-26	28 cm E		zrn	chl, src	src	gm = 15-25% qtz, 70-80% fsp, minor chl+dusty alt zrn, <0.15 mm odd, elongate brown/red mineral large cubic red opaque mineral with qtz charged core, 2.0 mm possible synchysite
	07-P3-27	42 cm E	Qtz <<1%	zrn	chl		gm = 20-30% qtz, 65-75% fsp, <5% chl, <5% dusty opaque quartz, <1.5 mm, subrounded radiating brown fans in qtz vein, spherulitic synchysite(?) almost opaque red mineral spherulites both relict and 'fresh'
	07-P3-28	56 cm E	Qtz <<1%	zrn	chl	chl, qtz	gm = 25-35% qtz, 50-60% fsp, minor chl+dusty opaques qtz, eu- to subhedral, 0.3 mm zrn, <0.1 mm, subhedral
South	**07-P3-29**	**22 cm S**		**zrn**	**chl, cc,** minor src	**qtz,** qtz-cc-chl-hm, qtz-cc	gm = 25-35% qtz, 55-65% fsp, <5% chl, minor dusty opaq brown titanite(?) or synchysite (?)
	07-P3-30	36 cm S	Qtz <<<1%	zrn	src, chl	qtz, src-chl	gm = 10-20% qtz, 70-80% fsp, 5% chl, minor dusty opaque qtz, rounded, 0.2 mm minor red/orange dusty opaque mineral zrn, <0.1 mm
	07-P3-31	50 cm S		zrn	chl, cc	qtz-cc-musc	gm = 15-25% qtz, 70-80% fsp, <5% chl, 1% cc laths, minor dusty opaques zrn, <0.1 mm, lath-like calcite laths large intergrown chl and dusty orangey/brown mineral
	07-P3-32	64 cm S	Qtz <1%		chl, src		gm = 10-15% qtz, 75-85% fsp, minor chl, dusty opaque minerals, cc relict perlite qtz, euhedral, intermediate bubble layer, <0.4 mm zrn, <50 µm, pyrimidal to cubic rare cc laths, mainly patchy cc replacement

Table 4-2: Petrography of aphyric rhyolites from the grid experiment on Prosser outcrop 2.

+	Sample	Grid Location	Phenocryst[2]	Microphenocrysts[3]	Alteration[4]	Veins[5]	Comments[6]
South	**07-P3-33**	**1 m S**	**Qtz <1%**	**zrn**	**chl**	**qtz, qtz-hm**	**gm = 35-45% qtz, 45-55% fsp, minor chl, dusty opaque** qtz <0.7 mm, subhedral-subrounded perlitic fracturing, See Figure 4.2 B zrn, <0.1 mm, euhedral
	07-P3-34	2 m S	Qtz <3% (mostly relict)	zrn	chl, src	qtz-ab-chl,	gm = 50-60% qtz, 25-35% chl, <10% src, <5% fsp veins, <5% dusty brown mineral, minor Fe Ti oxide minerals qtz an- to subhedral, <0.4 mm relict spherulites zrn, <0.2 mm, clot of several together
West	**07-P3-35**	**14 cm W**	**Qtz <1%**	**zrn**	**chl, minor src**		gm = 45-55% qtz, 45-55% fsp, minor chl and dusty alterati zrn, <0.2 mm qtz, eu- to sub-hedral, <0.5 mm some relict perlite lots of dusty brown and brown/red (rutile?) minerals
	07-P3-36	**28 cm W**	**Qtz <<1%**	**zrn**	**chl**	**cc-qtz**	gm = 40-50% qtz, 45-55% fsp, minor chl and dusty alterati qtz <0.6 mm, eu- to subhedral large mottled brown mineral, 1.5 mm relict hyaloclastite shards, block to cuspate
	07-P3-37	42 cm W	Qtz <1%	zrn	src, chl	qtz	gm = 40-60 % src, 20 % qtz, 20 % dusty crypto- crystalline material, 5-10 % chl qtz phenos, sub- to anhedral, <0.6 mm, porphoblastic <1 % dusty black opaque clots of minerals
	07-P3-38	56 cm W	Qtz <<<1%	zrn	src, chl	qtz	gm = 30-40 % src, 15-25 % fsp, 10-20 % qtz, <15% dusty crypto- crystalline material, <5 % chl, <<1 % dusty brown-opaque minera qtz phenocrysts, anhedral, <0.3 mm
	07-P3-39	2 m W	Qtz <<<1%	zrn	src, chl	qtz, chl	gm = 30-40 % fsp, 25-35 % qtz, 5-15% src, <5 % chl, 1% dusty brown material zrn euhedral, contain melt inclusions, <0.2 mm
	07-P3-40	3 m W		zrn	src, chl	qtz, src chl	gm = 25-40 % fsp, 20-30 % qtz, 10-30 % src, <5 % chl, spherulites

[1] bold = least altered samples; [2] qtz = quartz; [3] zrn = zircon; [4] carb = carbonate; chl = chlorite; src = sericite; cc = calcite; 5 ab = albite; hm = hematite
[6] gm = groundmass; plag = plagiocalse; alt = alteration; fsp = feldspar

(albitization and sericitization) and sparse chloritization. Comparing these least altered samples to those of the above studies (Prior et al., 1999b; Koopman et al., 1999 and Schandl et al., 1999) in Table 4-3 an agreement on 10 of the 15 criteria for 'freshness' in these papers is shown. In this study the samples show similar REE patterns (described below, section 4.3.2), have comparable alteration indices, major element chemistries, Hf and Th contents. The tantalum concentrations in samples from Prosser Township are slightly higher than the other studies. It should be noted that the Prior et al. (1999b) and the Schandl et al. (1999) studies use NAA to determine their HFSE while in this study and Koopman et al. (1999) ICP-MS is the analytical method which may account for the difference. The Prosser township samples are consistently higher in zirconium and zinc contents but these are minor discrepancies given the overall agreement. It should be noted that all of the other studies base their alteration criterion strictly on lithogeochemical data whereas this study is the only one that incorporates petrographic criteria.

The least altered samples in Prior et al. (1999b) satisfy all of the criteria (Table 4-3) except for the La/Ta ratio. Three of the four least altered samples of Schandl et al. (1999) are rhyolitic tuffs noted as having been sericitized (Schandl et al., 1999, their Table 3, samples KC.507G, H and J). The whole rock composition (Table 3, Schandl et al., 1999) of the sericitized samples have been significantly altered based on their K_2O and H_2O^+ contents. The REE content of these tuffaceous least altered samples are higher than that of their associated massive rhyolite sample. This is typically found for sericitized rhyolites (Koopman et al., 1999, Figure 15; Schandl et al., 1999; Fig. 5C). Based on the above discrepancies, the altered samples of Schandl et al.'s, (1999) study were excluded in the determination of an aphyric rhyolite protolith composition as they are relatively altered, suffered from significant mobilization of their major elements and also have variable REE contents. The least altered sample in Koopman et al. (1999) satisfies most criteria except the bound water, Cu and Zn values as well as the La/Ta ratio.

The arithmetic averages of least altered samples from this study are higher in zinc, zirconium and tantalum content in comparison to previous results (Table 4-3). Upon comparison of the REE contents sample 08-P3-24 has substantially lower REE concentrations than its counterparts and is therefore omitted from the average least

Table 4-3: Compilation of 'least altered' rhyolite samples and their discrimination criteria.

	Study		Prior et al., 1999b	Koopman et al., 1999	This Study	This Study Least Altered Rhyolites					
	Criteria		Avg. 6 Least Altered	Avg. 5 Least Altered	Avg. 6	07-P3-18	07-P3-24	07-P3-29	07-P3-33	07-P3-35	07-P3-36
Koopman et al., 1999*	REE Profiles	similar to the FIIIb rhyolites	x[2]	x	x	x	low	x	x	x	x
Prior et al., 1999b Footwall Rhyolite[1]	Na_2O (wt %)	>2.0	x	x	x	x	x	x	x	x	x
	L.O.I. (wt %)	<2.2	x	x	x	x	x	x	x	x	x
	CO_2 (wt %)	<1.8	x	x	x	x	x	x	x	x	x
	H_2O^+ (wt %)	<1.1	x	>	x	x	x	x	=	x	x
	Cu (ppm)	<11	x	>	x	x	x	x	x	x	x
	Zn (ppm)	<70	x	>	>	>	x	>	>	>	>
	Alumina Saturation index	<1.7 %	x		x	x	x	x	x	x	x
	Isikawa index	<0.6 %	x	x	x	x	x	x	x	x	x
	Goodfellow index	<0.45 %	x	x	x	x	x	x	x	x	x
Schandl et al., 1999	Hf (ppm)	7-14	x	x	x	<	<	x	<	x	x
	Zr (ppm)	200-300	x	x	>	>	>	>	>	>	>
	Th (ppm)	6-14	x	x	x	x	x	x	x	x	x
	Ta (ppm)	1.2-3.0	x	x	>	x	x	>	>	>	>
	La/Ta	20.2-25.8	>	>	x	>	<	>	<	>	<
	Yb/Ta	3.3-8.5	x	x	x	x	x	x	x	x	x
	Flat REE with Neg Eu		x	x	x	x	x	x	x	x	x

* Koopman et al., (1999) use 3 criteria. The other 2 is the comparison with Prior et al., (1999b) and the last is O-isotope date. See text for further explaination.

[1] Alumina saturation index = Al/(2Ca+Na+K) after Shand (1951). Isikawa index = $(K_2O+MgO)/(MgO+K_2O+CaO+Na_2O)$ after Isikawa et al. (1976). Goodfellow index = $(MgO+FeO_t)/(FeO_t+MgO+K_2O+CaO+Na_2O)$ after Goodfellow (1975) and Riverin and Hodgson (1980).

[2] x - fulfills the criteria; > means this rhyolite has a concentration or ratio that exceeds the discriminant criteria; < means this rhyolite has a concentration or ratio that is below the discriminant criteria; = means this rhylite has a concentration equal to that of the discrimnant criteria; low means this rhyolite has low overall REE contents.

altered rhyolite composition. In summary the least altered rhyolites of this study are higher in Zn, Zr and Ta compared to the least altered samples of prior studies.

4.2.5 Electron microscopy

One sample B1a within the vicinity of the grid was chosen for electron microprobe analysis in order to determine mineral chemistry and to analyze indistinct mottled aggregates of brown material common to many of the thin sections (Fig. 3-4E). These aggregates of mottled brown to opaque material usually have an anhedral massive or a spherulitic habit, however sometimes clear, better developed acicular crystals are present. The following were identified in these indistinct masses: allanite (Fig. 4-4A), monazite, xenotime (Fig. 4-4A), and the presence of polycrase-Y [(Y, Ca, Ce, U, Th)(Ti, Nb, Ta)$_2$O$_6$] (Fig. 4-4B), synchysite-Ce [Ca(LREE)(CO$_3$)$_2$F] (Fig. 4-4C), iimorite-Y [Y$_2$(SiO$_4$)(CO$_3$)], and gerenite-Y[(Ca,Na)$_2$(Y,REE)$_3$Si$_6$O$_{18}$*2(H$_2$O)] were inferred by analysis of electron dispersive spectra by Dr. Anthony Mariano, Carlisle, MA (see Appendix A.2). Allanite, monazite and xenotime were found disseminated throughout the rock, but never in any significant concentration. The polycrase was found as a 10 μm grain within a quartz vein. Iimorite and gerenite were found as two subhedral patchy intergrown minerals that could be replacing another phase. Lastly synchysite was found as poorly formed spherulitic growths some of which were nucleated on the corners of zircon crystals.

4.2.6 Paragenesis

Given the petrographic observations presented above a simple paragenetic sequence has been inferred. The average lithogeochemistry of each major alteration types and their relative elemental enrichments-depletions are summarized in Table 4-4 and described in detail below in (Section 4.2.7; Fig. 4-5).

A least altered sample exhibits a hyaloclastite texture (Fig. 4.2C) that is preserved as a fine-grained polycrystalline quartz infilling the fractures. The glass shards of the hyaloclastite are now coarser polycrystalline quartz however there is a slight dusty residue of impurities along the contact which creates the contrast between the clast and the interstitial quartz filling. Similarly the perlite cores are intergrown albite and quartz

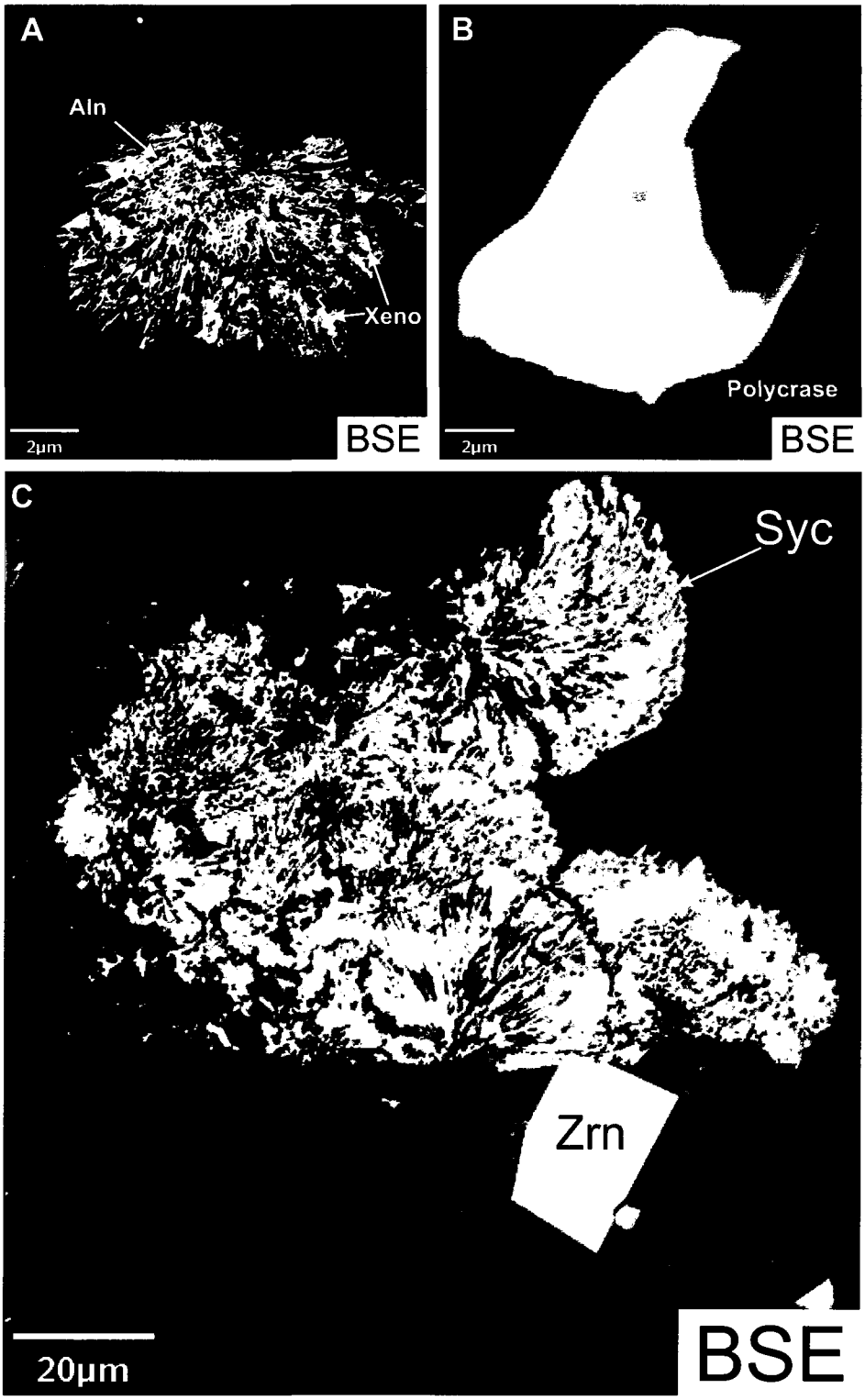

Figure 4.4: Sample B1. Backscatter images. A. Poorly developed intergrowth of allanite (Aln) with xenotime (Xeno). B. Polycrase crystal within quartz vein. C. Spherulitic growth of synchysite (Syc) crystals. Zircon (Zrn) also present.

crystals while the conchoidal fractures themselves are in-filled with the same fine-grained polycrystalline quartz as found in the hyaloclastite. Crystallization of the volcanic glass is inferred to be responsible for the textural and mineralogical variations seen at the microscopic scale in the least-altered samples. Given this inference it follows that the intergrown albite crystals are recrystallized from an original glass and that this texture is therefore likely an isochemical (or near-isochemical) reaction which preserves the protolith composition (see below).

The next major alteration phase is the destructive sericitization that forms along flow bands and other internal structures within the coulée. The timing of sericite alteration is unclear however; some sericite must be related to tectonism as it defines a fabric (Fig. 4.2D). It should also be noted that the sericitization is spatially restricted to the northern part of the grid (Fig. 4.7). It has also been observed that samples taken between the underlying contact and the grid show decreasing potassium as they near the grid. The association between sericitization and the addition of potassium is established below (Fig. 4.5A, described below) which, with the spatially restricted extent of these sericitized samples, suggests that the intensity of sericitization increases to the north, toward the underlying contact.

The last major alteration is the destructive addition of chlorite to this rock. There is only one sample (07-P3-34) that consists of ~30 vol. % groundmass chlorite which has a pseudo-breccia texture (Fig. 4.2G). This lone sample is unique and therefore neither a definitive spatial relationship nor a relative timing between alterations can be established. However the intensity of the chloritization suggests that it is related to regional greenschist metamorphism.

4.2.7 Alteration Lithogeochemistry

It has been shown in the previous sections that the least altered specimens determined on the basis of petrography are consistent with the geochemical criteria of Prior et al. (1999b), Schandl et al. (1999) and Koopman et al. (1999). In this section the geochemical data of the grid specimens are examined to further define alteration and compare with what has been done around the Kidd Creek deposit.

To do this, a temporal enrichment-depletion diagram has been devised, which allows the examination of element mobility with respect to discrete alteration events. As shown above albitization precedes sericitization and chloritization replaces albitized samples. Thus, in Figure 4-5 the elements are sequentially normalized showing the progressive enrichments and depletions of the average alteration composition (there is only one chloritized sample: 07-P3-34) normalized to the preceding alteration event. As an example, CaO during albitization is depleted by 9%, a further 52% during sericitization to a total of -61% relative to the least altered composition. Finally, during chloritization the relative CaO concentration is enriched by a factor of almost three (from -61% to +32% above the average albitized sample). This represents in absolute terms a net increase of 22% above the least altered composition (i.e. Table 4-4: 0.27 wt % to 0.33 wt %).

The three major types of alteration have been normalized in Figure 4-5 to the average precursor composition. From the major element plot (Fig. 4-5A) it is evident that albitized samples have the least variation and are slightly depleted in all oxides, except potassium and fluorine which are significantly depleted and silica, manganese and ferric iron, which are slightly enriched. During sericitization potassium, fluorine and magnesium are highly enriched suggesting that the sericite being formed is mainly muscovite which likely has significant fluorine as the volatile species. There is also always minor chloritization associated with sericitization which likely explains the magnesium enrichment. There is also a consistent pattern of mobility to CaO and CO_2, both of which are enriched in the chloritized sample. This suggests that in addition to chloritization the late stage alteration includes minor carbonitization. This is not surprising as CaO is added and calcite is described as a replacement mineral in many of the thin sections. It is also of note that the two HFSE, titanium and aluminum, are depleted in the same relative proportions and that both are mirror images of the silica trend suggesting that they are dilution effects. It is also of note that the ferric and ferrous irons have very distinct and separate patterns from other major elements. During albitization Fe_2O_3 is enriched relative to FeO suggesting oxidization. During both sericitization and chloritization both types of iron are enriched suggesting metasomatic addition of iron.

Table 4-4: Compilation of average alteration lithogeochemical analyses

Alteration	Average Least Altered	% Change[3]	Average Albitized[4] Rhyolite	% Change	Average Sericitized[4] Rhyolite	% Change	Chloritized[4] Rhyolite
Comment[1]	Avg. 5		Avg. 9		Avg. 7		07-P3-34
Major Elements							
SiO_2	75.85	3.5	78.52	-2.5	76.56	0.4	78.8
TiO_2	0.14	-10.3	0.13	8.1	0.14	-4.4	0.12
Al_2O_3	12.67	-10.9	11.29	6.4	12.01	-3.6	10.88
Fe_2O_3	0.56	10.1	0.62	50.6	0.93	10.7	0.68
FeO	1.80	-4.2	1.73	6.1	1.83	23.4	2.13
MnO	0.03	7.6	0.03	3.7	0.04	16.1	0.04
MgO	0.84	-13.4	0.73	99.1	1.45	72.9	1.26
CaO	0.27	-8.8	0.25	-52.0	0.12	32.0	0.33
Na_2O	5.95	-3.8	5.72	-53.1	2.69	-28.0	4.12
K_2O	0.86	-50.2	0.43	535.9	2.73	161.1	1.12
P_2O_5	0.01	0.0	0.01	0.0	0.01	0.0	0.01
L.O.I.	1.06	-15.7	0.90	95.4	1.75	67.5	1.5
Total	100.25	0.3	100.54	-0.1	100.44	0.7	101.23
Trace Elements							
Crystalline Moisture	1.04	-11.0	0.92	81.0	1.67	45.1	1.34
CO_2	0.12	-4.9	0.11	-57.7	0.05	105.0	0.23
F	432	-31.0	298	224.3	968	104.5	610
S	0.02	-32.7	0.02		b.d.		b.d.
Cl	0.02	28.6	0.03	-50.0	0.02	-33.3	0.02
Ag	b.d.[2]		b.d.		b.d.		b.d.
As	2	14.3	2	2.1	2	-41.7	1
Ga	26.69	-4.2	25.56	31.4	33.57	5.7	27.00
Mo	2.99	-30.4	2.08	45.6	3.03	113.6	4.45
Sn	7	1.3	7	7.8	7	-12.9	6
Ba	115.4	-33.0	77.3	152.0	194.8	30.5	100.9
Be	5.04	-25.1	3.77	-9.7	3.41	7.9	4.07
Bi	0.20	5.4	0.21	3.8	0.22	-22.8	0.161
Cd	0.17	-5.7	0.16	3.9	0.17	41.8	0.23
Co	0.10	155.6	0.26	-55.3	0.11	-60.9	0.1
Cr	b.d.		25		b.d.		b.d.
Cs	0.61	-55.5	0.27	641.6	2.02	166.0	0.72
Cu	7.4	-2.4	7.2	-32.7	4.9	38.5	10.0
Li	10.06	-19.9	8.06	112.3	17.10	75.0	14.1
Ni	b.d.		b.d.		b.d.		b.d.
Rb	31.06	-61.2	12.04	684.2	94.46	247.9	41.9
Sb	0.05	-11.1	0.04	-1.9	0.04		b.d.
Sr	67.40	-14.8	57.44	-24.4	43.43	-56.5	25.00
Tl	0.10	-53.2	0.05	602.4	0.32	172.2	0.12
V	b.d.		b.d.		b.d.		b.d.
W	0.57	-9.6	0.51	10.6	0.57		b.d.
Zn	92.00	-3.1	89.11	23.8	110.29	104.2	182
HFSE							
Hf	14.15	-7.4	13.10	4.4	13.68	-2.6	12.76
Nb	45.18	-7.7	41.70	6.6	44.47	-9.2	37.85
Pb	12.32	-11.9	10.86	-37.8	6.76	-21.7	8.5
Sc	1.78	-2.0	1.74	-4.2	1.67	-14.0	1.5
Ta	3.08	-6.9	2.87	5.6	3.03	-2.3	2.8
Th	9.25	-7.9	8.52	1.7	8.66	-1.8	8.37
Ti	676.20	-2.9	656.67	3.9	682.29	-10.2	590.00
U	2.10	-8.3	1.92	3.9	2.00	-1.7	1.89
Y	194.11	-6.1	182.30	-19.7	146.38	-10.3	163.58
Zr	368.00	-7.6	339.89	5.1	357.14	-6.7	317.00
REE							
La	74.07	1.5	75.18	-40.6	44.65	-6.9	70.02
Ce	173.10	2.4	177.24	-34.5	116.01	-10.2	159.1
Pr	23.15	0.8	23.33	-40.2	13.95	-8.5	21.34
Nd	105.35	0.5	105.92	-40.7	62.79	-6.2	99.41
Sm	26.77	-1.4	26.39	-36.2	16.84	-6.7	24.61
Eu	4.80	-6.6	4.48	-35.0	2.91	-16.3	3.75
Gd	29.16	-5.8	27.46	-29.1	19.47	-6.1	25.78
Tb	5.10	-7.2	4.74	-22.8	3.66	-8.5	4.333
Dy	32.40	-6.5	30.29	-19.4	24.41	-8.9	27.6
Ho	6.92	-6.1	6.50	-18.7	5.28	-6.8	6.055
Er	19.11	-5.1	18.13	-17.2	15.01	-6.5	16.95
Tm	3.06	-4.6	2.92	-15.2	2.47	-6.1	2.74
Yb	19.81	-4.6	18.90	-13.4	16.36	-5.7	17.83
Lu	2.98	-4.3	2.86	-12.5	2.50	-4.1	2.74

[1] Arithmetic average of N# of samples; [2] b.d. = below detection limit;

[3] % Change = Elemental percent change of alteration type relative to precursor composition. See Figure 4-5.

[4] albitized sample is normalized to least altered average; sericitized is normalized to albitized average; and, chloritized is normalized to average albitized composition.

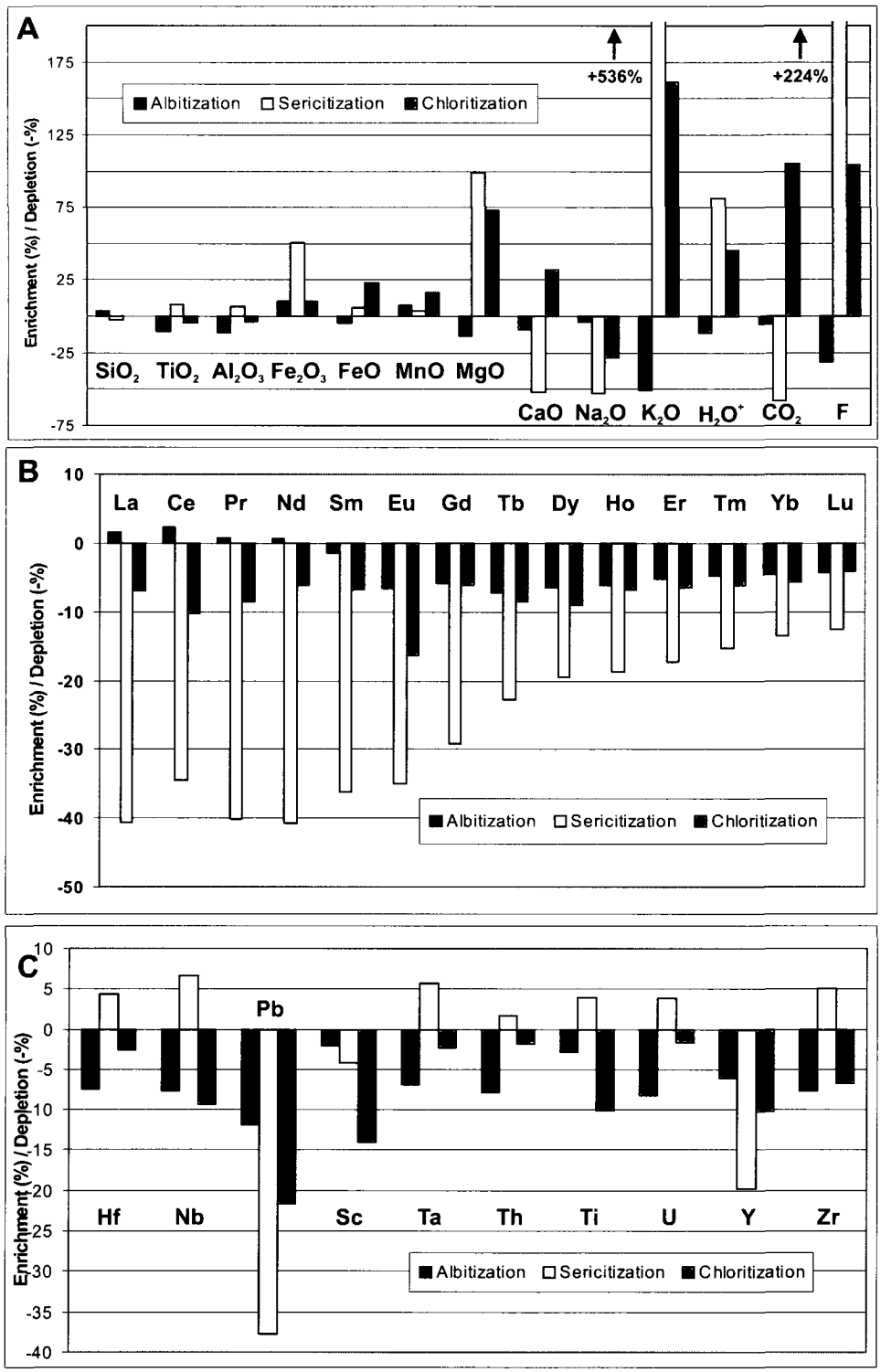

Figure 4.5: Temporal Enrichment-Depletion (TED) diagrams. Each element is normalized three times based on the results of the petrography - On the left in blue to the least altered specimen; in the middle (yellow) to the average albitized specimen; and, on the right (green) to the average albitized specimen. A. Major element chemistry. B. Rare earth elements. C. High field strength elements.

The REE have considerable variation in their behavior (Fig. 4-5B). During the initial albitization the REE were only mobilized up to a maximum of 7% (Tb), although relative to the least altered the LREE were slightly enriched whereas the HREE were depleted. Sericitization has consistently depleted the REE, particularily the LREE (up to 40% La, Pr and Nd). The chloritized sample has moderately depleted the REE, on average 7%. Europium is depletion twice as much as the other REE (16%) during chloritization. The net sum of the alterations have depleted the rare earth elements, most of which occurred during sericitization.

For the most part the HFSE show consistent behavior (Fig. 4-5C) however Pb (N.B. Pb^{4+} is a HFSE), Sc and Y are anomalous. Pb and Y vary consistently and were extremely mobile during sericitization. Pb and Sc have multiple valence states which may explain their atypical behavior relative to the rest of the HFSE. As Y has a similar ionic radius and valence state to Ho and shows comparable variations and it is interpreted as having a similar alteration history. By far, sericitization has mobilized the HSFE whereas albitization and chloritization have had comparably minor impacts, typically <10 %. Other than Pb, Sc and Y, the HFSE were enriched by 3-6 % during sericitization. During albitization it is clearly shown that Sc and Ti were the least mobile and with the exception of Pb the other HFSE were depleted by only <8 %. Ti has a low overall variance except during chloritization where it is twice as depleted as in the other alterations.

Throughout alteration Th, U, Hf and Ta were the least depleted, only up to ~10 %. For Th and U a 10% enrichment or depletion, regardless of the corrections for dilution, is ±1.3 and ±0.3 ppm, respectively, of their concentrations (e.g. Table 4-1, Sample 18: Th = 8.46, U = 1.94). The 2σ analytical errors for Th and U are ±0.4 and ±0.2 ppm, respectively, which are less than than the variation for these analyses therefore this alteration is statistically significant. Hf has concentrations and instrumental errors similar to Th. It should also be noted here that Ta shows depletions up to 8 %, throughout all grid samples the Ta content varies between only 2.7 and 3.5 ppm (Table 4-1). Nonetheless this is significant as the 2σ error for the RGM-1 rhyolite standard for Ta is ±0.024 ppm (Burnham and Schweyer, 2004). Together these results show that throughout the alteration of these formerly glassy phenocryst-poor rhyolites, the HFSE are the best conserved elements, within 10 %. Furthermore the grid data may be used to assess the

maximum resolution of lithogeochemical variability. This result agrees with prior studies noted above and makes them most useful for lithogeochemical discrimination.

4.2.8 Recognition of Alteration through Major Element plots

Removing the least altered samples, the rest of the grid samples can be divided into three groups: Those that are albitized (typically they maintain many original textures i.e. perlite, but are described as having high concentrations of intergrown albite), those that are sericitized (whose original textures have been destroyed by sericite), and the one (07-P3-34) that has been chloritized. It is clear that least altered and albitized samples have over 4.5 wt % Na_2O and less than 1 wt % K_2O. In Figure 4-6A the least altered sample 07-P3-36 is separate from the rest of the least altered samples and has lower sodium and higher potassium contents. This sample also has a high MgO (Fig. 4-6D) and low REE (Table 4-1) contents. These factors and its spatial association (Fig. 4-7), suggest that this sample has been moderately sericitized as seen from the enrichments and depletion from Figure 4-5A. Chloritization and sericitization are easily separated geochemically from the least altered and albitized samples as both sericite and chlorite have low Na_2O and high K_2O contents (Fig. 4-6AB).

The difference between least altered and albitized rocks is more difficult to ascertain (Fig. 4-6C, D; sericitized and chloritized samples have been removed for clarity) as even the least altered samples contain ~50 vol. % (compared to ~70 vol. % for albitized samples) albite within the groundmass. As a result there is a very little basis to separate these two groups in terms of the major element chemistry except to say that large SiO_2 contents greater than ~77 wt % correspond with heavily albitized samples. Chemically sample 07-P3-25 appears to be one of the least altered samples. This contrasts with the petrography which shows this to have a pseudo-breccia texture. The associated alteration could not be pervasive otherwise it would have a much lower Na_2O content.

Overall there is a distinct spatial distribution of these alterations (Fig. 4-7). The least altered samples fall around grid center (except 07-P3-33) whereas the albitized samples (25, 26, 27, 28, 30, 31 and 32) lie along the south and east arms of the grid. The chloritized sample is alone in the most extreme south of the grid and is the closest sample

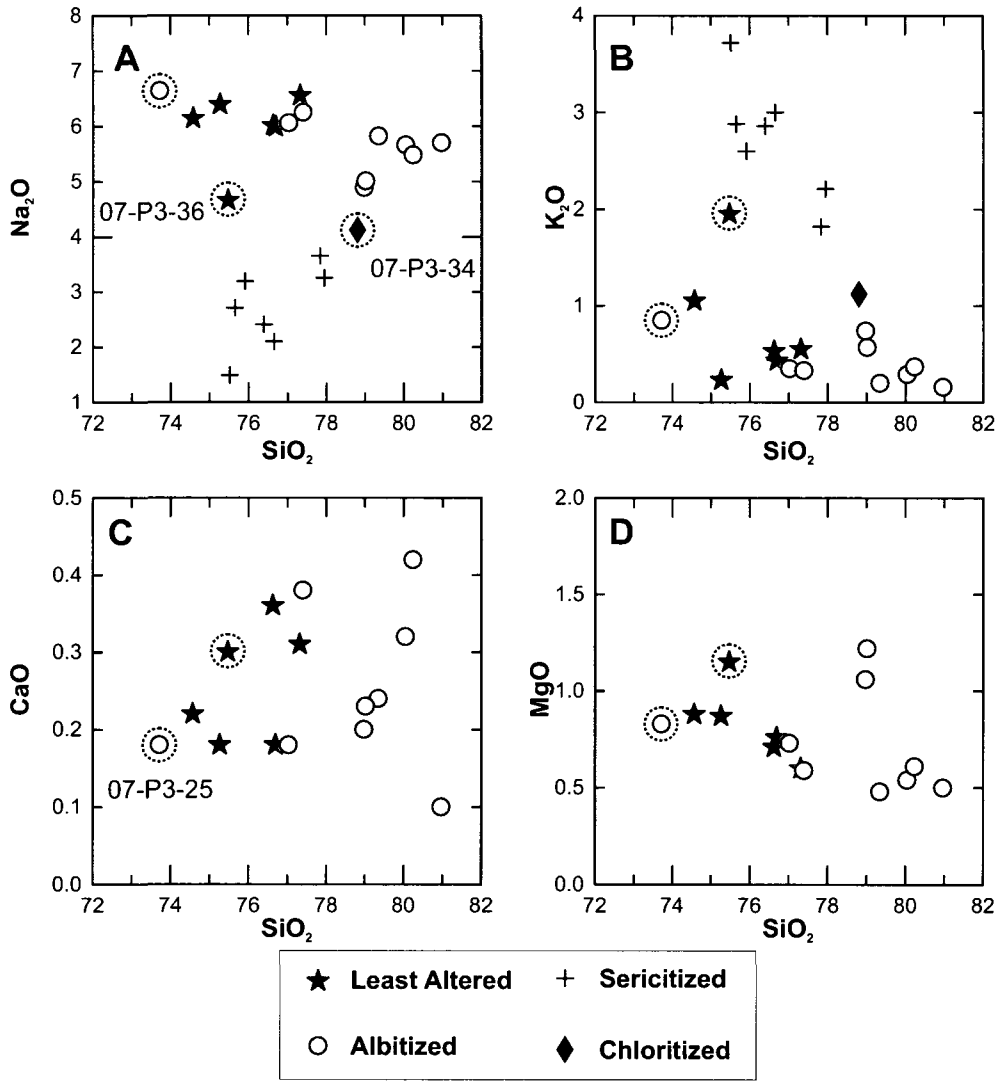

Figure 4-6: Major element plots. A. Na_2O vs. SiO_2. Note least altered and albitized samples have Na_2O contents above 4.5 wt % while chloritized and sericitized have less than 4.5 wt %. Note that there is only one chloritized sample. Also the least altered sample 07-P3-36 has been circled in all plots in this figure. B. K_2O vs. SiO_2. C. CaO vs. SiO_2. D. MgO vs. SiO_2. Errors are smaller than symbols.

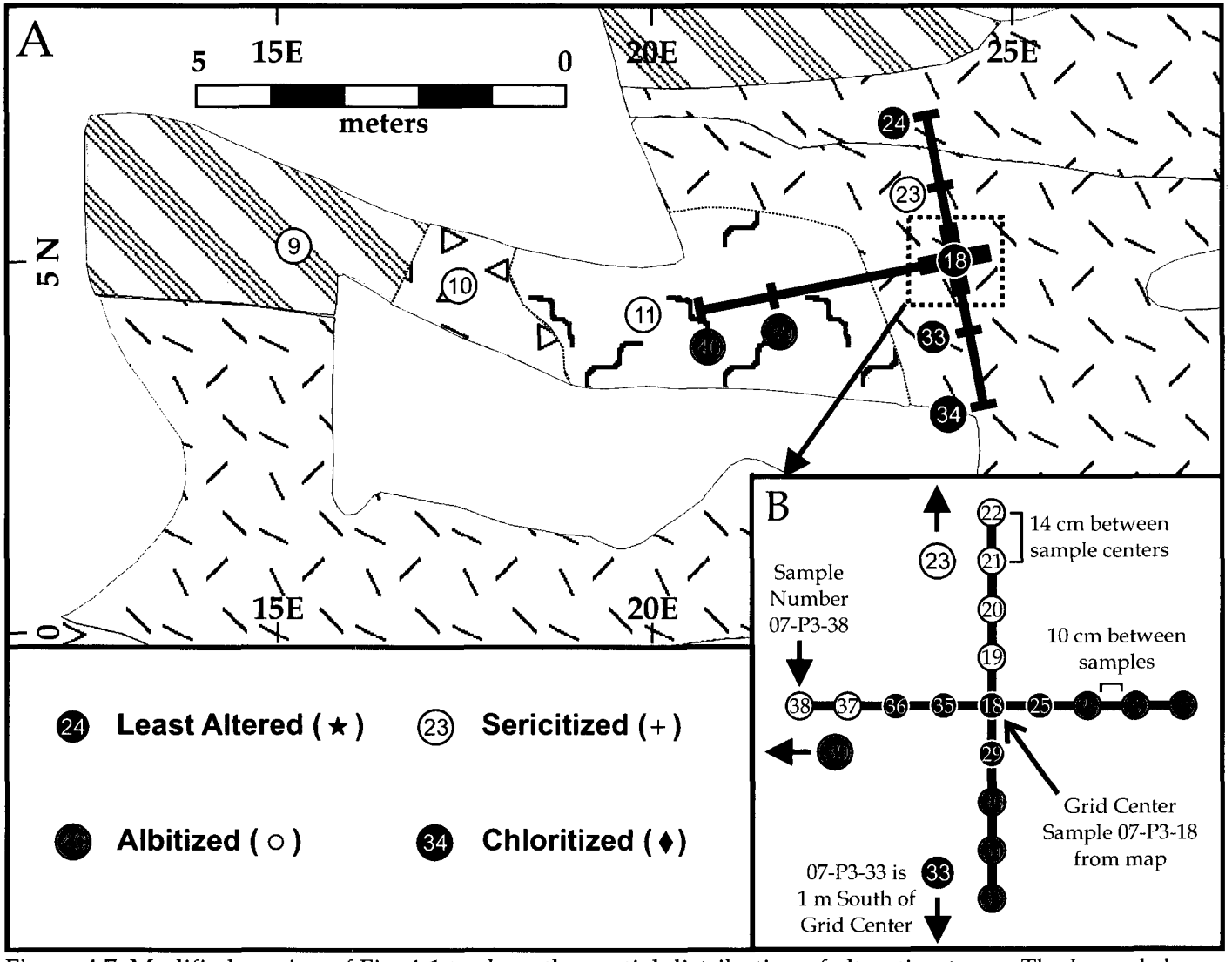

Figure 4.7: Modified version of Fig. 4-1 to show the spatial distribution of alteration types. The legend shows the colour of the alteration used in Figure 4-4 while the symbols in brackets are those used in Figure 4-5.

to the contact with overlying tuff. It should be noted that sample 24, the REE depleted specimen is in the most northern part of the grid in a different unit.

To view the spatial variations of the 10 cm spacing samples (Fig. 4.1B; Fig. 4.7B) kriged surfaces of representative major, rare earth and high field strength elements have been interpolated using ArcGIS in Figure 4.8. The 10 cm spaced samples show equal variation to that of the 1 meter spaced samples and therefore have not been displayed. Aluminum (Fig. 4.8A) shows a 1.5 wt. % variation over ~15 cm. Sodium (Fig. 4.8B) and potassium (Fig. 4.8C) show a general inverse relationship as expected from the whole rock binary plots. The REE (Fig. 4.8D-F) show the strongest variation within 10 cm of grid center (07-P3-18). Between either 10 cm east or west of grid center and 10 cm north of grid center the REE range from their maximum concentrations to their minimum concentrations. The same variation from maximum to minimum concentration is evident in the HFSE however; maximum concentration center around 10 cm W for the REE is at 20 cm W in the HFSE. These extreme variations strongly suggest that there are very small scale factors controlling the trace element variability. Given that the HFSE and REE vary similarly but not coherently leads to the inference that there are separate processes and minerals which have mobilized these elements. This observation is probably explained by the presence the rare earth and high field strength element-bearing minerals observed in Figure 4.4. There is no consistent variation between major and trace elements which leads to the conclusion that the major alterations do not control the trace element variations. So, although the REE are strongly mobilized during sericitization as displayed by the temporal enrichment-depletion diagrams, sericitization cannot explain the mobilization of the REE and HFSE displayed here.

4.2.9 Classification of aphyric rhyolites

As a result of the above results it is clear that while the REE are moderately mobile, with the exception of Pb and Y the HFSE are essentially conserved. By extension of these results the discrimination diagram, Nb/Zr vs. Al_2O_3/TiO_2, developed by Prior (1996; Prior et al., 1999a) is applicable to the Kidd-Munro rhyolites as it uses the HFSE elements. Their diagram distinguishes between the sequence capping QP rhyolite and the underlying aphyric rhyolites at Kidd Creek. Because the grid samples are 'aphyric'

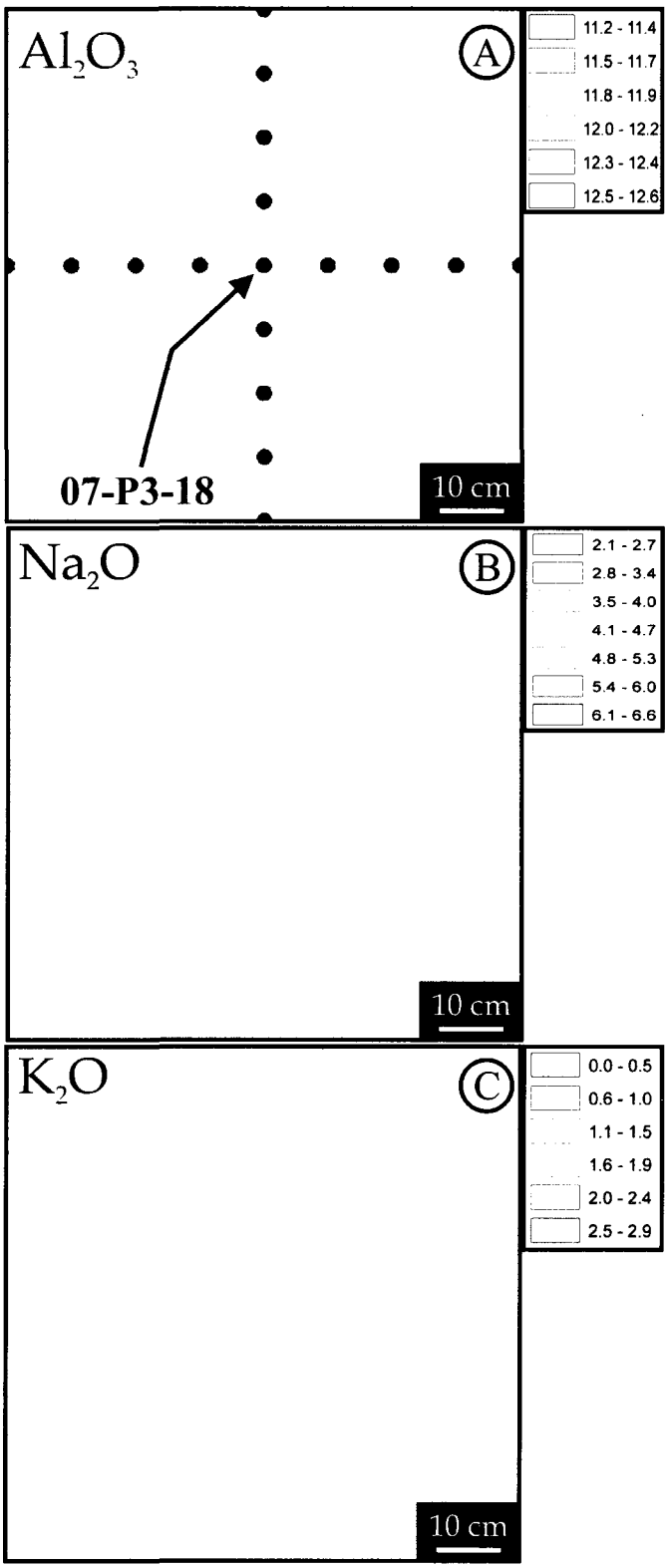

Figure 4.8: 10 cm grid samples elemental variation. A) Al_2O_3 wt. %. B) Na_2O wt. %. C) K_2O wt. %. Note grid center is sample 07-P3-18.

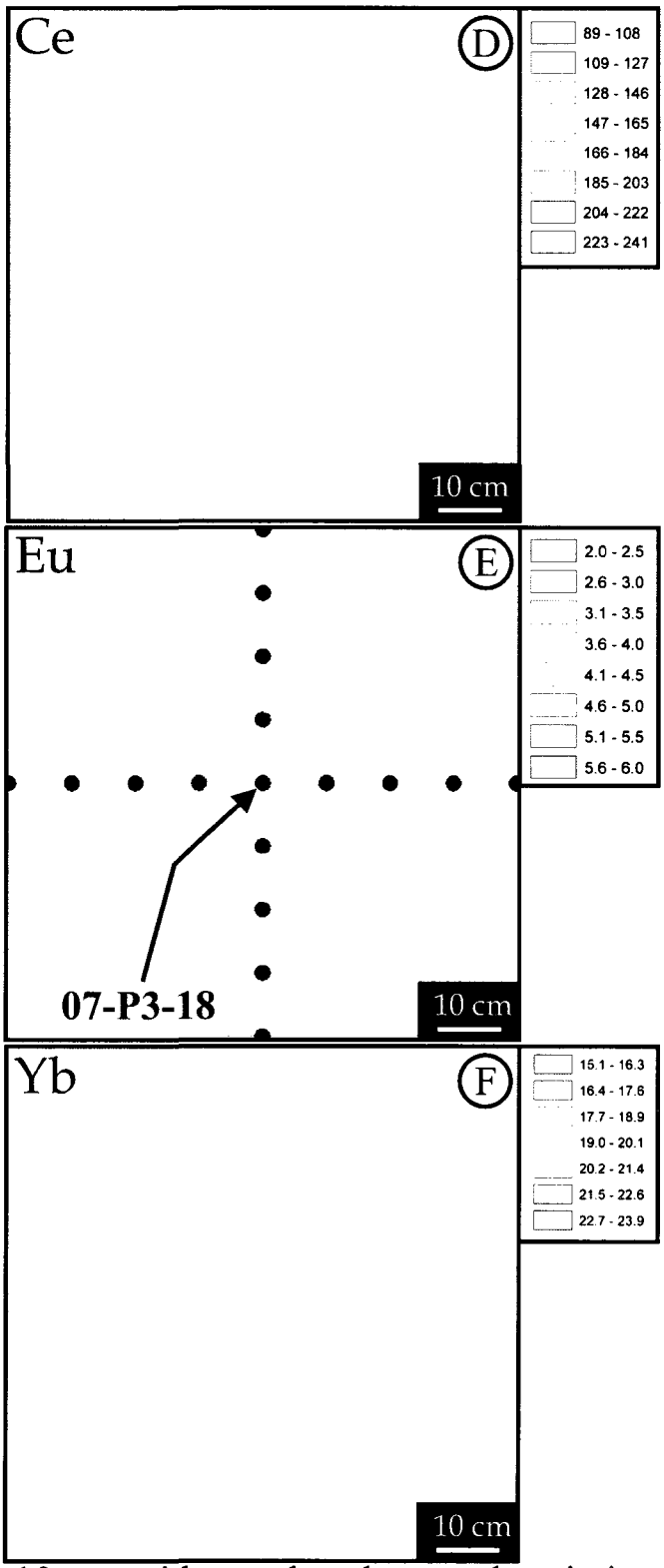

Figure 4.8: 10 cm grid samples elemental variation continued. D) Cerium ppm. E) Europium ppm. F) Ytterbium ppm. Note grid center is sample 07-P3-18.

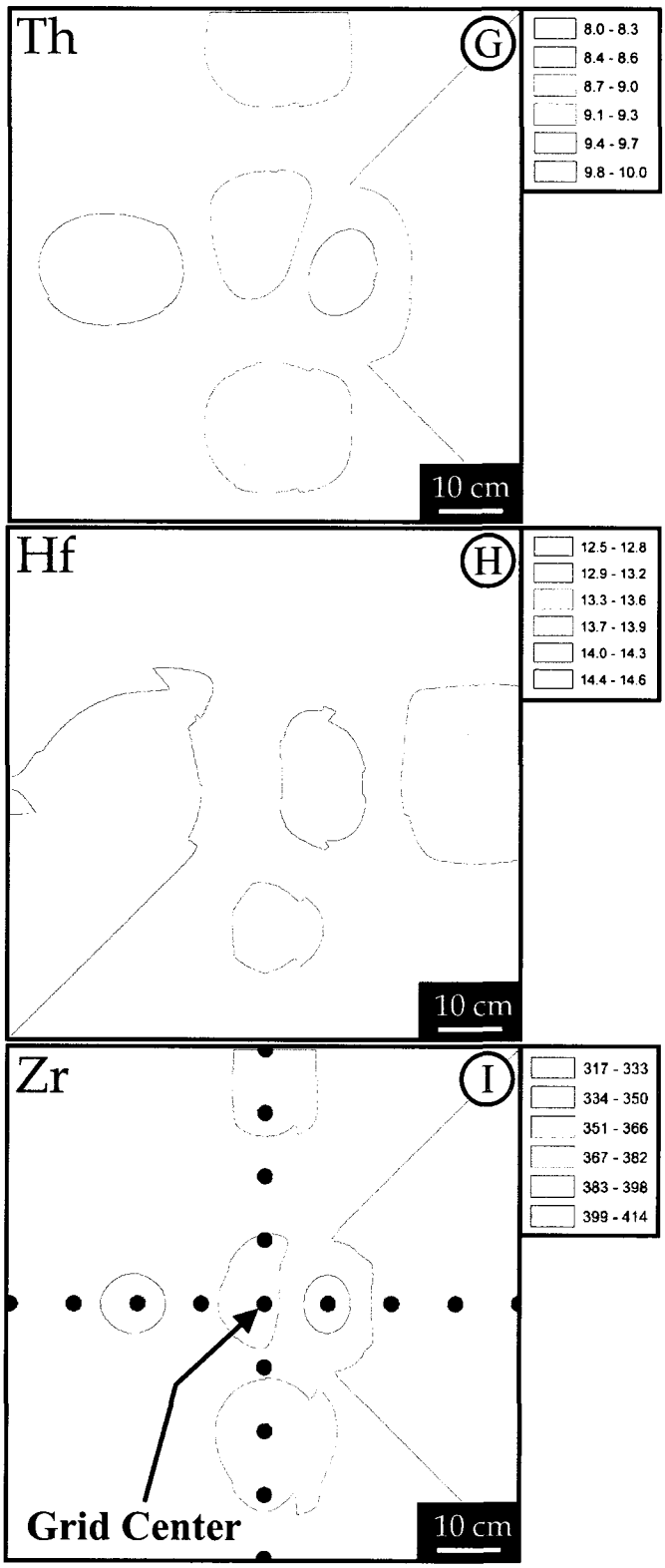

Figure 4.8: 10 cm grid samples elemental variation continued. G) Thorium ppm. H) Hafnium ppm. I) Zirconium ppm.

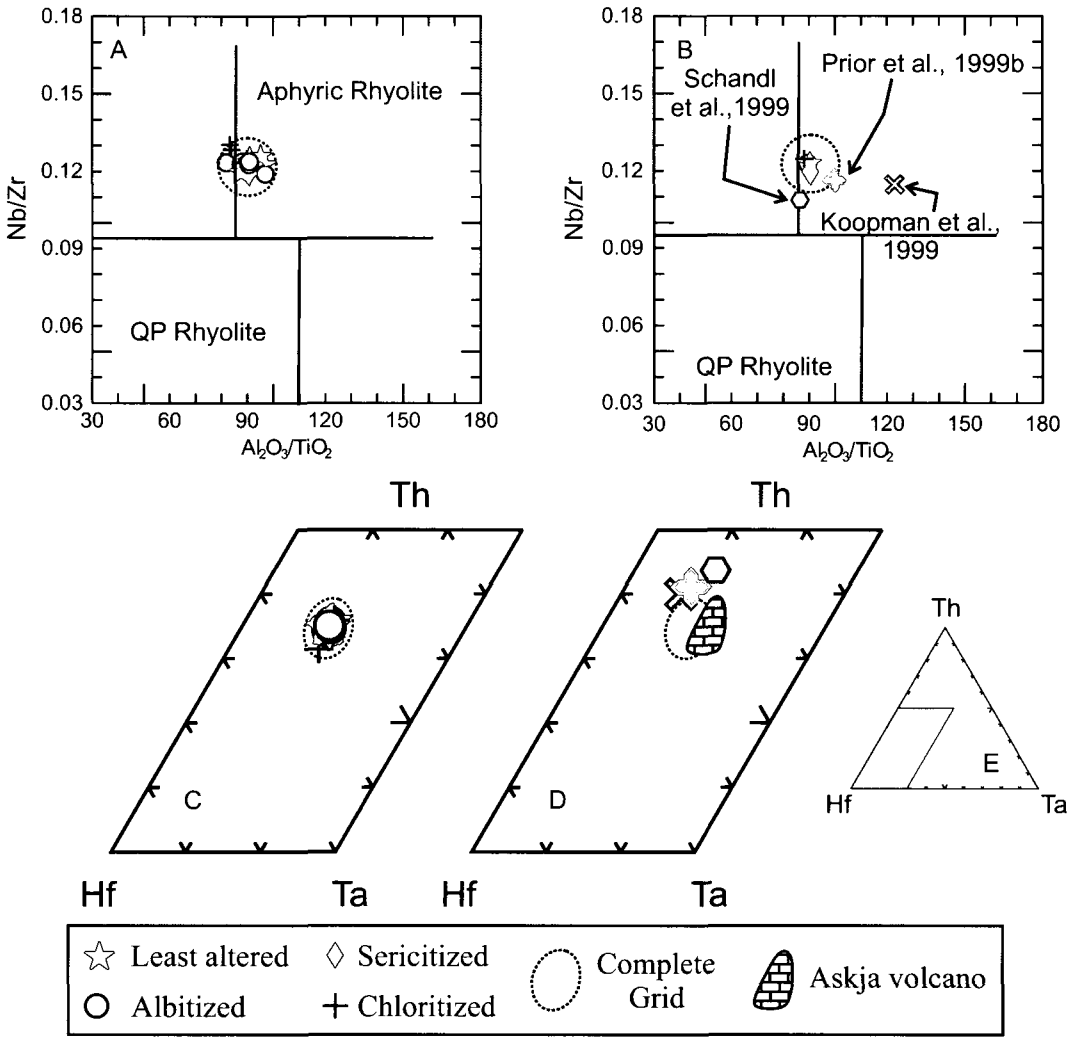

Figure 4.9: A. Nb/Zr vs. Al_2O_3/TiO_2 discrimination diagram of Prior (1996; Prior et al., 1999) showing all grid samples. B. Comparison between Kidd Creek studies and this study. Grey field contains all grid samples. C. Portion of ternary diagram (E) containing all grid samples. Axis ticks indicate 10 percentiles. D. Same field as (C), grid data field (grey) compared to the published studies (symbols as in B) and Askja volcano, Iceland (from Schandl and Gorton (2002). E. Portion of the ternary plot in C and D. Error bars are smaller than the symbols.

rhyolites and as shown in Chapter 2 and they correlate with the stratigraphy at Kidd Creek one expects them to plot within the aphyric field. Indeed, all but three samples fit into the aphyric field (Fig. 4-9A), indicating that they are part of the lower member rhyolites. Comparing the rocks of this study with those of Prior et al., (1999), Schandl et al., (1999) and Koopman et al., (1999) it is clear that there is general consistency between the average of the least altered rhyolites from each study (Fig. 4.9B). Although Schandl et al., (1999)'s average least altered rhyolite plots nearly out of the field, as noted above, this may be due to the fact that Schandl et al., (1999) include only one coherent lava sample while the other three samples are sericitized rhyolitic tuffs. Koopman et al., (1999)'s average least altered composition plots almost in the center of the field and upon examination of their least altered sample it contains 2.72 wt % K_2O and only 2.09 wt % Na_2O indicating it is closer geochemically to the sericitized group of this study.

Using error propagation techniques (see Appendix A.3 for calculations) for the components of the discrimination diagram of Prior (1996; Prior et al., 1999a) the error in the Al_2O_3/TiO_2 ratio is ± 1.1 and in the Nb/Zr ratio is ± 0.0086. This is important as the 2σ error bars for individual samples are smaller than the data symbols on the plots (Fig. 4-9A, B and Fig, 4-10). The variation among the samples has been qualitatively delineated by means of a circle which circumscribes the lithogeochemical variation at the centimeter to meter scale. Conceptually the size of this circle encapsulates the lithogeochemical variation due to inhomogeneities and alteration in any given sample of rhyolite.

On the ternary diagram of Schandl et al., (1999) the grid samples (Fig. 4-9C) plot lower than those of the Kidd Creek studies (Fig. 4-9D). Figure 4-9D includes data of the average least altered 21 samples of the Kidd Creek studies as well the field of 22 samples from the Prosser township rhyolites. The addition of this study's results to those of the Kidd Creek studies form a trend between ~30 and ~45 % along the Th and Hf axis. This trend is congruent with the Askja field of Schandl and Gorton (2002, and references therein).

4.3 Geochemistry of rhyolitic stratigraphy in Prosser Township

4.3.1 Classification and identification of rhyolite

Some aphyric rhyolites of this study plot in the quartz-porphyritic (QP) rhyolite field (Fig. 4-10A) within the Nb/Zr vs. Al_2O_3/TiO_2 rhyolite discrimination diagram of Prior (1996). This misidentification also occurs for the brecciated rhyolitic lobes (Samples 07-P3-12, 13; Fig. 4-10B) and the coherent rhyolitic lobes (Samples 07-P3-3, 4, 6; Fig. 4-10C). The tuffaceous samples of the pumice- and spatter-rich tuff breccia also plot in the QP rhyolite field (e.g. Sample 07-P3-5; Fig. 4-10D). Overall the rhyolites, except those described or interpreted to be late intrusive phases based on petrography and field relationships, plot within their expected fields. The aphyric rhyolite samples from this study that plot in the quartz-porphyritic field have been described as rhyolitic dykes (Samples 43, 45) or as either coherent (Samples 3, 6) or brecciated (Samples 4, 12, 13) lobes within the tuffaceous units between the rhyolite coulées. In all of these three cases the petrography (Chapter 3) shows that they are heavily altered and are chlorite-rich relative to the lesser altered quartz-porphyritic unit that caps the sequence. This relatively extreme alteration has led to the misclassification of these rhyolites as aphyric rhyolites in the field.

Removing the above samples there are two true outliers using this classification scheme, samples 41 and 48. Sample 07-P2-41 comes from a poorly exposed flow-banded rhyolite at the southern extreme of Prosser Outcrop 1 (Fig. 2.3). This may very likely be a large rhyolite dyke similar to the thin rhyolite dykes (samples 07-P2-43A-B and 07-P2-45) just underlying it. Sample 07-P2-48 however is a block within a block-bearing tuff which separates two flow banded rhyolite coulées. The rhyolitic block (07-P2-48) lies within a tuff that has a matrix (07-P2-49) and other blocks (07-P2-47) which plot well within the aphyric rhyolite field (Fig. 4-10B, C). It has been interpreted that this unit was produced by a dome collapse event and therefore it likely incorporated an accidental lithic clast thus providing a possible explanation for the compositional mixing of aphyric and quartz-porphyritic rhyolites.

The stratigraphy between coherent rhyolites is composed of units that are non-descript and described as brown tuffs. In Figure 4-10D the tuffaceous units plot adjacent

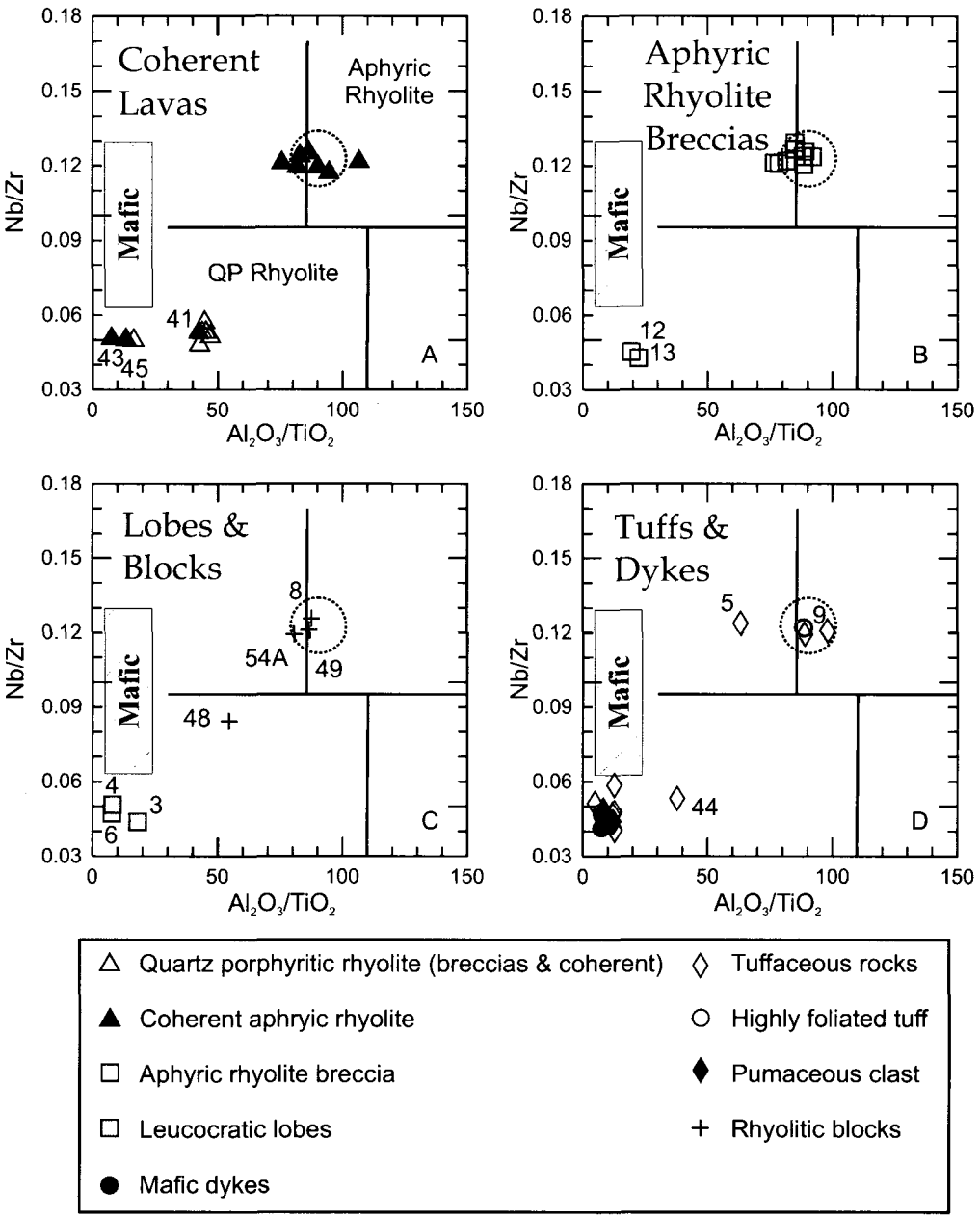

Figure 4.10: Nb/Zr vs. Al_2O_3/TiO_2 rhyolite discrimination diagram of Prior (1996; Prior et al., 1999a) A. Coherent aphyric and quartz porphyitic lavas. B. Rhyolite flow breccias from flows in A. C.Leucocratic lobes and rhyolitic blocks. D. Tuffaceous units from all brown tuffs and the pumice- and spatter-rich tuff breccia. The highly foliated tuff and mafic dyke samples are also present. Aphyric and QP rhyolite fields are labeled in A and diagonally striped field (Mafic) is the mafic volcanic field of Prior et al., (1999a). 2-sigma error in analysis is smaller than the data points. Grey circle is a qualitative estimate of the inter-sample variation at the cm to m scales.

to the coherent rhyolites (Fig. 4-10A), away from the mafic volcanic field of Prior et al., (1999a). This association with the coherent rhyolites strongly suggests that these are indeed rhyolitic tuffs. The pumice- and spatter-rich tuff breccia that underlies the quartz-porphyritic rhyolite at the top of this stratigraphy has a similar lithogeochemical signature to the quartz-porphyritic rhyolite and not that of the underlying aphyric rhyolite. This would imply that the quartz-porphyritic rhyolite magma erupted very explosively before producing the effusive quartz-porphyritic rhyolite. The mafic dykes plot with the pumice- and spatter-rich tuff breccia samples, the intrusive coherent lobes and the quartz porphyritic rhyolite. This association will be discussed further with the REE lithogeochemistry in section 4.3.2.

On the Hf-Th-Ta ternary diagram the same association between some of the aphyric rhyolites with the quartz-porphyritic coherent lavas is shown (Fig. 4-11A), note 7 of 11 samples of the aphyric rhyolite stack within the grid rhyolite field (grey shaded field). With the addition of the coherent and brecciated intrusive lobes, the compositional spectrum between aphyric and quartz-porphyritic rhyolites is in-filled (Fig. 4-11B) but not extended. However, the tuffaceous samples (Fig. 4-11B) extend the trend towards the Hf apex. Although there is no simple stratigraphic evolution in this space, there appears to be an overall trend parallel to the Th and Hf join. This trend is not displayed at Kidd Creek (Fig. 4-11D; striped field) from the data of Schandl et al. (1999).

4.3.2 Rare earth element lithogeochemistry

The rare earth elements have long been used to infer the tectono-magmatic affinity of magmas. The Prosser Township lavas (Fig. 4-12) show a tholeiitic trend typified by a relatively flat REE pattern. The grid aphyric rhyolite samples have been plotted in Figure 4.12A for comparison of the mobility of an aphyric rhyolite at the deci-meter and meter scales (see also Fig. 4.5B). Within the grid samples one can see that the average least altered, ablitized and chloritized samples have near identical patterns and concentrations. The sericitized samples show significantly lower LREE concentrations at around 150-200 times chondrite compared with 300 times chondrite in the least altered samples. The sericitized samples have lower HREE contents but are around 100 times chondrite compared with 120 times chondrite in the least altered samples. Despite the

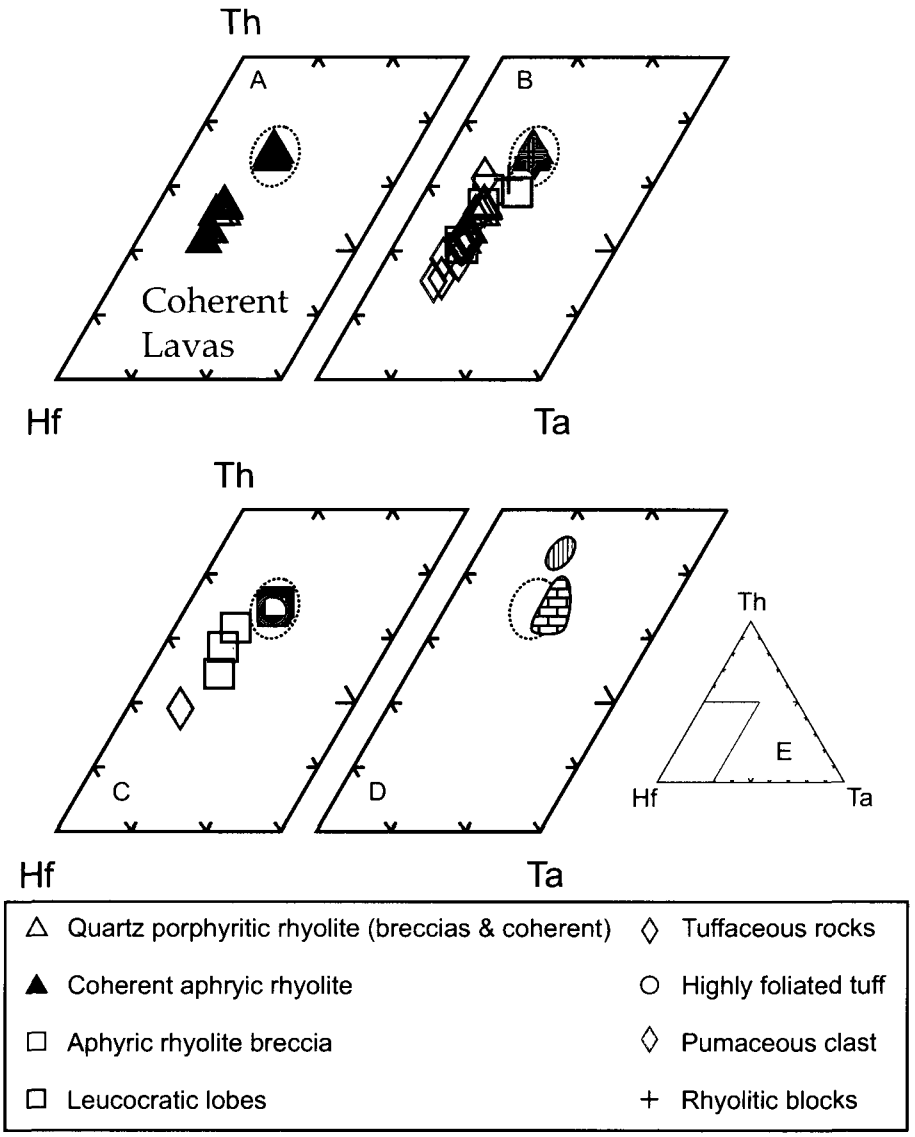

Figure 4.11: Hf-Th-Ta ternary diagram. A. Coherent quartz-porphyritic and aphyric lavas. B. Coherent lavas brown tuffs, leucocratic lobes and rhyolitic blocks. C. Aphyric rhyolite breccia, pumaceous and highly foliated tuff samples. D. Grid samples in shaded grey, Askja Volcano, Iceland in brick pattern and Kidd Creek deposit data from Schandl et al., (1999) in vertical stripes. E. Portion of ternary diagram in A-D.

strong agreement of average analyses, the grid samples show a wide variation in REE patterns at the meter scale ranging from 125-425 times chondrite in the LREE and 80-160 times chondrite in the HREE. This variation is greater than the range shown for all other aphyric (Fig. 4.12B) and quartz-porphyritic (Fig. 4.12C) lavas sampled across the outcrops for this study. The greatest variation within the grid samples is shown graphically in Figure 4.8 where the great difference is found between samples 10 cm apart! Nonetheless the overall REE profile does not change and can therefore be used to interpret tectonomagmatic affinity.

Both coherent aphyric (Fig. 4.12B) and quartz-porphyritic (Fig. 4.12C) rhyolite have moderate slope in the light REE, moderate Eu anomaly and flat heavy REE around 90 times chondrite. These patterns are very similar to those published rhyolites of Koopman et al., (1999), Schandl et al., (1999) and Prior et al., (1999b). Two coherent rhyolites aphyric samples are anomalous; 07-P2-43 and 07-P2-45. Sample 43 was described as an aphyric leucocratic dyke in the field and sample 45 has been heavily altered. The trend of these two samples is similar to the overlying rhyolites except is ~30 and ~50 times chondrite and therefore these results are interpreted to be attributed to dilution.

The associated breccia samples show similar trends and concentrations to their coherent counterparts (Fig. 4.12D). There are two samples (07-P3-12 and 07-P3-13) which do not follow this trend. Both of these samples come from a mineralized brecciated leucocratic lobe interpreted to be an intrusive lobe. Sample 12 is a lenticular leucocratic breccia which is amygdaloidal and appears to be a late phase unrelated to the adjacent coherent aphyric rhyolite. The sample 12 breccia has distinctive "V" trend indicative of major REE redistribution. Sample 13 is a mineralized matrix of sample 14, a brecciated aphyric lobe, both lobe and matrix have identical signatures but the matrix is 80 times chondrite relative to the clast which is 200 times chondrite. Therefore the differences in total REE concentrations are interpreted to be purely the product of dilution.

The pumice- and spatter-rich tuff breccia samples (Fig. 4.12E) have relatively flat REE patterns, weak Eu anomalies and plot between 20 and 70 times chondrite. The flat profile parallels the overlying quartz porphyritic but lacks the strong Eu anomaly. Given

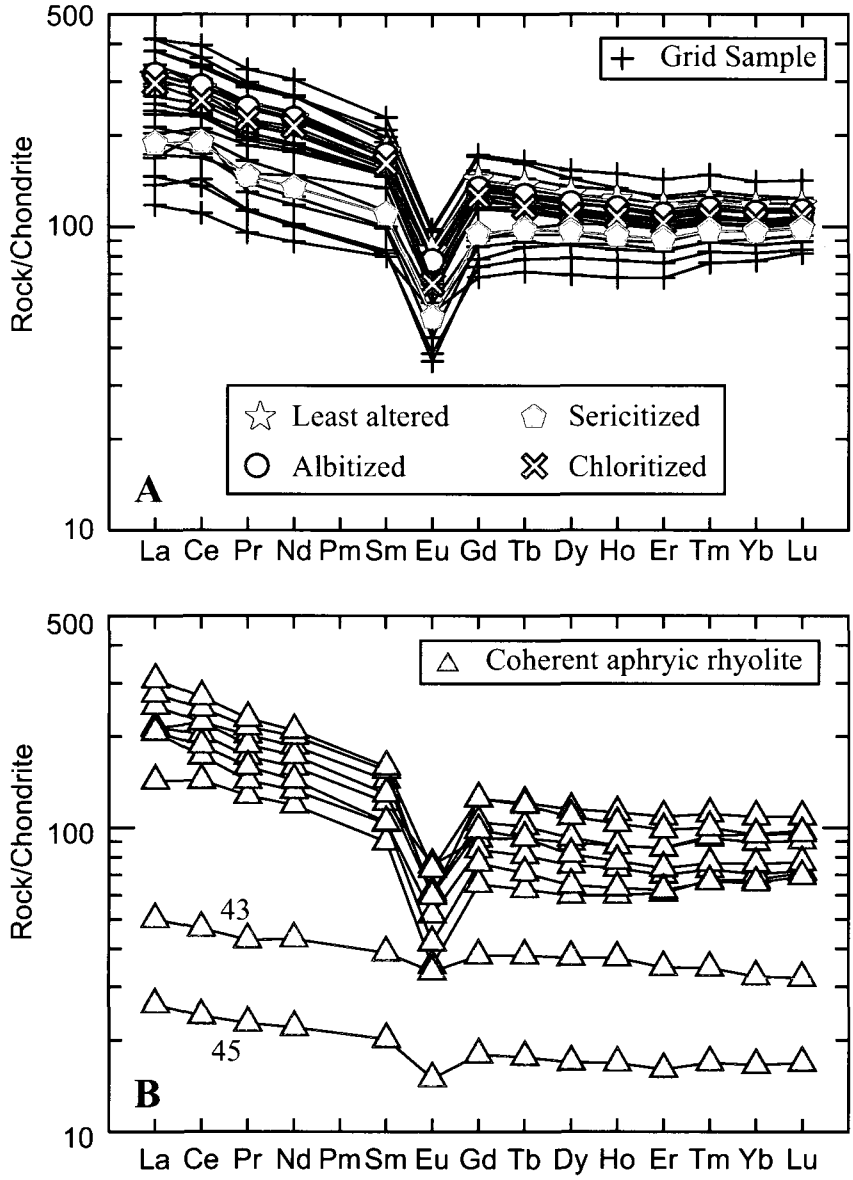

Figure 4.12: Rare earth element plots normalized to Sun and McDonough (1989). A) Average least altered sample, average ablitized, average sericitized and the chloritized sample. Each '+' is a grid sample. B) Coherent aphryic rhyolites. Samples 07-P2-43 and 07-P2-45 are rhyolitic dykes near the stratigraphic top of Outcrop 1.

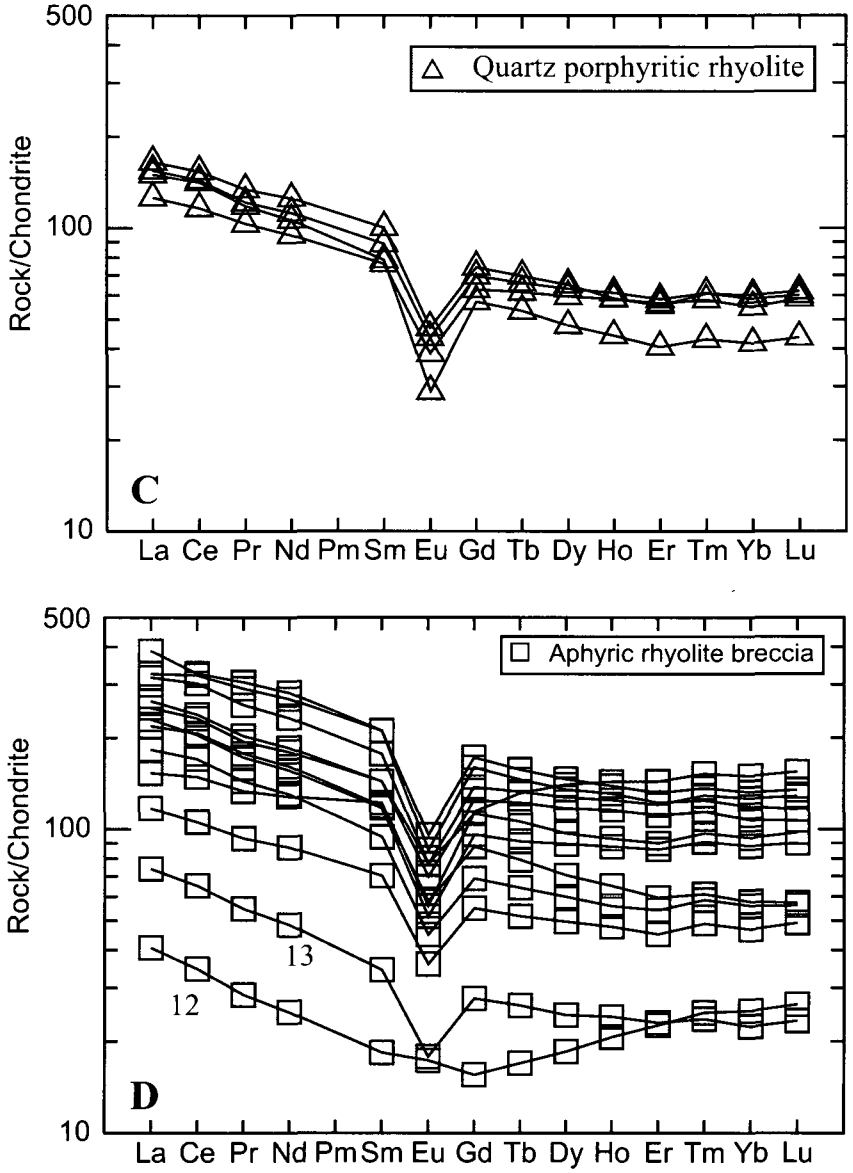

Figure 4.12: Rare earth element plots normalized to Sun and McDonough (1989) continued. C) Coherent quartz-porphyritic rhyolite samples. D) Brecciated aphyric rhyolite samples. Samples 07-P3-12 and 07-P3-13 come from a mineralized brecciated lobe-like intrusive in Outcrop 2.

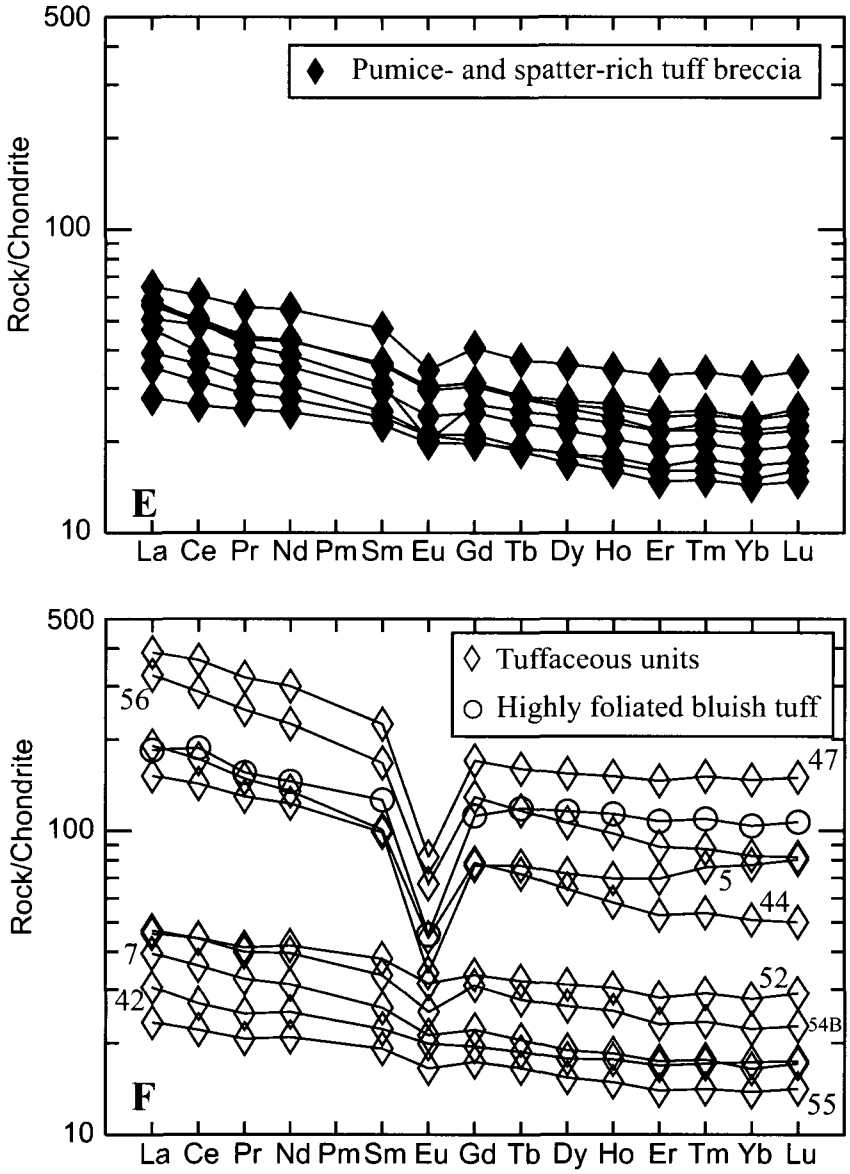

Figure 4.12: Rare earth element plots normalized to Sun and McDonough (1989) continued. E) Pumice- and spatter-rich tuff breccia samples. F) Brown tuffaceous unit samples and the highly foliated bluish tuff. Number adjacent to trend are the sample number suffixes.

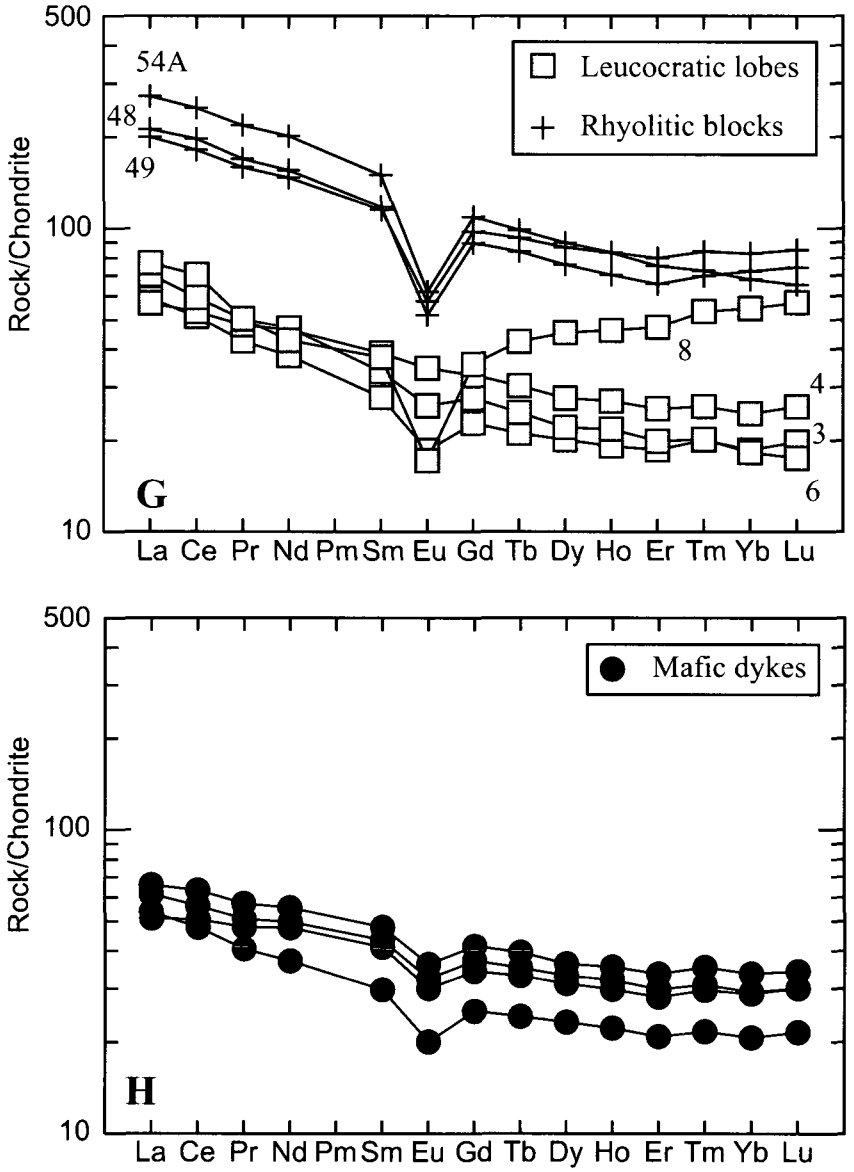

Figure 4.12: Rare earth element plots normalized to Sun and McDonough (1989) continued. G) Late intrusive rhyolite which includes well defined leucocratic lobes and other less well characterized fragmental rocks from with the brown tuffaceous units. H) Mafic dyke samples.

the extreme variation in total REE concentrations displayed here it is suggested that the tuff breccia has suffered the affects of dilution. This interpretation is further justified by the abundance of matrix chlorite which is also found filling the porosity of the pumice and spatter clasts. The similarity with the quartz porphyritic rhyolite and intermediate REE concentrations suggest that this is an intermediate if not acidic rock. Furthermore this rock is relatively coarse and is therefore has been the most diluted of all units. Moreover the HFSE data clearly show its rhyolitic nature (Fig. 4.10D). The pumice and spatter clast compositions have been independently confirmed by Grogan (2009).

The brown tuffaceous units (Fig. 4.12F) appear to have a bimodal distribution. The first population (07-P3-5, 07-P2-44, 07-P2-47 and 07-P2-56) has an identical trend to the adjacent coherent aphyric rhyolites and therefore these samples represent rhyolitic tuffs. This result is consistent with the interpretation of the HFSE element plots above. The second population has a relatively flat REE profile between 25 and 50 times chondrite (Samples 07-P3-7, 42, 52, 54B and 55). This second group includes a vesicular tuff (07-P3-7) adjacent to an intrusive lobe (07-P3-6) and samples 07-P2-52 and 07-P2-54B which are tuff samples adjacent to a lenticular breccia which has formed a peperite. Samples 07-P2-42 and 07-P2-55 were taken from a poorly exposed area of Outcrop 1. Given the close association between the tuff samples, the peperite and brecciated intrusive lobes these samples are interpreted to be contaminated with intrusive fragmental material and do not accurately represent the tuff from which they were derived. Furthermore the low REE contents of these samples are similar to the concentrations within the coherent intrusive lobes (07-P3-4 & 07-P3-6) described below.

The leucocratic lobes, samples 07-P3-3, 07-P3-4 and 07-P3-6 (Fig. 4.12G) well defined leucocratic aphyric lobes that have a moderately sloped REE profile starting around 70 times chondrite. These lobes are comparable to the intrusive lobe-associated group of tuffaceous units and the pumice- and spatter-rich tuff breccia although they have slightly higher LREE contents. There is one exception (07-P3-8) within the lobe samples which has a distinct "v-shaped" REE pattern and appears to be heavily enriched in the HREE.

The rhyolitic blocks include samples 07-P2-48, 07-P2-49 and 07-P2-54A (Fig. 4.12G) which come from block-bearing tuff in Outcrop 1. These blocks all have typical

aphyric rhyolite REE signature seen above which confirms their association with the adjacent coulées.

Finally, the mafic dykes (Fig. 4.12H) have similar REE trends to the late intrusive lobes and the pumice- and spatter-rich tuff breccia described above. The dykes have a relatively flat REE profile with a small Eu anomaly and plot between 50 and 70 times chondrite. The REE trend and overall concentration of the mafic dykes largely overlaps the tuff breccia, the tuffaceous units and the leucocratic lobes but have a LREE slope that is intermediate between the tuffs and leucocratic lobes. There are therefore two simple explanations of the REE signature of these mafic dykes: 1 – the dykes have been overprinted by redistribution of the REE from the host volcanoclastic rocks, or; 2 – the mafic dykes are more intermediate in composition, or a combination of these two explanations. The fact that there is a large overlap in their REE patterns while a stark contrast in the field description exists suggests that the lithogeochemical signature of these thin dykes and their host rocks have been homogenized.

4.4 Lesher et al.'s geochemical exploration tool

Lesher at al. (1986) were the first to compile data showing the favorable association between FIII-type rhyolites and Cu-Zn-Pb volcanic associated massive sulfide deposits within the Superior Province. A similar classification was proposed by Barrie et al. (1993). The classification by Lesher et al. (1986) was subsequently modified by Hart et al. (2004) who further discussed the petrogenesis of each of the rhyolite types. The FIIIb-type rhyolite variety, as found at the Kidd Creek deposit, has flat REE patterns, high silica content (67-84 wt %), high Y content (72-238 ppm), low Zr/Y ratio (1.7-6.2), high Yb content (5-32 ppm), low normalized La_N/Yb_N (1.1-4.9) and a large negative Eu* anomaly (Eu* = 0.20-0.61). The FIIIb-type ryolite is thought to be formed from high-temperature, low-pressure partial melting of tholeiitic basalts at shallow depth (Lesher et al., 1986).

In Table 4-5 the classification of Lesher et al., (1986) as summarized by Hart et al., 2004 has been compared to the chemistry of the aphyric grid rhyolite and both quartz-porphyritic and aphyric rhyolites of Prosser Township. The overall rhyolite

Table 4-5: Exploration vectoring tool criteria for FIIIB rhyolites of Prosser Township (Hart et al., 2004 after Lesher et al., 1986)

Criterion[1]	Data from Hart et al., 2004					This Study			
	FI	FII	FIIIa	FIIIb	FIV			FIIIb	
Lithology	Dacite-rhyolite	Dacite-rhyolite	Rhyodacite-high silica rhyolite			Totals	Grid Range	Coherent Aphyric Rhyolites	Coherent QP Rhyolite
SiO_2 (wt %)	64-72	64-81	67-78	67-84	69-81	43-83	73-81	43-83	72-79
TiO_2 (wt %)	0.16-0.65	0.16-0.89	0.21-0.99	0.09-0.73	0.09-0.57	0.09-1.51	0.11-0.15	0.09-1.51	0.23-0.30
Y (ppm)	6-31	11.73	25-96	72-238	18-63	29-243	103-243	29-180	70-97
Zr/Y	8.8-31	3.2-12.1	3.9-7.7	1.7-6.2	0.67-4.8	1.6-6.7	1.6-3.3	1.6-3.8	4.2-6.7
Yb (ppm)	0.43-3.8	1.3-7.9	3.4-9.3	5-32	1.5-8.4	2-24	13-24	2-18	7-10
$[La/Yb]_{cn}$	5.8-34	1.7-8.8	1.5-3.5	1.1-4.9	0.22-2.1	1.42-3.85	1.42-3.85	1.44-3.09	2.13-3.35
Eu/Eu*	0.87-1.5	0.35-0.91	0.37-0.94	0.20-0.61	n.d.	0.43-0.88	0.45-0.71	0.43-0.88	0.43-0.56

[1] $_{CN}$ = chondrite normalized to the values of Nakamura (1974); Eu/Eu* calculated by linear interpolation between chondrite-normalized Sm and Gd

characteristics of Prosser Township fit within the limitation of an FIIIb rhyolite although some have a higher concentration of TiO_2, a larger negative Eu anomaly and cover a slightly larger range of Y concentrations. The large REE and Y mobility presented above can easily cover the small differences between the classification scheme and the Prosser Township rhyolites. It should be noted here that the variation present in the one rock represented by the grid samples represents a large portion of the allowable ranges covering over half of the range of the SiO_2, Y, Yb, $[La/Yb]_{CN}$ and Eu* contents of the Lesher et al., (1986) classification scheme. Nonetheless the ranges of this classification are sufficient to allow for the variation in element concentrations presented above and therefore it continues to be a useful way to discriminate between favorably associated and unfavorable rhyolites hosting Cu-Zn-Pb volcanic massive sulfide deposits.

4.5 Summary

The detailed petrography of the grid rhyolites shows that they have been variably altered from an originally glassy phenocryst-poor perlitic rhyolite to various combinations of chloritized, sericitized and albitized metavolcanic rocks. The affects of chemical alteration on the rhyolites can be minimized by taking samples which have primary textures such as perlitic fracturing and hyaloclastite zones that are preserved almost exclusively in quartz. Given this the least altered protolith lithogeochemistry presented here robustly represents the protolith composition (Table 4-1) of an aphyric rhyolite in Prosser Township.

The mobility of major and trace elements occur as independent phenomenon and although there is an association between sericitization and trace element abundances there is no observed consistency between them nor is there any reason why this would be the case. The processes responsible for mobilization of these elements are poorly understood. However the presence of synchysite, gerenite, iimorite and polycrase has been documented for the first time here providing the Prosser Township rhyolites as an excellent candidate for understanding these mechanisms.

Despite the variations in major elements, they are useful to discriminate the major alteration phases. The coulée studied here has three main alterations which include

albitization, sericitization and chloritization. The albitized samples closely resemble the least altered rhyolites except they contain more albite. Chemically least altered and albitized are indistinguishable although the albitized samples generally have SiO_2 contents in excess of 78 wt. %. Albitization is inferred to be the result of recrystallization of a primary glass. Sericitized samples are easily distinguishable from least altered samples as they contain K_2O contents greater than ~1.0 wt. % and Na_2O contents below ~4.0 wt. %. The major element chemistry of the chloritized sample plots between the two above groups but displays very little variation within the REE and HFSE and therefore reflects the protolith trace element chemistry. Chloritization was a major alteration within the volcaniclastic rocks however; constantly shows wide variation in total REE concentration but does not change the REE profile suggesting that chloritization is the cause of the dilution of the tuffs lithogeochemical signatures.

The variability exhibited by the REE cover a large portion of the classification scheme of Lesher et al., 1986) and therefore it remains a useful tool. The presence of HFSE bearing minerals may explain these trace element variations however element mobility should be tested locally to assure the accuracy of future studies. Regardless of the drastic mobility seen here, the REE profiles remain relatively intact and can therefore be used reliably to assess the tectono-magmatic affinity of these lavas. Furthermore the HFSE have shown very little mobility (<10%) and preserve a chemostratigraphic evolution within Prosser Township. Building on the framework established here, the continuity of the stratigraphy may be used to extend the stratigraphy into adjacent townships using the Hf-Th-Ta diagram developed by Schandl et al., (1999). Given the limited sampling, Kidd Creek would be prime candidate to fully test whether or not this magmatic evolution is consistent as it is not shown by the data of Schandl et al., (1999).

Chapter 5 – Zircon Thermometry

5.1 Introduction

Barrie (1995) has applied the zirconium saturation thermometer of Watson and Harrison (1983) to the classification scheme of Lesher et al., (1986; see Chapter 4) and demonstrated that the FIIIb rhyolites at Kidd Creek originated from a source that was likely 840-940°C. Barrie (1995) concluded that >90 % of VMS mineralization is associated with rhyolites that have high zircon saturation temperatures. Barrie (1995) further states that high temperature melts are generally depolymerized lavas and can therefore accommodate higher contents of incompatible elements. The results also have implications for the nature of pyroclastic rocks, and the morphology of coherent volcanic facies as temperature is an important factor affecting viscosity. Barrie (1995) inferred that because of the high temperatures that welding was more likely in the vent proximal facies and that the formation of coherent flows was also enhanced. Hart et al., (2004) have further used the thermal constraints of Barrie (1995) to assess their petrogenetic model.

The rhyolite coulées of Prosser Township are quite thin (~10 m) in comparison to many other modern rhyolite coulées in Idaho, USA (Manley, 1996), Ponza, Italy (Scutter et al., 1998) and at Noranda, Québec (de Rosen-Spence, et al., 1980). To test the hypothesis that their slender nature resulted from eruption at or above their liquidus as inferred by Hart et al., (2004 and references therein) we have employed both the traditional zircon saturation thermometer and a new titanium-in-zircon thermometer to measure the temperatures of formation of the zircons.

5.2 Zircon saturation thermometer

The Watson and Harrison (1983) zircon saturation thermometer uses, among other parameters, the whole rock zirconium content and the distribution coefficient (see Appendix A.4 for zircon analyses) between zirconium in zircon and the melt, D_{Zr}. It also uses a melt composition parameter, M, which is the molar ratio [(Na + K + 2Ca) / (Al * Si)]. Watson and Harrison's experiment led them to describe the following relationship (Equation 1) between zirconium saturation and temperature (T) (usually in the source region of the melt; Watson and Harrison, 1983):

$$\ln D_{Zr}^{zircon/melt} = \{-3.80 - [0.85(M - 1)]\} + 12900/T \quad (1)$$

The ability of the melt to become saturated in Zr is dependant on many factors most importantly, the composition of the melt.

The application of the zircon saturation thermometer has inherent problems when applied to Archean rocks, which are invariably altered. The foremost problem is determining the melt composition parameter, M, because this requires knowing the protolith composition of the highly mobile elements, Na and K. For instance, Prior et al. (1999a, Table 4) reported high variability for Kidd Creek rhyolites, with K_2O variations up to 573% and Na_2O of 17%. The respective variations for this study are 2225% and 346%.

5.3 Titanium-in-zircon thermometer

Recently Watson et al. (2006) have improved upon the zircon thermometer developed by Zack at al., (2004) introducing the widely applicable titanium saturation-in-zircon thermometer. This uses solely the titanium content of the zircon to derive a crystallization temperature for the zircon via the relationship (Equation 2):

$$T(^\circ C)_{zircon} = \frac{5080 \pm 30}{(6.01 \pm 0.03) - \log(Ti)} - 273 \quad (2)$$

Where Ti is the concentration of titanium in ppm. Titanium is a relatively immobile element and zircon is a refractory mineral thus one expects the technique to be more robust than the original zirconium saturation thermometer of Watson and Harrison (1983). The titanium saturation-in-zircon thermometer requires coexistence of rutile and zircon within the sample which permits the assumption that the activity of titanium is equal to 1 ($\alpha_{TiO2} = 1$). Rutile has not been observed in the Prosser Township rhyolite samples. However, Watson and Harrison (2005) state that if the presence of rutile can not be established, then the Ti-in-zircon temperatures values should be regarded as minimum estimates. In this study the presence of rutile has not been confirmed but may be present as an inclusion in zircon within the grid sample 07-P3-34 (see section 4.2.3). The petrography has also shown that throughout all of the many and varied types of alteration and deformation (including the highly-foliated tuff; Chapter 3: Fig. 3-2E, Fig. 3-4G), that

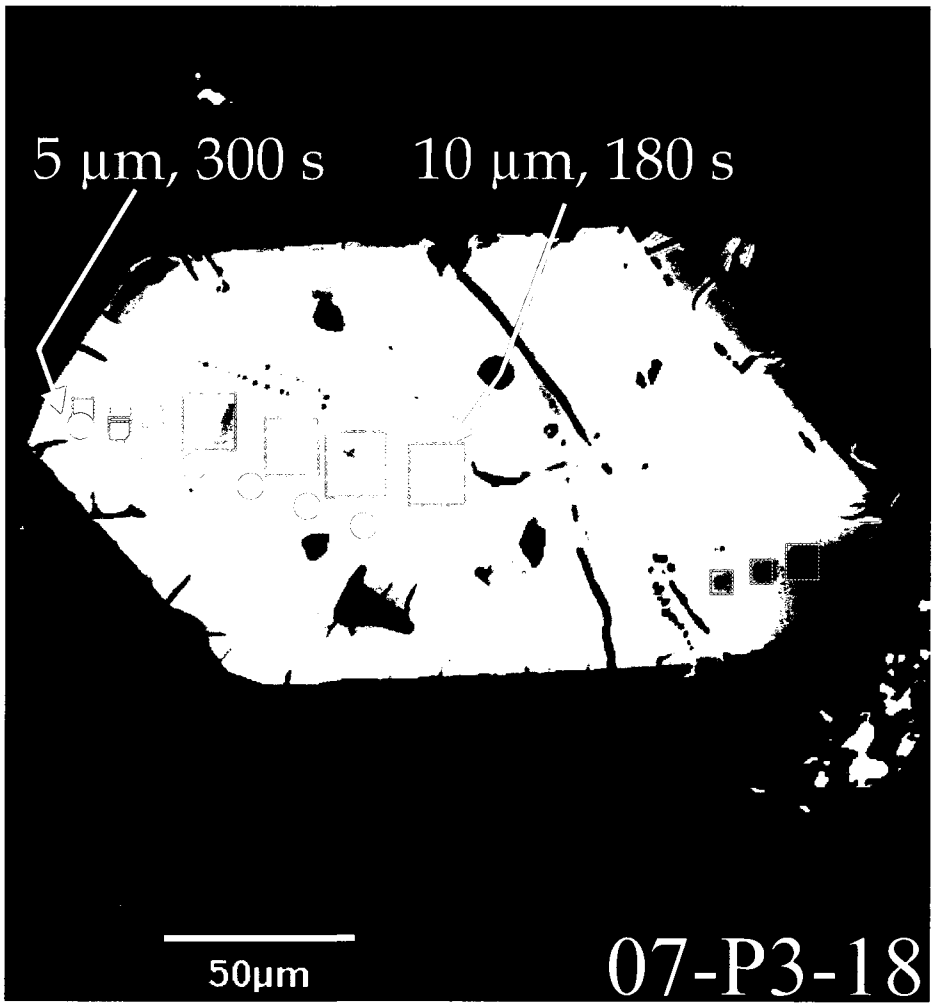

Figure 5-1: Zircon from aphyric rhyolite sample 07-P3-18. Note "burn" marks outline in dashed lines for a 10 µm beam width. Analyses for 180 s. A second series of analyses was tested to confirm the result that there was no titanium above the detection limit. The second set of analyses, white dots, were conducted with a 5 µm beam width and 300 s analysis count time. See Appendix A.5 for analysis results.

zircon is the only mineral phase that has been resistant to alteration. A variety of samples 07-P3-15, 07-P3-18, 07-P1-60 and 07-P1-83 were chosen for analysis by this method as their zircons are the most euhedral and interpreted to be primary igneous zircons. These samples constitute aphyric rhyolites from the flows of Outcrop 2 as well as both the aphyric and quartz-porphyritic rhyolite of Outcrop 3.

5.4 Analytical Methods

One of the major issues with the Watson et al., (2006) thermometer is that at low temperatures (<900°C) zircon will only contain ~50 ppm Ti. Consequently, in their study they used an ion microprobe in addition to an electron microprobe to determine the titanium concentrations. In this study a Camebax MBX electron microprobe, housed at Carleton University, department of Earth Sciences and National Institute of Science and Technology (NIST) standard glasses (SRM 610 and SRM 612) that have geometric mean Ti concentrations of 423 ppm and 47 ppm, respectively (Pearce et al., 1997), were used. In order to reduce analytical errors in the analyses, 3 of 4 spectrometers simultaneously measured titanium and the background spectrum in the zircon crystals with a focused beam at 15 kV accelerating potential and sample currents around 190 nA, for 180 or 300 s. Furthermore the three PET crystal spectrometers were used to measure titanium only and no other elements were analyzed, therefore the spectrometers did not move during the individual analyses. Concentrations were calculated from the average titanium counts measured by the three spectrometers. The analysis time was adjusted to 300 s once a zircon crystal was found with sufficient Ti (typically around 190 ppm Ti) to be measured reliably. The three spectrometers showed a good agreement in titanium concentration except at concentrations less than 20 ppm. The lower limit of detection was calculated as the average of 11 titanium analyses of four standards to be 26 ppm (Appendix A.5). Zircons which have less than 26 ppm Ti have been omitted from temperature calculations. Multiple spots within the same region of the zircon were measured using the specified analytical conditions for 180 and 300s to determine the precision of the results (Fig. 5-1).

5.5 Results

5.5.1 Ti-in-zircon thermometer

Of the eight zircons analyzed, only three contained titanium concentrations sufficient to be used in the calculation (see Appendix A.5 for lower limit of detection calculations and Appendix A.6 for the complete database of standard and sample analyses). One zircon crystal from sample 08-P3-18, (a least altered aphyric rhyolite) has an intermediate zone that crystallized at 1077°C. Near the rim this zircon has Ti concentrations (37 ppm) that yield a temperature estimate of 871°C ± 15° (Fig. 5-2A, B; Table 5-1). This zircon has concentric and sector zoning which complicates the interpretation. However, the rim analyses of this zircon, points 24 and 26, both have low concentrations of Ti, <26 ppm and 33 ppm, respectively. The two other zircons with sufficient Ti concentrations were found in the quartz porphyritic rhyolite (Sample 07-P1-83). One of these zircons shows a continuous concentric zonation surrounding a very high-temperature core >1100°C and a much cooler rim (~890°C; Table 5-1; Fig. 5-2C, D). This zircon (Fig. 5-2C, D) exhibits a cooling trend from core to rim. The second, larger zircon (Fig. 5-2E, F) shows a distinct oval core with a 20 μm euhedral overgrowth. The core grew at considerably hotter temperatures (>1060°C; Table 5-1) than a zone near the rim which grew at ~860°C. There is an abrupt transition from high temperatures in the core (Analysis 18; Table 5-1; Fig. 5-2F) to cool rim temperature estimates (~850°C; Table 5-1). The outer most rim analyzed at points 25, 26 and 28 (Fig 5-2F) contained Ti concentrations below the detection limit (26 ppm) suggesting that it grew at temperatures below 830°C.

Several other small zircons (<60 μm) from samples 07-P3-15, 07-P3-18, 07-P1-60 and 07-P1-83 (Appendix A.6) including the large zircon from 08-P3-18 in Fig. 5-1) were analyzed. However they contained titanium concentrations below the minimum limit of detection suggesting their growth occurred at temperatures below 830°C.

5.5.2 Zircon saturation thermometer

The three zircons found to have sufficient titanium to be used in the Ti-in-zircon thermometer (Watson et al., 2006) were subsequently used to estimate temperatures using the zircon saturation thermometer (Watson and Harrison, 1983). For this calculation the

Table 5-1: Titanium saturation of zircons containing titanium concentrations above the 26 ppm lower detection limit.

Sample	Zircon	Point[1]	Note[2]	Ti, Spec. 1[3]	Ti, Spec. 2[3]	Ti, Spec. 3[3]	Average Ti (ppm)	Temperature (°C)	+/- (°C:°C)
07-P3-18	1	23	int	0.004	0.003	0.003	33	858	14:14
07-P3-18	1	25	int	0.020	0.015	0.018	177	1077	19:18
07-P3-18	1	26	near rim	0.005	0.003	0.003	37	871	14:15
07-P1-83	1	9	light core	0.030	0.027	0.028	283	1155	20:21
07-P1-83	1	10	light core	0.022	0.021	0.021	213	1107	19:19
07-P1-83	1	11	outer core	0.009	0.008	0.008	83	969	16:17
07-P1-83	1	12	int	0.005	0.004	0.004	43	888	14:15
07-P1-83	1	13	near rim	0.003	0.002	0.001	b.d.	-	-
07-P1-83	2	15	int	0.004	0.003	0.003	33	858	14:14
07-P1-83	2	16	repeat pt. 15	0.003	0.003	0.002	27	837	13:14
07-P1-83	2	17	repeat pt. 15	0.004	0.005	0.004	43	888	15:15
07-P1-83	2	18	outer core	0.022	0.021	0.018	203	1099	19:19
07-P1-83	2	19	int core	0.017	0.017	0.014	160	1062	18:18
07-P1-83	2	20	int core	0.020	0.019	0.017	187	1086	21:19
07-P1-83	2	21	core	0.020	0.020	0.019	197	1094	20:19
07-P1-83	2	27	repeat pt. 20	0.014	0.013	0.012	130	1031	18:18
07-P1-83	2	8	repeat pt. 20	0.016	0.021	0.018	183	1083	19:19

[1] points for sample 07-P3-18 Line 3 and 07-P1-83 line 1 in Figure 5-2 (see Appendix A.5 for complete database); [2] int = intermediate zone within crystal;

[3] titanium concentrations from individual PET spectrometers in wt. %.

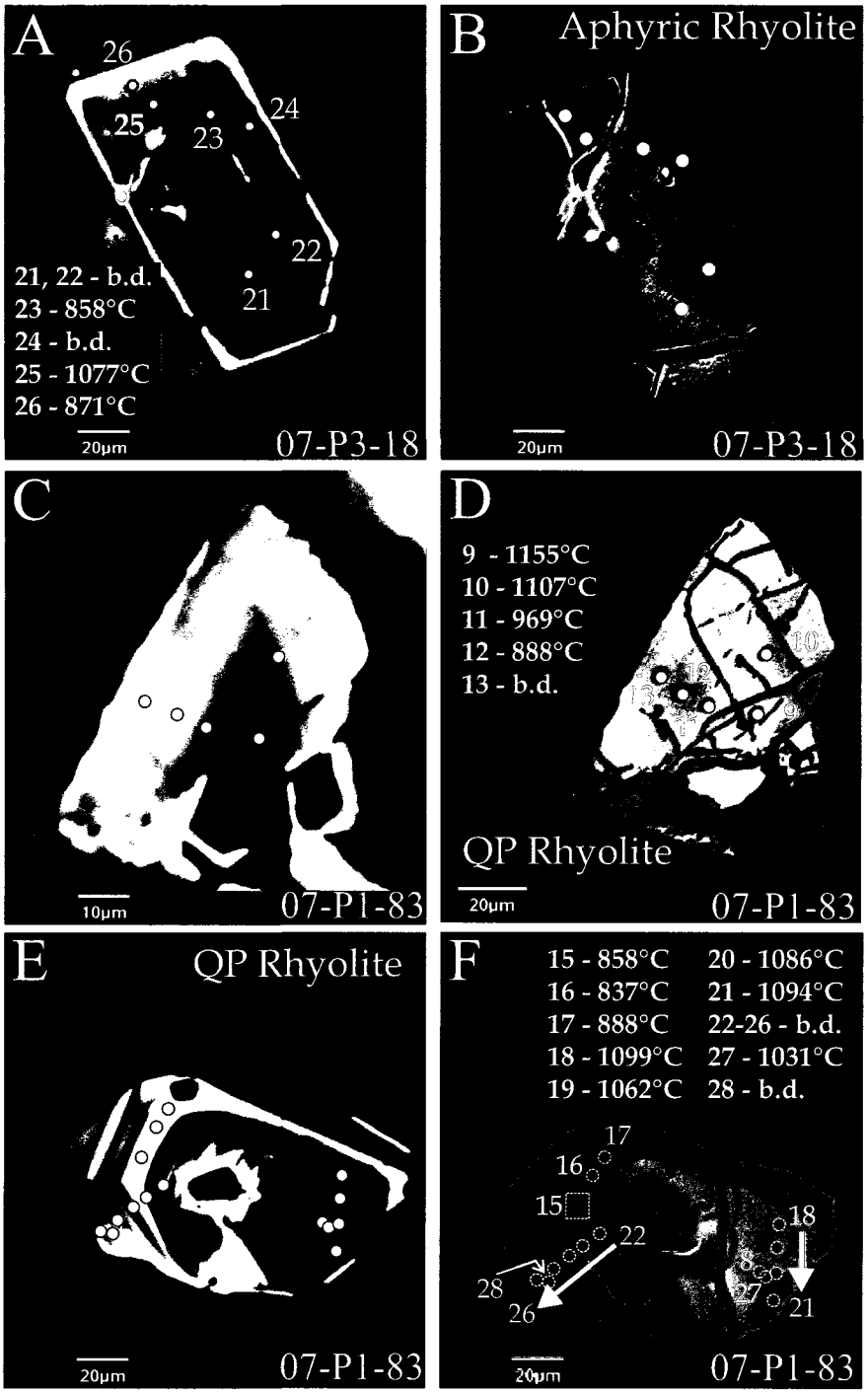

Figure 5-2: Ti-in-zircon saturation thermometry. A) Cathodoluminescences image of zircon from sample 07-P3-18 (b.d. = below detection limit) B) BSE image of zircon in A. C) Sample 07-P1-83. CL image of a zoned zircon. D) BSE image of zircon in C. E) CL image of zircon from sample 07-P1-83. F) BSE image of zircon in E. See Table 5-1 and Appendix A.5 for complete data.

concentrations of Na, K, Ca, Al, Si and Zr were taken from bulk rock data and the Zr content of the zircon was measured by electron microprobe. The results are shown graphically in Figure 5-3 and tabulated in Table 5-2. Based on the data of Table 5-2 there is little intra-zircon variation in the temperatures calculated using the zircon saturation thermometer. The zircon in the aphyric rhyolite, 07-P3-18, appears to be derived from source around ~980°C. In contrast both zircons from the quartz porphyritic rhyolite have a higher temperature (1025°C) cores.

5.6 Comparison and Discussion

There is limited correlation between the results of the two zircon thermometry techniques used here (Table 5-2; Fig. 5-3). The data from the zircon saturation thermometer (980°C) of the aphyric sample (07-P3-18) lie directly in the middle of the range of values of the Ti-in-zircon thermometer (858-1077°C). The same is true for both zircons within the quartz porphyritic rhyolite, where the zircon saturation thermometer produces temperatures of 1027°C and 1025°C, and the Ti-in-zircon thermometer has a temperature range of 888-1155°C and 837-1099°C, respectively. However, in detail one can see that these results are in conflict because if the melt only became saturated in zirconium at 1025°C how could zircon crystals have grown at 1100-1150°C? The zircon saturation thermometer has, in both cases, returned temperatures which lie in the middle of the temperature range defined by the titanium-in-zircon thermometer.

The results from the zircon saturation thermometer of Watson and Harrison (1983) are not particularly sensitive to the saturation of zirconium in the melt and are heavily influenced by the melt composition. The determination of the parameter M is based on an accurate whole rock protolith composition which in this case, as discussed in Chapter 4, comes from a metamorphically altered sample. Due to the mobility of the alkali metals Na and K during alteration and metamorphism, the M parameter is variable. Furthermore the distribution coefficients, which are calculated using whole rock zirconium concentrations, have a wide range. In Table 4-1 the grid samples alone have Zr contents that vary between 315 and 418 ppm. This variation alone can change the calculated temperature by ~75°C. Additionally, the complex zoning and obvious resorption textures of these zircons suggest that at least one of the zircons may have been

Table 5-2: Comparison of results from Ti-in-zircon thermomter and Zircon saturation thermometer

Thermometer			Watson et al., 2004		Watson and Harrison, 1983	
Sample	**Zircon**	**Position[1]**	**Analysis[2]**	**Temperature (°C)**	**Analysis**	**Temperature (°C)**
07-P3-18	1	core	21	n.d.	6	985
	1	int	22	n.d.	7	983
Fig. 5-2A, B	1	int	23	858	8	986
	1	int	24	n.d.	9	986
	1	int	25	1077	10	985
	1	near rim	26	871	11	985
	1	rim			12	984
07-P1-83	1	light core	9	1155	19	1028
	1	light core	10	1107	20	1027
Fig. 5-2C, D	1	outer core	11	969	21	1027
	1	int	12	888	22	1027
	1	near rim	13	n.d.	23	1027
07-P1-83	2	int	15	858	-	-
	2	repeat # 15	16	837	-	-
Fig. 5-2E, F	2	repeat # 15	17	888	-	-
Fig. 5-3	2	outer core	18	1099	-	-
	2	int core	19	1062	-	-
	2	int core	20	1086	18	1027
	2	repeat # 20	27	1031	-	-
	2	repeat # 20	8	1083	13	1026
	2	core	21	1094	14	1027
	2	outer core	22	n.d.	15	1025
	2	outer core	23	n.d.	16	1025
	2	int	24	n.d.	17	1025
	2	int	25	n.d.	-	-
	2	rim	26	n.d.	-	-

[1] int = intermediate zone within crystal; [2] Analyses as shown in Figure 5-2;

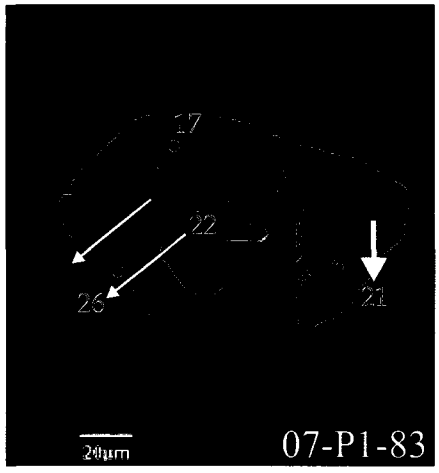

Ti-saturation in zircon thermometry *Watson et al., 2006*	Zr-saturation zircon thermometry *Watson and Harrison, 1983*
15 - 858°C	18 - 1027°C
16 - 837°C	17 - 1025°C
17 - 888°C	16 - 1025°C
18 - 1099°C	15 - 1025°C
19 - 1062°C	14 - 1027°C
20 - 1086°C	13 - 1026°C
21 - 1094°C	
22-26 - b.d.	
27 - 1031°C	
28 - b.d.	

Figure 5-3: A comparison of zircon saturation thermometry of Watson and Harrison (1983) and the more recent Watson et al., (2006) titanium in zircon thermometer. Analysis point 15 has been removed for clarity. See Figure 5-2F for location.

recycled and therefore the history of saturation of zirconium within the melt is open to question.

In contrast, the Ti-in-zircon thermometer results in zircon crystallization temperatures, which rely solely on *in situ* measurements of titanium concentration within a zircon crystal. All of the results from the Ti-in-zircon thermometer show the expected progression from high-temperature core to lower temperatures towards the rim. In the case of the second zircon from sample 07-P3-83, which shows a rounded core (Fig. 5-2E, F), the results exhibit a thermal gap between ~890°C and ~1030°C consistent with the physical evidence that a resorption texture exists and suggests that the crystal experienced conditions wherein the melt became Zr under-saturated, partially dissolving the crystal. The change in saturation likely occurred because the temperature was raised or because the melt composition changed, or both.

Due to the fact that there is less ambiguity as to what temperature the titanium-in-zircon thermometer records, the fact that experiments by Zack et al., (2004) and Watson et al., (2006) have confirmed their results over a wider range of conditions and because the results of this study display the expected growth trend (i.e. from hot core to cool rim), it is therefore concluded that the Ti-in-zircon thermometer is a much more robust description of the magmatic temperatures than the temperature calculated using the zircon saturation thermometer. It is important that the contradiction between these thermometers be noted and that the temperatures estimated from the Watson and Harrison (1983) be used with extreme caution as it appears that this method may not accurately reflect the eruption temperatures of the rhyolitic rocks of the Kidd-Munro assemblage.

Within the population (8 zircons from 4 samples) of zircon crystals sampled in this study, from both aphyric and quartz porphyritic rhyolites, it is clear that all started growth at temperatures around 1050-1100°C as shown by their core temperatures. Below this temperature, the aphyric rhyolite (sample 07-P3-18) experienced a later growth phase at a temperature of about 850°C without any record of high temperature (>830°C) growth between these two end-member regimes. The two zircons from the quartz-porphyritic rhyolite (sample 07-P1-83) show different thermal histories. One of which appears to have been recycled while the other records a complete thermal history between 880-1150°C. In addition there are 5 other small zircons noted which appear to have grown

entirely below ~830°C. Despite the complex histories two important conclusions can be drawn: 1 – three zircons with old cores preserve a high temperature growth originating around 1150°C, and; 2 – all eight zircons preserve a low temperature growth period below ~830°C.

The results presented here suggests that the interpretation of the zircon saturation temperatures Barrie (1995) should be further re-assessed using the Ti-in-zircon thermometer. The results also show that the FIIIb rhyolites of Prosser Township grew in a melt that was below 830°C. This melt was likely produced from a magma that was around 1150°C, which is significantly hotter than the 840-940°C estimate presented by Barrie (1995) as inferred from the zircon saturation thermometer.

Furthermore, the results from the Ti-in-zircon thermometer may be used to assess the local scale conditions of formation of VMS-associated rhyolites and their thermal histories.

Chapter 6 – Discussion

6.1 – Volcanic Architecture

6.1.1 Nature of the protolith?

The presence of hyaloclastite shards perlitic fractures, flow bands and lava lobes demonstrates that the rhyolites of the Kidd Munro Assemblage, Prosser Township were glassy rocks. This is consistent with the fact that these lavas have ~2 vol. % phenocrysts in what are locally termed the aphyric lavas, and up to ~10 vol. % in the quartz-porphyritic rhyolite. Although the rocks were subjected to recrystallization it is concluded that they were originally glassy phenocryst-poor high-silica rhyolites.

A similar pseudo-spherulitic albite intergrowth texture to that of this study has been described by Gifkins and Allen (2001) in the felsic rocks from the Mount Read Volcanics in Tasmania. They have shown that albite replaced the massive cores of perlite whereas nearby fractures are filled by a sericite-quartz-feldspar mixture. An important difference between their rocks and the least altered rocks of this study is that there is no sericite in the fractures but rather polycrystalline quartz. Gifkins and Allen (2001) concluded that the sericite within both the hyaloclastite and perlite fractures represents a metamorphosed equivalent of an early smectite alteration of the volcanic glass. They argue that the fractures were sealed with smectite (subsequently replaced by sericite) and that the fibro-radial (spherulitic) feldspar-quartz-sericite is a replacement of diagenetic zeolites (their Figs. 11A, B, E). The fibro-radial texture is inferred to be a relict of original fibrous zeolites, though zeolites were not observed in their rocks.

Furthermore they state that the alteration fronts are controlled by primary structures as evidenced by the abundant sericite within fractures. The late quartz-feldspar-sericite alteration in the Mount Read Volcanics is restricted to the perlite cores. This led Gifkins and Allen (2001) to suggest that the glassy core of perlite was more permeable or more readily altered during diagenesis than the clay-filled fractures. Unlike the Mount Read volcanic rocks the replacement of the groundmass glass by feldspar and quartz is widespread within the least altered rocks found in the middle, more massive portions of the Prosser Township flows.

Using the least altered aphyric rhyolite density, 2.71 g/cm^3, of Koopman et al., (1999) for the Kidd Creek mine rhyolite, the least altered composition of this study (Table 4-4) and pure albite ($NaAlSi_3O_8$; density = 2.62 g/cm^3) calculations show it is possible to directly convert 39 vol. % (see Appendix A.7) of the rhyolitic glass to albite without the addition of new material and that the change in volume is negligible (~3%). This is comparable to the estimates of 45-55 vol. % albite in the least altered samples (Table 4-2). The density of Koopman et al., (1999) is from a rhyolite that has experienced some sericitization as it has 2.72 wt. % K_2O and therefore is more dense than the protolith here. If some anorthite component is added, the proportion of glass converted to plagioclase increases.

The least altered samples found in the coulée interiors in Prosser Township lack sericite along fractures and therefore likely did not experience significant clay alteration. The cores of these flows display evidence for anhydrous recrystallization only which may have been produced through metamorphic reordering of rhyolitic glass largely to albite and quartz. Given the above calculations and the petrographic evidence presented for the Prosser Township rocks I would suggest that similar processes caused the cores of the perlite described by Gifkins and Allen (2001) to be recrystallized to albite-quartz and that this albite-quartz mixture is what is to be expected as an isochemical remnant of the rhyolite glass protoliths. Surrounding these albite-quartz remnants in perlite cores, the rest of the Mount Read rhyolite was apparently destructively altered to various sericite-chlorite-quartz-epidote mixtures. Similarly in Prosser Township samples taken away from the core of the coulées are chloritized and sericitized. The remnants of protolith glass, though texturally changed, are not unexpected in these rocks as both 'fresh' rhyolitic (e.g. Allen et al., 2008) and basaltic (e.g. Monecke et al., 2004) glasses have been found on the modern sea floor. Thus, chemically unaltered glass is expected to be preserved in the ancient rock record.

The argument put forth by Gifkins and Allen (2001) that the pseudo-spherulitic or radial texture of the albite is a product of metamorphic coarsening of diagenetic zeolites can be alternately explained by the tendency for spherulitic growth to occur under diffusion limited conditions (e.g. Lofgren, 1974), the environment one expects during the ordering of glass into crystals of albite and quartz. Unlike spherulites that are grown as a

result of quenching, the ones observed here are coarse and intergrown with polycrystalline material, likely as a result of the long time-scales of metamorphism.

The albitized samples which contain up to 80 vol. % (Table 4-2) groundmass albite are exceptional. This is only a visual estimate and is over-estimated as there are always very small ~10 μm polycrystalline quartz crystals which are intimately intergrown with the albite. Veins of albite were also described crosscutting the rock and are interpreted as a later phase. This is an independent event as it brittlely cuts the rock and therefore may be unrelated to the major recrystallization of rhyolitic glass to albite and quartz. Furthermore, the average chemical composition of least altered and albitized samples are within ± 10% of each other with the exceptions of K and F (Table 4-1; Fig. 4-5). Therefore it is concluded that neither the exceptional high albite-content samples nor the albite veins represent a significant departure from the general lithogeochemistry of the rhyolites.

If the least altered samples represent rocks that have neither experienced extensive sea floor alteration nor hydrothermal alteration then they have likely only been modified during burial and regional metamorphism.

6.1.2 Coulée Morphologies

Mapping shows that the Prosser Township rhyolites are thin flows. These coulées are similar to the subaqueous silicic lava flows described by McPhie et al., (1993) and are conceptualized in Figure 6-1. This general morphology is almost identical to the coulée in Prosser Outcrop 1 and is also present at Outcrop 2 however in the latter outcrop it has been obscured by the intrusion of rhyolite lobes/dykes into the volcanic pile as described in Chapter 2 and discussed below (section 6.1.3).

These coulées show all of the classic features of subaqueous rhyolite flows (McPhie et al., 1993 and references therein): lack or poorly developed basal breccia (Fig. 2.3), well developed breccia carapace, flow banding parallel near the base and more chaotic near the flow-top (Fig. 2.4D), hyaloclastite (both within the breccias, Fig. 4-4H, and *in situ,* Fig. 4-2C), abundant peperite (Fig. 2.4A) along the base of the flow and lobate or pod-like projections associated with a coherent lava (Fig. 2.4B). Given the fact

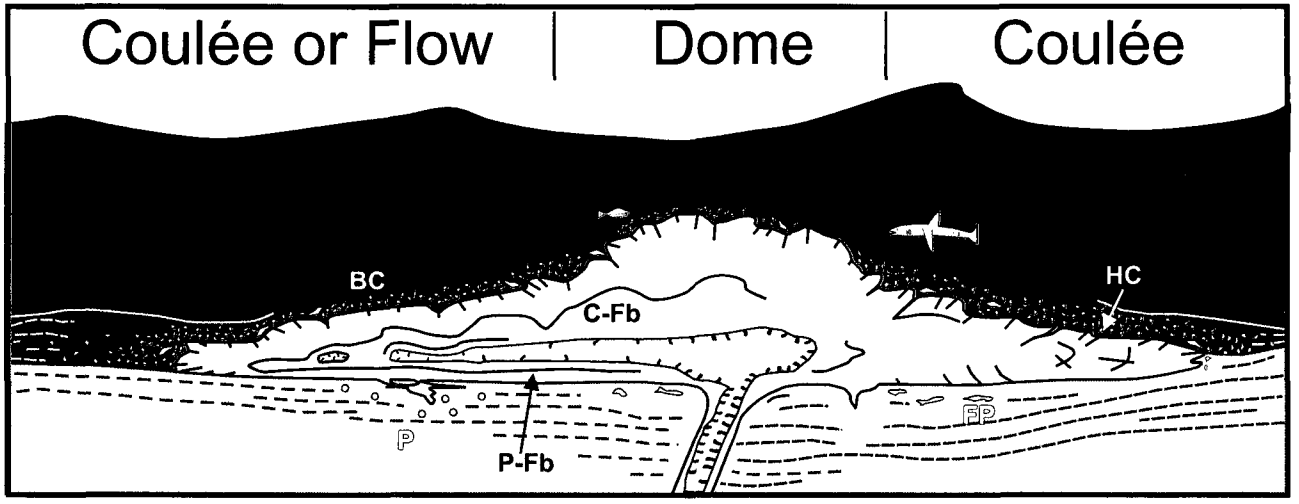

Figure 6.1: Conceptual model for coulée morphology. The coulée to dome transition is defined by aspect ratios crossing from greater than to less than unity (Cas and Wright, 1987). Key features are denoted by the following letters: BC = breccia carapace; P = peperite; P-Fb = parallel laminar flow-banding; C-Fb = chaotic flow banding; FP = fluidal pumice; HC = hyaloclastite. Also of note is the lack of a basal breccia. Inspired by McPhie et al., (1993).

that the above diagnostic features are well preserved in the Prosser Township rhyolites it is concluded that they are subaqueous effusive lavas, i.e., subaqueous coulées.

These coulées may have flowed significant distances from their source. Based on observations of the coulées of the Torfajökull region, Iceland, those of the Mono Craters Volcanic chain in Long Valley, California, USA, and those of the Rosse Roche of Lipari, Italy (A. Cabrera, 2008; personal communication), the maximum flow-distance from a vent is 2-3 kilometres. As many modern flows are substantially thicker (>30 m) than those described here, the most analogous rhyolite flows (in terms of aspect ratio) are the 1480 AD (Larsen, 1984) mixed rhyolites of the Torfajökull area, south-central Iceland that are <20 m thick. While there are many coulées in this region, the Námshraun flow is comparable to the Prosser Township flows because it is a phenocryst-poor rhyolite with the following dimensions (McGarvie, 1984; Wilson et al., 2007): ~870 m long and 4-10 m in thickness and 32-152 m in breath. The southern flow of Námshraun is confined to a relatively steep valley (19°: Wilson et al., 2007) before it fans out onto a flat (3°) braided river valley floor. Based on a Newtonian-model Wilson et al., (2007), have calculated an apparent viscosity of ~4 x 10^7 Pa s and an effusion rate of 1.5-2.7 m^3 s^{-1} that produced a total southern coulée volume of 1.6 x 10^6 m^3. This lava was emplaced from a relatively small vent (~10 m long and probably ~3 m wide) in a very short period of time (2.5-5 days). The modeling paired with empirical observations resulted in Wilson et al., (2007) inferring that the lava advance was cooling-limited.

In comparison, the least altered rhyolite composition from Prosser Township yields a viscosity of 7.8 x 10^6 Pa s at ~850°C using the compositional based viscosity model of Giordano et al., (2007). This is five times less than that of the Námshraun rhyolite described above. It is clear that even viscous high silica rhyolite lavas may produce thin coulées such as those observed in Prosser Township. If the above analogy is even remotely applicable one may be able to reconstruct a reasonable model for the eruptive conditions of the Prosser Township lavas.

There is one major difference between the Námshraun and Prosser Township coulées, which is the subaqueous emplacement of the latter lavas, a factor that may very well have changed the flow scale dynamics in comparison to subaerial flows, but may not

have an affect on the overall rheology. For instance, it is known that rhyolitic crypto-domes and domes scale similarly.

Lacking any other evidence but based upon the abundant pumice associated with the Prosser Township rocks we do not expect the rhyolites were erupted in the deep ocean. However, the idea that the depth of vesiculation is limited by confining water pressure (e.g Fisher and Schmincke, 1984) is invalid because it is based purely on static conditions and has been experimentally and theoretically been concluded otherwise (Wohletz, 2003).

6.1.3 Stratigraphic architecture

Over the three mapped outcrops at least three complete coulées were definitely recognized in cross section: outcrops 1 (2 coulées) and 2 (1, possibly 2 coulées). In addition, there are two to three other possible flows. There may be two flows mapped in outcrop 2, where there is a recessive layer within the coulée that may mark a contact (around 7 m N; 24 m E; Fig.2.5). The two rhyolites mapped in Outcrop 3 are poorly exposed, as only the top of the underlying aphyric rhyolite and the basal part of the overlying quartz-porphyritic rhyolite are exposed. Between these rhyolite coulées are chloritized tuffaceous units.

The chloritized tuffs have lithogeochemical signatures that consistently plot adjacent to the associated coherent rhyolites plots (Fig. 4.10; Fig. 4.11). The pumice- and spatter-rich tuff breccia unit underlying the quartz porphyritic rhyolite has the same lithogeochemical signature as the quartz porphyritic rhyolite and not that of the underlying aphyric rhyolite. This is interpreted to mean that the quartz porphyritic rhyolite magma erupted explosively before producing effusive domes and flows.

It has been argued above (Chapter 2) that the pumice- and spatter-rich tuff breccia shows signs of synvolcanic alteration because of the asymmetric alteration of pumice and spatter clasts. Both types of clasts are heavily altered near the base of the unit whereas towards the top they have undeformed amygdules, no quenched margins and a very low degree of chloritization. The pumice- and spatter-rich tuff breccia also exhibits an apparent symmetric grading in pumice clasts. In subaqueous explosive eruptions it is common for some pumice blocks to become water logged, as such it is theorized that they

continuously settle out of the eruption column (e.g. Fiske and Matsuda, 1964, Allen and McPhie, 2000; Gifkins et al., 2002; Mueller, 2003; Kano, 2003; Allen and Stewart, 2003; Kano and Yoshikawa, 2005; Allen et al., 2007; Allen et al., 2008) whereas other blocks may form a pumice raft at the water's surface that gradually sinks and becomes dispersed and deposited. Unlike the classic examples (e.g. Allen and McPhie, 2000 and Kano, 2003) the pumice- and spatter-rich tuff breccia's pumice-rich top layer is closely associated with fluidal spatter clasts. The association of spatter and pumice, the synvolcanic alteration and the lack of sorting or bedding suggests that tuff breccia was erupted violently, deposited hot without much reworking and as a single unit. Therefore it is interpreted that the pumice- and spatter-rich tuff breccia is a submarine pyroclastic flow. To the author's knowledge there has been no detailed description in the current literature of a modern equivalent to the rhyolitic pumice- and spatter-rich tuff breccia. This may simply be a product of our lack of exploration of these complex volcanic terrains in the modern oceans. However, somewhat analogous materials may be found in the description of submarine pyroclastic flows of Fiske (1963) or Kano (1996).

Figure 6-2 summarizes this stratigraphic and geochemical evolution of the Prosser Township rocks in 5 depositional events. The stratigrapic sequence of Prosser Township shows a general, though discontinuous, increase in the Hf-Th ratio at near constant Ta in Hf-Th-Ta space from the aphyric to the quartz porphyritic rhyolite. In Figure 6-2A an aphyric rhyolite coulée (#1; Figure 6-2) is emplaced and is depicted to have a composition equivalent to all of the coherent aphyric rhyolites. These flows are intercalated with tuffaceous units (#2; Fig. 6-2B) that have compositions similar to the above aphyric rhyolite, but more evolved toward the Hf apex. Contemporaneous with the emplacement of lavas and tuffs are the injection of rhyolitic dykes, sills and lobes (#3; Fig. 6-2C) into the volcanic pile either along contacts or along preferential stratigraphic layers. These intrusive rhyolites have compositions similar to the tuffaceous units and bridge the gap between end-member coherent rhyolite compositions. The sequence of aphyric rhyolite flows and tuffs is terminated by a distinct pumice- and spatter-rich tuff breccia (#4; Fig. 6-2D) which is interpreted to be a pyroclastic flow. The majority (7 of 9) of the tuff breccia samples have a lithogeochemical character that plots adjacent to the quartz porphyritic rhyolite (inset plot Fig. 6-2D, analysis 4) toward the Hf apex. It is not

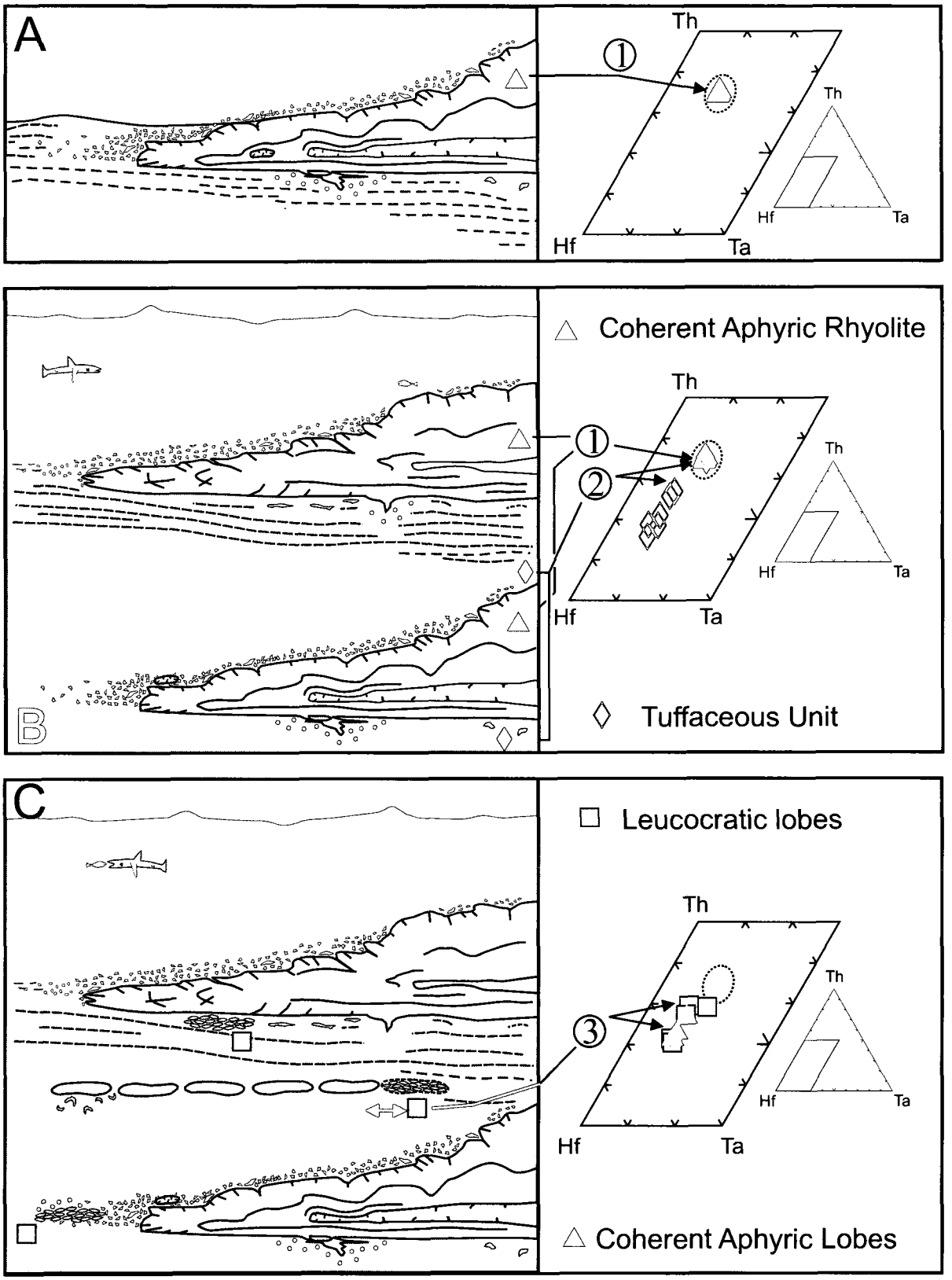

Figure 6-2: Caption with Figure 6-2D.

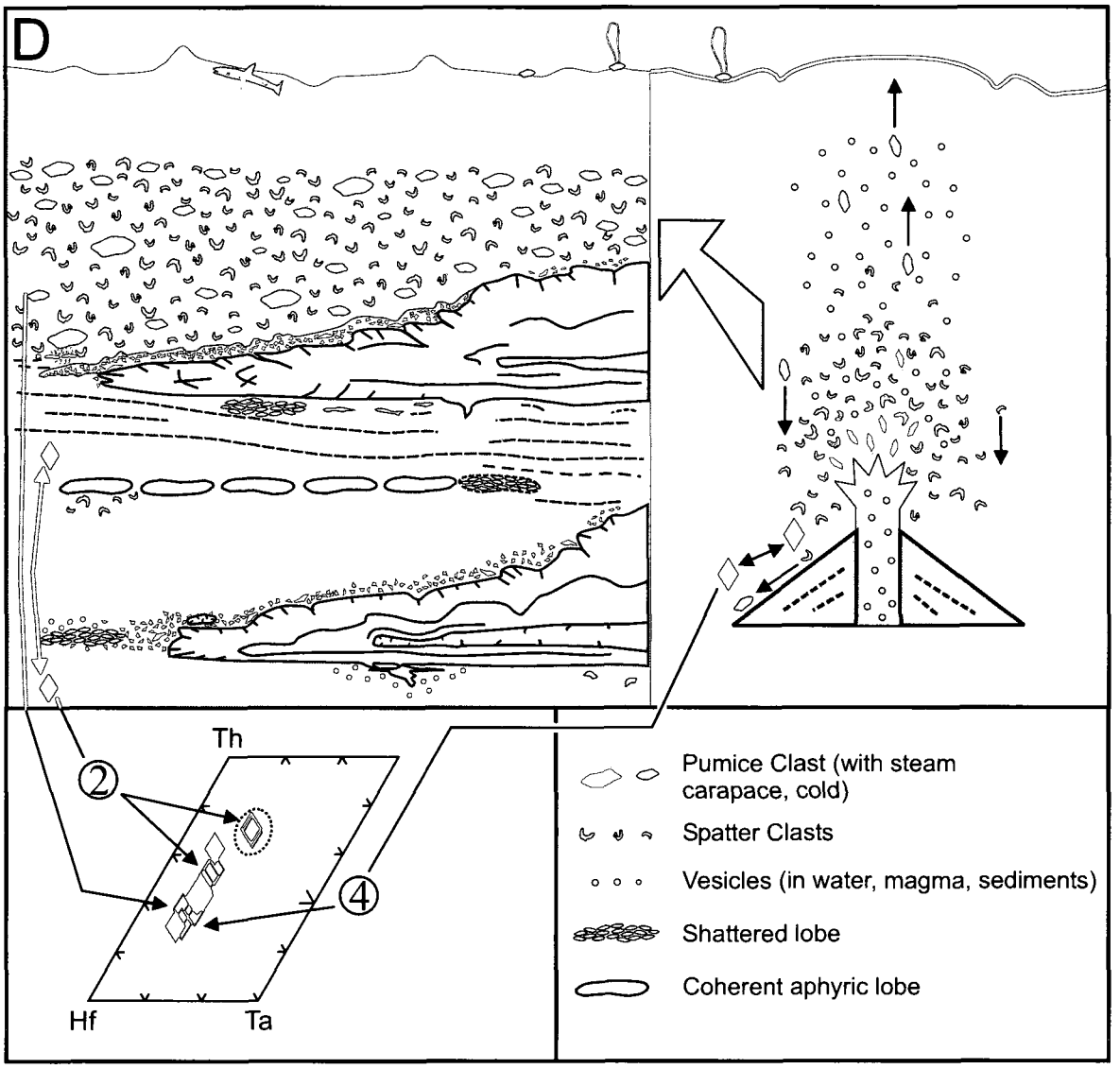

Figure 6-2: Volcanic evolution. Symbols and geochemical plots are connected by lines to the relevant rock type. A) Aphyric rhyolite coulée (1) is either buried in rhyolitic tuffaceous material derived from explosive volcanism or hemi-pelagic sediment. B) Tuffaceous units (2) have similar Hf-Th-Ta signature to that of the intercalated aphyric rhyolite flows. C) Coherent or brecciated intrusive lobes (3) intrude into the volcanic pile along preferred stratigraphic levels and along flow contacts. The intrusive phases have a lithogeochemical signature intermediate between the end-member aphyric and QP rhyolite. D) Pyroclastic pumice- and spatter-rich tuff breccia (4) is deposited from a violent subaqueous explosive eruption. The tuff breccia displays a syn-volcanic alteration manifested by a change in colour. The pumice and spatter from this unit exhibits the most evolved Hf-Th-Ta compositions in Prosser Township.

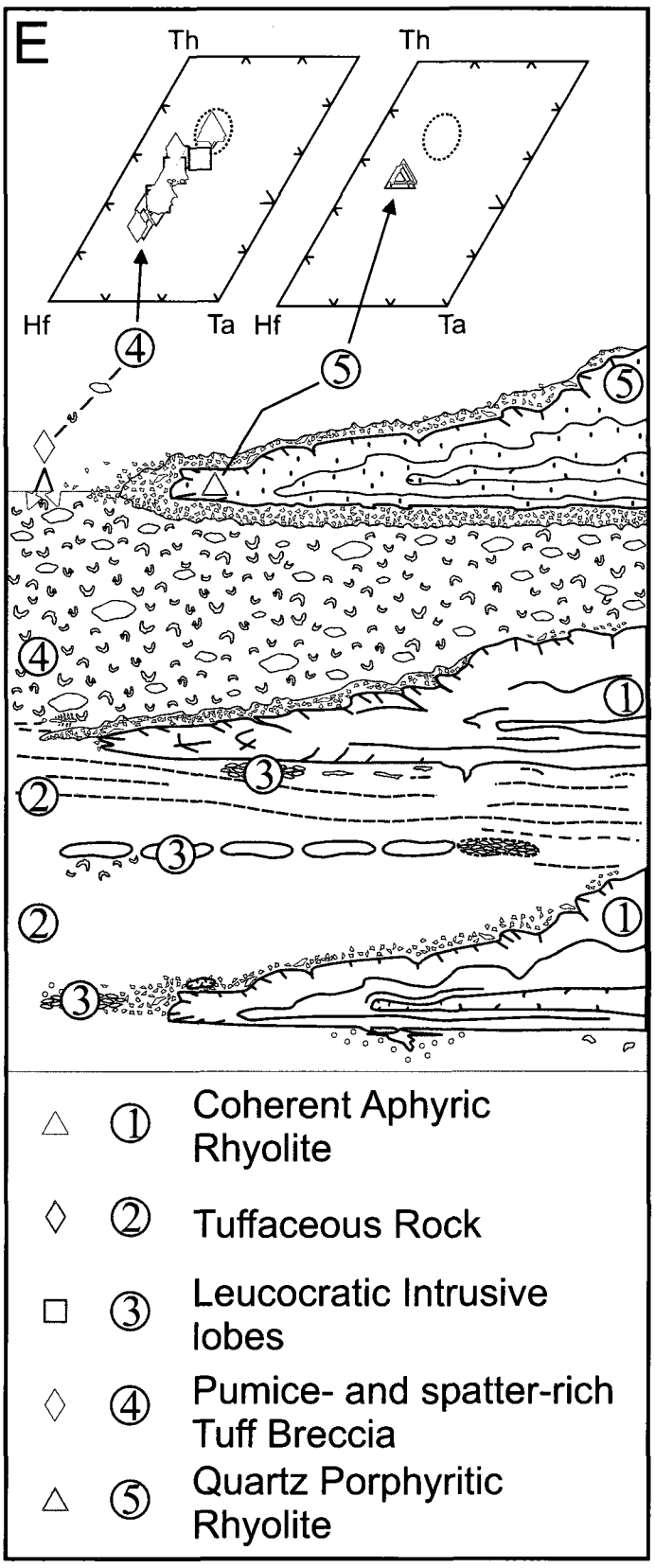

Figure 6-2: Volcanic evolution continued.
E) Finally the sequence capping quartz porphyritic rhyolite is emplaced sealing in the porous and permeable tuff breccia (4). The quartz porphyritic rhyolite (5) has an evolved litho-geochemical signature (right inset) but is intermediate to other samples when all felsic units are plotted (left inset).

clear whether or not the tuff breccia represents a single pulse of material or multiple units although the synvolcanic alteration suggests that it is a single unit. By analogy with modern flows the morphology of the coulées places them at a maximum distance of 1 km from the vent. The abundance of spatter clasts within the pyroclastic flow suggests that the vent maybe much closer. Although there is a paucity of detailed descriptions of modern submarine pyroclastic density flows, the theoretical framework for hot (possibly up to ~500°C) pumice-rich density flows has been put forth by Allen et al., (2008).

The final stage of deposition in this sequence is that of the quartz porphyritic rhyolite (#5; Fig. 6-2E). The overall morphology of this unit is unknown as only the basal part of the unit is exposed. The lithogeochemical signature of the quartz porphyritic rhyolite is slightly less evolved, plotting toward the Th apex, in comparison to the underlying tuff breccia (right-side inset plot; Fig. 6-2E). So, although there is a general trend between apices, from aphyric rhyolites with lower Hf/Th ratio to the higher Hf/Th ratios of the quartz porphyritic rhyolite, it is not a simple progression. The tuffaceous units appear to be locally slightly more evolved forms of the effusive lavas with which they are associated. The complex chemo-stratigraphic relationships reported may reflect the magmatic processes which gave rise to the rhyolites.

To summarize the sequence in Prosser Township which at the start of this project was considered to be composed of alternating flows of felsic and mafic rocks consists of proximal rhyolite coulées and tuffs, and one of the latter was arguably deposited as a pyroclastic flow. Though there has been textural modification, these rhyolites were initially glassy, phenocryst-poor, flow-banded, high-silica rhyolites similar to those found in the Torfajökull region of Iceland, although subaqueously deposited. Alteration has resulted in significant modification of the lithogeochemistry however the high field strength elements have been proven to be relatively immobile and preserve protolith compositions which reflect a complex magmatic history becoming more enriched in Hf with stratigraphic height in the sequence.

6.2 – Comparison with the Kidd Creek deposit

6.2.1 Explosive rhyolite volcanism

The overall stratigraphy of Prosser Township shows a similar progression of units to the Kidd Creek mine stratigraphy described by Prior (1996; Prior et al., 1999a, b) and DeWolfe (2004). The progression in the felsic units is from interbedded aphyric lavas and tuffs, to the capping quartz porphyritic rhyolite. In further detail it is most analogous to the North Rhyolite of the mine where there is no evidence for basaltic volcanism (DeWolfe, 2004). This lack of evidence for basaltic volcanism combined with the fact that the cessation of mineralization accompanied the eruption of the QP rhyolite suggests that the Kidd Creek hydrothermal system was developed and terminated within a felsic dominated magma chamber. The only rocks that is not present in the mapped outcrops of Prosser Township and that are found at the North Rhyolite are the local graphitic argillites.

Due to the similarities in stratigraphy it is suggested that the sequence in Prosser Township represents a continuation of the equivalent rocks found at the Kidd Creek mine site as has been put forth by Berger et al., (2007). This would in turn suggest that there is significant unexploited potential for mineralization within Prosser Township, especially mineralization hidden by overburden given the paucity of outcrops. Furthermore in Prosser Outcrop 3, the equivalent of the mineralized Middle Member is found in the pumice- and spatter-rich tuff breccia which is bound by aphyric and quartz porphyritic lavas. As shown in this study the pumice- and spatter-rich tuff breccia is a very porous and permeable member. This tuff breccia, as exhibited in outcrop, may have provided an excellent fluid pathway. Although it was originally rhyolite it was intensely chloritized and now contains ~53 wt. % relative to the initial estimated >70 wt. % SiO_2. This dilution is evident from the suppressed REE signatures in Figure 4.12E.

Recent studies by Allen et al., (2008) on the submarine pumice clasts from the Myojin Knoll document vesicularities of 73-80 vol. % with an interconnectivity of >97 %, though on the low end of permeability for pumice from this, unit is 2.4×10^{-12} m^2. This degree of vesicularity is typical for several other subaqueous rhyolitic pumices (Wright et al., 2003 and Allen and McPhie, 2000) and is much higher than the basaltic

equivalent (27-65 vol. %; Eissen, et al., 2003). Although it can not unequivocally be determined here, a similar permeability and original vesicularity is inferred for the pumice clasts of Prosser Township. Permeability is difficult to ascertain as it is dependant, among other parameters, on the texture of the pumice and orientation of the clasts. The tuff breccia of Prosser Township has an estimated preserved concentration of <40 vol. % pumice clasts while the pumice units referenced above are almost entirely composed of pumice clasts. Nonetheless this tuff breccia represents a porous and permeable host rock suitable for the precipitation of hydrothermal mineralization.

6.2.2 Effusive rhyolite volcanism

Hart et al., (2004) favours a low pressure, high temperature source for the formation of the FIII type rhyolite suggesting derivation through the partial melting of a hydrated basalt protolith. In this case they state that due to an inflection in the amphibole stability field, clinopyroxene becomes the stable residual phase thus controlling the trace element signature. They further conclude that a 10 % partial melt will produce a rhyolite that is weakly depleted in HREE, metaluminous, enriched in silica and due to the high temperature-induced depolymerization, accommodated more HFSE in the melt. Hart et al., (2004) also states that as mafic lavas are rare or not found in the some FIII VMS hosting bimodal sequences, than they may not constitute a significant source of erupted material.

Although the study of Hart et al., (2004) provides a useful model for the petrogenesis the extrapolation of the conditions of magma-genesis to those of eruption is difficult. This study shows minimum zircon crystallization temperatures over a variety of temperatures from >1100°C down to <830°C. Due to the consistency of zircon temperatures at crystal rims and because the estimates represent minimum temperatures it is interpreted that the eruption temperature of these melts was at or below 830°C. This study also shows that the zircon saturation thermometer of Watson and Harrison (1984) is not reliable for altered rocks and as a consequence the inferences made by Barrie et al., (1993) and Barrie (1995) regarding the eruption conditions should not be treated with skepticism. Their conclusions are dependant on interpretation of complex zirconium saturation of the melt, in part based on whole rock alkali-element measures and conflict

with the crystallization temperatures present here. Therefore it is strongly advised that the Ti-in-zircon thermometer of Watson et al., (2006) be used because it has been more robustly defined, is not based on bulk rock concentrations of alkali elements and produces apparently less ambiguous crystallization temperatures. Furthermore calculations of the liquidus temperatures using MELTS (Ghiorso and Slack, 1995) determined the liquidus to be ~981°C and therefore much higher than the ~830°C recorded within the zircon growth. As a consequence of the relatively low eruption temperatures measured in this study, the existence of phenocrysts in almost every sample and the much high calculated liquidus temperature, it is concluded that these lavas were erupted hot (~800°C) but were not erupted near their liquidus temperatures as suggested by Barrie (1995).

In addition to the relatively high eruption temperature, it has been suggested that these lavas were rich in volatiles (Barrie, 1995; Schandl et al., 1999), including F and Cl which suppressed crystallization and depolymerise the melt however. However as is shown in this study, as well as by the lithogeochemistry of least altered protoliths of Prior et al., (1999ab), Koopman et al., (1999) and Schandl et al., (1999), the volatile content of the protolith was likely low. Furthermore this study shows that the F was mainly added in association with post-eruption sericitization. Of course significant degassing associated with eruption is likely to have occurred making the discussion of protolith concentrations in regard lava viscosity futile.

Furthermore high volatile contents have been used to explain the suppression of a chemical fractionation as well as the thin flow morphologies however, this study has shown a chemical evolution trend within the high field strength elements Hf-Th-Ta and has reconciled the formation of thin coulées without invoking high volatile contents or super-heating as a mechanisms. The best modern analogue for these lavas comes from the Torfajökull region of Iceland which is a subaerial (partially paleo-subglacial) system.

6.2.3 Inferences from high field strength element lithogeochemistry

The chemistry of the rhyolites in Prosser Township fits well with the Kidd Creek mine chemo-stratigraphy. Given the similarities, the rhyolite discrimination diagram of Prior (1996; Prior et al., 1999a) has been used to separate the Lower member aphyric

lavas and their volcaniclastic equivalents from the quartz porphyritic (QP) rhyolites of the Upper and Middle member. The discrimination diagram of Prior (1999a) works well for both coherent and clastic facies and also allows confirmation of the interpretation that rhyolitic dykes, sills and lobes were intruded into the volcanic pile.

In contrast to Schandl et al.'s, (1999) work, there is an apparent evolutionary trend, between the Hf and Th apices in the Hf-Th-Ta discrimination diagram, in the Prosser Township rhyolites. Although not seen in the ternary plot of Schandl et al., (1999) they clearly document a correlation ($r = 0.99$) between Th and Hf. However, Schandl et al., (1999) argue that, although this linear trend covers a large variety of units (rhyolites, tuffs, lapillistones to greywackes and argillite), it does not represent a magmatic evolutionary trend because there is a wide range of Al_2O_3 concentrations. Schandl et al., (1999) argue that because the Bishop Tuff and Cerro Toledo rhyolites have near constant Al_2O_3 concentrations, the range documented at Kidd Creek is due to alteration. However, Schandl et al., (1999) fails to establish any comparison between chemical fractionation processes (e.g. crystal fractional or partial melting) at Kidd Creek with those of either the Bishop Tuff or the Cerro Toledo rhyolites which would permit or preclude the chemical variations in Al_2O_3.

Moreover, Schandl et al., (1999) go on to explain the aluminum variation as a product of mass gain/loss effects and extrapolate this to the other HFSE for example Th (see their Fig. 3). However, this is fallacious as Prior et al. (1999a) have pointed out, since mass gains/losses do not change elements not involved in the mass changes and therefore the ratio remains constant. In the diagrams of Schandl et al. (1999) the ratio (slope of an Th vs Hf plot) is indeed constant ($r = 0.99$) and thus it is most likely that these trends do represent a magmatic evolutionary vectors especially given that they do cover a wide variety of units throughout the stratigraphy.

In this study it has been demonstrated that the HFSE are the least mobile elements and that the evolutionary trend associated with these elements is much larger than the post-cooling additions and losses of these elements. To conclude, the binary plots and ternary plots of the HFSE do represent magmatic trends and may be used to track the chemostratigraphic evolution of this large and complex volcanic system.

Despite the fact that Schandl et al., (1999) conclude that variations in HFSE are due to mass gains/losses they have developed the Hf-Th-Ta diagram to assess magmatic trends at the Kidd Creek deposit. Schandl et al., quote Stix and Gorton (1993) who state that the HFSE are incorporated in accessory phases during fractional crystallization such that high silica rhyolites would be expected to show a clear magmatic evolution away from the hafnium apex by the removal of hafnium in zircons left behind in the restite. In Prosser Township the trend is exactly the opposite, as in general rocks further up the stratigraphy have compositions that plot closer to the Hf apex. This can be explained by the petrologic observation of the aphyric rhyolites that form the bulk of the stratigraphy. The aphyric rhyolites commonly have a ~1 vol. % phenocrysts but also zircon microphenocrysts. In Table 4-2 one see that only one of the twenty-three samples does not have an observed zircon microphenocryst! This implies that the zircons were not physically segregated in the magma chamber – they were erupted thus explaining the increase in Hf. The association between the zircons, the Hf-Th-Ta chemistry and aphyric lavas bolsters the argument that the Ti-in-zircon thermometry temperatures presented here more accurately represent the near eruption conditions.

6.3 Conclusions

In conclusion the Prosser Township outcrops represent a felsic volcanic system that has produced both explosive and effusive high silica rhyolite rocks, some of which are exceptionally preserved. These proximal facies have been intruded by coherent and brecciated lobes which are often poorly defined in the field but are separable from the aphyric lavas as they have trace element signatures similar to the quartz porphyritic rhyolite. The eruption sequence in Prosser Township alternates between thin coulées and tuffs which are capped by two distinct units, a pumice- and spatter-rich tuff breccia and a quartz porphyritic rhyolite.

These coulées have well preserved cores that display perlitic fractures and hyaloclastite unaltered by clay which have experienced near-isochemical recrystallization of rhyolitic glass to a mixture of quartz and plagioclase, likely during burial or regional metamorphism. These glassy rhyolites formed thin flows by normal effusive eruption and

do require neither near-liquidus eruption temperatures nor high contents of depolymerising agents such as F or Cl. These phenocryst-poor lavas erupted at temperatures close to 830°C.

The evidence for primary textures from detailed petrography and coherent geochemical indices has permitted a robust estimate of protolith composition with a degree of confidence unparalleled in other published studies. This is important because it affects every interpretation of the lithogeochemistry. Although these findings have not changed the major inferences based on the rare earth and high field strength elements, it has provided a robust test of their mobility. In fact the mobility of the rare earth elements across a single flow is equal to the variation found in all coherent rhyolite units throughout this sequence! Nonetheless this variation does not exceed the chemical range of the rhyolite classification scheme of Lesher et al., (1986) and strengthens the petrogenetic model put forth by Hart et al., (2004). Although the REE are quite mobile the HFSE throughout albitization, sericitization and chloritization vary by less than 10%. This result confirms the application of the rhyolite discrimination diagram of Prior et al., (1999a) which provides an easy, reliable means of distinguishing between felsic end-members. Furthermore the Hf-Th-Ta diagram of Schandl et al., (1999) may be reliably used to track the magmatic evolution of this Archean volcanic system.

Finally the mineralized Middle member of the Kidd Creek mine is found in Prosser Township as a pumice- and spatter-rich tuff breccia which contains ~40 vol. % highly vesicular clasts. More importantly this tuff breccia was likely porous, permeable and water logged at the time of deposition and as such may have provided an excellent host for hydrothermal mineralization.

References

Allen, S.R., and McPhie, J., 2000. Water-settling and resedimentation of submarine rhyolitic pumice at Yali, eastern Aegean, Greece. Journal of Volcanology and Geothermal Research. Vol. 95, p. 285-307.

Allen S.R., Hayward, B.W., and Mathews, E., 2007. A facies model for submarine volcaniclastic apron: The Miocene Manukau Subgroup, New Zealand. Geological Society of America Bulletin. Vol. 119, p. 725-742.

Allen, S.R., Fiske, R.S., and Cashman. K.V., 2008. Quenching of steam-charged pumice: Implications for submarine pyroclastic volcanism. Earth and Planetary Science Letters. Vol. 274, p. 40-49.

Ayer, J.A., Berger, B.R., and Trowell, N.F., 1999. Geological compilation of the Lake Abitibi area, Abitibi greenstone belt. Ontario Geological Survey, Map P.3398, scale 1:100 000.

Ayer, J., Amelin, Y., Corfu, F., Kamo, S., Ketchum, J., Kwok, K., and Trowell, N., 2002. Evolution of the southern Abitibi greenstone belt based on U-Pb geochronology: autochthonous volcanic construction followed by plutonism, regional deformation and sedimentation. Precambrian Research. Vol. 115, p. 63-95.

Ayer, J., Thurston, P.C., Batemam, R., Dubé, B., Gibson, H.L., Hamilton, H.A., Hathway, B., Hocker, S.M., Houlé, M.G., Hudak, G., Ispolatov, V.O., Lafrance, B., Lesher, C.M., MacDonald, P.J., Péloquin, A.S., Piercey, S.J., Reed, L.E., and Thompson, P.H., 2005. Overview of results from the Greenstone Architecture Project: Discover Abitibi Initiative. Ontario Geological Survey, Open File Report 6154.

Bailey, R.A., Dalrymple, G.B. and Lanphere, M.A., 1976. Volcanism, structure and geochronology of Long Valley Caldera, Mono County, California. Journal of Geophysical Research. Vol. 81, p. 725-744.

Barrie, C.T., Ludden, J.N., and Green, T.H., 1993. Geochemistry of volcanic rocks associated with Cu-Zn and Ni-Cu deposits in the Abitibi subprovince. Economic Geology. Vol. 88, p. 1341-1358.

Barrie, C.T., 1995. Zircon thermometry of high-temperature rhyolites near volcanic-associated massive sulfide deposits, Abitibi subprovince, Canada. Geology. Vol. 23, p. 169-172.

Barrie, C.T., Cousens, B.L., Hannington, M.D., Bleeker, W., and Gibson, H.L., 1999. Finite element heat and fluid-flow computer simulations of a deep ultramafic sill model for the giant Kidd Creek volcanic-associated massive sulfide deposit, Abitibi subprovince, Canada. In: M.D. Hannington and C.T. Barrie, eds, Economic Geology Monograph 10, p. 497-510.

Berger, B.R. and McIlraith, S.J., 2007. GIS compilation: Bedrock geology of Prosser Township. Ontario Geological Survey Miscellaneous Release - Data 226. Available at http://www.geologyontario.mndm.gov.on.ca/mndmaccess/mndm_dir.asp?type=pub&id=MRD226.

Berger, B.R., Ayer, J.A., McNicoll, V.J., and Bleeker, W., 2007. The Kidd-Munro Project: Stratigraphy of the Kidd-Munro assemblage in Prosser Township and area based on geology, geochemistry and new geochronology. In: Summary of field work and other activities, Ontario Geological Survey, Open File Report 6213, p. 5-1 to 5-8.

Brooks, E.R., Wood, M.M., Garbutt, P.L., 1982. Origin and metamorphism of peperite and associated rocks in the Devonian Elwell Formation, northern Sierra Nevada, California. Geological Society of America Bulletin. Vol. 93, p. 1208-1231.

Burnham, O.H. and Schweyer, J., 2004. Trace element analysis of geological samples by inductively coupled plasma mass spectrometry at the Geoscience Laboratories: Revised capabilities due to improvements to instrumentation. In: Summary of field work and other activities, 2004, Ontario Geological Survey, Open File Report 6145, p. 54-1 to 54-20.

Campbell, I.H., Franklin, J.M., Gorton, M.P., Hart, T.R., and Scott, S.D., 1981. The role of subvolcanic sills in the generation of volcanic massive sulfide deposits. Economic Geology. Vol. 76, p. 2248-2253.

Campbell, I.H., Coad, P., Franklin, J.M., Gorton, M.P. and Scott, S.D., 1982. Rare earth elements in volcanic rocks associated with Cu-Zn massive sulfide mineralization: A preliminary report. Canadian Journal of Earth Science. Vol. 19, p. 619-623.

Campbell, I.H., Lesher, C.M., Franklin, J.M., Gorton, M.P. and Thurston, P.C., 1984. Rare-earth element mobility in alteration pipes below massive Cu-Zn sulphide deposits. Chemical Geology. Vol. 45, p. 185-202.

Cas, R.A.F. and Wright, J.V., 1987. Volcanic Successions: London, Allen and Unwin. 528 p.

DeWolfe, Y. M., 2004. Volcanic reconstruction of the Archean North Rhyolite, Kidd Creek mine, Timmins, Ontario, Canada. Unpublished M.Sc. thesis. Sudbury, Ontario, Laurentian University, 149 p.

Fisher, R.V., 1961. Proposed classification of volcaniclastic sediments and rocks. Geological Society of America Bulletin. Vol. 72, p. 1409-1414.

Fisher, R.V., and Schmincke, H.-U., 1984. Pyroclastic Rocks: Berlin, Springer-Verlag. 472 p.

Fiske, R.S., 1963. Subaqueous pyroclastic flows in the Ohanapecosh Formation, Washington. Geological Society of America Bulletin. Vol. 74, p. 391-406.

Fiske, R.S. and Matsuda, T., 1964. Submarine equivalent of ash flows in the Tokiwa Formation, Japan. American Journal of Science. Vol. 262, p. 76-106.

Galley, A.G., Hannington, M.D., and Jonasson, I.R., 2007. Volcanogenic massive sulphide deposits. In: Goodfellow, W.D., eds, Mineral Deposits of Canada: A Synthesis of Major Deposit-Types, District Metallogeny, the Evolution of Geological Provinces, and Exploration Methods 2007: Geological Association of Canada, Mineral Deposits Division, Special Publication No. 5, p. 141-161.

Gibson, I.L. and Walker, G.P.L., 1963. Some composite rhyolite/basalt lavas and related composite dykes in eastern Iceland. Proceeding of the Geological Association. Vol. 74, p. 301-318.

Gifkins, C.C., and Allen, R.L., 2001. Textural and chemical characteristics of diagenetic and hydrothermal alteration in the glassy volcanic rocks: Examples from the Mount Read Volcanics, Tasmania. Economic Geology. Vol. 96, p. 973-1002.

Gifkins, C.C., McPhie, J., and Allen, R.L., 2002. Pumiceous rhyolitic peperite in ancient submarine volcanic successions. Journal of Volcanology and Geothermal Research. Vol. 114, p. 181-203.

Giordano, D., Russel, J.K., and Dingwell, D.B., 2008. Viscosity of magmatic liquids: A model. Earth and Planetary Science Letters. Vol. 271, p. 123-134.

Goodfellow, W.D., 1975. Major and minor element halos in volcanic rocks at Brunswick No. 12 sulphide deposit, New Brunswick, Canada. In: Elliot, I.L., and Fletcher, W.K., eds, Geochemical exploration 1974: Amsterdam, Elsevier, p. 279-295.

Gresens, R.L., 1967. Composition-volume relationships of metasomatism. Chemical Geology. Vol. 2, p. 47-65.

Grogan, P., 2009.

Hall, S.H., 1978. The stratigraphy of northern Lipari and the structure of the Roche Rosse rhyolite flow and its implications. Unpublished B.Sc. thesis, Leeds, United Kingdom, University of Leeds.

Hannington, M.D., Barrie, C.T., and Bleeker, W., 1999a. The giant Kidd Creek volcanogenic massive sulfide deposit, western Abitibi subprovince, Canada: Preface and introduction. In: M.D. Hannington and C.T. Barrie, eds, Economic Geology Monograph 10, p. 1-30.

Hannington, M., Bleeker, W., and Kjarsgaard, I., 1999b. Sulfide mineralogy, geochemistry, and ore genesis of the Kidd Creek deposit: Part I. North, Central, and South Orebodies. In: M.D. Hannington and C.T. Barrie, eds, Economic Geology Monograph 10, p. 267-296.

Hart, T.R., Gibson, H.L. and Lesher, C.M., 2004. Trace element geochemistry and petrogenesis of felsic volcanic rocks associated with volcanogenic massive Cu-Zn-Pb sulfide deposits. Economic Geology. Vol. 99, p. 1003-1013.

Huston, D.L., and Taylor, B.E., 1999. Genetic significance of oxygen and hydrogen isotope variations at the Kidd Creek volcanic-hosted massive sulphide deposit, Ontario, Canada. In: M.D. Hannington and C.T. Barrie, eds, Economic Geology Monograph 10, p. 335-350.

Isikawa, Y., Sawaguchi, T., Iwaya, S., and Horiuchi, M., 1976. Delineation of prospecting targets for Kuroko deposits based on modes of volcanism of underlying dacite and alteration haloes [in Japanese with English abstract]. Mining Geology. Vol. 26, p. 105-117.

Jackson, S.L., and Fyon, A.J., 1991. The Western Abitibi Subprovince in Ontario. In: Geology of Ontario, Ontario Geological Survey, Special Vol. 4/1, pp. 405-482.

Kano, K., 1996. A Miocene coarse volcaniclastic mass-flow deposit in the Shimane Peninsula, SW Japan: product of a deep submarine eruption? Bulletin of Volcanology. Vol. 58, p. 131-143.

Kano, K., 2003. Subaqueous pumice eruptions and their products: a review. In: White, J.D.L., Smellie, J.L., and Clague, D.A., eds, Geophysical Monograph Series, Vol. 140, p. 213-229.

Kano, K., and Yoshikawa, T., 2005. Suaqueous eruption and emplacement of OT2 in the middle Miocene Iizuka Formation, Noto Peninsula, Japan. Journal of Volcanology and Geothermal Research. Vol. 147, p. 309-328.

Koopman, E.R., Hannington, M.D., Santaguida, F., and Cameron, B.I., 1999. Petrology and geochemistry of proximal hydrothermal alteration in the mine rhyolite at Kidd Creek. In: M.D. Hannington and C.T. Barrie, eds, Economic Geology Monograph 10, p. 267-296.

Larsen, G., 1984. Recent volcanic history of the Veidivotn fissure swarm, southern Iceland – an approach to volcanic risk assessment. Journal of Volcanology and Geothermal Research. Vol. 22, p. 33-58.

Lesher, C.M., Goodwin, A.M., Campbell, I.H., and Gorton, M.P., 1986. Trace-element geochemistry of ore-associated and barren, felsic metavolcanic rocks in the Superior Province, Canada. Canadian Journal of Earth Science. Vol. 23, p. 222-237.

Lofgren, G., 1974. An experimental study of plagioclase crystal morphology: Isothermal crystallization. American Journal of Science. Vol. 274, p. 243-273.

Manley, C. R., 1996. Physical volcanology of a voluminous rhyolite lava flow: The Badlands lava, Owyhww Plateau, southwestern Idaho. Journal of Volcanology and Geothermal Research. Vol. 71, p. 129-153.

McGarvie, D.W., 1984. Torfajökull: A volcano dominated by magma mixing. Geology. Vol. 12, p. 685-688.

McPhie, J., Doyle, M. and Allen, R., 1993. Volcanic Textures: Hobart, University of Tasmania, Centre for Ore Deposit and Exploration Studies. 198 p.

Monecke, T., Renno, A.D., and Herzig, P.M., 2004. Primary clinopyroxene spherulites in basaltic lavas from the Pacific-Antarctic Ridge. Journal of Volcanology and Geothermal Research. Vol. 130, p. 51-59.

Mueller, W.U., 2003. A subaqueous eruption model for shallow-water, small volume eruptions: Evidence from two Precambrian examples. In: White, J.D.L., Smellie, J.L., and Clague, D.A., eds. Geophysical Monograph Series, Vol. 140, p. 189-203.

Muirhead, E.M.M., and Hutchinson, R.W., 1999. Mass change profiles in the footwall of the Kidd Creek orebody. In: M.D. Hannington and C.T. Barrie, eds, Economic Geology Monograph 10, p. 297-308.

Ontario Geological Survey 2007. Precambrian geology of Prosser Township; Ontario Geological Survey, Preliminary Map P.3593, scale 1:20 000.

Pearce, N.J.G., Perkins, W.T., Westgate, J.A., Gorton, M.P., Jackson, S.E., Neal, C.R., and Chenery, S.P., 1997. A compilation of new and published major and trace element data for NIST SRM 610 and NIST SRM 612 glass reference materials. The Journal of Geostandards and Geoanalysis. Vol. 21, p. 115-144.

Pilote, P., McNicoll, V.J., Daigneault, R., and Moorhead, J., 2007. Geology of the western Malartic Group and correlations across the Abitibi belt (2 of 3). Ministère des Ressources naturelles et de la Faune, Québec Exploration 2007, Abstracts of oral presentations and posters, 2007, p. 82.

Prior, G.J., 1996. Volcanology and geochemistry of Archean rhyolites and related volcaniclastic rocks associated with the Kidd Creek volcanogenic massive sulfide deposit, Abitibi greenstone belt, Superior Province, Canada. Unpublished Ph.D. thesis, Ottawa, Canada, Carleton University. 302 p.

Prior, G.J., Gibson, H.L., Watkinson, D.H. and Cook, R.E., 1999a. Anatomy, lithogeochemistry, and emplacement mechanisms for the QP rhyolite, Kidd Creek mine, Timmins, Ontario. In: M.D. Hannington and C.T. Barrie, eds, Economic Geology Monograph 10, p. 123-142.

Prior, G.J., Gibson, H.L., Watkinson, D.H., Cook, R.E., and Hannington, M.D., 1999b. Rare earth and high field strength element geochemistry of the Kidd Creek rhyolites, Abitibi greenstone belt, Canada: Evidence for Archean felsic volcanism and massive sulfide ore formation in an Iceland-style rift environment. In M.D. Hannington and C.T. Barrie, eds, Economic Geology Monograph 10, p. 457-484.

Proulx, N., 2008. Development of textural and chemical heterogeneities in high-silica rhyolites, Mono-Inyo chain, eastern California. Unpublished B.Sc. thesis, Ottawa, Canada, University of Ottawa. 67 p.

De Rosen-Spence, A.F., Provast, G., Dimroth, E., Gochnauer, K., Owen, V., 1980. Archean subaqueous felsic flows, Rouyn-Noranda, Quebec, Canada, and their quarternary equivalents. Precambrian Research. Vol. 12, p. 43-77.

Riverin, G., and Hodgson, C.J., 1980. Wall-rock alteration at the Millenbach Cu-Zn mine, Noranda, Quebec. Economic Geology. Vol. 75, p. 424-444.

Schandl, E.S., and Gorton, M.P., 1991. Postore REE mobility at Kidd Creek and at other Archean massive sulphide deposits. Economic Geology. Vol. 86, p. 1546-1553.

Schandl, E.S., Gorton, M.P., and Bleeker, W.A., 1999. A systematic study of rare earth and trace element geochemistry of the host rocks to the Kidd Creek volcanogenic massive sulfide deposit. In: Hannington and Barrie, eds. Economic Geology Monograph 10, p. 309-334.

Schandl, E.S., and Gorton, M.P., 2002. Application of high field strength elements to discriminate textonic settings in VMS environments. Economic Geology. Vol. 97, p. 629-642.

Scutter, C.R., Cas, R.A.F., Moore, C.L., and de Rita, D., 1998. Facies architecture and origin of a submarine rhyolitic lava flow-dome complex, Ponza, Italy. Journal of Geophysical Research. Vol. 103, p. 27 551-27 566.

Shand, S.J., 1951. Eruptive rocks. John Wiley and Sons, New York. 488 p.

Skilling, I.P., White, J.D.L., and McPhie, J., 2002. Peperite: a review of magma-sediment mingling. Journal of Volcanology and Geothermal Research. Vol. 114, p. 1-17.

Sumner, J.M., Blake, S., Matela, R.J., and Wolff, J.A., 2005. Spatter. Journal of Volcanology and Geothermal Research. Vol. 142, p. 49-65.

Sun, S.S., and McDonough, W.F., 1989. Chemical and isotopic systematics of oceanic basalts; implications for mantle composition and processes. In: Saunders, A.D., and Norry, M.J., eds., Magmatism in the ocean basins. Geological Society Special Publicaitons. Vol. 42, p. 313-345.

Thurston, P.C., 1981. Economic evaluation of Archean felsic volcanic rocks using REE geochemistry. In: Glover, J.E., and Groves, D.I., eds., Archean Geology: Second International Symposium, Perth, 1980. Geological Society of Australia, Special Publication No. 7, p. 439-450.

Watson, E.B., and Harrison, T.M., 1983. Zircon saturation revisited: temperature and composition effects in a variety of crustal magma types. Earth and Planetary Science Letters. Vol. 64, p. 295-304.

Watson, E.B., Wark, D.A., and Thomas, J.B., 2006. Crystallization thermometers for zircon and rutile. Contributions to Mineralogy and Petrology. Vol. 151, p. 413-433.

White, J.D.L. and Houghton, B.F. 2006. Primary volcaniclastic rocks. Geology. Vol. 34, p. 677-680.

White, J.D.L., McPhie, J., and Skilling, I., 2000. Peperite: a useful genetic term. Bulletin of Volcanology. Vol. 62, p. 65-66.

Wilson, L., Fagents, S.A., Robshaw, L.E., and Scott, E.D., 2007. Vent geometry and eruption conditions of the mixed rhyolite-basalt Námshraun lava flow, Iceland. Journal of Volcanology and Geothermal Research. Vol. 164, p. 127-141.

Wohletz, K.H., 2003. Water/magma interactions: Physical considerations for the deep submarine environment. In: White, J.D.L., Smellie, J.L., and Clague, D.A., eds. Geophysical Monograph Series, Vol. 140, p. 25-49.

Zack, T., Moraes, R., Kronz, A., 2004. Temperature dependence of Zr in rutile: empirical calibrations of a rutile thermometer. Contributions to Mineralogy and Petrology. Vol. 148, p. 471-488.

Appendix A.1: Duplicate lithogeochemical analyses

OGS Sample No.	Sample	SiO_2[1]	TiO_2	Al_2O_3	Fe_2O_{3t}	FeO	MnO	MgO	CaO	Na_2O	K_2O	P_2O_5	L.O.I.	Total
Units		wt. %	wt. %	wt. %	wt. %	wt. %	wt. %	wt. %	wt. %	wt. %	wt. %	wt. %	wt. %	wt. %
07BRB502	07-P3-002	-[2]	-	-	-	-	-	-	-	-	-	-	-	-
07BRB509	07-P3-009	-	-	-	-	-	-	-	-	-	-	-	-	-
07BRB510	07-P3-010	79.15	0.12	10.59	2.28	1.69	0.02	0.89	0.26	5.23	0.48	0.01	0.83	99.86
07BRB511	07-P3-011	-	-	-	-	-	-	-	-	-	-	-	-	-
07BRB512	07-P3-012	-	-	-	-	-	-	-	-	-	-	-	-	-
07BRB519	07-P3-019	-	-	-	-	-	-	-	-	-	-	-	-	-
07BRB520	07-P3-020	-	-	-	-	1.78	-	-	-	-	-	-	-	-
07BRB524	07-P3-024	-	-	-	-	-	-	-	-	-	-	-	-	-
07BRB525	07-P3-025	73.84	0.16	13.83	2.9	-	0.04	0.83	0.19	6.62	0.86	0.01	0.98	100.26
07BRB529	07-P3-029	-	-	-	-	-	-	-	-	-	-	-	-	-
07BRB530	07-P3-030	80.12	0.12	10.48	2.31	1.72	0.03	0.61	0.43	5.42	0.37	0.01	0.83	100.73
07BRB531	07-P3-031	-	-	-	-	-	-	-	-	-	-	-	-	-
07BRB535	07-P3-035	-	-	-	-	-	-	-	-	-	-	-	-	-
07BRB536	07-P3-036	-	-	-	-	-	-	-	-	-	-	-	-	-
07BRB539	07-P3-039	-	-	-	-	-	-	-	-	-	-	-	-	-
07BRB540	07-P3-040	-	-	-	-	1.95	-	-	-	-	-	-	-	-
07BRB542	07-P2-042	-	-	-	-	-	-	-	-	-	-	-	-	-
07BRB545	07-P2-045	-	-	-	-	-	-	-	-	-	-	-	-	-
07BRB547	07-P2-047	-	-	-	-	-	-	-	-	-	-	-	-	-
07BRB549	07-P2-049	-	-	-	-	-	-	-	-	-	-	-	-	-
07BRB550	07-P2-050	78.35	0.14	11.87	1.75	0.38	0.05	0.38	0.69	4.80	1.39	0.01	1.42	100.85
07BRB552	07-P2-052	-	-	-	-	-	-	-	-	-	-	-	-	-
07BRB555	07-P2-054B	-	-	-	-	-	-	-	-	-	-	-	-	-
07BRB557	07-P2-056	-	-	-	-	-	-	-	-	-	-	-	-	-
07BRB559	07-P2-058A	-	-	-	-	-	-	-	-	-	-	-	-	-
07BRB560	07-P2-058B	70.04	0.19	15.18	3.39	1.93	0.04	1.00	0.60	3.21	3.48	0.01	2.44	99.58
07BRB561	07-P2-059	-	-	-	-	-	-	-	-	-	-	-	-	-
07BRB563	07-P1-061	-	-	-	-	-	-	-	-	-	-	-	-	-
07BRB568	07-P1-069	-	-	-	-	-	-	-	-	-	-	-	-	-
07BRB569	07-P1-070	-	-	-	-	-	-	-	-	-	-	-	-	-
07BRB570	07-P1-071	68.1	0.79	13.28	7.22	5.46	0.07	2.82	0.7	4.48	0.73	0.14	2.54	100.87
07BRB572	07-P1-073	-	-	-	-	-	-	-	-	-	-	-	-	-
07BRB576	07-P1-079	-	-	-	-	-	-	-	-	-	-	-	-	-
07BRB577	07-P1-081	-	-	-	-	-	-	-	-	-	-	-	-	-
07BRB579	07-P1-083	-	-	-	-	-	-	-	-	-	-	-	-	-
07BRB580	07-P1-084	79.37	0.23	10.1	3.37	2.16	0.04	0.96	0.24	4.94	0.15	0.02	1.05	100.47

[1] see Chapter 4 for analytical method; [2] - = no duplicate analyses; [3] b.d. = below detection limit

Appendix A.1: continued

Sample	Crystalline Moisture	Free Moisture	F	CO_2	S	Ag	As	Ga	Mo	Sn	Ti	Y	Ba	Be	Bi	Cd
Units	wt. %	wt. %	ppm	wt. %	wt. %	ppm	ppm	ppm	ppm	ppm	ppm	ppm	ppm	ppm	ppm	ppm
07-P3-002	-	-	-	-	-	-	-	-	-	-	-	-	121.7	0.88	0.068	0.07
07-P3-009	-	-	554	-	-	0	3	33	3	9	693	154	-	-	-	-
07-P3-010	0.9	0.11	-	-	-	-	-	-	-	-	-	-	-	-	-	-
07-P3-011	-	-	-	-	-	-	-	-	-	-	-	-	1114	1.57	0.21	0.08
07-P3-012	-	-	-	0.05	2.32	-	-	-	-	-	-	-	-	-	-	-
07-P3-019	-	-	-	-	-	b.d.[3]	0	40	4	9	707	138	-	-	-	-
07-P3-020	1.61	0.12	1272	0.02	0	-	-	-	-	-	-	-	-	-	-	-
07-P3-024	-	-	-	-	-	-	-	-	-	-	-	-	87.3	1.59	0.139	0.12
07-P3-025	-	-	-	-	-	-	-	-	-	-	-	-	-	-	-	-
07-P3-029	-	-	-	-	-	b.d.	0	25	2	8	775	192	-	-	-	-
07-P3-030	0.83	0.07	-	-	-	-	-	-	-	-	-	-	-	-	-	-
07-P3-031	-	-	-	0.08	0.01	-	-	-	-	-	-	-	-	-	-	-
07-P3-035	-	-	612	-	-	-	-	-	-	-	-	-	-	-	-	-
07-P3-036	-	-	-	-	-	-	-	-	-	-	-	-	187.1	4.22	0.176	0.15
07-P3-039	-	-	-	-	-	0	2	22	1	6	637	145	-	-	-	-
07-P3-040	1.19	0.06	-	-	-	-	-	-	-	-	-	-	-	-	-	-
07-P2-042	-	-	-	9.33	0.18	-	-	-	-	-	-	-	-	-	-	-
07-P2-045	-	-	-	-	-	-	-	-	-	-	-	-	142.1	1.02	0.082	0.05
07-P2-047	-	-	1296	-	-	-	-	-	-	-	-	-	-	-	-	-
07-P2-049	-	-	-	-	-	b.d.	1	17	4	5	475	131	-	-	-	-
07-P2-050	0.98	0.1	-	-	-	-	-	-	-	-	-	-	-	-	-	-
07-P2-052	-	-	-	3.71	0.27	-	-	-	-	-	-	-	-	-	-	-
07-P2-054B	-	-	-	-	-	-	-	-	-	-	-	-	147.4	1.31	0.046	0.05
07-P2-056	-	-	-	1	0.01	-	-	-	-	-	-	-	-	-	-	-
07-P2-058A	-	-	-	-	-	b.d.	b.d.	18	3	4	664	158	-	-	-	-
07-P2-058B	1.87	0.12	-	-	-	-	-	-	-	-	-	-	-	-	-	-
07-P2-059	-	-	373	-	-	-	-	-	-	-	-	-	-	-	-	-
07-P1-061	-	-	-	0.41	0.36	-	-	-	-	-	-	-	-	-	-	-
07-P1-069	-	-	-	-	-	-	-	-	-	-	-	-	208.5	0.75	0.047	0.1
07-P1-070	-	-	-	-	-	1	5	15	1	b.d.	7472	24	-	-	-	-
07-P1-071	2.6	0.11	-	-	-	-	-	-	-	-	-	-	-	-	-	-
07-P1-073	-	-	-	0.82	0	-	-	-	-	-	-	-	-	-	-	-
07-P1-079	-	-	537	-	-	-	-	-	-	-	-	-	-	-	-	-
07-P1-081	-	-	-	-	-	-	-	-	-	-	-	-	146.6	1.3	b.d.	0.05
07-P1-083	-	-	-	-	-	b.d.	0	25	1	6	1388	91	-	-	-	-
07-P1-084	1.13	0.06	-	-	-	-	-	-	-	-	-	-	-	-	-	-

Appendix A.1: continued

Sample	Ce	Co	Cr	Cs	Cu	Dy	Er	Eu	Ga	Gd	Hf	Ho	La	Li	Lu	Mo	Nb	Nd	Ni	Pb
Units	ppm	ppm	ppm	ppm	ppm	ppm	ppm	ppm	ppm	ppm	ppm	ppm	ppm	ppm	ppm	ppm	ppm	ppm	ppm	ppm
07-P3-002	18.4	46.1	145	0.172	57	4.6	2.76	1.119	16.99	4.15	3.05	0.99	7.38	33.9	0.439	0.84	5.12	12.58	107	3.8
07-P3-009	-	-	-	-	-	-	-	-	-	-	-	-	-	-	-	-	-	-	-	-
07-P3-010	-	-	-	-	-	-	-	-	-	-	-	-	-	-	-	-	-	-	-	-
07-P3-011	85.8	0.7	14	1.7	3	15.3	10.22	2.05	14.64	13.28	10.55	3.457	33.78	2.6	1.799	3.38	33.54	55.13	3	3.4
07-P3-012	-	-	-	-	-	-	-	-	-	-	-	-	-	-	-	-	-	-	-	-
07-P3-019	-	-	-	-	-	-	-	-	-	-	-	-	-	-	-	-	-	-	-	-
07-P3-020	-	-	-	-	-	-	-	-	-	-	-	-	-	-	-	-	-	-	-	-
07-P3-024	66.7	0.3	7	0.121	4	17.9	11.27	2.904	19.18	13.96	11.65	3.891	27.19	6.6	2.062	1.99	37.98	41.03	1	7.2
07-P3-025	-	-	-	-	-	-	-	-	-	-	-	-	-	-	-	-	-	-	-	-
07-P3-029	-	-	-	-	-	-	-	-	-	-	-	-	-	-	-	-	-	-	-	-
07-P3-030	-	-	-	-	-	-	-	-	-	-	-	-	-	-	-	-	-	-	-	-
07-P3-031	-	-	-	-	-	-	-	-	-	-	-	-	-	-	-	-	-	-	-	-
07-P3-035	-	-	-	-	-	-	-	-	-	-	-	-	-	-	-	-	-	-	-	-
07-P3-036	144.5	0.1	8	1.448	5	30.5	17.53	4.161	29.69	26.24	15.01	6.445	58.24	15.5	2.883	3.61	47.01	84.14	0	8.7
07-P3-039	-	-	-	-	-	-	-	-	-	-	-	-	-	-	-	-	-	-	-	-
07-P3-040	-	-	-	-	-	-	-	-	-	-	-	-	-	-	-	-	-	-	-	-
07-P2-042	-	-	-	-	-	-	-	-	-	-	-	-	-	-	-	-	-	-	-	-
07-P2-045	15.3	52.5	320	0.807	81	4.6	2.77	0.926	16.49	3.93	2.36	0.991	6.38	28.7	0.453	0.53	3.97	10.8	172	2.1
07-P2-047	-	-	-	-	-	-	-	-	-	-	-	-	-	-	-	-	-	-	-	-
07-P2-049	-	-	-	-	-	-	-	-	-	-	-	-	-	-	-	-	-	-	-	-
07-P2-050	-	-	-	-	-	-	-	-	-	-	-	-	-	-	-	-	-	-	-	-
07-P2-052	-	-	-	-	-	-	-	-	-	-	-	-	-	-	-	-	-	-	-	-
07-P2-054B	27.2	53.8	289	0.401	82	6.6	3.88	1.458	20.18	6.23	2.94	1.438	11.19	82.1	0.579	0.79	5.98	18.31	165	1.8
07-P2-056	-	-	-	-	-	-	-	-	-	-	-	-	-	-	-	-	-	-	-	-
07-P2-058A	-	-	-	-	-	-	-	-	-	-	-	-	-	-	-	-	-	-	-	-
07-P2-058B	-	-	-	-	-	-	-	-	-	-	-	-	-	-	-	-	-	-	-	-
07-P2-059	-	-	-	-	-	-	-	-	-	-	-	-	-	-	-	-	-	-	-	-
07-P1-061	-	-	-	-	-	-	-	-	-	-	-	-	-	-	-	-	-	-	-	-
07-P1-069	25	34.9	11	1.367	33	5.4	3.18	1.391	16.21	5.16	3.51	1.18	11.31	25.6	0.497	0.55	6.46	16.47	21	2.6
07-P1-070	-	-	-	-	-	-	-	-	-	-	-	-	-	-	-	-	-	-	-	-
07-P1-071	-	-	-	-	-	-	-	-	-	-	-	-	-	-	-	-	-	-	-	-
07-P1-073	-	-	-	-	-	-	-	-	-	-	-	-	-	-	-	-	-	-	-	-
07-P1-079	-	-	-	-	-	-	-	-	-	-	-	-	-	-	-	-	-	-	-	-
07-P1-081	31.7	34.4	12	6.995	26	7.1	4.16	1.769	23.39	6.42	4.45	1.512	14.27	20.7	0.655	0.35	7.94	20.28	26	0.7
07-P1-083	-	-	-	-	-	-	-	-	-	-	-	-	-	-	-	-	-	-	-	-
07-P1-084	-	-	-	-	-	-	-	-	-	-	-	-	-	-	-	-	-	-	-	-

Appendix A.1: continued

Sample	Pr	Rb	Sb	Sc	Sm	Sn	Sr	Ta	Tb	Th	Ti	Tl	Tm	U	V	W	Y	Yb	Zn	Zr
Units	ppm	ppm	ppm	ppm	ppm	ppm	ppm	ppm	ppm	ppm	ppm	ppm	ppm	ppm	ppm	ppm	ppm	ppm	ppm	ppm
07-P3-002	2.65	1	0.13	30.6	3.54	0.83	410	0.3	0.714	0.8	6114	0.017	0.436	0.19	205	0.2	29.27	2.816	91	114
07-P3-009	-	-	-	-	-	-	-	-	-	-	-	-	-	-	-	-	-	-	-	-
07-P3-010	-	-	-	-	-	-	-	-	-	-	-	-	-	-	-	-	-	-	-	-
07-P3-011	12.12	123.6	0.05	1.5	13.99	5.24	20	2.4	2.301	6.98	493	0.552	1.756	1.49	4	0.6	91.86	11.31	16	272
07-P3-012	-	-	-	-	-	-	-	-	-	-	-	-	-	-	-	-	-	-	-	-
07-P3-019	-	-	-	-	-	-	-	-	-	-	-	-	-	-	-	-	-	-	-	-
07-P3-020	-	-	-	-	-	-	-	-	-	-	-	-	-	-	-	-	-	-	-	-
07-P3-024	8.86	4.9	0.04	1.5	12	5.15	85	2.6	2.648	7.67	573	0.029	1.95	1.72	3	0.3	101.3	13.09	65	301
07-P3-025	-	-	-	-	-	-	-	-	-	-	-	-	-	-	-	-	-	-	-	-
07-P3-029	-	-	-	-	-	-	-	-	-	-	-	-	-	-	-	-	-	-	-	-
07-P3-030	-	-	-	-	-	-	-	-	-	-	-	-	-	-	-	-	-	-	-	-
07-P3-031	-	-	-	-	-	-	-	-	-	-	-	-	-	-	-	-	-	-	-	-
07-P3-035	-	-	-	-	-	-	-	-	-	-	-	-	-	-	-	-	-	-	-	-
07-P3-036	18.55	80.1	0.07	1.9	22.89	8.08	66	3.3	4.705	9.57	709	0.226	2.788	2.17	1	0.5	177	18.43	92	381
07-P3-039	-	-	-	-	-	-	-	-	-	-	-	-	-	-	-	-	-	-	-	-
07-P3-040	-	-	-	-	-	-	-	-	-	-	-	-	-	-	-	-	-	-	-	-
07-P2-042	-	-	-	-	-	-	-	-	-	-	-	-	-	-	-	-	-	-	-	-
07-P2-045	2.2	32.2	0.16	30.6	3.19	0.8	217	0.3	0.684	0.81	5496	0.122	0.442	0.2	207	0.3	29.86	2.857	112	81
07-P2-047	-	-	-	-	-	-	-	-	-	-	-	-	-	-	-	-	-	-	-	-
07-P2-049	-	-	-	-	-	-	-	-	-	-	-	-	-	-	-	-	-	-	-	-
07-P2-050	-	-	-	-	-	-	-	-	-	-	-	-	-	-	-	-	-	-	-	-
07-P2-052	-	-	-	-	-	-	-	-	-	-	-	-	-	-	-	-	-	-	-	-
07-P2-054B	3.79	2.8	0.31	33.1	5.22	1.87	175	0.4	1.039	1.11	6293	0.012	0.596	0.28	226	0.3	46.48	3.709	120	103
07-P2-056	-	-	-	-	-	-	-	-	-	-	-	-	-	-	-	-	-	-	-	-
07-P2-058A	-	-	-	-	-	-	-	-	-	-	-	-	-	-	-	-	-	-	-	-
07-P2-058B	-	-	-	-	-	-	-	-	-	-	-	-	-	-	-	-	-	-	-	-
07-P2-059	-	-	-	-	-	-	-	-	-	-	-	-	-	-	-	-	-	-	-	-
07-P1-061	-	-	-	-	-	-	-	-	-	-	-	-	-	-	-	-	-	-	-	-
07-P1-069	3.53	12.7	0.12	26.6	4.47	1.13	102	0.5	0.857	1.09	7790	0.075	0.499	0.27	205	0.2	34.36	3.128	96	139
07-P1-070	-	-	-	-	-	-	-	-	-	-	-	-	-	-	-	-	-	-	-	-
07-P1-071	-	-	-	-	-	-	-	-	-	-	-	-	-	-	-	-	-	-	-	-
07-P1-073	-	-	-	-	-	-	-	-	-	-	-	-	-	-	-	-	-	-	-	-
07-P1-079	-	-	-	-	-	-	-	-	-	-	-	-	-	-	-	-	-	-	-	-
07-P1-081	4.3	8.5	0.11	30.5	5.48	1.15	83	0.6	1.061	1.44	8981	0.04	0.653	0.36	236	0.5	47.55	4.149	106	173
07-P1-083	-	-	-	-	-	-	-	-	-	-	-	-	-	-	-	-	-	-	-	-
07-P1-084	-	-	-	-	-	-	-	-	-	-	-	-	-	-	-	-	-	-	-	-

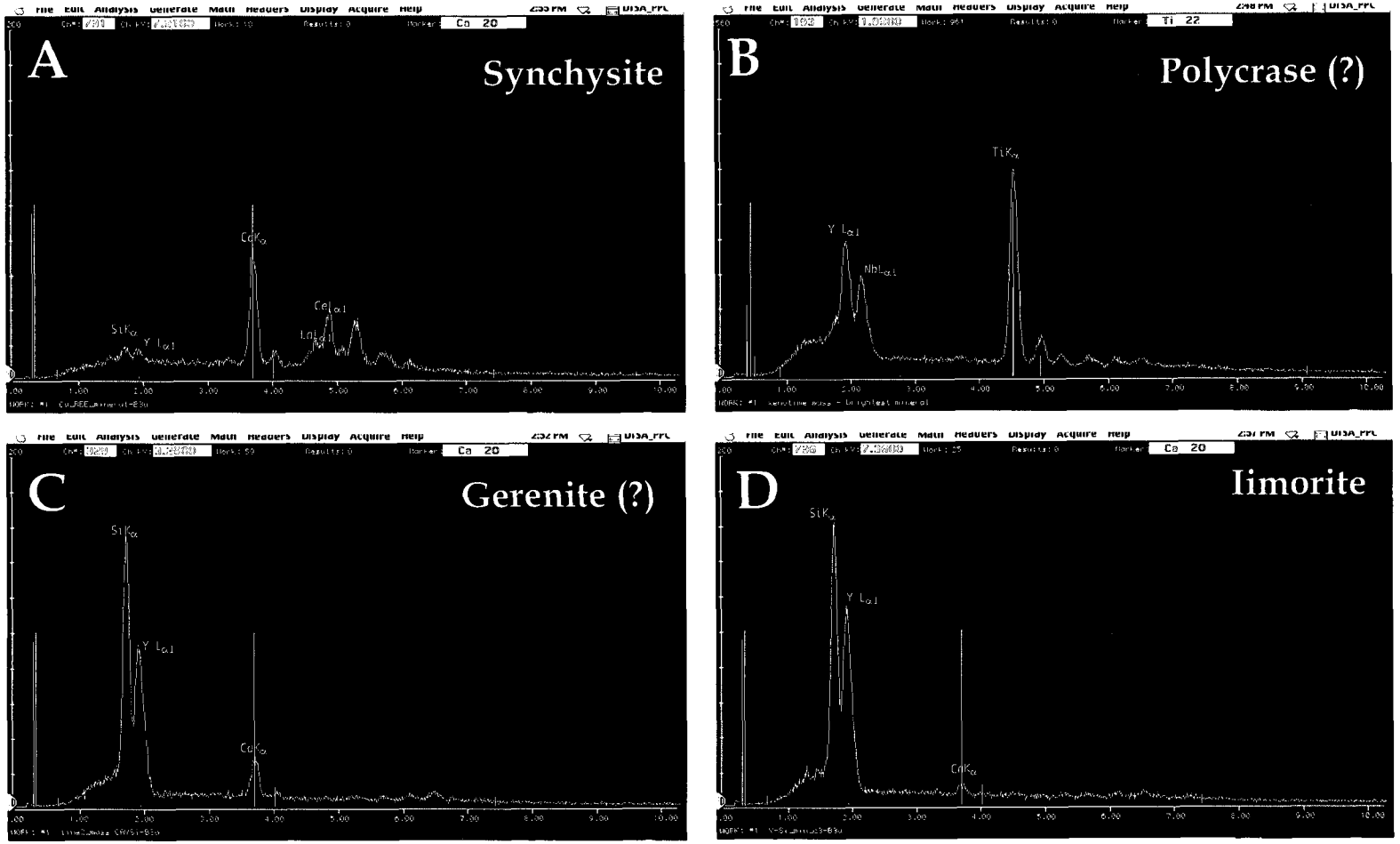

Appendix A.2: Rare earth element bearing minerals. A) Electron dispersive spectra (EDS) of synchysite. B) EDS of polycase. C) EDS of gerenite. D) EDS of iimorite. Identification of mineral spectra by Dr. Anthony Mariano.

Appendix A.3: Error Propagation

$$\frac{\Delta z}{z} = \sqrt{\left(\frac{\Delta x}{x}\right)^2 + \left(\frac{\Delta y}{y}\right)^2}$$

where Δz is the error, z is the ratio (element x/element y), Δx and Δy are the errors associated with their respective elements, x and y in ppm.

According to Burnham and Schweyer (2004) the analytical error for Nb and Zr are 5% and an error of 1 % for Al_2O_3 and TiO_2.

Example:
For Nb (47.2 ppm) and Zr (389 ppm) of sample 07-P3-33

$$\Delta z = \sqrt{\left(\frac{2.36}{47.2}\right)^2 + \left(\frac{19.45}{389}\right)^2} * \frac{47.2}{389}$$

Δz = 0.0086, for the Nb/Zr axis

Appendix A.4: Zircon crystal analyses for determination of Zircon saturation thermometry

Sample	B1A	B1A	B1A	B1A	18L3-8	18L3-9	18L3-10	18L3-11	18L3-12	18L3-13
Analysis	23	24	25	26	6	7	8	9	10	11
Notes[1]					core	core	rim	core	int	int
SiO_2	33.035	33.037	33.063	32.838	32.66	33.11	32.67	32.53	32.42	32.75
TiO_2	0.003	0.01	0.007	0.018	n.d.[3]	n.d.	n.d.	n.d.	n.d.	n.d.
Al_2O_3	b.d.[2]	b.d.	0.006	b.d.	n.d.	n.d.	n.d.	n.d.	n.d.	n.d.
FeO	0.045	0.054	0.076	0.022	n.d.	n.d.	n.d.	n.d.	n.d.	n.d.
CaO	0.01	0.007	0.001	0.013	0.00	0.00	0.02	0.00	0.01	0.00
P_2O_5	0.071	b.d.	b.d.	0.078	0.02	0.02	0.04	0.01	0.03	0.04
F	b.d.	b.d.	0.041	0.011	n.d.	n.d.	n.d.	n.d.	n.d.	n.d.
Sc_2O_3	b.d.	0.002	0.015	0.011	n.d.	n.d.	n.d.	n.d.	n.d.	n.d.
Nb_2O_5	b.d.	b.d.	b.d.	b.d.	n.d.	n.d.	n.d.	n.d.	n.d.	n.d.
La_2O_3	b.d.	0.016	b.d.	b.d.	n.d.	n.d.	n.d.	n.d.	n.d.	n.d.
Ce_2O_3	0.004	0.02	0.008	0.013	n.d.	n.d.	n.d.	n.d.	n.d.	n.d.
Nd_2O_3	b.d.	0.042	0.014	b.d.	n.d.	n.d.	n.d.	n.d.	n.d.	n.d.
Gd_2O_3	0.099	0.143	b.d.	0.138	n.d.	n.d.	n.d.	n.d.	n.d.	n.d.
Dy_2O_3	0.147	b.d.	0.068	0.164	n.d.	n.d.	n.d.	n.d.	n.d.	n.d.
Er_2O_3	0.154	0.01	0.024	0.053	n.d.	n.d.	n.d.	n.d.	n.d.	n.d.
Yb_2O_3	0.17	0.02	0.186	0.141	n.d.	n.d.	n.d.	n.d.	n.d.	n.d.
Y_2O_3	0.749	b.d.	0.005	0.444	0.47	0.48	0.60	0.77	0.59	0.38
PbO_2	b.d.	0.042	b.d.	b.d.	n.d.	n.d.	n.d.	n.d.	n.d.	n.d.
Bi_2O_5	b.d.	0.004	0.039	b.d.	n.d.	n.d.	n.d.	n.d.	n.d.	n.d.
ZrO_2	64.989	66.214	66.398	66.995	65.99	67.13	65.33	65.18	65.53	65.87
HfO_2	1.448	1.768	1.732	1.632	1.66	1.46	1.31	1.56	1.39	1.62
ThO_2	0.039	0.003	b.d.	0.096	n.d.	n.d.	n.d.	n.d.	n.d.	n.d.
UO_2	0.035	0.023	0.068	0.023	n.d.	n.d.	n.d.	n.d.	n.d.	n.d.
Total	100.998	101.414	101.75	102.689	100.81	102.19	99.97	100.04	99.97	100.65

[1] core = microphenocryst core zone, int = intermediate zone, rim = rim of microphenocryst; [2] b.d. = below detection limit ; [3] n.d. = not determined

Appendix A.4: Continued.

Sample	18L3-14	83L1-1	83L1-2	83L1-3	83L1-4	83L1-5	83L1-6	83L3-1	83L3-2	83L3-3	83L3-4	83L3-5
Analysis	12	13	14	15	16	17	18	19	20	21	22	23
Notes[1]	rim	int-core	int	int	int	rim	core	core	core	core	int	rim
SiO_2	32.87	32.87	32.87	32.84	32.71	32.69	32.70	32.68	32.98	32.75	32.73	33.16
TiO_2	n.d.	n.d.	n.d.	n.d.	n.d.	n.d.	n.d.	n.d.	n.d.	n.d.	n.d.	n.d.
Al_2O_3	n.d.	n.d.	n.d.	n.d.	n.d.	n.d.	n.d.	n.d.	n.d.	n.d.	n.d.	n.d.
FeO	n.d.	n.d.	n.d.	n.d.	n.d.	n.d.	n.d.	n.d.	n.d.	n.d.	n.d.	n.d.
CaO	0.00	0.01	0.03	0.00	0.02	0.01	0.02	0.00	0.01	0.00	0.01	0.00
P_2O_5	0.00	0.03	0.01	0.00	0.00	0.00	0.07	0.02	0.00	0.00	0.00	0.00
F	n.d.	n.d.	n.d.	n.d.	n.d.	n.d.	n.d.	n.d.	n.d.	n.d.	n.d.	n.d.
Sc_2O_3	n.d.	n.d.	n.d.	n.d.	n.d.	n.d.	n.d.	n.d.	n.d.	n.d.	n.d.	n.d.
Nb_2O_5	n.d.	n.d.	n.d.	n.d.	n.d.	n.d.	n.d.	n.d.	n.d.	n.d.	n.d.	n.d.
La_2O_3	n.d.	n.d.	n.d.	n.d.	n.d.	n.d.	n.d.	n.d.	n.d.	n.d.	n.d.	n.d.
Ce_2O_3	n.d.	n.d.	n.d.	n.d.	n.d.	n.d.	n.d.	n.d.	n.d.	n.d.	n.d.	n.d.
Nd_2O_3	n.d.	n.d.	n.d.	n.d.	n.d.	n.d.	n.d.	n.d.	n.d.	n.d.	n.d.	n.d.
Gd_2O_3	n.d.	n.d.	n.d.	n.d.	n.d.	n.d.	n.d.	n.d.	n.d.	n.d.	n.d.	n.d.
Dy_2O_3	n.d.	n.d.	n.d.	n.d.	n.d.	n.d.	n.d.	n.d.	n.d.	n.d.	n.d.	n.d.
Er_2O_3	n.d.	n.d.	n.d.	n.d.	n.d.	n.d.	n.d.	n.d.	n.d.	n.d.	n.d.	n.d.
Yb_2O_3	n.d.	n.d.	n.d.	n.d.	n.d.	n.d.	n.d.	n.d.	n.d.	n.d.	n.d.	n.d.
Y_2O_3	0.15	0.07	0.16	0.03	0.16	0.07	0.25	0.48	0.40	0.59	0.29	0.34
PbO_2	n.d.	n.d.	n.d.	n.d.	n.d.	n.d.	n.d.	n.d.	n.d.	n.d.	n.d.	n.d.
Bi_2O_5	n.d.	n.d.	n.d.	n.d.	n.d.	n.d.	n.d.	n.d.	n.d.	n.d.	n.d.	n.d.
ZrO_2	66.32	66.71	65.92	67.00	67.20	66.76	66.21	65.62	66.04	66.14	66.14	65.86
HfO_2	1.56	1.32	1.07	1.03	1.09	1.41	0.88	1.34	1.19	1.08	1.06	1.27
ThO_2	n.d.	n.d.	n.d.	n.d.	n.d.	n.d.	n.d.	n.d.	n.d.	n.d.	n.d.	n.d.
UO_2	n.d.	n.d.	n.d.	n.d.	n.d.	n.d.	n.d.	n.d.	n.d.	n.d.	n.d.	n.d.
Total	100.90	101.01	100.05	100.90	101.17	100.95	100.14	100.14	100.63	100.56	100.23	100.63

Appendix A.4: Continued.

Sample	60L1-9	60L1-10	60L1-11	18L4-1	18L4-2	18L4-3	18L4-4	18L4-5	18L4-6
Analysis	24	25	26	27	28	29	30	31	32
Notes[1]	rim	core	rim	rim	int	int	int	int	core
SiO_2	32.92	32.95	32.32	32.95	32.33	32.78	32.75	32.71	32.65
TiO_2	n.d.	n.d.	n.d.	n.d.	n.d.	n.d.	n.d.	n.d.	n.d.
Al_2O_3	n.d.	n.d.	n.d.	n.d.	n.d.	n.d.	n.d.	n.d.	n.d.
FeO	n.d.	n.d.	n.d.	n.d.	n.d.	n.d.	n.d.	n.d.	n.d.
CaO	0.00	0.02	0.03	0.00	0.01	0.00	0.00	0.00	0.00
P_2O_5	0.01	0.10	0.01	0.01	0.00	0.02	0.04	0.07	0.00
F	n.d.	n.d.	n.d.	n.d.	n.d.	n.d.	n.d.	n.d.	n.d.
Sc_2O_3	n.d.	n.d.	n.d.	n.d.	n.d.	n.d.	n.d.	n.d.	n.d.
Nb_2O_5	n.d.	n.d.	n.d.	n.d.	n.d.	n.d.	n.d.	n.d.	n.d.
La_2O_3	n.d.	n.d.	n.d.	n.d.	n.d.	n.d.	n.d.	n.d.	n.d.
Ce_2O_3	n.d.	n.d.	n.d.	n.d.	n.d.	n.d.	n.d.	n.d.	n.d.
Nd_2O_3	n.d.	n.d.	n.d.	n.d.	n.d.	n.d.	n.d.	n.d.	n.d.
Gd_2O_3	n.d.	n.d.	n.d.	n.d.	n.d.	n.d.	n.d.	n.d.	n.d.
Dy_2O_3	n.d.	n.d.	n.d.	n.d.	n.d.	n.d.	n.d.	n.d.	n.d.
Er_2O_3	n.d.	n.d.	n.d.	n.d.	n.d.	n.d.	n.d.	n.d.	n.d.
Yb_2O_3	n.d.	n.d.	n.d.	n.d.	n.d.	n.d.	n.d.	n.d.	n.d.
Y_2O_3	0.05	0.54	0.37	0.29	0.39	0.40	0.39	0.35	0.39
PbO_2	n.d.	n.d.	n.d.	n.d.	n.d.	n.d.	n.d.	n.d.	n.d.
Bi_2O_5	n.d.	n.d.	n.d.	n.d.	n.d.	n.d.	n.d.	n.d.	n.d.
ZrO_2	66.71	64.36	65.32	66.09	66.09	65.42	65.23	64.93	64.43
HfO_2	1.75	1.32	1.13	1.60	1.39	1.49	1.38	1.41	1.65
ThO_2	n.d.	n.d.	n.d.	n.d.	n.d.	n.d.	n.d.	n.d.	n.d.
UO_2	n.d.	n.d.	n.d.	n.d.	n.d.	n.d.	n.d.	n.d.	n.d.
Total	101.45	99.31	99.17	100.94	100.20	100.11	99.79	99.47	99.12

Appendix A.5: Lower limit of detection determination

Element-Standard	Concentration	peak (cps)*	background (cps)*	Time total (peak + bkg)	m[1]	Squareroot[1] Rb/T	Lower Limit of Detection wt. %[1]	Lower Limit of Detection (ppm)
Ti-Cr Augite	0.29	432	126.5	60	1053.4483	1.4520	0.004	39
Ti-Cr Augite	0.29	603.19	179.4	60	1461.3448	1.7292	0.003	33
Ti-Cr Augite	0.29	603.19	179.4	150	1461.3448	1.0936	0.002	21
Ti-hypersthene	0.06	188.21	129	60	986.8333	1.4663	0.004	42
Ti-hypersthene	0.06	258.29	176	60	1371.5000	1.7127	0.004	35
Ti-SRM 612	0.005	190.4	182.1	150	1660.0000	1.1018	0.002	19
Ti-SRM 612	0.005	131.5	125.7	150	1160.0000	0.9154	0.002	22
Ti-SRM 612	0.005	182.5	173.6	150	1780.0000	1.0758	0.002	17
Ti-zircon	0.0135	330.97	309.38	300	1599.2593	1.0155	0.002	18
Ti-zircon	0.0135	349.63	330.48	300	1418.5185	1.0496	0.002	21
Ti-zircon	0.0117	240.2	224.89	300	1308.5470	0.8658	0.002	19
Total Average							0.003	26

* cps = counts per second; [1] see below for explanation of the calculated columns.

$$LLoD = \frac{2\sqrt{2}}{m} * \sqrt{\frac{Rb}{T}}$$

where LLoD is the lower limit of detection, m is (Rp-Rb/concentration), Rp is the counts per second for the peak, Rb is the counts per second for the background and T is time.

Appendix A.6: Complete Ti-in-zircon data set including standard analyses.

Sample	Analysis	Analysis Length (seconds)	Comment[1]	Line	Position[2] X	Position[2] Y	Spectrometer - Ti (wt. %) 1	Spectrometer - Ti (wt. %) 2	Spectrometer - Ti (wt. %) 3	Spectrometer Error 1-sigma 1	Spectrometer Error 1-sigma 2	Spectrometer Error 1-sigma 3
Samples												
07-P3-15	35	300	core	1	6655	21828	0.001	b.d.[3]	b.d.	0.00001	-	-
07-P3-15	36	300	rim	1	6633	21822	0.002	b.d.	0.001	0.00001	-	0.00001
07-P3-18	2	180	10 µm square, core, Fig. 5.1	1	10387	18488	0.002	0.001	0.001	0.00141	-	0.00087
07-P3-18	3	180	10 µm square, int, Fig. 5.1	1	10363	18488	0.003	b.d.	b.d.	0.00147	-	-
07-P3-18	4	180	10 µm square, int, Fig. 5.1	1	10348	18496	0.001	0.001	0.004	-	-	0.00128
07-P3-18	5	180	10 µm square, int, Fig. 5.1	1	10336	18498	0.001	b.d.	b.d.	0.00071	-	-
07-P3-18	6	180	5 µm square, int, Fig. 5.1	1	10324	18500	0.002	0.001	0.002	0.00101	0.00074	0.00098
07-P3-18	7	300	5 µm square, int, Fig. 5.1	1	10308	18500	0.002	0.002	0.002	0.00001	0.00001	0.00001
07-P3-18	8	300	5 µm square, int, Fig. 5.1	1	10298	18500	0.001	0.002	0.004	0.00001	0.00001	0.00003
07-P3-18	9	300	repeat 7, Fig. 5.1	1	10288	18500	b.d.	0.003	0.001	-	0.00002	0.00001
07-P3-18	10	300	int, right side Fig. 5.1	1	10479	18467	b.d.	b.d.	0.002	-	-	0.00001
07-P3-18	11	300	middle int, right side Fig. 5.1	1	10491	18471	b.d.	b.d.	0.002	-	-	0.00001
07-P3-18	12	300	rim, right side Fig. 5.1	1	10503	18475	0.002	b.d.	0.001	0.00001	-	0.00001
07-P3-18	13	300	repeat 8	1	10298	18497	0.001	0.001	0.002	0.00001	0.00001	0.00001
07-P3-18	14	300	circle in nearest core, Fig. 5.1	1	10324	18545	b.d.	0.001	0.003	-	0.00001	0.00002
07-P3-18	14a	300	repeat 14	1	10382	18455	b.d.	b.d.	0.001	-	-	0.00063
07-P3-18	15	300	repeat 3	1	10351	18456	b.d.	b.d.	b.d.	-	-	-
07-P3-18	16	300	repeat 4, circles Fig. 5.1	1	10338	18458	b.d.	b.d.	b.d.	-	-	-
07-P3-18	17	300	repeat 5, circles Fig. 5.1	1	10325	18460	b.d.	b.d.	b.d.	-	-	-
07-P3-18	18	300	repeat 6, circles Fig. 5.1	1	10311	18461	b.d.	b.d.	b.d.	-	-	-
07-P3-18	19	300	repeat 7, circles Fig. 5.1	1	10298	18463	b.d.	b.d.	b.d.	-	-	-
07-P3-18	20	300	repeat 8, circles Fig. 5.1	1	10285	18465	b.d.	b.d.	b.d.	-	-	-
07-P3-18	21	300	Figure 5.2A, B	3	19058	18276	b.d.	b.d.	b.d.	-	-	-
07-P3-18	22	300	Figure 5.2A, B	3	19052	18302	b.d.	b.d.	b.d.	-	-	-
07-P3-18	23	300	Figure 5.2A, B	3	19015	18345	0.004	0.003	0.003	0.00002	0.00002	0.00002
07-P3-18	24	300	Figure 5.2A, B	3	19037	18348	b.d.	b.d.	b.d.	-	-	-
07-P3-18	25	300	Figure 5.2A, B	3	18994	18351	0.02	0.015	0.018	0.00012	0.00009	0.00011
07-P3-18	26	300	Figure 5.2A, B	3	18990	18362	0.005	0.003	0.003	0.00003	0.00002	0.00002
07-P3-18	27	300	Figure 5.2A, B	3	18984	18367	b.d.	b.d.	b.d.	-	-	-
07-P1-60	28	300	rim	1	14131	10060	0.003	0.001	0.003	0.00102	0.00047	0.0009
07-P1-60	29	300	dark zone in CL, int	1	14120	10045	0.002	b.d.	b.d.	0.00001	-	-
07-P1-60	30	300	light zone in CL, int	1	14110	10027	0.001	b.d.	b.d.	0.00001	-	-
07-P1-60	31	300	opposite rim to analysis 28	1	14101	10009	b.d.	b.d.	b.d.	-	-	-
07-P1-60	32	300	core	2	6657	17796	b.d.	b.d.	b.d.	-	-	-

Appendix A.6: Complete Ti-in-zircon data set including standard analyses.

Sample	Analysis	Analysis Length (seconds)	Comment[1]	Line	Position[2] X	Position[2] Y	Spectrometer - Ti (wt. %) 1	Spectrometer - Ti (wt. %) 2	Spectrometer - Ti (wt. %) 3	Spectrometer Error 1-sigma 1	Spectrometer Error 1-sigma 2	Spectrometer Error 1-sigma 3
07-P1-60	33	300	int	2	6657	17806	b.d.	b.d.	b.d.	-	-	-
07-P1-60	34	300	rim	2	6657	17815	b.d.	b.d.	b.d.	-	-	-
07-P1-83	15	300	Figure 5.2E, F	1	2850	4745	0.004	0.003	0.003	0.00104	0.00079	0.00076
07-P1-83	16	300	Figure 5.2E, F	1	2878	4758	0.003	0.003	0.002	0.00002	0.00002	0.00001
07-P1-83	17	300	Figure 5.2E, F	1	2891	4766	0.004	0.005	0.004	0.00002	0.00003	0.00002
07-P1-83	18	300	Figure 5.2E, F	1	2933	4751	0.022	0.021	0.018	0.00013	0.00013	0.00011
07-P1-83	19	300	Figure 5.2E, F	1	2933	4741	0.017	0.017	0.014	0.0001	0.0001	0.00008
07-P1-83	20	300	Figure 5.2E, F	1	2933	4730	0.02	0.019	0.017	0.00012	0.00011	0.0001
07-P1-83	21	300	Figure 5.2E, F	1	2933	4720	0.02	0.02	0.019	0.00012	0.00012	0.00011
07-P1-83	22	300	Figure 5.2E, F	1	2856	4739	0.001	0.002	b.d.	0.00001	0.00001	-
07-P1-83	23	300	Figure 5.2E, F	1	2849	4734	0.001	0.001	b.d.	0.00001	0.00001	-
07-P1-83	24	300	Figure 5.2E, F	1	2842	4729	0.001	0.002	b.d.	0.00001	0.00001	-
07-P1-83	25	300	Figure 5.2E, F	1	2835	4724	b.d.	0.001	b.d.	-	0.00001	-
07-P1-83	26	300	Figure 5.2E, F	1	2828	4719	b.d.	0.001	b.d.	-	0.00001	-
07-P1-83	27	300	repeat 20, Figure 5.2E, F	1	2948	4729	0.014	0.013	0.012	0.00115	0.00088	0.00095
07-P1-83	28	300	repeat 26, Figure 5.2E, F	1	2856	4716	b.d.	0.003	0.001	-	0.00076	0.00048
07-P1-83	8	300	repeat 20, Figure 5.2E, F	1	4232	5189	0.016	0.021	0.018	0.00114	0.00099	0.00097
07-P1-83	9	300	Figure 5.2C, D	3	2277	16417	0.03	0.027	0.028	0.0012	0.00097	0.00101
07-P1-83	10	300	Figure 5.2C, D	3	2240	16440	0.022	0.021	0.021	0.00013	0.00013	0.00013
07-P1-83	11	300	Figure 5.2C, D	3	2225	16425	0.009	0.008	0.008	0.00005	0.00005	0.00005
07-P1-83	12	300	Figure 5.2C, D	3	2218	16428	0.005	0.004	0.004	0.00003	0.00002	0.00002
07-P1-83	13	300	Figure 5.2C, D	3	2211	16432	0.003	0.002	0.001	0.00002	0.00001	0.00001
Standards												
ZIRC STD	1	150	-		33782	14547	0.002	b.d.	b.d.	0.00139	-	-
SRM 610	1	30	-		7197	31977	0.052	0.049	0.052	0.00302	0.0025	0.00255
SRM 610	2	30	-		7148	31977	0.051	0.048	0.052	0.00306	0.0025	0.00255
SRM 610	3	30	-		7148	31897	0.049	0.053	0.054	0.00069	0.00064	0.00065
SRM 610	4	30	-		7077	31766	0.054	0.051	0.053	0.00076	0.00061	0.00064
SRM 610	5	30	-		7006	31636	0.052	0.051	0.051	0.00073	0.00061	0.00061
SRM 612	6	150	-		6987	29071	0.007	0.005	0.005	0.00111	0.00094	0.00098
SRM 612	7	150	-		6922	29071	0.005	0.006	0.005	0.00113	0.00104	0.00096
SRM 612	8	150	-		6858	29071	0.004	0.005	0.005	0.00126	0.00097	0.00095
SRM 612	9	150	-		6793	29071	0.006	0.005	0.005	0.00109	0.00092	0.00091
SRM 612	10	150	-		6748	29038	0.006	0.004	0.005	0.00005	0.00003	0.00004
SRM 612	2	150	-		6837	29088	0.004	0.004	0.002	0.00214	0.00154	0.00147
SRM 612	3	150	-		6824	29038	0.002	0.006	0.007	0.00177	0.00209	0.00219
SRM 612	4	150	-		6834	28999	0.001	0.003	b.d.	-	0.00202	-
SRM 612	5	150	-		6889	28901	0.004	0.005	0.003	0.00125	0.00086	0.00083

[1] core = microphenocryst core zone, int = intermediate zone, rim = rim of microphenocryst; [2] position = EMP stage position; [3] b.d. = below detection limit.

Appendix A.7: Conversion of glass to quartz and albite

Table A: Lithogeochemistry

Reference	Least Altered aphyric	Normalized Anhydrous
Comment	Avg. 5	Least Altered
Units	wt. %	wt. %
SiO_2	75.85	76.47
TiO_2	0.14	0.14
Al_2O_3	12.67	12.77
Fe_2O_3	0.56	0.56
FeO	1.80	1.82
MnO	0.03	0.03
MgO	0.84	0.85
CaO	0.27	0.28
Na_2O	5.95	6.00
K_2O	0.86	0.87
P_2O_5	0.01	0.01
L.O.I.	1.06	-
Total	100.25	100.00

Table B: Mass conversion of glass to albite and non-albite components

Cation	Pure Albite	Least Altered Rock	Difference*	Least Altered Composition	
				Grams used to	Non-albite
Density (g/cm^3)	2.62	2.71		form Albite	grams
Units	grams	grams	grams	grams	grams
Si	42.51	35.45	-7.06	16.18	19.27
Ti		0.08			0.08
Al	13.61	6.71	-6.90	5.18	1.53
Fe(III)		0.39			0.39
Fe(II)		1.40	1.40		1.40
Mn		0.02			0.02
Mg		0.51			0.51
Ca		0.20			0.20
Na	11.600	4.41	**-7.19**	4.41	0.00
K		0.72	0.72		0.72
P		0.00			0.00
O	32.28	50.09	17.81	12.29	37.80
	100.00	100.00		38.06	61.91

* Na is the limiting cation as it has the greatest difference.

Table C: Mass to volume conversion using densities in Table B

	Albite	Non-albite	Total Volume
Volume (%)	14.5	22.8	37.4
Normalized	38.9	61.1	100.0